UNIVERSITY OF CALIFORNIA SAN DIEGO

Multiple-Scale Analyses of Forced, Nonlinear Waves: Graphene Hydrodynamics and Surface Water Waves

A dissertation submitted in partial satisfaction of the
requirements for the degree
Doctor of Philosophy

in

Physics

by

Thomas John Zdyrski

Committee in charge:

Professor Falk Feddersen, Chair
Professor John McGreevy, Co-Chair
Professor Daniel Arovas
Professor Patrick Diamond
Professor William Young

2021

The dissertation of Thomas John Zdyrski is approved, and it is acceptable in quality and form for publication on microfilm and electronically.

University of California San Diego

2021

DEDICATION

For my parents, who taught me that anything is possible when you dedicate yourself.

EPIGRAPH

Nature does not consist entirely, or even largely, of problems designed by a Grand Examiner to come out neatly in finite terms, and whatever subject we tackle the first need is to overcome timidity about approximating.

—*Sir Harold Jeffreys*

TABLE OF CONTENTS

LIST OF FIGURES

LIST OF TABLES

ACKNOWLEDGEMENTS

I will forever be thankful to Falk Feddersen: my advisor, my mentor and my friend. Your vast breadth of knowledge and humble demeanor are truly inspiring. I have been incredibly fortunate to have such a powerful advocate who is always willing to stand up for his students. Your tireless assistance every day of the week, and at all hours of the day, helped make daunting tasks feel surmountable. Our countless editing sessions have made me a better writer, and it fills me with great joy to know that my scientific writing style will always carry a touch of yours. You gave me the freedom to follow my curiosity, and even when that took me outside your extensive range of expertise, you still guided me and helped be grow. And throughout it all, you allowed me to try, occasionally stumble and ultimately succeed by offering gentle encouragement and sagely advice (even if I never switched from vim to emacs). Everyday, I am grateful that you took the risk to mentor a physics graduate student, in spite of the many bureaucratic hurdles and cultural differences. I have been blessed with the most amazing advisor, and you have molded me as a scientist in ways I will treasure for the rest of my life.

I owe a huge thanks to the Scripps community. The friendships and memories I shared with the Feddersen group will be treasured; Mike Kovatch, Derek Grimes, Greg Sinnett, Matt Spydell and Xiaodong Wu are the greatest coworkers a graduate student could have. I also value the frequent chats and advice from Hiro Matsumoto, Julia Fiedler, Adam Young and the rest of Mark Merrifield's and Bob Guza's group. Sarah Giddings has ensured that her and our groups stay connected and thriving, and my conference presentations benefited immeasurably from her group's feedback. Additionally, I owe many thanks to Bia Villas Boas and Nick Pizzo for their extremely constructive feedback and advice. I would also like to thank Bill Young for his many thought-provoking conversations and illuminating insights. Finally, I was fortunate enough to share two cohorts: one group of enthusiastic scholars in physical oceanography, and another collection of hard-working intellectuals in physics.

The physics department is filled with numerous dedicated, selfless individuals, and I couldn't possibly thank them all here. I am extremely grateful to my co-advisor John McGreevy for teaching me how to publish my first scientific paper. You are one of the most brilliant scientists I have ever met, and I was thrilled when you agreed to work with me on a project. You deepened my understanding of physics, and I learned so much from our meetings. Sharmila Poddar is often the first staff member prospective physics graduates meet; her compassion and care make the department more welcoming, while her protectiveness has enabled countless graduates to overcome the struggles of graduate school. Catherine McConney is one of the strongest proponents of physics graduates, and I am so grateful for her tireless advocating on behalf

of the graduate population. The Physics Graduate Council has been the most influential organization in my graduate career, and I thank every single member for their tireless volunteering. I am honored to have served on the Council, and I will cherish the times we all shared. I also owe a huge thanks to Jasmyn Hornbuckle and Erin Gerlach from the business office; without their help, we could not host the events that bring our department together and make us feel like a family. Finally, I can't give enough thanks to Brad Hanson, my teaching assistant supervisor and friend. Our countless intellectual conversations made my years as a graduate student infinitely more interesting. Thank you for enabling me to continue my studies while providing me with enriching and engaging employment.

Thank you to my little brother Christopher for motivating me to work harder and strive to be a better sibling. You helped fill every day of our childhood with fun and adventures, and your competitiveness constantly pushed me to improve. Even though we are now on opposite sides of the continent and reunions are rarer, I feel our bond has only strengthened—especially as you've begun your graduate student journey. You are becoming a fantastic scientist, and I look forward to seeing your many successes throughout your career. I can't wait to tell everyone that I knew you before you became a world-class biologist. And just remember: though you may be bigger and stronger than me now, you'll always be my little bro.

To my incredible parents, Terry and Tom: none of this would have been possible without your endless support and assistance. At a young age you taught me the importance of perseverance, whether in sports, martial arts or academics. I would never have attempted a doctorate if not for the determination and resolve you instilled in me. Mom, you nurtured and encouraged me in ways innumerable; from constantly cleaning up infant vomit to feeding me beef and potatoes through a straw after my jaw surgery, you have always done the tough jobs so I could thrive. Even my love of physics is owed to you, as your regular trips to and from my high school allowed me to pursue many after-school clubs and activities such as Shore Bowl, where I first encountered physics. And Dad, I have come to cherish your wisdom and teachings more and more as I've grown. From fixing mechanical devices to developing social skills to watching where my feet are, you have set me up to succeed in life in so many ways. And all throughout my academic career, you two have stood by me, listening to my struggles, encouraging my endeavors and celebrating my achievements. I can't begin to express how much I appreciate the infinite ways you have shown your love for me; I simply hope I can use the tools and gifts you have given me to make you proud.

Chapter 1, in full, is a reprint of the material as it appears in Effects of Dissipation on Solitons in the Hydrodynamic Regime of Graphene in Physical Review B by T. Zdyrski and J. McGreevy in 2019. The dissertation author was the primary investigator and author of this paper.

Chapter 2, in full, is a reprint of the material as it appears in Wind-Induced Changes to Surface Gravity Wave Shape in Deep to Intermediate Water in Journal of Fluid Mechanics by T. Zdyrski and F. Feddersen in 2020. The dissertation author was the primary investigator and author of this paper.

Chapter 3, in full, is a reprint of the material as it appears in Wind-Induced Changes to Surface Gravity Wave Shape in Shallow Water in Journal of Fluid Mechanics by T. Zdyrski and F. Feddersen in 2021. The dissertation author was the primary investigator and author of this paper.

Chapter 4, in full, is currently being prepared for submission for publication of the material to Journal of Fluid Mechanics by T. Zdyrski and F. Feddersen. The dissertation author was the primary investigator and author of this paper.

VITA

2015	A. B. in Physics *cum laude*, Princeton University
2017	M. S. in Physics, University of California San Diego
2021	Ph. D. in Physics, University of California San Diego

PUBLICATIONS

T. Zdyrski and J. McGreevy, "Effects of dissipation on solitons in the hydrodynamic regime of graphene", Phys. Rev. B **99**, 10.1103/PhysRevB.99.235435 (2019)

T. Zdyrski and F. Feddersen, "Wind-induced changes to surface gravity wave shape in deep to intermediate water", J. Fluid Mech. **903**, 10.1017/jfm.2020.628 (2020)

T. Zdyrski and F. Feddersen, "Wind-induced changes to surface gravity wave shape in shallow water", J. Fluid Mech. **913**, 10.1017/jfm.2021.15 (2021)

ABSTRACT OF THE DISSERTATION

Multiple-Scale Analyses of Forced, Nonlinear Waves: Graphene Hydrodynamics and Surface Water Waves

by

Thomas John Zdyrski

Doctor of Philosophy in Physics

University of California San Diego, 2021

Professor Falk Feddersen, Chair
Professor John McGreevy, Co-Chair

Nonlinear interactions in physical systems make analyzing the dynamics challenging. Multiple-scale analyses are asymptotic perturbation techniques useful for analyzing nonlinear systems that possess scale-separation between the relevant physical scales. Graphene is a two-dimensional lattice of carbon atoms which exhibits many unique electrical properties, such as a viscous, hydrodynamic regime where the electrons become strongly interacting. We consider both the Dirac fluid and Fermi liquid regimes in gated graphene, and we investigate the one-dimensional propagation of electronic solitons. By leveraging the scale-separation between the wave-propagation time scale and nonlinear-interaction time scale, we utilize a multiple-scale analysis to derive a Korteweg–de Vries (KdV)–Burgers equation governing the wave's evolution. We numerically solve the KdV–Burgers equation and analyze the viscous decay and entropy

production. Finally, we propose experimental realizations of these effects to measure the shear viscosity of graphene.

Surface water waves also possess nonlinear interactions and permit nonlinear, periodic waves of permanent form known as Stokes waves in intermediate- and deep-water. Wind forcing causes wave growth and decay, but it can also influence wave shape. To study the effect of wind on the shape of these nonlinear Stokes waves, we again utilize scale-separation between the wave-propagation time scale and the nonlinear-interaction time scale. We then analytically solve the resulting system for three different wind-induced surface pressure profiles (Jeffreys, Miles, and generalized Miles) to calculate the wind-induced changes to the wave's shape statistics, growth rate, and phase speed. These results are constrained by existing large eddy simulations and are consistent with prior laboratory experiments.

Shallow water supports surface waves known as solitary waves that balance nonlinearity and dispersion. By applying the same Jeffreys-type surface pressure forcing, we analyze the effect of wind on shallow-water wave shape. Another multiple-scale analysis yields a KdV–Burgers equation for the wave's profile, and we solve this numerically to investigate the wave's skewness and asymmetry resulting from the solitary waves's wind-induced, bound, dispersive tail. Extending this analysis to a planar, sloping bathymetry instead yields a variable-coefficient KdV–Burgers equation. Numerically solving this equation reveals the interaction of wind-forcing and shoaling on wave growth, width change, and rear-shelf generation.

Chapter 1

Effects of dissipation on solitons in the hydrodynamic regime of graphene

1.1 Abstract

We use hydrodynamic techniques to analyze the one-dimensional propagation of solitons in gated graphene on an arbitrary uniform background current. Results are derived for both the Fermi liquid and Dirac fluid regimes. We find that these solutions satisfy the Korteweg-de Vries-Burgers equation. Viscous dissipation and ohmic heating are included, causing the solitons to decay. Experiments are proposed to measure this decay and thereby quantify the shear viscosity in graphene.

1.2 Introduction

Graphene offers a promising platform to realize and explore the hydrodynamics of electrons [4]. Graphene serves as an excellent model system for theorists due to its simple electronic band structure; likewise, it is utilized by experimentalists for the relative ease of manufacturing pure samples. In certain thermodynamic regimes, the electrons in graphene become strongly interacting; hydrodynamics is a useful tool to study strongly interacting systems not amenable to ordinary perturbation methods. Hydrodynamics is applicable when systems rapidly thermalize and when both the mean-free path (l_{ee}) and mean-free time (τ_{ee}) are short compared to the relevant length and time scales of the problem [5]. When a system is in this regime, the main observables are conserved quantities: these are precisely the objects tracked by

hydrodynamics.

Graphene has two different hydrodynamic regimes. When the chemical potential μ is much larger than the temperature, $k_B T \ll \mu$, graphene behaves like an ordinary conductor and is described by Fermi liquid theory. First discovered by Landau [6] in 1959, Fermi liquid theory treats the electrons as a non-interacting Fermi gas and then turns on interactions adiabatically; thus, Fermi liquids exhibit *weakly* interacting quasiparticles. The excitations, no longer pure electron states, are instead described as quasiparticles. Though weak interactions imply long mean-free paths, graphene can actually exhibit hydrodynamic effects in this regime. The electrons in graphene only weakly interact with phonons (which typically disrupt the hydrodynamic signature), so it is still possible to have $l_{\text{ee}} \ll l_{phonon}$. Likewise, graphene samples can be made very pure; therefore, the impurity scattering distances can be made large compared to the mean-free path as well ($l_{\text{ee}} \ll l_{imp}$).

In the opposite limit—i.e. when $\mu \ll k_B T$—graphene enters a strongly coupled state known as a Dirac fluid (also known as a "quantum critical regime"). In the Fermi liquid regime, the presence of a Fermi surface imposes strong kinematic constraints on the possible scattering pathways; this prevents electrons far from the Fermi surface from interacting strongly. However, near charge neutrality, the Fermi surface shrinks, allowing electrons to interact *strongly*. The bare coupling constant α_0 gives a measure of this interaction strength. In the Dirac regime of graphene, α_0 can be of order unity; renormalization reveals the coupling to be marginally irrelevant, but for many laboratory conditions, it can still be on the order of 0.1 to 0.5: see Lucas and Fong [4] for more details. This strong coupling makes Dirac fluids ideal candidates for hydrodynamic analysis.

A hydrodynamic analysis of electron motion in graphene is governed by a number of phenomenological parameters. A derivative expansion can be utilized to derive the hydrodynamic equation [4]. The first-order corrections contain three such parameters: the shear viscosity η, the bulk viscosity ζ, and the "intrinsic" conductivity σ_Q. These cannot be predicted from the hydrodynamic theory and must be measured or calculated microscopically.

A number of experiments have measured the value of intrinsic conductivity [7, 8]. Similarly, there have been a number experimental proposals [9–12] for measuring η. While there have been a few measurements [13, 14] of η in the Dirac regime, many of the proposals—such as negative nonlocal resistance measurements [11]—only apply to the Fermi regime [4]. Therefore, different hydrodynamic predictions would be useful for investigating η in Dirac fluids.

Solitons—disturbances that propagate without changing shape, even after interacting with each

other—serve as prototypical hydrodynamics phenomena amenable to analytic tools. Solitons are made possible when dispersion balances focusing-nonlinearities. Graphene's hydrodynamic regime supports collective electron/hole sound waves called "first-sound" modes [15] or "demons" [16]; these sound modes can become solitons if dispersion balances focusing. Akbari-Moghanjoughi [17] analyzed solitons and periodic waves in both the 2D and 3D completely degenerate ($T = 0$) Fermi regimes. Solitons are permitted due to the inherently nonlinear nature of the hydrodynamic equations; to capture this behavior, a Bernoulli pseudo-potential was used to analyze the fully nonlinear equations. However, while this method predicted some parameters—such as minimum propagation speeds—it did not generate an analytic expression for the soliton's profile.

A different approach to studying solitons was presented by Svintsov et al. [18] using standard perturbation theory. This produced a Korteweg-de Vries (KdV) equation to describe the solitons' propagation and generated analytic approximations to the disturbances' shapes. Unlike the analysis of Akbari-Moghanjoughi [17], this linearized approach lacked a dispersive term to balance the nonlinearities. Instead, the graphene was placed on a gated substrate; this provided a weak dispersive force that permitted the formation of solitons.

While the analysis of solitons by Svintsov et al. [18] provided a more concrete result, it was limited to inviscid Fermi liquids. The present study will extend the results to include the Dirac regime as well. Whereas Svintsov et al. [18] used kinetic theory, we will instead treat the system using a systematic hydrodynamic expansion. Additionally, this paper will extend the results of both Svintsov et al. [18] and Akbari-Moghanjoughi [17] by including the effects of dissipation. This allows us to propose new experiments to measure the viscosity of the electron fluid. The derivation presented here is applicable to either the Dirac ($\mu \ll k_B T$) or Fermi ($k_B T \ll \mu$) regime, though it is unable to interpolate between the two. Nevertheless, our proposal offers an advantage over transport measurements in that its interpretation is less theory-laden.

In § 1.3 we will derive the governing equations. Section 1.4 will be devoted to the subtle aspects of normalization. Next, § 1.5 will detail the perturbation expansion for the special case of stationary solitons. Section 1.6 extends the analysis to the more general case of solitons on an arbitrary background flow. We will provide a short analysis of the results in § 1.7. Finally, in § 1.8, we will detail potential experimental setups using these solitons to measure graphene's viscosity.

1.3 Governing Equations

The electrons in graphene satisfy a pseudo-relativistic dispersion relation [4]

$$\varepsilon(\mathbf{p}) = \pm v_F |\mathbf{p}| \,, \tag{1.1}$$

with $\mathbf{p}$ the momentum, $v_F \approx c/300$ the Fermi velocity, and $\varepsilon(\mathbf{p})$ the energy density. This equation is valid near a Dirac point at $\mathbf{p} = 0$, and deviates from linearity when $|\mathbf{p}|a/\hbar \approx 1/2$ with a the distance between adjacent carbon atoms in the graphene.

Given the pseudo-relativistic dispersion, it is natural to write the conserved currents in relativistic notation with $x^\mu = (v_F t, \mathbf{x})^\mu$ and $\partial_\mu = (\partial_t / v_F, \boldsymbol{\nabla})_\mu$. Ignoring impurity and phonon scattering, the equations of motion are [4]

$$\partial_\mu J^\mu = 0 \,, \tag{1.2}$$

$$\partial_\mu T^{\mu\nu} = \frac{1}{v_F} F^{\nu\mu} J_\mu \,. \tag{1.3}$$

Here, $T^{\mu\nu}$ is the energy-momentum tensor, and $F^{\mu\nu}$ is the electromagnetic tensor (including self-interactions). Additionally, J^μ is the charge 4-current [1]. Note that we will be using Gaussian units with $e = |e|$ positive. Finally, we will include a factor of v_F in the time-like components of four-vectors, like $x^\mu = (v_F t, \mathbf{x})^\mu$, so that the metric $g^{\mu\nu} = \mathrm{diag}(-1, 1, 1, 1)^{\mu\nu}$ is dimensionless.

It is often preferable to write these equations in terms of more conventional quantities such as the fluid 3-velocity $\mathbf{u}$ and the (rest-frame) number density of charge carriers, $n = (n_{el} - n_{hol})$, with n_{el} (n_{hol}) the number density of electrons (holes). To do so, J^μ and $T^{\mu\nu}$ are expanded in the small parameter $l_{\mathrm{ee}}\delta$. In this equation, l_{ee} is the electron-electron scattering mean free path and δ is a characteristic inverse length scale of the observables. Since $\delta \sim \partial$ (with the partial derivative acting on slow observables) this is called the derivative expansion: see Lucas and Fong [4] for more details.

The expansions for $T^{\mu\nu}$ and J^μ become unwieldy at higher orders, but truncating at order $l_{\mathrm{ee}}\delta$ [2]

[1] Note that some of our variable definitions differ from those of Lucas and Fong [4] to better match usual conventions. The relevant changes (with the variables of Lucas and Fong [4] subscripted with L) are $J^\mu = -eJ^\mu_{\mathrm{L}}$, $F^{\mu,\nu} = -F^{\mu\nu}_{\mathrm{L}}/e$, and $\sigma_Q = e^2\sigma_{Q,\mathrm{L}}$.

[2] Note that, as mentioned previously, $\delta \sim \partial$; the factor of l_{ee} is implicit in the definitions of the dissipative coefficients σ_Q, η, and ζ [4].

we find [4]

$$J^\mu = -enu^\mu + \frac{\sigma_Q}{e}\mathcal{P}^{\mu\nu}\left(\partial_\nu\mu - \frac{\mu}{T}\partial_\nu T + eF_{\nu\rho}u^\rho\right)\,, \tag{1.4}$$

$$\begin{aligned} T^{\mu\nu} = (\varepsilon + P)\frac{u^\mu}{v_F}\frac{u^\nu}{v_F} + Pg^{\mu\nu} - \eta\mathcal{P}^{\mu\rho}\mathcal{P}^{\nu\alpha}\big(\partial_\rho u_\alpha \\ + \partial_\alpha u_\rho - \frac{2}{d}g_{\rho\alpha}\partial_\beta u^\beta\big) - \zeta\mathcal{P}^{\mu\nu}\partial_\alpha u^\alpha\,, \end{aligned} \tag{1.5}$$

with ε the energy density P pressure, μ chemical potential, and temperature T in the rest frame. We have defined the spacelike projection operator $\mathcal{P}^{\mu\nu} \coloneqq g^{\mu\nu} + u^\mu u^\nu/v_F^2$ and used $u^\mu u_\mu = -v_F^2$ to write the four-velocity as $u^\mu = \gamma(v_F, \mathbf{u})$ with $\gamma = 1/\sqrt{1-(|\mathbf{u}|/v_F)^2}$ a Lorentz factor. Further, we have chosen the Landau frame, where

$$u_\mu J^\mu = env_F^2 \quad \text{and} \quad u_\mu T^{\mu\nu} = -\varepsilon u^\mu\,. \tag{1.6}$$

It is sometimes more instructive to write-out four-vectors in terms of their three-vector and time-like components. For instance, J^μ is

$$\begin{aligned} J^0 = -\gamma env_F + \frac{\sigma_Q}{e}\Big[\frac{T\gamma^2}{v_F}\left(\frac{|\mathbf{u}|^2}{v_F^2}\frac{\partial}{\partial t} + \mathbf{u}\cdot\boldsymbol{\nabla}\right)\left(\frac{\mu}{T}\right) \\ + \gamma e\frac{\mathbf{E}\cdot\mathbf{u}}{v_F}\Big]\,, \end{aligned} \tag{1.7}$$

$$\begin{aligned} \mathbf{J} = -\gamma en\mathbf{u} + \frac{\sigma_Q}{e}\Big[T\left(\boldsymbol{\nabla} + \gamma^2\frac{\mathbf{u}}{v_F^2}D\right)\left(\frac{\mu}{T}\right) \\ + \gamma e\left(\mathbf{E} + \frac{\mathbf{u}}{v_F}\times\mathbf{B}\right)\Big]\,. \end{aligned} \tag{1.8}$$

where $D \coloneqq \partial_t + \mathbf{u}\cdot\boldsymbol{\nabla}$ is a material derivative.

To facilitate comparison with the existing literature, it is useful to re-write the spacelike components as $v_F\partial_\nu T^{i\nu} - u^i\partial_\nu T^{0\nu} = v_F F^{\mu i}J_\mu - u^i F^{\mu 0}J_\mu$. Thus, our system becomes

$$\partial_\mu J^\mu = 0\,, \tag{1.9}$$

$$\partial_\nu T^{0\nu} = F^{\mu 0}J_\mu\,, \tag{1.10}$$

$$v_F\partial_\nu T^{i\nu} - u^i\partial_\nu T^{0\nu} = v_F F^{\mu i}J_\mu - u^i F^{\mu 0}J_\mu\,. \tag{1.11}$$

1.3.1 Ideal Fluid

It is illuminating to temporarily consider the dissipationless case $\sigma_Q = \eta = \zeta = 0$. We are then able to write (1.9)–(1.11) in three-vector notation as

$$\frac{\partial}{\partial t}(\gamma n) + \boldsymbol{\nabla}\cdot(\gamma n \mathbf{u}) = 0\,, \tag{1.12}$$

$$\frac{\partial}{\partial t}\big(\gamma^2(\varepsilon+P)\big) + \boldsymbol{\nabla}\cdot\big(\gamma^2(\varepsilon+P)\mathbf{u}\big) - \frac{\partial P}{\partial t} = -\gamma n e \mathbf{E}\cdot\mathbf{u}\,, \tag{1.13}$$

$$\gamma^2\frac{(\varepsilon+P)}{v_F^2}\left(\frac{\partial \mathbf{u}}{\partial t} + \mathbf{u}\cdot\boldsymbol{\nabla}\mathbf{u}\right) + \left(\frac{\mathbf{u}}{v_F^2}\frac{\partial P}{\partial t} + \boldsymbol{\nabla}P\right) = -ne\gamma\left(\mathbf{E} + \frac{\mathbf{u}}{v_F}\times\mathbf{B} - \frac{\mathbf{u}}{v_F}\mathbf{E}\cdot\frac{\mathbf{u}}{v_F}\right)\,. \tag{1.14}$$

Then, it is clear that (1.9)–(1.11) represent charge, energy, and 3-momentum conservation, respectively.

1.3.2 Phonons and Heat Flow

We have neglected the interactions (emission, absorption, and scattering) with phonons in our governing equations, (1.9)–(1.11); we will now attempt to justify that choice. First, we consider the momentum equation (1.11).

The hydrodynamic regime is relevant when the electron-electron interaction time t_{ee} is the smallest timescale: $t_{\text{ee}} \ll t_{\text{char}} \ll t_d$ with t_{char} the soliton's propagation timescale and t_d its dissipation timescale. Following the standard prescription [4, 8, 19, 20], we will neglect phonon-induced momentum relaxation in the momentum conservation equation, (1.11), if the phonon-induced momentum-relaxation time $t^{(p)}_{\text{e-ph}}$ is much longer than the other timescales of interest, $t_{\text{ee}} \ll t_d \ll t_d \ll t^{(p)}_{\text{e-ph}}$.

To support the claim that such a regime exists, we now present sample numerical values that satisfy such a timescale hierarchy. Nevertheless, we stress that this is simply an example; the derivation in the remainder of the paper will be valid over a wide range of experimental parameters; see § 1.B for further details.

The electron-electron scattering time in the Dirac regime is [4]

$$t_{\text{ee}} \sim 0.1\,\text{ps} \times \left(\frac{100\,\text{K}}{T}\right)\,. \tag{1.15}$$

At $T = 60\,\text{K}$, this gives $t_{\text{ee}} = 0.17\,\text{ps}$. Using the sample values chosen in § 1.8, we find (cf. § 1.8.2) a

characteristic propagation time of $t_{\rm char} = 6.5\,{\rm ps}$. In that same section, we calculate a decay time of $t_d \approx 44\,{\rm ps}$. Finally, the electron-phonon momentum-relaxation time for acoustic phonons (with speed $v_s = 2\times 10^4\,{\rm m\,s^{-1}}$) is given by [21]

$$t_{\text{e-ph}}^{(p)} \sim \frac{10\,{\rm ps}}{(T/100\,{\rm K})\sqrt{n/(10^{12}\,{\rm cm^{-2}})}}\,. \tag{1.16}$$

This yields $t_{\text{e-ph}}^{(p)} = 280\,{\rm ps}$. Therefore, we see that we have $t_{\rm ee} \ll t_{\rm char} \ll t_d \ll t_{\text{e-ph}}$. Thus, with the experimental values chosen here, phonon-induced momentum relaxation can be neglected from (1.11).

Importantly, as shown in recent experiments [8], there does appear to exist an experimentally realizable regime where the requisite hydrodynamic condition $t_{\rm ee} \ll t_{char} \ll t_{\text{e-ph}}^{(p)}$ holds. Indeed, these experiments motivate us to suggest that such an approximation might be valid. Nevertheless, it would be useful to have a more refined estimate of the rate at which momentum and energy are lost to phonons.

Isothermal *vs.* Adiabatic

Now we consider the effect of phonons on the energy conservation equation (1.10). The energy conservation equation implicitly assumes our system is adiabatic: that is, the absence of energy sources/sinks presumes that heat neither enters nor leaves the system. In general, we could include terms (such as coupling to phonons) representing heat gain/loss. Instead, we could consider the opposite limit involving rapid heat transfer with the environment resulting in isothermal conditions. Under this assumption, the energy conservation equation is no longer needed; rather, the thermodynamic relations of § 1.3.3 could be used to relate our dynamic variables P and n, since T would no longer be dynamical. Therefore, (as in the case of Newton's calculation of sound-speed in air) it is important to determine whether adiabatic or isothermal conditions are more applicable.

The most likely thermalization pathway would involve energy loss to phonons: the soliton's location in the middle of the sample minimizes heat advection through the edge contacts; similarly, radiative cooling is far too slow to thermalize the system on relevant timescales [3]. Indeed, if the graphene is placed on a substrate, phonons are responsible for the majority of the heat transfer to the environment [23, 24].

[3] The Stefan-Boltzmann law would give a power loss rate of $P_r = \sigma\varepsilon\big[(T_0+T_1)^4 - T_0^4\big] \approx 4\sigma\varepsilon T_0^3 T_1$, with $\sigma = 5.67\times 10^{-8}\,{\rm W\,m^{-2}\,K^{-4}}$ and $\varepsilon \le 1$ graphene's emissivity. Using $\varepsilon \approx 1\,\%$ [22], $T_0 = 60\,{\rm K}$, and $T_1 = 0.1T_0 = 6.0\,{\rm K}$, we find a power loss density of $P_r = 2.9\times 10^{-7}\,{\rm kW\,cm^{-2}}$.

As we will calculate in § 1.8.3, graphene has a specific heat of $c_s = 4.5\times 10^{-9}\,{\rm J\,cm^{-2}\,K^{-1}}$. Therefore, the soliton's temperature will change at a rate of $P_r/c_s = 65\,{\rm K\,s^{-1}}$. Hence, it would take approximately $T_1 c_s/P_r = 93\,{\rm ms}$ for the system to thermalize with the environment via radiation.

For the isothermal condition to be applicable, the electrons must quickly lose energy to the environment: that is, the energy-relaxation time $t_{\text{e-ph}}^{(\varepsilon)}$ must satisfy $t_{\text{e-ph}}^{(\varepsilon)} \leq t_{\text{ee}} \ll t_{\text{char}} \ll t_{\text{e-ph}}^{(p)}$. However, single-phonon interactions are unlikely to extract heat quickly enough. Each phonon with wavenumber k carries a momentum $\hbar k$ while the electron fluid has momentum density $u(\varepsilon + P)/v_F^2 \sim u\varepsilon/v_F^2$. Likewise, phonons have energy $\hbar k v_s$ with sound speed v_s, while the electrons have energy density ε. Recall that we require the electron-electron momentum exchange rate $\dot{p}_{\text{ee}}$ to be much greater than the electron-phonon momentum relaxation rate $\dot{p}_{\text{e-ph}}$ in order for hydrodynamics to be valid: $\dot{p}_{\text{ee}} \gg \dot{p}_{\text{e-ph}}$. However, multiplying by v_s and re-writing in terms of the energy exchange rates yields $\dot{\varepsilon}_{\text{ee}} u v_s / v_F^2 \gg \dot{\varepsilon}_{\text{e-ph}}$. Given that $v_s \approx 2 \times 10^4 \,\mathrm{m\,s^{-1}} \ll v_F$ for acoustic phonons [25] and $u \approx 4.0 \times 10^5 \,\mathrm{m\,s^{-1}} \sim v_F$ for our system, we see that $\dot{\varepsilon}_{\text{ee}} \gg \dot{\varepsilon}_{\text{e-ph}}$. Hence, if phonon-induced momentum relaxation can be neglected, so can phonon-induced energy relaxation.

For isothermal conditions to be applicable, other thermalization pathways must be available. For instance, multiphonon supercollisions [25] can increase the energy flux relative to the momentum flux. However, under the assumption of weak phonon coupling, we can ignore the influence of multiphonon processes. Therefore, in the absence of other energy-relaxation mechanisms, it appears that adiabatic conditions are more appropriate for our system, with $t_{\text{ee}} \ll t_{\text{char}} \ll t_{\text{e-ph}}^{(p)} \ll t_{\text{e-ph}}^{(\varepsilon)}$.

In the body of this paper, we will use isothermal conditions: these are more common in the literature [17, 18] and are somewhat simpler. Nevertheless, adiabatic conditions appear to be more practical and are used for the derivation in § 1.C.

1.3.3 Thermodynamics

Currently, our system, (1.9) and (1.11), is underdetermined. This can be remedied by including a thermodynamic equation of state to relate ε and P.

In graphene, the photon-like dispersion relation for the electrons gives the pressure as $P = \varepsilon d$, with d the dimension of the system ($d = 2$ for graphene) [4]. Graphene has a natural energy scale at which the band structure's curvature becomes relevant. However, for temperatures much lower than this scale, $\Lambda \sim 10^4 \,\mathrm{K}$, there are only two energy scales in the problem: $k_B T$ and μ. Therefore, from dimensional analysis, the pressure must be expressed as [4]

$$P(\mu, T) = \frac{(k_B T)^{d+1}}{(\hbar v_F)^d} F\left(\frac{\mu}{k_B T}\right), \tag{1.17}$$

for a function F subject to constraints imposed by the positivity of the entropy density $s = \partial P/\partial T \geq 0$. Additionally, since our system is charge conjugation symmetric with $\mu \to -\mu$, F must be an even function.

In the Dirac regime ($\mu \ll k_B T$), P can be expanded as

$$P(\mu, T) = \frac{(k_B T)^{d+1}}{(\hbar v_F)^d} \Big[\mathcal{C}_0^D + \mathcal{C}_1^D \left(\frac{\mu}{k_B T} \right)^2 + \mathcal{C}_2^D \left(\frac{\mu}{k_B T} \right)^4 + \ldots \Big] . \tag{Dirac: 18}$$

Similarly, the carrier density can be expressed as

$$n(\mu, T) = \frac{\partial P}{\partial \mu} = \frac{(k_B T)^d}{(\hbar v_F)^d} \frac{\mu}{k_B T} \Big[2\mathcal{C}_1^D + 4\mathcal{C}_2^d \left(\frac{\mu}{k_B T} \right)^2 + \ldots \Big] . \tag{Dirac: 19}$$

Instead, in the Fermi regime ($\mu \gg k_B T$), we can write P as

$$P(\mu, T) = \frac{|\mu|^{d+1}}{(\hbar v_F)^d} \Big[\mathcal{C}_0^F + \mathcal{C}_1^F \left(\frac{k_B T}{\mu} \right)^2 + \mathcal{C}_2^F \left(\frac{k_B T}{\mu} \right)^4 + \ldots \Big] . \tag{Fermi: 20}$$

Likewise, the carrier density is given by

$$n(\mu, T) = (d+1) \frac{|\mu|^d \operatorname{sgn} \mu}{(\hbar v_F)^d} \Big[\mathcal{C}_0^F + \frac{d-1}{d+1} \mathcal{C}_1^F \left(\frac{k_B T}{\mu} \right)^2 + \frac{d-3}{d-1} \mathcal{C}_2^F \left(\frac{k_B T}{\mu} \right)^4 + \ldots \Big] . \tag{Fermi: 21}$$

Throughout the remainder of this paper, we will generically write $\mathcal{C}_0$, $\mathcal{C}_1$, etc; the current regime of interest will determine whether to use $\mathcal{C}^D$ or $\mathcal{C}^F$. Explicit expressions for these coefficients are given in § 1.A. It is important to reiterate that, for our isothermal system, T is not a dynamical quantity dependent on space or time, but is merely a parameter.

1.3.4 Electrostatics

While our electron fluid moves in d-dimensions ($d = 2$ for graphene), we will assume the electromagnetic field propagates in $d + 1$ dimensions (i.e. 3-space for graphene, as usual). We are only concerned with the electric potential ϕ since the magnetic terms are smaller by a factor of $v_F/c \approx 1/300$. The self-interaction of the charge distribution $n(x, t)$ generates an electric potential in the Lorenz gauge as

$$-\frac{1}{c^2}\frac{\partial^2\phi}{\partial t^2} + \nabla^2\phi = -4\pi J^0 = -4\pi[-en(x,t)\gamma]\,. \tag{1.22}$$

Note that we are using the $d+1$-dimensional Laplacian. Neglecting the $1/c^2$ time derivative gives Poisson's equation. For instance, with $d = 2$; this gives

$$\phi(\mathbf{x}, t) = -e\int \frac{n(y,t)\gamma}{|x-y|}\,\mathrm{d}^3y\ . \tag{1.23}$$

Making the quasi-static approximation that $\partial_t/\partial_x \ll c$—so we can neglect electrodynamic effects like $\partial_t\mathbf{A}$—we find

$$\mathbf{E} = e\int \frac{(\mathbf{x}-\mathbf{y})n(y,t)\gamma}{|x-y|^3}\,\mathrm{d}^3y\ . \tag{1.24}$$

This equation is highly non-local in n, and using it in the energy-momentum tensor equation would produce a complicated integro-differential equation. While we can deal with this (via a Fourier transform) for the linear approximation, going to higher orders would necessarily involve convolutions.

The main problem with this setup is that the Coulomb force is long-ranged; we can simplify this by using conducting gates. Since the electric field lines must be normal to conductors, placing conductors directly above and below the graphene will force $\mathbf{E}$ to be nearly normal to the graphene [18, 26]. Therefore, the x-component E_x will necessarily be small and can be handled perturbatively.

We impose gates a distance d_1 above and d_2 below the sample and fill the intervening space with a dielectric of relative permittivity κ. This gives a potential (in $d = 2$) of the form [18]

$$\phi = \frac{-\alpha\hbar v_F d_1 d_2}{e\kappa(d_1+d_2)}\left(1 + \frac{d_1 d_2}{3}\frac{\partial^2}{\partial x^2}\right)(\gamma n) + O(d_i\partial_x)^4\,. \tag{1.25}$$

Naturally, the electric field is given by the negative gradient of ϕ. Here, we have assumed that $d_i\partial_x \ll 1$. Furthermore, we have replaced $4\pi e^2/\hbar v_F$ with $\alpha(T)$, the renormalized coupling constant; this accounts for

the effect of screening and is given by [4]

$$\alpha(T) = \frac{4}{(4/\alpha_0) + \ln\left(10^4\,\mathrm{K}/T\right)}\,, \tag{1.26}$$

with $\alpha_0 \approx 1$ depending on the graphene's substrate. For the Dirac regime at $T = 60\,\mathrm{K}$ considered throughout this paper, this gives $\alpha \approx 0.439$.

For convenience, we will define the collection of coefficients

$$A \coloneqq \frac{\alpha\hbar v_F d_1 d_2}{\kappa(d_1 + d_2)}\,, \tag{1.27}$$

so that the potential is given as

$$\phi = -\frac{A}{e}\left(1 + \frac{d_1 d_2}{3}\frac{\partial^2}{\partial x^2}\right)(\gamma n) + O(d_i\partial_x)^4\,. \tag{1.28}$$

While (1.27) only applies for $d = 2$, we will use ϕ given by (1.28) for arbitrary dimension, with an appropriately chosen A.

The first term on the right-hand side of (1.28) represents the electric potential from a uniform charge density. The second term is a weakly non-local correction that causes a weak dispersion.

1.4 Dimensions, Units, and Regime of Interest

It will be helpful in the following sections to be rather precise in specifying a nondimensionalization scheme. For convenience, we will choose units where $k_B = \hbar = v_F = e = 1$. We still have one dimension unspecified; in order to fully specify our unit system, we will choose an arbitrary reference length $l_{\mathrm{ref}} = 50\,\mathrm{nm}$; this is chosen so that T is nondimensionalized to roughly unity (see below) [4].

In later sections, we will be performing a perturbation expansion to solve the nonlinear system of equations. There, we will use expansions of the form $f = f_0 + \varepsilon f_1 + f_2\varepsilon^2 + \ldots$ with $\varepsilon \ll 1$ a small parameter representing the size of perturbations.

Choosing the order of the problem's variables is very important. When collecting terms in perturbation theory, we assume that all variables and constants are order $O(1)$; the relative magnitude of

[4] After choosing $\hbar = v_F = k_B = e = 1$, all quantities will be expressed in various powers of length. If the parameters have been chosen correctly, there will exist a characteristic length Ξ shared by all quantities. It is most convienent to choose $l_{\mathrm{ref}} = \Xi$, though it is not strictly necessary—choosing l_{ref} otherwise will multiply all terms in each equation by the same factor of l_{ref}/Ξ.

terms is given solely by powers of ε. Let us emphasize that, unlike the choice of parameters to normalize above, this choice of nondimensionalization *is* physically relevant and determines our regime of interest.

Nondimensionalization sets the relative size of different terms and corresponds to a specification of our location in parameter space. Indeed, this choice dictates which terms and processes are relevant and which are negligible. Equivalently, this process can be viewed through the lens of dimensional analysis. Our system has seventeen variables (5 dynamic n, u, ε, P, and μ; 11 static: x, t, k_BT, d_i, κ, σ_Q/e^2, η, ζ, $\hbar$, v_F, and l_{ref}; and the previously defined perturbation scale ε). In total, there are 3 independent physical units (mass, length, and time). Therefore, the Buckingham Pi theorem implies there are 14 dimensionless parameters.

However, these 14 dimensionless parameters are not all independent. Our 3 thermodynamic equations ($\varepsilon = Pd$, as well as the definitions of P and n) reduce this number to 11. Furthermore, we have not yet specialized to solitons: in § 1.B, we will use dominant balance to impose 4 additional restrictions arising from our conservation equations, (1.9)–(1.11). This leaves a total of 7 independent nondimensional parameters: ε, m, p, q, $O(\sigma_Q\hbar)$, $O\big(\eta l_{\text{ref}}^d/\hbar\big)$, and $O\big(\zeta l_{\text{ref}}^d/\hbar\big)$, as defined in § 1.B [5].

Naturally, investigations of the Fermi and Dirac regimes entail different nondimensionalizations. Additionally, even without a set regime, there are different nondimensionalization choices highlighting different areas of parameter space. Section 1.B outlines a general nondimensionalization using dominant balance that encompasses various parameter spaces in both the Dirac and Fermi regimes. For concreteness, we will examine one particular nondimensionalization in the Dirac regime in this section. Nevertheless, the equations and solutions generated in the remainder of the paper are largely similar for both the Dirac and Fermi regimes; we will explicitly highlight the few terms that do differ between the two regimes. The nondimensionalization utilized in the Fermi regime is laid out in § 1.B.1.

1.4.1 Dirac Nondimensionalization

We will denote nondimensional variables with a caret. Restricting to the Dirac regime and using a bit of foresight, we will choose to nondimensionalize the dynamical and thermodynamic variables as

[5] As discussed in § 1.B.3, we could introduce three additional microscopic equations and eliminate η, ζ, and σ_Q/e^2 as independent quantities. However, we will refrain from doing so.

follows:

$$\begin{aligned} n &= \varepsilon^{(d+2)/4}\hat{n}l_{\rm ref}^{-d}\,, & u &= \hat{u}v_F\,,\\ \varepsilon &= \varepsilon^{(d+1)/4}\hat{\varepsilon}\hbar v_F l_{\rm ref}^{-d-1}\,, & P &= \varepsilon^{(d+1)/4}\hat{P}\hbar v_F l_{\rm ref}^{-d-1}\,,\\ \mu &= \varepsilon^{3/4}\hat{\mu}\hbar v_F l_{\rm ref}^{-1}\,, \quad \text{and} & T &= \varepsilon^{1/4}\hat{T}\hbar v_F l_{\rm ref}^{-1}k_B^{-1}\,. \end{aligned} \tag{1.29}$$

Here, we made use of the fact that we are in the Dirac regime ($\mu/T \ll 1$) and the thermodynamic equations of § 1.3.3 by ensuring

$$O\big(nl_{\rm ref}^d\big) = O\left(\frac{\mu l_{\rm ref}^{d+1}}{\hbar v_F}\left(\frac{Tl_{\rm ref}}{\hbar v_F}\right)^{d-1}\right) \tag{1.30}$$

and

$$O\left(\frac{Pl_{\rm ref}^{d+1}}{\hbar v_F}\right) = O\left(\frac{k_B T l_{\rm ref}}{\hbar v_F}\right)^{d+1}. \tag{1.31}$$

Note that we took μ to be small but finite; as we will see later, taking μ to be identically zero causes disturbances to be "frozen" in place.

The gating distance will be normalized as $d_i = l_{\rm ref}\hat{d}_i\varepsilon^{-(d+3)/4}$. The electrostatic coefficient A [defined for $d = 2$ in (1.27)] is normalized as $A = \hat{A}\varepsilon^{-(d+3)/4}\hbar l_{\rm ref}^{d-1}v_F$.

The dissipative "intrinsic" conductivity $\sigma_Q\hbar/e^2$ represents another non-dimensional parameter in our problem. In the hydrodynamic regime for $d = 2$, we have [27]

$$\frac{\sigma_Q}{e^2} \approx \frac{0.760}{2\pi\hbar\alpha(T)^2}\,, \tag{1.32}$$

with $\alpha(T)$ given by (1.26). We see that for $T \approx 60\,\mathrm{K}$, we have $\sigma_Q = 0.20e^2/\hbar$. Therefore, $\sigma_Q\hbar/e^2$ is now a second small parameter (in addition to ε). To make progress with our perturbation expansion we need to fix the magnitude of $\sigma_Q\hbar/e^2$ relative to ε. Since we will later choose $\varepsilon \sim 0.1$, we see that $\hat{\sigma}_Q = 0.20 \approx \sqrt{0.1}$. Thus, we will nondimensionalize σ_Q as $\sigma_Q = \hat{\sigma}_Q\varepsilon^{1/2}e^2 l_{\rm ref}^{2-d}/\hbar$.

According to Lucas and Fong [4], near the charge neutrality point with $d = 2$, the shear viscosity is given by

$$\eta \approx 0.45\frac{(k_B T)^2}{\hbar v_F^2\alpha(T)^2}\,. \tag{1.33}$$

For $T \approx 60\,\mathrm{K}$, we have $\eta l_{\rm ref}^2/\hbar = 1.1$. Therefore, we will choose $\eta = \varepsilon^0\hat{\eta}\hbar l_{\rm ref}^{-d}$. Though the bulk viscosity ζ is expected to be much smaller than η (due to approximate scale invariance), our setup is only sensitive to $\zeta + 2\eta(1 - 1/d)$; therefore, we will simply choose $\zeta = \varepsilon^0\hat{\zeta}\hbar l_{\rm ref}^{-d}$ as well. We can safely take $\hat{\zeta} \to 0$ without affecting the derivation.

In performing a derivative expansion, it is assumed that the relevant variables (n, ε, etc) vary on

length scales $\xi \gg l_{\text{ee}}$. If we normalize the length scales by ξ as $x = \hat{x}\xi$, then the derivatives are normalized according to § 1.B as

$$\frac{\partial}{\partial x} = \frac{1}{\xi}\frac{\partial}{\partial \hat{x}} = \frac{l_{\text{ref}}}{\xi}\frac{1}{l_{\text{ref}}}\frac{\partial}{\partial \hat{x}} = \varepsilon^{(d+5)/4}\frac{1}{l_{\text{ref}}}\frac{\partial}{\partial \hat{x}}\,. \tag{1.34}$$

For the remainder of this paper, carets denoting normalized variables will be dropped for convenience.

Note that, in addition to our perturbation expansion in terms of ε, we have already made use of two other expansions: one for ϕ expanding in $(\partial_x d_i)^2$ and one for $P(\mu, T)$ expanding in $(\mu/T)^2$. Using these normalizations, we see that both $(\partial_x d_i)^2$ and $(\mu/T)^2$ are of order ε, so all perturbation expansions in the problem have the same accuracy.

1.5 Perturbation Expansion

To analyze (1.9)–(1.11), it will be useful to expand the dependent variables in a perturbation series:

$$\mathbf{u} = \mathbf{u}_0 + \varepsilon\mathbf{u}_1 + \varepsilon^2\mathbf{u}_2 + \dots\,, \tag{1.35}$$

$$P = P_0 + \varepsilon P_1 + \varepsilon^2 P_2 + \dots\,, \tag{1.36}$$

$$n = n_0 + \varepsilon n_1 + \varepsilon^2 n_2 + \dots\,. \tag{1.37}$$

1.5.1 Perturbative Thermodynamics

We will be using the thermodynamic relationships of § 1.3.3 to write μ and T in terms of n and P; however, since T is non-dynamical, it will only have a constant T_0 component, but not a $T_1(x,t)$ contribution. It is useful to define m as the order of $(\mu_0/T_0)^2$; that is, $\varepsilon^m \coloneqq O(\mu/(k_B T))^2$. For the nondimensionalization specified in § 1.4, $m = 1$.

Expanding the thermodynamic variables and collecting powers of ε yields the following relations

for the Dirac regime:

$$P_0 = T_0^{d+1}\mathcal{C}_0\,, \tag{Dirac: 38}$$

$$n_0 = 2T_0^{d-1}\mu_0\mathcal{C}_1\,, \tag{Dirac: 39}$$

$$P_1 = P_0\left[\frac{\mathcal{C}_1}{\mathcal{C}_0}\left(\frac{\mu_0}{T_0}\right)^2\delta_{m,1}\right], \tag{Dirac: 40}$$

$$n_1 = n_0\left[\frac{\mu_1}{\mu_0} + 2\frac{\mathcal{C}_2}{\mathcal{C}_1}\left(\frac{\mu_0}{T_0}\right)^2\delta m,1\right], \tag{Dirac: 41}$$

$$\begin{aligned} P_2 = P_0\Bigg[&\frac{T_2}{T_0}(d+1)\frac{(d+1)d}{2} \\ &+ 2\frac{\mathcal{C}_1}{\mathcal{C}_0}\frac{\mu_1}{\mu_0}\left(\frac{\mu_0}{T_0}\right)^2\delta m,1 \\ &+ \frac{\mathcal{C}_2}{\mathcal{C}_0}\left(\frac{\mu_0}{T_0}\right)^4\delta_{m,1} + \frac{\mathcal{C}_1}{\mathcal{C}_0}\left(\frac{\mu_0}{T_0}\right)^2\delta_{m,2}\Bigg], \end{aligned} \tag{Dirac: 42}$$

$$\begin{aligned} n_2 = n_0\Bigg[&\frac{\mu_2}{\mu_0} + \frac{T_2}{T_0}(d-1) \\ &+ 6\frac{\mathcal{C}_2}{\mathcal{C}_1}\frac{\mu_1}{\mu_0}\left(\frac{\mu_0}{T_0}\right)^2\delta_{m,1} \\ &+ 3\frac{\mathcal{C}_3}{\mathcal{C}_1}\left(\frac{\mu_0}{T_0}\right)^4\delta_{m,1} + 2\frac{\mathcal{C}_2}{\mathcal{C}_1}\left(\frac{\mu_0}{T_0}\right)^2\delta_{m,2}\Bigg], \end{aligned} \tag{Dirac: 43}$$

with $\delta_{a,b}$ the Kronecker delta function.

Similarly, for the Fermi regime, we find

$$P_0 = |\mu_0|^{d+1}\mathcal{C}_0\,, \tag{Fermi: 44}$$

$$n_0 = |\mu_0|^d\,\mathrm{sgn}(\mu_0)\mathcal{C}_0(d+1)\,, \tag{Fermi: 45}$$

$$P_1 = P_0\left[\frac{\mu_1}{\mu_0}(d+1) + \frac{\mathcal{C}_1}{\mathcal{C}_0}\left(\frac{T_0}{\mu_0}\right)^2\delta_{m,-1}\right], \tag{Fermi: 46}$$

$$n_1 = n_0\left[\frac{\mu_1}{\mu_0}d + \frac{\mathcal{C}_1}{\mathcal{C}_0}\frac{d-1}{d+1}\left(\frac{T_0}{\mu_0}\right)^2\delta_{m,-1}\right], \tag{Fermi: 47}$$

$$\begin{aligned} P_2 = P_0\Bigg[&\frac{\mu_2}{\mu_0}(d+1) + \frac{\mu_1^2}{\mu_0^2}\frac{(d+1)d}{2} \\ &+ \frac{\mathcal{C}_1}{\mathcal{C}_0}(d-1)\frac{\mu_1}{\mu_0}\left(\frac{T_0}{\mu_0}\right)^2\delta_{m,-1} \\ &+ \frac{\mathcal{C}_2}{\mathcal{C}_0}\left(\frac{T_0}{\mu_0}\right)^4\delta_{m,-1} + \frac{\mathcal{C}_1}{\mathcal{C}_0}\left(\frac{T_0}{\mu_0}\right)^2\delta_{m,-2}\Bigg], \end{aligned} \tag{Fermi: 48}$$

$$
\begin{aligned}
n_2 = n_0 \Bigg[& \frac{\mu_2}{\mu_0} d + \frac{\mu_1^2}{\mu_0^2} \frac{d(d-1)}{2} \\
& + \frac{\mathcal{C}_1}{\mathcal{C}_0} \frac{(d-1)(d-2)}{d+1} \frac{\mu_1}{\mu_0} \left(\frac{T_0}{\mu_0} \right)^2 \delta_{m,-1} \qquad \text{(Fermi: 49)} \\
& + \frac{\mathcal{C}_2}{\mathcal{C}_0} \frac{d-3}{d+1} \left(\frac{T_0}{\mu_0} \right)^4 \delta_{m,-1} + \frac{\mathcal{C}_1}{\mathcal{C}_0} \frac{d-1}{d+1} \left(\frac{T_0}{\mu_0} \right)^2 \delta_{m,-2} \Bigg] .
\end{aligned}
$$

Using these equations, we can now write μ and P in terms of n at each order. In particular, we find

$$
\frac{P_1}{P_0} = \frac{n_1}{n_0} K_0 + \frac{\mathcal{C}_1}{\mathcal{C}_0} \left(\frac{\mu_0}{T_0} \right)^{2m} \left(\delta_{m,1} + \frac{1}{d} \delta_{m,-1} \right) . \tag{1.50}
$$

Here, we have defined K_0 as

$$
K_0 = \begin{cases} 0 & m > 0 \text{ (Dirac regime)} \\ (d+1)/d & m < 0 \text{ (Fermi regime)} \end{cases} . \tag{1.51}
$$

As a side note, it is straightforward to show with thermodynamic identities that K_0 is the leading order term in the ratio of bulk modulus B to pressure P; that is, $K_0 = B_0/P_0$.

1.5.2 Conservation Equations

First, let us investigate a scenario with a constant, uniform background flow $u_0 \neq 0$ chosen such that the perturbations are stationary in the laboratory frame. This will both simplify the mathematics and be experimentally interesting. To accomplish this, we will only permit variations on long timescales (this will be important when including dissipation). Mathematically, we accomplish this by normalizing the time variable as $t = \varepsilon \hat{t}_1 \xi / v_F$ such that $\partial_{t_1} = \varepsilon O(\partial_{\hat{x}})$.

Expanding the governing equation, we find Leading Order:

$$
\frac{\partial}{\partial x} \left(\gamma^2 n_0 u_1 + u_0 n_1 \right) = 0 , \tag{1.52a}
$$

$$
\frac{\partial}{\partial x} \left(\gamma P_1 + u_0 \gamma^3 (\varepsilon_0 + P_0) u_1 + \gamma A n_0 n_1 + \gamma^3 A n_0^2 u_0 u_1 \right) = 0 . \tag{1.52b}
$$

First-Order Correction:

$$
\begin{aligned}
&\frac{\partial}{\partial x}\big(\gamma^2 n_0 u_2 + u_0 n_2\big) = \\
&\quad - \gamma^2\big(u_0\gamma^2(2+u_0^2)n_0u_1 + n_1 + n_0u_0u_1\big)\frac{\partial u_1}{\partial x} - \gamma^2 u_1\frac{\partial n_1}{\partial x} \\
&\quad + \gamma u_0 A\sigma_Q\frac{\partial^2 n_1}{\partial t_0\partial x} + \gamma A\sigma_Q\frac{\partial^2 n_1}{\partial x^2} + \gamma^3 u_0 A\sigma_Q n_0\left(\frac{\partial^2 u_1}{\partial x^2} + u_0\frac{\partial^2 u_1}{\partial t_0\partial x}\right) \\
&\quad + \Theta(-m)\gamma\sigma_Q\frac{\partial^2}{\partial x^2}\left(\mu_1 - \frac{T_0}{\mu_0}T_1\right),
\end{aligned}
\tag{1.53a}
$$

$$
\begin{aligned}
&\frac{\partial}{\partial x}\big(\gamma P_2 + u_0\gamma^3(\varepsilon_0+P_0)u_2 + \gamma A n_0 n_2 + \gamma^3 A n_0^2 u_0 u_2\big) = \\
&\quad - \gamma^3\big(u_0(\varepsilon_1+P_1) + (1+u_0^2)u_1\gamma^2(\varepsilon_0+P_0)\big)\frac{\partial u_1}{\partial x} - A n_1\gamma\frac{\partial n_1}{\partial x} + A n_0 u_0 u_1\gamma^3\frac{\partial n_1}{\partial x} - \gamma A n_0\frac{d_1 d_2}{3}\frac{\partial^3 n_1}{\partial x^3} \\
&\quad - A n_0^2(1+u_0^2)u_1\gamma^5\frac{\partial u_1}{\partial x} - A n_0^2 u_0\gamma^3\frac{d_1 d_2}{3}\frac{\partial^3 u_1}{\partial x^3} - A n_0 u_0 u_1\gamma^3\frac{\partial n_1}{\partial x} - 2A n_0 u_0 n_1\gamma^3\frac{\partial u_1}{\partial x} \\
&\quad + \gamma^4\left[\zeta + 2\eta\left(1-\frac{1}{d}\right)\right]\left(u_0^2\frac{\partial^2 u_1}{\partial t_0^2} + 2u_0\frac{\partial^2 u_1}{\partial t_0\partial x} + \frac{\partial^2 u_1}{\partial x^2}\right).
\end{aligned}
\tag{1.53b}
$$

Here, we have defined $\gamma = 1/\sqrt{1-u_0^2}$ (with $v_F = 1$) and used the electrostatic coupling A according to (1.28). Additionally, we have used the Heaviside function

$$
\Theta(-m) = \begin{cases} 0 & m > 0 \text{ (Dirac regime)} \\ 1 & m < 0 \text{ (Fermi regime)} \end{cases}. \tag{1.54}
$$

1.5.3 Leading Order Equations

Using the thermodynamic relation $\varepsilon = Pd$, the leading order equations can be manipulated as

$$
\gamma^2 d\left(An_0 + \frac{P_0K_0}{n_0}\right)\big[(1.52\text{a})\big] - \gamma d u_0\big[(1.52\text{b})\big]
$$

yielding

$$
0 = \gamma^2 d\big[An_0^2 + \gamma^2 P_0\big(K_0 - u_0^2(d+1)\big)\big]u_1\,. \tag{1.55}
$$

We want nontrivial perturbations $u_1 \neq 0$, so we require the terms in square brackets to vanish. We see that this gives an equation for u_0 required to make the leading order solutions time-independent:

$$
u_0 = \pm\sqrt{\frac{[K_0/(d+1)] + [An_0^2/P_0(d+1)]}{1 + [An_0^2/P_0(d+1)]}}\,. \tag{1.56}
$$

It is easy to check that $u_0^2 < 1$ for $d \neq 1$; this is required, otherwise $\gamma = 1/\sqrt{1-u_0^2}$ would be imaginary.

Additionally, if we restrict to solutions bounded in x, we can require each term inside ∂_x from (1.52a) and (1.52b) to be zero, giving

$$u_1 = -\frac{u_0}{\gamma^2 n_0} n_1 + U_1 \,. \tag{1.57}$$

Here, we have included a constant, uniform current $U_1(x, t_0, t_1) = U_1$; this will allow us—at the next order—to cancel the disturbance's propagation speed (similar to our use of u_0 at this order).

1.5.4 First-Order Corrections

Now, we can do the same for the first-order corrections. Manipulating them as before,

$$\gamma^2 d\left(An_0 + \frac{P_0 K_0}{n_0}\right)\big[(1.53\text{a})\big] - \gamma d u_0 \big[(1.53\text{b})\big] \,,$$

gives

$$\gamma^2 d\big[An_0^2 + \gamma^2 P_0\big(K_0 - u_0^2(d+1)\big)\big] u_2 = \text{RHS} \,. \tag{1.58}$$

Here, the right-hand side (RHS) depends only on n_1, u_1, ε_1 and P_1. However, inserting our solution for u_0 causes the left-hand side to vanish, giving us our desired compatibility condition on n_1. Thus, we have the compatibility equation

$$\mathcal{A}\frac{\partial n_1}{\partial t_1} + \mathcal{F}\frac{\partial n_1}{\partial x} + \mathcal{B} n_1 \frac{\partial n_1}{\partial x} + \mathcal{C}\frac{\partial^3 n_1}{\partial x^3} = \mathcal{G}\frac{\partial^2 n_1}{\partial x^2} \,, \tag{1.59}$$

with

$$\mathcal{A} = 2\gamma^2 \frac{P_0 d}{n_0} u_0^2 (d + 1 - K_0)\,, \tag{1.60a}$$

$$\begin{aligned}\mathcal{B} = -\gamma^2 \frac{P_0}{n_0^2 d} u_0 \Big(& d^2 u_0^2 [4(d+1) - K_0(d+3)] \\ & + (d+1)\Theta(-m) - K_0 d^2 \Big)\,,\end{aligned} \tag{1.60b}$$

$$\mathcal{C} = -Ad \frac{d_1 d_2}{3} n_0 u_0\,, \tag{1.60c}$$

$$\begin{aligned}\mathcal{F} = \gamma^2 \frac{P_0 d}{n_0} u_0 \Bigg(& 2U_1 \gamma^2 (d + 1 - K_0) u_0 \\ & + \frac{\mathcal{C}_1}{\mathcal{C}_0} \left(\frac{\mu_0}{T_0} \right)^{2m} \left[u_0^2 (d+1) \left(\frac{1}{d} \delta_{m,-1} + \delta_{m,1} \right) \right. \\ & \left. - \left(\frac{d-1}{d^2} \delta_{m,-1} + 2\delta_{m,1} \right) \right] \Bigg)\,,\end{aligned} \tag{1.60d}$$

$$\begin{aligned}\mathcal{G} = \frac{\gamma^3}{n_0} \Bigg(& \sigma_Q \gamma^2 \left(\frac{P_0}{n_0} \right)^2 u_0^2 (d+1)(d+1-K_0) \\ & \times \left[d u_0^2 + \underbrace{\Theta(-m) - K_0 \frac{d}{d+1}}_{=0} \right] \\ & + d u_0^2 \left[\zeta + 2\eta \left(1 - \frac{1}{d} \right) \right] \Bigg)\,,\end{aligned} \tag{1.60e}$$

This is known as the KdV-Burgers (KdVB) equation. Note the underbraced term in $\mathcal{G}$ vanishes in both the Dirac and Fermi regimes.

1.5.5 Ideal Fluid

Before tackling the full KdVB equation, it is beneficial to consider the simpler inviscid problem with $\sigma_Q = \eta = \zeta = 0$. In this case, we find $\mathcal{G} = 0$ and the KdV-Burgers equation reduces to the KdV equation. The KdV equation has soliton solutions of the form

$$\begin{aligned}n_1(x, t_1) = c_1 \operatorname{sgn}(\mathcal{B}\mathcal{C}) \operatorname{sech}^2 \Bigg(& \sqrt{\frac{c_1 |\mathcal{B}|}{12 |\mathcal{C}|}} \\ & \times \left[x - \left(\frac{c_1 |\mathcal{B}|}{3 |\mathcal{A}|} \operatorname{sgn}(\mathcal{A}\mathcal{C}) + \frac{\mathcal{F}}{\mathcal{A}} \right) t_1 \right] \Bigg)\,,\end{aligned} \tag{1.61}$$

for arbitrary, order-1 constant $c_1 > 0$.

Substituting the coefficients, we find

$$n = n_0 + \varepsilon c_1 \operatorname{sgn}(\mathcal{BC}) \operatorname{sech}^2\left(\frac{x+vt}{W}\right), \tag{1.62}$$

with

$$v = -\varepsilon\left(\frac{c_1|\mathcal{B}|}{3|\mathcal{A}|}\operatorname{sgn}(\mathcal{AC}) + \frac{\mathcal{F}}{\mathcal{A}}\right), \tag{1.63}$$

and

$$W = \sqrt{\frac{12|\mathcal{C}|}{c_1|\mathcal{B}|}}\,. \tag{1.64}$$

Let us seek a soliton which is stationary in the laboratory frame; we have already accomplished $\partial_{t_0} n_1 = 0$ by a choice of u_0; we can similarly set $\partial_{t_1} n_1 = 0$ by an appropriate choice of U_1. If we choose U_1 so that $\mathcal{F} = -c_1\mathcal{B}/3 \operatorname{sgn}\mathcal{BC}$, then the soliton is stationary:

$$n = n_0 + \varepsilon c_1 \operatorname{sgn}(\mathcal{BC}) \operatorname{sech}^2\left(\frac{x}{W}\right). \tag{1.65}$$

1.5.6 Dissipation

Now, we return to the full KdVB equation (1.59). It does not appear that the KdV-Burgers equation with $\mathcal{G} \neq 0$ has an analytic, solitonic solution. However, if $\mathcal{G} \ll (\mathcal{A}, \mathcal{B}, \mathcal{C})$, then an approximate solution is given by (1.62) but with time-dependent c_1, as described in Mei et al. [28]. For clarity, we can factor out this smallness as $\mathcal{G} = \delta\tilde{\mathcal{G}}$ so that $\delta \ll 1$ and $\tilde{\mathcal{G}}$ is the same order as $\mathcal{A}$. Then, another short multiple scales expansion for n_1 can be done in $\delta = O(\mathcal{G}/\mathcal{A})$. To be consistent with our original perturbation series, we require that $\varepsilon \ll \delta \ll 1$.

As usual, we expand n_1 as $n_1 = n_1^{(0)} + \delta n_1^{(1)}$ and $\partial_{t_1} = \partial_{\tau_0} + \delta\partial_{\tau_1}$. Then, to leading order, the equation

$$\mathcal{L}_0 n_1^{(0)} \coloneqq \mathcal{A}\partial_{\tau_0} n_1^{(0)} + \mathcal{F}\partial_x n_1^{(0)} + \frac{\mathcal{B}}{2}\partial_x\left(n_1^{(0)}\right)^2 \tag{1.66}$$

$$+ \mathcal{C}\partial_x^3 n_1^{(0)} = 0\,, \tag{1.67}$$

where we have again defined the linear operator $\mathcal{L}_1$ acting on $n_1^{(1)}$. This is the ordinary KdV equation; therefore, $n_1^{(0)}$ has the solution given by (1.61) with order-1 free parameter $c_1 > 0$.

At next order in δ, we must allow the constant c_1 to become time-dependent on a slow time-scale

$c_1 = c_1(\tau_1)$. Then, our equation is

$$\begin{aligned}\mathcal{L}_1 n_1^{(1)} &\coloneqq \mathcal{A}\partial_{\tau_0} n_1^{(1)} + \mathcal{F}\partial_x n_1^{(1)} + \mathcal{B}\partial_x\left(n_1^{(0)} n_1^{(1)}\right) \\ &\quad + \mathcal{C}\partial_x^3 n_1^{(1)} \\ &= -\mathcal{A}\partial_{\tau_1} n_1^{(0)} + \tilde{\mathcal{G}}\partial_x^2 n_1^{(0)}\,, \end{aligned} \tag{1.68}$$

where we have again defined the linear operator $\mathcal{L}_1$ acting on $n_1^{(1)}$.

For certain inhomogeneous terms in (1.68), it is possible to generate secular (i.e. unbounded) growth; since this is clearly no longer a localized solution, we wish to avoid this. Here, we will utilize a multiple scales approach, though it will differ slightly from the method used in § 1.6 since the homogeneous operator $\mathcal{L}_0$ is nonlinear. Following the example of Mei et al. [28], we note that $\mathcal{L}_0$ and $-\mathcal{L}_1$ are adjoints:

$$\int \mathrm{d}x \left(n_1^{(1)}\mathcal{L}_0 n_1^{(0)} + n_1^{(0)}\mathcal{L}_1 n_1^{(1)}\right) = 0\,. \tag{1.69}$$

Then, substituting the right-hand sides of (1.67) and (1.68), we get the compatibility condition

$$\int n_1^{(0)}\left(\mathcal{A}\partial_{\tau_1} n_1^{(0)} - \tilde{\mathcal{G}}\partial_x^2 n_1^{(0)}\right)\mathrm{d}x = 0\,. \tag{1.70}$$

Inserting the soliton solution for $n_1^{(0)}$, we get an equation for $c_1(\tau_1)$:

$$\dot{c}_1 = -\frac{c_1^2|\mathcal{B}|\tilde{\mathcal{G}}}{|\mathcal{C}|\mathcal{A}}\frac{4}{45}\,. \tag{1.71}$$

Then, solving this equation and converting back to time t_1 gives

$$c_1(t_1) = \frac{c_1(0)}{1 + \frac{t_1}{t_d}} \quad \text{with} \quad t_d = \frac{45\mathcal{A}|\mathcal{C}|}{4c_1(0)\mathcal{G}|\mathcal{B}|}\,, \tag{1.72}$$

with $c_1(0)$ the initial value of the parameter $c_1(t_1)$. Recall that this is derived under the assumption that $\varepsilon \ll O(\mathcal{G}/\mathcal{A}) \ll 1$.

Additionally, we can solve the KdV-Burgers equation numerically for arbitrary $\mathcal{G}$; this shows similar behavior to the analytic approximation (cf. figures 1.1 and 1.2). That is, the soliton slowly decays as it progresses.

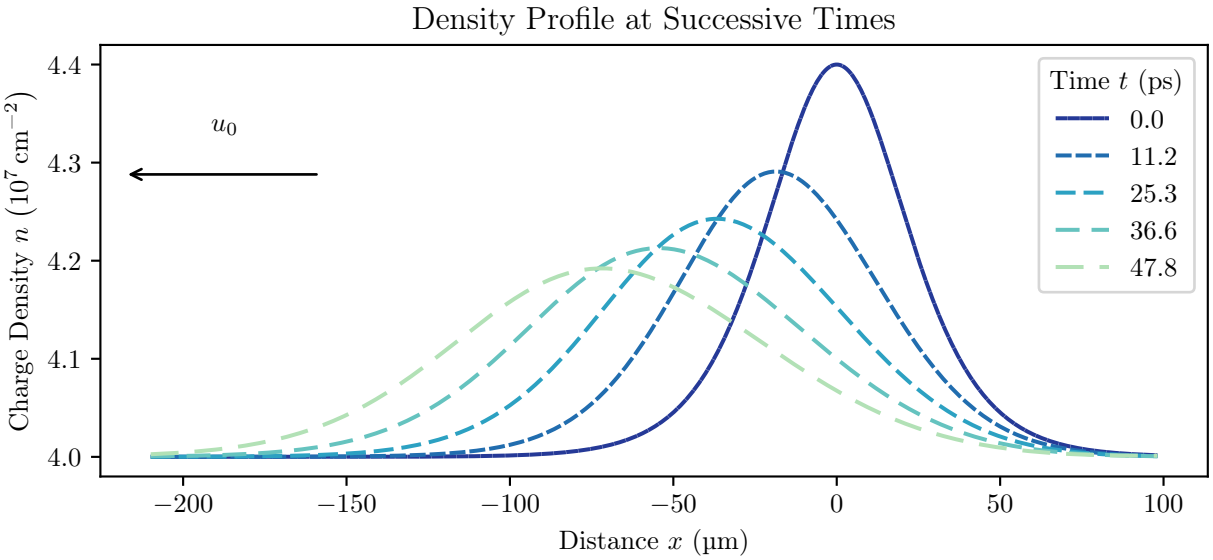

Figure 1.1. Solitonic solution to KdV-Burgers. Values used were $\mathcal{A} = 0.88$, $\mathcal{B} = -0.70$, $\mathcal{C} = -0.060$, $\mathcal{F} = -1.1$, and $\mathcal{G} = 0.53$ with the height normalized to 4.0×10^8 cm^{-2}. This choice of parameters gives a soliton propagating in the $+x$ direction and a counter-current u_0 in the $-x$ direction (indicated by the arrow).

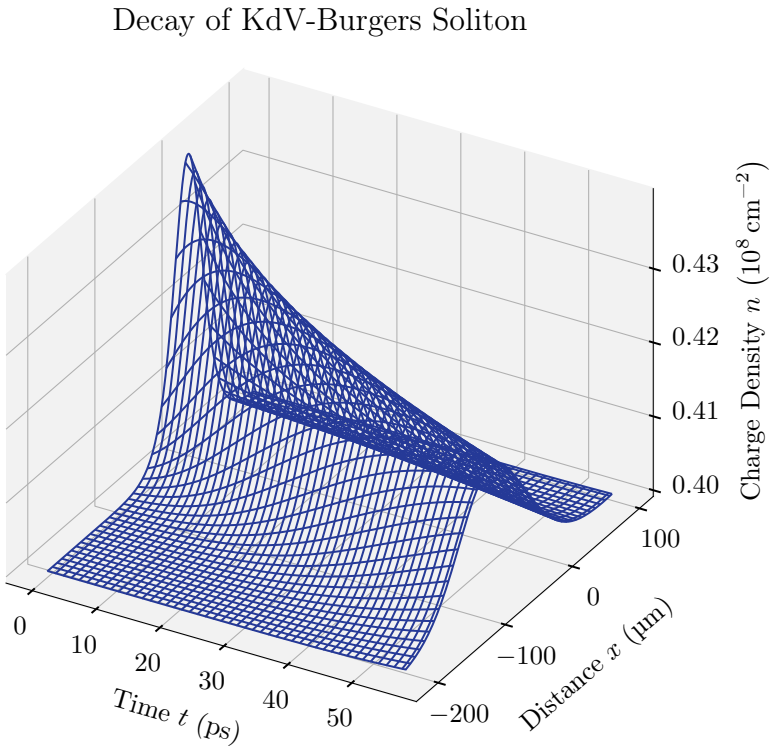

Figure 1.2. Solitonic solution to KdV-Burgers showing decay as a function of time. Values used were $\mathcal{A} = 0.88$, $\mathcal{B} = -0.70$, $\mathcal{C} = -0.060$, $\mathcal{F} = -1.1$, and $\mathcal{G} = 0.53$ with the height normalized to 4.0×10^8 cm^{-2}.

1.6 Multiple Scales Expansion

Now, we wish to study the previous solitonic solution in more generality. Here, we will allow for an arbitrary uniform, time-independent background current u_0.

As we have seen previously, the nonlinearities affect the propagation velocity v (cf. (1.63)). This is an example of a singular perturbation and requires the use of singular perturbation theory. Singular methods such as Poincaré-Lindstedt are only applicable to steady or periodic solutions. Since we are interested in decaying solutions, we need to make use of the method of multiple scales. Note that this approach is similar to that employed by Akbari-Moghanjoughi [29] in the study of partially degenerate electron-ion plasmas.

First, unlike the previous section, we will nondimensionalize the timescale so that $\partial_t = \partial_x$. Now, if we introduce a series of timescales $t_0 = t$, $t_1 = \varepsilon t$, $t_2 = \varepsilon^2 t$, ... each presumed independent, the chain rule gives

$$\frac{\partial}{\partial t} = \frac{\partial}{\partial t_0} + \varepsilon \frac{\partial}{\partial t_1} + \varepsilon^2 \frac{\partial}{\partial t_2} + \dots \,. \tag{1.73}$$

Further, we now assume that each variable is a function of all time scales: $n = n(x, t_0, t_1, t_2, \ldots)$.

If we again restrict to 1D motion and collect terms by powers of ε we get the following equations:
Leading Order:

$$\frac{\partial n_1}{\partial t_0} + \gamma^2 n_0 u_0 \frac{\partial u_1}{\partial t_0} + u_0 \frac{\partial n_1}{\partial x} + n_0 \gamma^2 \frac{\partial u_1}{\partial x} = 0 \,, \tag{1.74a}$$

$$\gamma^3(\varepsilon_0 + P_0)\frac{\partial u_1}{\partial t_0} + \gamma u_0 \frac{\partial P_1}{\partial t_0} + u_0 \gamma^3(\varepsilon_0 + P_0)\frac{\partial u_1}{\partial x} + \gamma \frac{\partial P_1}{\partial x} + A n_0 \gamma \frac{\partial n_1}{\partial x} + A n_0^2 u_0 \gamma^3 \frac{\partial u_1}{\partial x} = 0 \,, \tag{1.74b}$$

First-Order Correction:

$$\frac{\partial n_2}{\partial t_0} + \gamma^2 n_0 u_0 \frac{\partial u_2}{\partial t_0} + u_0 \frac{\partial n_2}{\partial x} + n_0 \gamma^2 \frac{\partial u_2}{\partial x} = \mathrm{RHS} \,, \tag{1.75a}$$

$$\gamma^3(\varepsilon_0 + P_0)\frac{\partial u_2}{\partial t_0} + \gamma u_0 \frac{\partial P_2}{\partial t_0} + u_0 \gamma^3(\varepsilon_0 + P_0)\frac{\partial u_2}{\partial x} + \gamma \frac{\partial P_2}{\partial x} + A n_0 \frac{\partial n_2}{\partial x} = \mathrm{RHS} \,. \tag{1.75b}$$

Again, we have used the electrostatic coupling A according to (1.28). See § 1.D for the terms on the right-hand side.

Notice that, as is often the case for multiple scales analyses, the linear operator acting on n_1, u_1, etc in (1.74a) and (1.74b) is identical to the linear operator acting on n_2, u_2, etc in (1.75a) and (1.75b). Furthermore, since this operator is linear, we do not need to employ the operator formalism of § 1.5.6, but

can instead use a linear algebraic approach similar to § 1.5 (with the addition of another timescale, t_1).

1.6.1 Leading Order Equations

Using $\varepsilon = Pd$ and combining equations like

$$\gamma^2 d\left[An_0\frac{\partial}{\partial x} + \frac{P_0K_0}{n_0}\left(u_0\frac{\partial}{\partial t_0} + \frac{\partial}{\partial x}\right)\right]\big[(1.74\text{a})\big] - \gamma d\left(\frac{\partial}{\partial t_0} + u_0\frac{\partial}{\partial x}\right)\big[(1.74\text{b})\big]$$

gives

$$\begin{aligned} 0 = \gamma^2 d\Bigg(&-\gamma^2 P_0(d+1-u_0^2K_0)\frac{\partial^2 u_1}{\partial t_0^2} \\ &- 2\gamma^2 P_0 u_0(d+1-K_0)\frac{\partial^2 u_1}{\partial t_0 \partial x} \\ &+ \left\{An_0^2 + \gamma^2 P_0\left[-u_0^2(d+1)+K_0\right]\right\}\frac{\partial^2 u_1}{\partial x^2}\Bigg). \end{aligned} \tag{1.76}$$

This wave equation has solutions $f(x+v_0t_0) + g(x-v_0t_0)$ with v_0 given by

$$v_0^{(\pm)} = \frac{-u_0(d+1-K_0)}{d+1-u_0^2K_0} \pm \frac{1}{\gamma(d+1-u_0^2K_0)} \tag{1.77}$$

$$\times\sqrt{\frac{K_0(d+1)}{\gamma^2} + \frac{An_0^2}{P_0}(d+1-u_0^2K_0)}\,. \tag{1.78}$$

We will take the (+) sign so that $v_0 = v_0^{(+)}$; the other can be recovered by taking $u_0 \to -u_0$ and $v_0 \to -v_0$. Further, we restrict to unidirectional solutions $u_1(x,t_0,t_1) = f(x \pm v_0t_0, t_1)$ for a definite choice of $\pm$; here, we choose (+) as well—the other propagation direction can be recovered by taking $v_0 \to -v_0$.

For stationary perturbations ($v_0 = 0$), we can solve for u_0 to recover the result from § 1.5:

$$u_0 = \pm\sqrt{\frac{[K_0/(d+1)] + [An_0^2/P_0(d+1)]}{1+[An_0^2/P_0(d+1)]}}\,. \tag{1.79}$$

For reference, the velocity of propagation in the absence of a background flow ($u_0 = 0$) is

$$v_0 = \pm\sqrt{\frac{1}{d+1}}\sqrt{K_0 + \frac{An_0^2}{P_0}}\,. \tag{1.80}$$

In general, n_1, u_1, and P_1 have traveling wave solutions; neglecting solutions of the form $f(x-$

$u_0 t_0, t_1)$ that are simply advected by the background current, we find solutions given by

$$n_1(x, t_0, t_1) = n_1(x + v_0 t_0, t_1) + F_1(t_1)\,, \tag{1.81a}$$

$$\begin{aligned} u_1(x, t_0, t_1) = &-\frac{(u_0 + v_0)}{n_0 \gamma^2 (1 + u_0 v_0)} n_1(x + v_0 t_0, t_1) \\ &+ F_2(t_1)\,, \end{aligned} \tag{1.81b}$$

Here, we have arbitrary functions $F_1(t_1)$ and $F_2(t_2)$; by imposing boundary conditions $n_1 = 0$ at $x = \pm\infty$, we set $F_1 = 0$. We will allow $U_1(t_2) \coloneqq F_2(t_2)$ to remain arbitrary; this uniform background current can be superimposed on the soliton solution as in § 1.5 if desired [6].

Now, we can also see why it was important to take $\mu_0 \ll T_0$ small but finite. Had $\mu = 0$ identically, then the thermodynamic relations would require $n_0 = 0$. Then, the leading order charge conservation equation (1.74a) would give $\partial_{t_0} n_1 + u_0 \partial_x n_1 = 0$; i.e. charge density perturbations are simply advected along by the background flow. That is, the density perturbations lack any dynamic propagation and are "frozen-in." Since the other dependent variables are proportional to n_1, we see P_1 and u_1 are similarly affected. Hence, if we want a dynamic disturbance, we require $\mu_0 \neq 0$; intuitively, this is understandable as there are no net charge carriers at the Dirac point.

1.6.2 First-Order Corrections

Now considering the first-order corrections, preventing secular growth of the higher-order terms (i.e. n_2, u_2, etc) requires imposing a compatibility condition on the lower-order terms (i.e. n_1, u_1, etc). We can manipulate the system as

$$\begin{aligned} \gamma^2 d \left[A n_0 \frac{\partial}{\partial x} + \frac{P_0 K_0}{n_0} \left(u_0 \frac{\partial}{\partial t_0} + \frac{\partial}{\partial x} \right) \right] &\big[(1.75\text{a})\big] \\ - \gamma d \left(\frac{\partial}{\partial t_0} + u_0 \frac{\partial}{\partial x} \right) &\big[(1.75\text{b})\big] \end{aligned}$$

[6] Note that it is possible to generate a stationary soliton by appropriate choice of F_1 instead, though the resulting coefficients will be different.

which gives

$$\begin{aligned}
&\gamma^2 d\Bigg(-\gamma^2 P_0(d+1-u_0^2K_0)\frac{\partial^2 u_2}{\partial t_0^2} \\
&\quad - 2\gamma^2 P_0 u_0(d+1-K_0)\frac{\partial^2 u_2}{\partial t_0 \partial x} \\
&\quad + \left\{An_0^2 + \gamma^2 P_0\left[-u_0^2(d+1)+K_0\right]\right\}\frac{\partial^2 u_2}{\partial x^2}\Bigg) \\
&= \mathrm{LOT}\,,
\end{aligned} \tag{1.82}$$

where LOT represents lower-order terms (i.e. n_1, u_1, etc).

It is instructive here to change variables to $\chi_0^{(\pm)} = x + v_0^{(\pm)} t_0$. Then, the equation becomes

$$\begin{aligned}
&\gamma^4 P_0 d\big(d+1-u_0^2K_0\big)\left(v_0^{(+)}-v_0^{(-)}\right)^2 \\
&\qquad \times \frac{\partial}{\partial \chi_0^{(-)}}\frac{\partial}{\partial \chi_0^{(+)}} u_2 \\
&= \mathrm{LOT}
\end{aligned} \tag{1.83}$$

This is where we encounter an apparent problem. Upon inserting our solutions for the lower-order terms, we find the right-hand side depends on products and derivatives of $f\left(\chi_0^{(+)}\right)$. This implies that the LOT are solely functions of $\chi_0^{(+)}$.

However, we see that functions of the form $f(\chi^{(+)})$ are also solutions to the homogeneous equation in (1.82) due to the presence of the $\partial_{\chi_0^{(-)}}$ operator.

So, products and derivatives of $f(\chi_0^{(+)})$ appear as inhomogeneous forcing terms that give rise to secular terms. For instance, terms proportional to $f^{(4)}\left(\chi_0^{(+)}\right)$ give rise to solutions of the form $\chi_0^{(-)} f^{(3)}\left(\chi_0^{(+)}\right)$. This grows unbounded in $\chi_0^{(-)}$—and hence, in time t. This will eventually cause $|u_2| > |u_1|$, invalidating the perturbation expansion. Thus, unless the LOT vanish identically, they will give rise to $\chi_0^{(\pm)}$-secular terms in u_2—i.e. solutions growing unbounded in t_0 or x.

Hence, we require the right-hand side to vanish and we are left with the desired compatibility equation:

$$0 = \frac{\partial}{\partial \chi_0^{(+)}}(\mathrm{KdVB}[n_1])\,. \tag{1.84}$$

Here, (KdVB[n_1]) represents the Korteweg-de Vries-Burgers equation, discussed earlier, acting on n_1:

$$\begin{aligned}\mathcal{A}'\frac{\partial n_1}{\partial t_1}+\mathcal{F}'\frac{\partial n_1}{\partial \chi_0^{(+)}}+\mathcal{B}'n_1\frac{\partial n_1}{\partial \chi_0^{(+)}}\\ +\mathcal{C}'\frac{\partial^3 n_1}{\partial {\chi_0^{(+)}}^3}-\mathcal{G}'\frac{\partial^2 n_1}{\partial {\chi_0^{(+)}}^2}n_1=0\,;\end{aligned} \tag{1.85}$$

see § 1.E for the functional form of the coefficients.

The solution to the KdV-Burgers equation was already derived in § 1.5.6 and is simply reiterated here for convenience:

$$\begin{aligned}n_1\left(\chi_0^{(+)},t_1\right)=c_1(t_1)\,\mathrm{sgn}(\mathcal{B}'\mathcal{C}')\,\mathrm{sech}^2\left(\sqrt{\frac{c_1|\mathcal{B}'|}{12|\mathcal{C}'|}}\right.\\ \left.\times\left[\chi_0^{(+)}-\left(\frac{c_1|\mathcal{B}'|}{3|\mathcal{A}'|}\,\mathrm{sgn}(\mathcal{A}'\mathcal{C}')+\frac{\mathcal{F}'}{\mathcal{A}'}\right)t_1\right]\right),\end{aligned} \tag{1.86}$$

where

$$c_1(t_1)=\frac{c_1(0)}{1+t_1/t_d} \tag{1.87}$$

with

$$t_d=\frac{45\mathcal{A}'|\mathcal{C}'|}{4c_1(0)|\mathcal{B}'|\mathcal{G}'}\,, \tag{1.88}$$

with $c_1(0)$ the initial amplitude of the soliton.

1.7 Analysis

Nondimensionalizing helped ensure that all quantities were order $O(1)$ and any information about their magnitude was solely contained in ε prefactors. However, having ordinary, dimensional expressions is more useful for comparing with experiments or existing literature. Therefore, the KdV-Burgers coefficients are written in terms of ordinary, dimensional variables in §§ 1.E and 1.F [7]. Note that the coefficients are still dimensionless and order unity [8].

[7] A few terms were simplified using Kronecker deltas in §§ 1.E and 1.F. For instance, substituting the dimensional expressions into $\mathcal{G}'$ generates an ε^{-q} term multiplying σ_Q and an ε^{-p} term multiplying η and ζ. However, these can be neglected: as mentioned at the end of § 1.B, σ_Q carries an implicit $\delta_{q,0}$ while η and ζ have implicit $\delta_{q,0}$ and $\delta_{q,0}O(\zeta)/O(\eta)$, respectively. Similarly, the thermodynamic contribution of $\mathcal{F}'$ has a factor of ε^{-m^2}; however, given the presence of the Kronecker deltas, this is equivalent to ε^{-1}.

[8] Actually, as written, the coefficients in §§ 1.E and 1.F have all had a common factor of $\varepsilon^{p/2-q/2}\sqrt{O(\sigma_Q)/O(\eta)}$ removed for brevity.

The observables that characterize the system, to this order, are the amplitude, width, speed, and decay period of the soliton. The amplitude is simply given by

$$|n_1| = l_{\text{ref}}^{-d}\varepsilon^{(d+2)/4}\varepsilon c_1(t)\,\text{sgn}(\mathcal{B}'\mathcal{C}') \coloneqq n_{\max}\,. \tag{1.89}$$

We can use $n_{\max}$ to eliminate c_1 in the following expressions [9]. Furthermore, we will factor out the explicit factors of ε and l_{ref} from the KdV-Burgers coefficients; we will denote the original, order unity, coefficients with a caret. Then, we can write the speed as

$$\begin{aligned} v &\coloneqq v_0 - \varepsilon v_F\left(\frac{c_1\hat{\mathcal{B}}'}{3\hat{\mathcal{A}}'}\,\text{sgn}(\mathcal{B}'\mathcal{C}') + \frac{\hat{\mathcal{F}}'}{\hat{\mathcal{A}}'}\right) \\ &= v_0 - \frac{n_{\max}\mathcal{B}'}{3\mathcal{A}'} - v_F\frac{\mathcal{F}'}{\mathcal{A}'}\,. \end{aligned} \tag{1.90}$$

Similarly, the width is given by

$$W \coloneqq \xi\sqrt{\frac{12\left|\hat{\mathcal{C}}'\right|}{c_1\left|\hat{\mathcal{B}}'\right|}} = \sqrt{\frac{12\mathcal{C}'}{n_{\max}\mathcal{B}'}}\,. \tag{1.91}$$

Finally, the soliton decays with

$$n_{\max}(t) \coloneqq l_{\text{ref}}^{-d}\varepsilon^{(d+6)/4}c_1(t)\,\text{sgn}(\mathcal{B}'\mathcal{C}') = \frac{n_{\max}(0)}{1+t/t_d}\,, \tag{1.92}$$

and decay period

$$t_d \coloneqq \frac{1}{\varepsilon}\frac{45\hat{\mathcal{A}}'\left|\hat{\mathcal{C}}'\right|\xi}{4c_1(0)\hat{\mathcal{G}}'|\hat{\mathcal{B}}|'v_F} = \frac{45\mathcal{A}'\mathcal{C}'}{4n_{\max}(0)v_F\mathcal{G}'\mathcal{B}'}\,. \tag{1.93}$$

Here, $n_{\max}(0)$ is the initial value of $n_{\max}$. The factor of ε in the first equality came from converting our $\hat{t}_1/\hat{t}_d$ to $t\varepsilon\xi/\hat{t}_d v_F \coloneqq t/t_d$.

We see that, upon re-dimensionalizing, c_1 and ε never appear alone. Therefore, simply defining $n_{\max}$ as their combination causes all ε and c_1 to drop out, showing that this is a one-parameter family of solutions. Note that these results hold in general for all nondimensionalizations specified in § 1.B. Similarly, notice that the factors of l_{ref} have all canceled: the observables are all independent of l_{ref}, as they must be since l_{ref} is arbitrary.

As mentioned in § 1.4, not all of the system's parameters are independent. It is helpful to re-iterate here which can be set freely. Taking into account the thermodynamic relations, one experimentally useful

[9] Hence, c_1 is the normalized, order-unity analog of $n_{\max}$.

set of independent parameters would be T_0, n_0, $n_{\max}(0)$, $u = u_0 + \varepsilon U_1$, d_1, d_2, and κ.

1.7.1 Relation to Previous Results

As mentioned in the introduction, Svintsov et al. [18] performed a similar perturbative analysis of solitons, though that analysis was restricted to the inviscid, Fermi liquid regime. It is straightforward to compare the inviscid results presented in § 1.5.5 to those of Svintsov et al. [18].

First, our results for v_0 in the case of no background flow, $u_0 = 0$, are in agreement for the regime where $\mu/T \gg 1$ and $\mu/T > 0$, but they differ otherwise. However, this is to be expected: in setting up the problem, Svintsov et al. [18] neglect the contribution of holes. If the contribution of holes is included in their thermodynamic quantities, then our results are in agreement in both Fermi regimes, $|\mu/T| \gg 1$.

Nevertheless, the leading-order Dirac-regime speed v_0 used by Svintsov et al. [18] and derived in Svintsov et al. [30] has a minor error. There, the terms $ik^2\Sigma_j^2 v_F/\omega\langle p_j^{-1}\rangle$, with $j = e$ or h for electrons/holes, appear in (28) and (29) of Ref. [30]. These terms arise from the $\boldsymbol{\nabla}(v_F\langle p_j\rangle)/2$ terms in the momentum conservation equations, (8) and (9) of Ref. [30]. This corresponds to our pressure terms $\boldsymbol{\nabla}P_j$ (though we combine P_e and P_h as $P = P_e + P_h$). The issue arises when Svintsov et al. [30] restricts to leading order terms when calculating v_0. As we showed in (1.50), $\boldsymbol{\nabla}P/P \sim \varepsilon^2$ in the Dirac regime (i.e. $K_0 = 0$), while the inclusion of these $ik^2\Sigma_j^2 v_F/\omega\langle p_j^{-1}\rangle$ terms in Svintsov et al. [30] implicitly assumes $\boldsymbol{\nabla}P/P \sim \varepsilon$. On removing these terms from the leading-order equations, the results Svintsov et al. [30] are consistent with ours.

Furthermore, the Fermi-Dirac distribution function chosen by Svintsov et al. [18] differs from the one chosen by Lucas and Fong [4] (and hence, used in this paper): Svintsov et al. [18] chose $f(\mathbf{p})$ as

$$f(\mathbf{p}) = \frac{1}{1 + \exp((\varepsilon(\mathbf{p}) - \mathbf{u}\cdot\mathbf{p} - \mu)/k_B T)}\,, \tag{1.94}$$

while Lucas and Fong [4] chose the manifestly covariant

$$f(\mathbf{p}) = \frac{1}{1 + \exp((p^\nu u_\nu - \mu)/k_B T)}\,, \tag{1.95}$$

with $p^\nu = (|\mathbf{p}|, \mathbf{p})$ and $u^\nu = (1, \mathbf{u})/\sqrt{1 - |\mathbf{u}|^2/v_F^2}$. This choice of distribution function is preferable as it preserves the form of the dispersion relation $\varepsilon = v_F|\mathbf{p}|$ under Lorentz boosts (with $\gamma = 1/\sqrt{1 - (u/v_F)^2}$).

After accounting for these differences, our results are nearly in agreement. A few typographical

errors [10] remain in the KdV equation and corresponding soliton solution and dispersion relation of Svintsov et al. [18]. After repairing these errors, we have consistent solutions and dispersion relations.

It is worth noting Svintsov et al. [18] also use an isothermal assumption, though it is not directly stated; this assumption is utilized when stating the formula [11]

$$\frac{\mathrm{d}\varepsilon}{\varepsilon} = 2\xi\frac{\mathrm{d}n}{n} + (3-4\xi)\frac{\mathrm{d}T}{T}\,, \tag{1.101}$$

with $\xi \coloneqq n^2/\varepsilon\langle\varepsilon^{-1}\rangle$, and $\langle\varepsilon^{-1}\rangle \neq \varepsilon^{-1}$ is the average inverse energy. While ε depends on both n and T the corresponding formula for $\mathrm{d}\varepsilon/\varepsilon$ in Svintsov et al. [18] only has the $\mathrm{d}n/n$ term. In the Fermi regime, $|\mu/T| \gg 1$ and $\xi = 3/4$, so this is a valid simplification. However, in the Dirac regime, $\xi \ll 1$, and the $\mathrm{d}T/T$ term cannot be neglected unless the system is isothermal, $\mathrm{d}T = 0$.

[10] The sign of the β^2 term multiplying $u\partial_x u$ in (16) of Ref. [18] should be flipped. Additionally, the expression for $F(\nu)$ in (26) should read

$$\begin{aligned} F(\nu) = \tilde{s}_0^2 - \frac{\beta^2}{2} - \frac{\beta_0^2}{1+\nu} \\ - \frac{\beta_0^2\beta^2}{(1+\nu)^2}\frac{5-6\xi}{1-\beta^2} + \frac{\nu\beta_0^2(3-4\xi)}{(1+\nu)^2}\,. \end{aligned} \tag{1.96}$$

In the KdV equation, (27), the coefficient of the $\nu\partial_\zeta\nu$ term should be

$$(1-\xi)\left(2\tilde{s}_0^2 - \frac{4}{3}\xi + 4\beta_0^2\right). \tag{1.97}$$

Also, the solution to the KdV equation, (28), should be

$$\delta n(z) = \delta n_{\max}\cosh^{-2}\left[\frac{z}{2}\sqrt{\frac{\mathbf{2}}{d_1 d_2}\frac{s_0^2}{2s_0^2 - v_F^2}\frac{\delta n_{\max}}{n_0}}\right], \tag{1.98}$$

with (29) changed to

$$\delta n_{\max} = \mathbf{3}\frac{n_0}{2}\frac{u_0^2 - s_0^2}{s_0^2}\,, \tag{1.99}$$

with corrections highlighted in bold.

For the $u_0 \neq 0$ case, (34) should be adjusted by flipping the sign of the γ term multiplying the $u_0\partial_x\delta u$ term. Furthermore, the dispersion relation, (36), should read

$$s_\pm = \frac{u_0(2-2\xi_0+\gamma) \pm \sqrt{s_0^2(1+\gamma) + u_0^2\big[(2-2\xi_0+\gamma)^2 - (1+\gamma)\big(3-\frac{10}{3}\xi_0+\gamma\big)\big]}}{1+\gamma}\,. \tag{1.100}$$

[11] Note that Svintsov et al. [18] include factors of γ in the definitions of ε and n; here, they have been factored out to match our definitions.

1.7.2 Role of gating

Our setup involves the use of conducting gates to screen the electrostatic interactions and make the problem local, and hence more mathematically tractable. However, Akbari-Moghanjoughi [17] instead considered solitons in ungated graphene; that analysis was restricted to the inviscid, $T = 0$ Fermi regime with no background flow [12]. While Akbari-Moghanjoughi [17] also derived solitonic solutions, a number of the properties differed markedly from those derived here.

First, Akbari-Moghanjoughi [17] found that there exists a critical propagation velocity v_c that separates periodic, wavelike solutions ($v < v_c$) and solitonic solutions ($v > v_c$). This was found to be $v_c = 3/\sqrt{38}$ for $d = 2$ and $v_c = 2/3$ for $d = 3$. However, there appears to be a small error in the derivation: (7) for ϕ involves a term $n^{-2/3}$ which should be $n^{-3/2}$. Repeating the derivation with this change shows that the critical propagation velocity is actually $v_c = 1/\sqrt{d}$. Our ($u_0 = 0$, Fermi regime) solutions have velocity

$$v = \frac{1}{\sqrt{d}}\sqrt{1 + \frac{An_0^2 d}{P_0(d+1)}} + \varepsilon v_1 \geq \frac{1}{\sqrt{d}} = v_c\,, \tag{1.102}$$

where we have used the fact that $\operatorname{sgn} v_1 = \operatorname{sgn} v_0$. Thus, we see that our soliton's speeds are bounded *below* by the critical speed, while Akbari-Moghanjoughi [17] found that solitons speeds should be bounded *above* by the critical speed.

Another difference involves the relation between the soliton height and speed. Using our expression for v_1, we found that the total speed with $u_0 = 0$ is

$$v = v_0\left(1 + \varepsilon\frac{c_1|\mathcal{B}|}{3|v_0\mathcal{A}|}\right) \tag{1.103}$$

while the soliton height is εc_1, with a free parameter $c_1 > 0$ [13]. Thus, increasing the height corresponds to increasing the speed, and *vice versa*. However, Akbari-Moghanjoughi [17] found that increasing the height causes the speed to *decrease*. Nevertheless, we both find the same, inverse relation between the height and width (as required by total charge conservation).

Furthermore, Akbari-Moghanjoughi [17] finds only dark ($n_1/n_0 < 0$) solitons. However, our

[12] Note that Akbari-Moghanjoughi [17] uses a different terminology. There, the term "Dirac fluid" refers to massless fermions (as in graphene) while "Fermi liquid" refers to massive fermions. Both of these are dealt with in the completely degenerate $T = 0$ limit. By contrast, we follow the terminology of Lucas and Fong [4] to analyze both a "Fermi liquid" ($k_B T \ll \mu$) and "Dirac fluid" ($\mu \ll k_B T$) regime for massless fermions. Therefore, the "Dirac" results in Akbari-Moghanjoughi [17] correspond to our $T = 0$ Fermi regime, while the "Fermi" results correspond to massive fermions not discussed here. Interestingly, bilayer graphene can induce such an effective mass for the quasiparticle excitations [31].

[13] Here we used the fact that $\operatorname{sgn}(\mathcal{A}'\mathcal{C}') = \operatorname{sgn}(v_0)$ for $u_0 = 0$

solutions only give *bright* ($n_1/n_0 > 0$) solitons. Referring to (1.86), we have $\mathrm{sgn}(n_1) = \mathrm{sgn}\,(\mathcal{B}'\mathcal{C}')$. Here, we will consider the Dirac ($m > 0$) and Fermi ($m < 0$) cases separately. For the Dirac regime, with $K_0 = 0$, it is readily apparent that $\mathcal{B}'\mathcal{C}'$ (cf. § 1.E) is positive, yielding bright solitons.

Showing that the same holds true in the Fermi regime, with $K_0 = (d+1)/d$, is more involved. Using the expressions for $\mathcal{B}'$ and $\mathcal{C}'$ from § 1.E, we see

$$\mathrm{sgn}\left(\frac{n_1}{n_0}\right) = \mathrm{sgn}\left(3d(u_0+v_0)^2 - (1+u_0v_0)^2\right). \tag{1.104}$$

We see that this is clearly positive when $u_0 = 0$; using the expression for v_0, we find it only crosses zero [14] when u_0 is given by

$$\begin{aligned} u_0 = \pm 1 \quad \text{or} \quad & \frac{\sqrt{2\lambda(3d-1)+4} \pm \lambda\sqrt{3d}}{2-\lambda} \\ \text{or} \quad & -\frac{\sqrt{2\lambda(3d-1)+4} \pm \lambda\sqrt{3d}}{2-\lambda}, \end{aligned} \tag{1.105}$$

with $\lambda \coloneqq An_0^2/P_0(d+1)$ as before. Finally, it can be checked that each of these solutions are larger (in magnitude) than unity; that is, $\mathcal{B}'\mathcal{C}'$ does not cross zero in the range $u_0 \in (-1, 1)$. Thus, for $|u_0| < 1$, we find that $n_1/n_0 > 0$, and only bright solitons are permitted. Note that the adiabatic $\mathcal{B}'$ and $\mathcal{C}'$ coefficients in § 1.F are identical to their isothermal Fermi counterparts: therefore, the same reasoning shows the adiabatic system only has bright solutions, too.

Thus, it appears that a number of our findings are directly opposed to those of Akbari-Moghanjoughi [17]. While one might be tempted to compare the results of Akbari-Moghanjoughi [17] with our solutions by taking the gating distance $d_i \to \infty$, various quantities (e.g. v_0, W, etc) would no longer be order-1, violating our expansion assumptions. Instead, it appears that the presence or absence of gates can create qualitatively different results. However, this should not be surprising: the electric field with gates is given by derivatives of the density $E \propto \partial_x n + (d_1 d_2/3)\partial_x^3 n + \ldots$. On the other hand, the electric field without gates is given by the *anti-derivative* of n: $E(x) \propto \int \mathrm{d}y\, n(x)/|x-y|^2$. More specifically, the x-k Fourier transform of the electric potential with gates is $\hat{\phi} \propto (1 - k^2 d_1 d_2/3 + \ldots)\hat{n}$; highly-dispersive, large k-modes *increase* the electric field's magnitude. The potential without gates is $\hat{\phi} \propto -\hat{n}/k^2$, so large k-modes *decrease* the electric field's magnitude. Given that this is the only difference between the setup of the two problems, it appears that this is the origin of the differences in the results [15].

[14] Note that this expression has a removable singularity at $u_0 = 0$; however, the double-sided limit exists and is 0.

[15] A number of other minor differences exist between our work and that of Akbari-Moghanjoughi [17]: there, velocities were normalized by c, giving $v_c = c/\sqrt{d}$. However, we found it more useful to normalize by v_F—yielding $v_c = v_F/\sqrt{d}$. This difference arose because Akbari-Moghanjoughi [17] chose to define

1.7.3 Energy and Entropy

It is interesting to determine the rate of energy loss by the soliton to dissipation. We can accomplish this by integrating the KdV-Burgers equation (1.59). Using (1.81b) to replace n_1 with u_1, we get (with new coefficients denoted by primes)

$$\mathcal{A}'\partial_{t_1}u_1 + \mathcal{F}'\partial_x u_1 + \mathcal{C}'\partial_x^3 u_1 + \mathcal{B}'u_1\partial_x u_1 = \mathcal{G}'\partial_x^2 u_1\,. \tag{1.106}$$

Multiplying this equation by u_1 gives

$$\begin{aligned}\frac{1}{2}\mathcal{A}'\partial_{t_1}u_1^2 + \frac{1}{2}\mathcal{F}'\partial_x u_1^2 \\ + \mathcal{C}'\partial_x\big(u_1\partial_x^2 u_1\big) - \frac{1}{2}\mathcal{C}'\partial_x(\partial_x u_1)^2 + \frac{1}{3}\mathcal{B}'\partial_x u_1^3 \\ = \mathcal{G}'\partial_x(u_1\partial_x u_1) - \mathcal{G}'(\partial_x u_1)^2\,.\end{aligned} \tag{1.107}$$

If we integrate once over all of x-space and impose boundary conditions $u_1 = \partial_x u_1 = 0$ at $x = \pm\infty$, we find

$$\frac{1}{2}\left(\partial_{t_1} + \frac{\mathcal{F}'}{\mathcal{A}'}\partial_x\right)\int \mathrm{d}x\, u_1^2 = -\frac{\mathcal{G}'}{\mathcal{A}'}\int \mathrm{d}x\,(\partial_x u_1)^2\,. \tag{1.108}$$

The left-hand side represents the time rate-of-change of the kinetic energy in a moving reference frame; this is more easily seen if the background current U_1 is removed so $\mathcal{F}' = 0$.

Using the expressions for $\mathcal{A}'$ and $\mathcal{G}'$ (cf. § 1.E), the right-hand side is negative semi-definite for the case with no background flow $u_0 = 0$. Thus, we see that—as expected—the viscosity causes the kinetic energy to decrease.

When $u_0 \neq 0$, it is more difficult to see that $\mathcal{G}'/\mathcal{A}' \geq 0$, as it must be for viscosity to remove energy. Here, we will again treat the Dirac and Fermi regimes separately. Starting with the Dirac case and

$u^\mu = (c, \mathbf{u})/\sqrt{1-(u/c)^2}$ following Zhu and Ji [32], while we defined $u^\mu = (v_F, \mathbf{u})/\sqrt{1-(u/v_F)^2}$. Again, the choice of v_F, as opposed to c, is preferred since it preserves the form of the dispersion relation. Replacing the original choice of u^μ (involving c) with our choice (involving v_F) in Akbari-Moghanjoughi's derivation yields $v_c = v_F/\sqrt{d}$, i.e. our minimum propagation speed.

Finally, our expressions for the pressure differ slightly: it appears Akbari-Moghanjoughi [17] considered only $g = 2$ spin degeneracy in (4), rather than graphene's $g = 4$ spin/valley degeneracy. This only affects the normalization constant (A_{2D} or A_{3D} in, for example, (11)), and the subsequent conclusions are unaffected.

using the expressions for $\mathcal{A}'$ and $\mathcal{G}'$ from § 1.E, we find

$$\begin{aligned}\operatorname{sgn}\left(\frac{\mathcal{G}'}{\mathcal{A}'}\right) = \operatorname{sgn}\Bigg(&\sigma_Q\gamma^2\left(\frac{P_0}{n_0}\right)^2\frac{(u_0+v_0)^4}{1+u_0v_0}(d+1)^2 \\ &+ (u_0+v_0)^2\left[\zeta + 2\eta\left(1-\frac{1}{d}\right)\right]\Bigg),\end{aligned} \tag{1.109}$$

The only questionable term is $\sigma_Q/(1+u_0v_0)$. This term is positive for

$$|u_0| < \frac{1}{\sqrt{1+[An_0^2/P_0(d+1)]}}\,. \tag{1.110}$$

However, it blows up when $|u_0| \to 1/\sqrt{1+\lambda}$, with $\lambda \coloneqq An_0^2/P_0(d+1)$. This causes u_1 and P_1 to become unbounded and invalidates our perturbation expansion. Thus, $|u_0| < 1/\sqrt{1+\lambda}$ is a constraint on the allowed parameters that make our derivation consistent. Under this constraint, $\mathcal{A}'\mathcal{G}' \geq 0$ in the Dirac regime, as it must be.

In the Fermi regime, we instead have

$$\begin{aligned}\operatorname{sgn}\left(\frac{\mathcal{G}'}{\mathcal{A}'}\right) = \operatorname{sgn}\Bigg(&\sigma_Q\gamma^2\left(\frac{P_0}{n_0}\right)^2(d+1)\frac{(u_0+v_0)^2}{(1+u_0v_0)} \\ &+ \frac{d}{d+1}\frac{(u_0+v_0)^2\left[\zeta+2\eta\left(1-\frac{1}{d}\right)\right]}{(u_0+v_0)[v_0(d-u_0^2)+u_0(d-1)]}\Bigg).\end{aligned} \tag{1.111}$$

It is easy to show [16] that $(u_0+v_0)[v_0(d-u_0^2)+u_0(d-1)] > 0$ for $d > 1$ and $|u_0| < 1$; recall that we already required $|u_0| < 1$, otherwise $\gamma = 1/\sqrt{1-u_0^2}$ would blow up. Therefore, the η and ζ terms are positive.

As in the Dirac regime, we also have a $\sigma_Q/(1+u_0v_0)$ term. Though v_0 is different in the Fermi regime, the same reasoning also shows that this quantity is similarly positive for $|u_0| < 1/\sqrt{1+\lambda}$. Thus, as long as $|u_0| < 1/\sqrt{1+\lambda}$, we see that our theory is well-defined, $\mathcal{A}'\mathcal{G}' \geq 0$, and viscosity causes energy to decrease, as required by the second law of thermodynamics. Finally, note that the adiabatic $\mathcal{G}'$ in § 1.F differs slightly from this isothermal Fermi $\mathcal{G}'$; nevertheless, it shares the same questionable terms. Thus, the same exact reasoning shows $\mathcal{G}'/\mathcal{A}' \geq 0$ for the adiabatic regime [17].

[16] This can be seen by noting that the expression is positive for $u_0 = 0$ and only crosses zero at ± 1, $\pm\sqrt{1+\lambda d}$, or $\pm\sqrt{1+\lambda d}/\sqrt{1+\lambda}$, with $\lambda \coloneqq An_0^2/P_0(d+1)$. These are each greater than (or equal to) unity for $d \geq 1$; therefore, the entire expression is non-negative for $|u_0| \leq 1$.

[17] The $\mu_0 n_0$ term is non-negative because $\operatorname{sgn}\mu_0 = \operatorname{sgn} n_0$; cf. (Dirac: C143).

To further investigate the soliton's decay, it is helpful to analyze entropy generation. Lucas and Fong [4] provide the following formula [18] for the divergence of the entropy current s^μ

$$\begin{aligned}\partial_\mu s^\mu = \frac{1}{T}\partial_\mu u_\nu \big[\eta \mathcal{P}^{\mu\rho}\mathcal{P}^{\nu\alpha}\big(\partial_\rho u_\alpha + \partial_\alpha u_\rho - \frac{2}{d} g_{\rho\alpha}\partial_\beta u^\beta\big) \\ + \zeta \mathcal{P}^{\mu\nu}\partial_\alpha u^\alpha\big] + \frac{\sigma_Q}{T}\left(T\partial_\mu \frac{\mu}{T} + F_{\mu\rho}u^\rho\right) \\ \times \mathcal{P}^{\mu\nu}\left(T\partial_\nu \frac{\mu}{T} + F_{\nu\rho}u^\rho\right) .\end{aligned} \tag{1.112}$$

For simplicity, consider the case with no background flow, $u_0 = U_1 = 0$. Upon implementing our usual nondimensionalization in the Dirac regime (cf. § 1.4) we see the highest-order terms are

$$\begin{aligned}\partial_\mu s^\mu = \frac{\eta}{T_0}\partial^i u_1^j \big[\partial_i (u_1)_j + \partial_j (u_1)_i - \frac{2}{d} g_{ij}\partial_k u_1^k\big] \\ + \frac{\zeta}{T_0}\big(\partial_k u_1^k\big)^2\end{aligned} \tag{1.113}$$

Then, restricting to 1-dimensional motion and using our thermodynamic relations and first-order solutions, we find

$$\partial_\mu s^\mu = (\partial_x n_1)^2 \left[\zeta + 2\eta\left(1 - \frac{1}{d}\right)\right]\frac{v_0^2}{T_0 n_0^2} + O(\varepsilon)\,. \tag{1.114}$$

We see that entropy is generated at locations where the derivative of n_1 is largest: for solitons, this occurs at the leading and trailing faces (figure 1.3). Further, as the soliton spreads out, the entropy production slows over time (figure 1.4). Finally, for the Dirac regime, σ_Q-induced entropy production is suppressed to sub-leading order; η and ζ are the main producers of entropy.

1.8 Experimental Proposal

Here, we will briefly detail the applicability of this theory to experiment.

1.8.1 Values of Parameters

It has been more convenient to deal with nondimensional variables throughout the derivation. However, we now convert back to dimensionful quantities to better understand their physical magnitude. It is worth emphasizing that this conversion is dependent on the nondimensionalization we chose. The values calculated in this section are specific to the Dirac regime nondimensionalization laid out in § 1.4; a

[18] Note that we have added an additional factor to the σ_Q term in order to account for the electrostatic interactions.

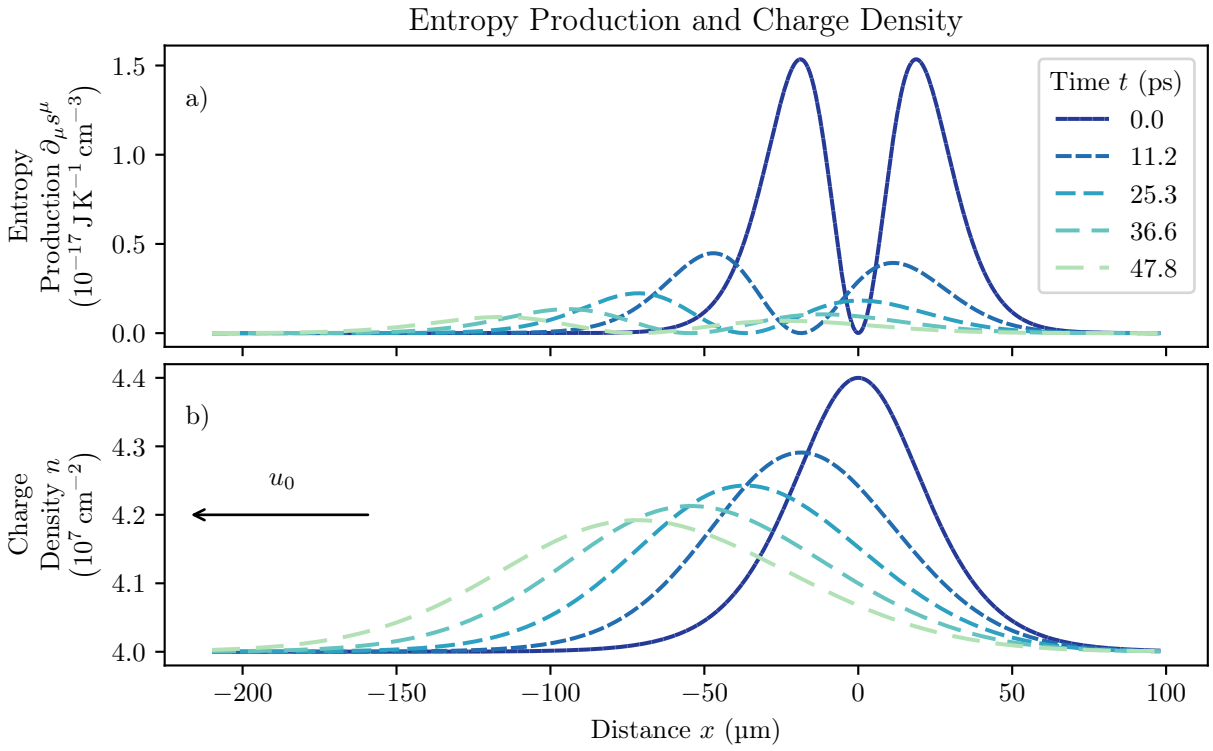

Figure 1.3. The entropy production $\partial_\mu s^\mu$ (a) and soliton charge density n_1 (b) at select times. Values used were $\mathcal{A} = 0.88$, $\mathcal{B} = -0.70$, $\mathcal{C} = -0.060$, $\mathcal{F} = -1.1$, and $\mathcal{G} = 0.53$ with the height normalized to 4.0×10^8 cm^{-2}.

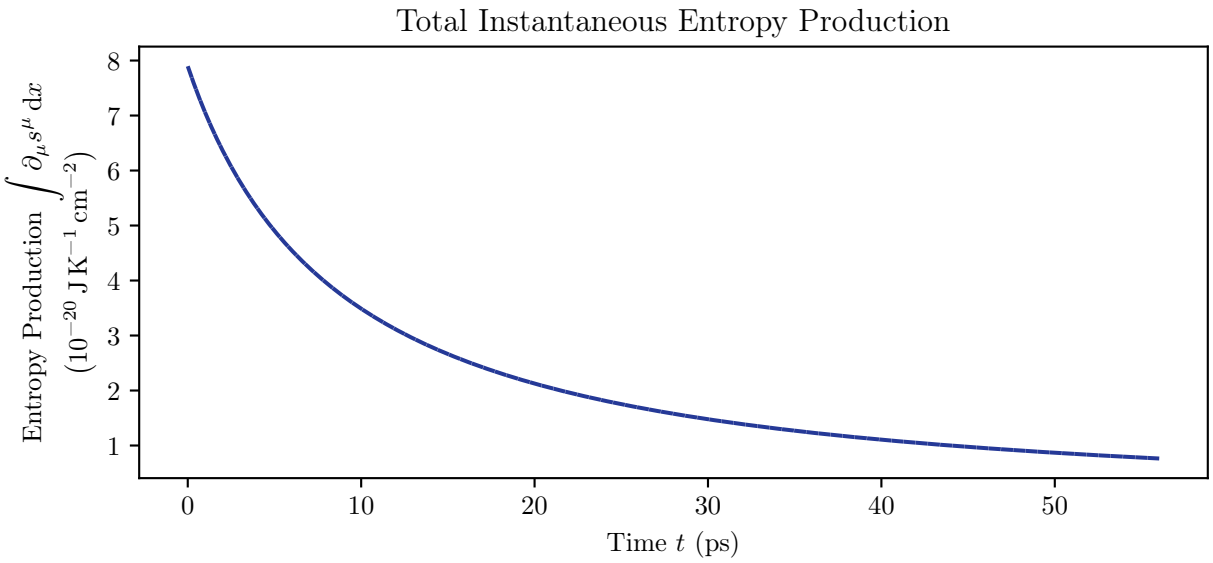

Figure 1.4. The instantaneous entropy production $\partial_\mu s^\mu$ as a function of time. Values used were $\mathcal{A} = 0.88$, $\mathcal{B} = -0.70$, $\mathcal{C} = -0.060$, $\mathcal{F} = -1.1$, and $\mathcal{G} = 0.53$ with the height normalized to 4.0×10^8 cm^{-2}.

Table 1.1. Values of the various parameters in terms of the small parameter ε. Sample values are given for $\varepsilon = 0.1$ and dimension $d = 2$.

	ε-dependence	Sample Nondim. Value	Sample Dim. Value
n_0	$\varepsilon\hat{n}_0$ $4 \times 10^{10}\,\mathrm{cm}^{-2}$	1.0	$4.0 \times 10^{9}\,\mathrm{cm}^{-2}$
d_i	$\varepsilon^{-5/4}\hat{d}_i$ 50 nm	1.0	890 nm
A	$\varepsilon^{-5/4}\hat{A}$ $5.3 \times 10^{-36}\,\mathrm{J\,m}^2$	0.22	$2.1 \times 10^{-35}\,\mathrm{J\,m}^2$
T_0	$\varepsilon^{1/4}\hat{T}_0$ 150 K	0.70	60 K
P_0	$\varepsilon^{3/4}\hat{T}_0^3$ $8.4 \times 10^{-7}\,\mathrm{N\,m}^{-1}$	$1.1\hat{T}_0^3$	$5.9 \times 10^{-8}\,\mathrm{N\,m}^{-1}$
μ_0	$\varepsilon^{3/4}\frac{\hat{n}_0}{\hat{T}_0}$ 2.1×10^{-21} J	$1.1\frac{\hat{n}_0}{\hat{T}_0}$	6.1×10^{-22} J
σ_Q	$\varepsilon^{1/2}\hat{\sigma}_Q$ $0.24\,\mathrm{k}\Omega^{-1}$	0.63	$0.048\,\mathrm{k}\Omega^{-1}$
η	$\hat{\eta}$ $4.2 \times 10^{-20}\,\mathrm{kg\,s}^{-1}$	1.1	$4.8 \times 10^{-20}\,\mathrm{kg\,s}^{-1}$

similar analysis could be performed for the Fermi regime nondimensionalization specified in § 1.B.1.

The dimensional and nondimensional values of the various parameters in the problem are listed in table 1.1. For the remainder of this section, we will specialize to dimension $d = 2$. Note that we are using the values $v_F = c/300$ [4] and $l_{\mathrm{ref}} = 50\,\mathrm{nm}$. For computing the sample values, we have chosen $\varepsilon = 0.1$. We see that all of the nondimensional parameters are approximately equal to unity, as required. However, there are a few points to note.

In previous experiments, the distance between the graphene and the gates d_i $(i = 1, 2)$ was usually on the order of 300 nm [33]. We require a larger gate distance of $d_i = 890\,\mathrm{nm}$ corresponding to $\hat{d}_i = 1.0$. The static dielectric constant κ must be chosen relative to d_1 and d_2. For the remaining normalizations to be consistent, we require $\kappa \approx 1$. That is, the graphene should be suspended from its contacts with vacuum filling the gap between the graphene sheet and the conducting gates.

It is important to reiterate the way we nondimensionalized the intrinsic conductivity. At a temperature of 60 K, σ_Q/e^2 has a fixed value of $0.20\hbar^{-1}$. We needed to relate the relative sizes of nondimensional parameters ε and $\sigma_Q\hbar/e^2$ to solve the problem. Our derivation assumed $\varepsilon \sim 0.1$, so that $\varepsilon^{1/2} \sim \sigma_Q\hbar/e^2$. This fixes the value of $\hat{\sigma}_Q$ as $\hat{\sigma}_Q = 0.20\varepsilon^{-1/2}$.

Notice that if ε is increased, then the numerical value of $\hat{\sigma}_Q$ decreases; hence, the intrinsic conductivity becomes a higher-order correction and drops out of our first-order solutions. Conversely, if ε is decreased, $\hat{\sigma}_Q$ could grow large and require a different nondimensionalization for σ_Q. For ε small enough, it would be more appropriate to take $\sigma_Q = \varepsilon^0\hat{\sigma}_Q e^2/\hbar$. This alternative would require different nondimensionalizations for all variables (cf. § 1.B); nevertheless, similar solutions would result (though the viscosity would no longer appear in the first-order corrections). Similar considerations also apply for η,

though it is considerably simpler given that $\eta l_{\text{ref}}^d/\hbar \approx 1$.

It is also useful to determine the values of the parameters appearing as coefficients in the KdV and KdV-Burgers equations (i.e. $\mathcal{A}$, $\mathcal{B}$, $\mathcal{C}$, and $\mathcal{G}$). For instance, consider the case with $v_0 = 0$, $u_0 > 0$, and $U_1 = 0$; we will also set $\zeta = 0$ and choose $c_1 = 1.0$. Using the above values and the bare thermodynamic coefficients $\mathcal{C}_0$ and $\mathcal{C}_1$ (cf. § 1.A), we find $\mathcal{A} = 0.88$, $\mathcal{B} = -0.70$, $\mathcal{C} = -0.060$, $\mathcal{F} = -1.1$, and $\mathcal{G} = 0.53$ (cf. figure 1.1). Importantly, we see that $\mathcal{B}$, $\mathcal{C}$, and $\mathcal{G}$ are all roughly the same order, implying nonlinearity, dispersion, and dissipation are equally important.

1.8.2 Source and Signal

As we discussed in § 1.4, the characteristic length of the disturbance ξ is related to l_{ref} as $\xi = l_{\text{ref}}/\varepsilon^{(d+5)/4}$. For $d = 2$ and $\varepsilon = 0.1$ with graphene's $l_{\text{ref}} = 50\,\text{nm}$, we find a pulse width of approximately $2.8\,\mu\text{m}$. For the $u_0 = 0$ case, the propagation speed is approximately $v = 0.43 v_F \sim 0.43c/300$, giving a bandwidth of roughly $v/\xi = 150\,\text{GHz}$.

If we consider the stationary soliton case $v_0 = 0$, we need to source a background current $u_0 \neq 0$ to counteract its propagation. In § 1.5, we found that $u_0 = 0.40 v_F = 4.0 \times 10^5\,\text{m}\,\text{s}^{-1}$; with a charge density of $n_0 = 4.0 \times 10^9\,\text{cm}^{-2}$, we need a current density of $K_0 = |e n_0 u_0| = 2.5\,\text{A}\,\text{m}^{-1}$.

As shown previously, the system has a (dimensional) characteristic decay time of

$$t_d = \frac{45 l_{\text{ref}} \mathcal{A} |\mathcal{C}|}{4 \varepsilon^{11/4} v_F \mathcal{G} |\mathcal{B}|} \,. \tag{1.115}$$

Inserting the previously chosen values for these coefficients, we find $t_d \approx 44\,\text{ps}$.

To estimate the magnitude of the signal, we first calculate the background chemical potential $\mu_0 = \varepsilon^{3/4} \hbar v_F l_{\text{ref}}^{-1} \hat{\mu}_0 = 6.1 \times 10^{-22}\,\text{J}$. From this, we find the background voltage $V_0 = \mu_0/e = 3.8\,\text{mV}$. Then, the signal voltage $V_1 = \mu_1/e$ would be a factor of $\varepsilon \sim 0.1$ smaller, or $380\,\mu\text{V}$.

1.8.3 Joule Heating

For the non-propagating case ($v_0 = 0$), a large uniform background current u_0 flows through the graphene; this will cause Joule heating of the entire sample due to graphene's resistance. It is worthwhile to verify that this heating occurs sufficiently slowly so as not to interfere with the soliton's propagation and decay.

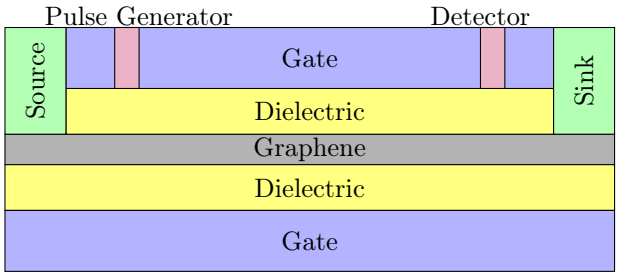

Figure 1.5. Side view of the proposed experimental setup; the graphene is sandwiched between two layers of dielectric, and further sandwiched between two conducting gates. A source and sink on either edge of the graphene generate the background current u_0. The pulse generator produces the soliton and the detector detects it.

The power produced, per unit area, by Joule heating is

$$P_J = K_0^2 \rho \,, \tag{1.116}$$

with resistivity ρ and surface current density K_0. As a worst-case scenario, assuming the graphene does not lose any heat to the environment, this power goes solely towards heating the graphene.

The specific heat of graphene [34] at 60 K is approximately $60\,\mathrm{mJ\,g^{-1}\,K^{-1}}$. Given an atomic mass of $12.01\,\mathrm{g\,mol^{-1}}$ for carbon and an atomic density of $6.3\,\mathrm{mol\,cm^{-2}}$ for carbon atoms in graphene [35], we find a specific heat of $c_s = 4.5 \times 10^{-9}\,\mathrm{J\,cm^{-2}\,K^{-1}}$.

Therefore, the soliton's temperature will change at a rate of $P_J/c_s = 3.0\,\mathrm{K\,ns^{-1}}$. Given that the suggested experiment would be measuring the soliton's temperature anomaly $T_1 = \varepsilon T_0$, it would only be sensitive to Joule heating after a temperature change of similar magnitude had been generated. Hence, it would take approximately $T_1 c_s / P_J = 2.0\,\mathrm{ns}$ for the system to heat appreciably. Given that this time is long compared to the characteristic timescales of the problem (t_{char} and t_d), we are justified in neglected Joule heating.

Notice that the characteristic Joule-heating time is also long compared to the electron-phonon scattering time; this implies the electrons and graphene lattice would thermalize relatively quickly compared to the Joule heating time. This is why we utilized the specific heat of the entire graphene system (electrons and lattice) as opposed to the specific heat of only the electrons.

1.8.4 Experimental Setup

The solitonic solutions we have derived offer a means to experimentally measure the viscosity η of graphene. In particular, the viscous coefficients σ_Q, η, and ζ all enter into the coefficient we have denoted

$\mathcal{G}$. Therefore, if the value of $\mathcal{G}$ can be measured, then the viscosity can be determined.

Referring to the expression for $\mathcal{G}$, we see that η only appears in the combination $\zeta + 2\eta(1 - 1/d)$; hence, it is this quantity that can be determined from experiment. In practice, we expect $\zeta \ll \eta$, and thus this procedure offers an estimate for η [4]. Furthermore, determining η from $\mathcal{G}$ requires knowing the values of all the other parameters P_0, n_0, etc. Most of these are experimentally determined and hence known; the only other necessary quantity is the intrinsic conductivity σ_Q. Previous measurements of this quantity exist [7, 8]; therefore, it can be treated as a known quantity.

An initial disturbance needs to be generated in the graphene; for instance, this can be accomplished via a short voltage spike produced by a thin contact placed laterally atop the sample (cf. figure 1.5). It is well known that the KdV equation causes a localized profile to split into a series of left- and right-moving solitons [36] sorted by height. After the disturbance is allowed to propagate a sufficient distance, the individual solitons should have separated enough to be separately distinguished. The actual population of solitons generated by the pulse will be dependent on the contact's shape and voltage profile: the distribution of soliton heights and widths can be determined by the inverse scattering transform [37].

Given that the solitons represent a localized change in the charge density, it should be possible to detect them with a voltmeter; a voltage time-series could then reconstruct the soliton profile. The dissipative terms cause two measurable effects: a change in the propagation speed and a decay of the soliton's height. This requires measuring either the soliton's speed or amplitude as a function of time. Depending on the particular experimental setup, one effect might be more accessible than the other. Next, we describe two possible experimental setups.

No Propagation

Without a background current $u_0 = 0$, the soliton propagates at a speed $v \approx v_F \approx c/300$. Such a fast propagation speed could make measurement difficult. One way to mitigate this is to impose a counter-current u_0 in the opposite direction of propagation; as detailed in § 1.5, it is possible to choose a background current $u_0 + \varepsilon U_1$ such that the soliton is stationary in the laboratory frame $v_0 + \varepsilon v_1 = 0$. Doing this should make obtaining the height measurements much easier. In fact, the speed measurements are still feasible in this setup since the dissipation causes v_1, and hence the control current U_1, to decay over time.

One possible barrier to implementation of this method is the boundary condition of graphene. So far, we have neglected boundary effects by assuming one-dimensional propagation; depending on graphene's

boundary conditions, this might not be justified. Graphene most likely satisfies one of two possible boundary conditions [38]: either a no-slip boundary ($\mathbf{u} = 0$) or no-stress (no normal velocity gradient, i.e. $[\hat{n} \cdot \boldsymbol{\nabla}]\mathbf{u} = 0$ with $\hat{n}$ the boundary unit normal). If the actual boundary is no-slip, our 1-dimensional propagation assumption is violated; in this case, the sample must be sufficiently wide to ignore edge effects, or a different experimental setup (cf. the next section) is needed. Conversely, a no-stress boundary permits our one-dimensional soliton solution. There is some experimental evidence that no-stress boundaries are the correct boundary type [4], and theory predicts that weakly disordered edges at low temperature ($T \lesssim 40\,\mathrm{K}$) have a slip-length on the order of 50 µm. Therefore, it is plausible that, for graphene samples of width at most $\sim 100\,\mu\mathrm{m}$, a no-stress boundary condition is appropriate, allowing for large u_0 counter-current.

No Background Current

If graphene instead possesses a no-slip boundary condition, a different experimental method will be needed. For this setup, we will not use a background flow, $u_0 = 0$. Then, the boundary conditions are mostly irrelevant, since the fluid velocity is now of order $O(u_1) = \varepsilon v_F$ and can therefore be made small. For this setup, height measurements are more suitable; after one decay period τ_0, the height decreases by a factor of $\frac{1}{2}$ while the propagation velocity changes by a factor of $\delta v / v_0 = \frac{1}{2}\varepsilon \ll 1$.

Following the method proposed by Coelho et al. [39], we recommend periodically producing a voltage pulse and measuring a set distance away. By averaging over many realizations, it should be possible to obtain a wave profile. This could be repeated at a few locations, thereby measuring the decay rate as a function of downstream position.

This method is likely more difficult experimentally given that it requires taking measurements at multiple locations sequentially. However, it has the benefit of being theoretically sound regardless of graphene's boundary conditions.

1.9 Conclusion

Graphene offers a fantastic environment for studying strong-coupling phenomena. Hydrodynamic analysis presents a useful set of tools for analyzing the long-wavelength physics in such a clean, strongly-coupled system. The Fermi liquid regime has much in common with ordinary metals and has been the focus of many experiments in graphene; meanwhile, the Dirac fluid regime hosts a number of intriguing phenomena. When graphene is placed in a hydrodynamic regime, the electrons obey relativistic Navier-Stokes equations and can form solitonic solutions. An ordinary perturbation expansion was used to derive

the special case of a stationary soliton on a background counter flow. Additionally, a full multiple scales asymptotic analysis was utilized to treat the general case with arbitrary background flow. These methods furnished analytic approximations to the shape and speed of the predicted solitons. This analysis did not deal with the boundary conditions of the fluid flow; this offers an interesting avenue for future research.

By including dissipation in our system, we were able to model the decay of the solitons. The analysis showed that dissipation causes both a decay of the soliton's height as well as its speed. This decay rate offers a means to experimentally measure dissipation in the hydrodynamic regime of graphene. The results of this paper help elucidate the connection between solitons in the Fermi and Dirac regimes of graphene and put forward a new method for measuring hydrodynamically relevant parameters such as the intrinsic conductivity and shear viscosity.

1.10 Acknowledgments

Special thanks to Falk Feddersen for his invaluable support and input. The computations in this paper were performed by using MAPLE™ [40]. This work was supported in part by funds provided by the U.S. Department of Energy (D.O.E.) under cooperative research agreement DE-SC0009919. Chapter 1, in full, is a reprint of the material as it appears in Effects of Dissipation on Solitons in the Hydrodynamic Regime of Graphene in Physical Review B by T. Zdyrski and J. McGreevy in 2019. The dissertation author was the primary investigator and author of this paper.

1.A Thermodynamic Coefficients

Following Lucas and Fong [4], we can derive the pressure for weak coupling, starting from the grand canonical ensemble for a free Fermi gas in d dimensions

$$\begin{aligned} P(\mu,T) &= -\frac{\Phi_G}{V} = \frac{k_B T}{V}\sum_{A,\mathbf{p}} \ln(\mathcal{Z}_{A,\mathbf{p}}) \\ &= k_B T \sum_A \int \frac{\mathrm{d}^d\mathbf{p}}{(2\pi\hbar)^d} \ln\Big(1+e^{(q_A\mu-\varepsilon_A(\mathbf{p}))/k_BT}\Big) \\ &= -\frac{4(k_BT)^{d+1}\Omega_{d-1}(d-1)!}{(2\pi\hbar v_F)^d}\big(\mathrm{Li}_{d+1}(-e^{\mu/k_BT}) \\ &\quad + \mathrm{Li}_{d+1}(-e^{-\mu/k_BT})\big)\,. \end{aligned} \tag{1.117}$$

Here, we have Φ_G the grand potential, $\mathcal{Z} = \exp(-\Phi_G/k_BT)$ the grand partition function, and V the volume. We made use of the fact that, for a free Fermi gas, the grand partition function is separable over modes (A and $\mathbf{p}$): $\mathcal{Z} = \prod_{A,\mathbf{p}} \mathcal{Z}_{A,\mathbf{p}}$. Additionally, we have the excitation energy $\varepsilon_A(\mathbf{p}) = v_F|\mathbf{p}|$, $\Omega_{d-1} = 2\pi^{d/2}/\Gamma(d/2)$ the surface area of a unit $(d-1)$-sphere, Γ is the gamma function, and Li_d the polylogarithm of order $d+1$. Note that the sum over species runs over spin/valley degeneracy (giving a factor of 4) as well as electrons/holes with $q_A = \pm 1$. More specifically, $\sum_A \ln(\mathcal{Z}_A) = 4\ln(\mathcal{Z}_1(\mu,T)) + 4\ln(\mathcal{Z}_1(-\mu,T))$.

Likewise, the carrier density is given by

$$\begin{aligned} n(\mu,T) = \frac{\partial P}{\partial \mu} &= \frac{4(k_BT)^d\Omega_{d-1}(d-1)!}{(2\pi\hbar v_F)^d} \\ &\quad \times \left(-\mathrm{Li}_d(-e^{\mu/k_BT}) + \mathrm{Li}_d(-e^{-\mu/k_BT})\right). \end{aligned} \tag{1.118}$$

We can develop series (asymptotic) expansions in Dirac (Fermi) regimes.

In the Dirac regime ($\mu \ll k_BT$), the polylogarithm can be approximated as [41]

$$\mathrm{Li}_s(-e^z) = -\sum_{k=0}^{\infty} \eta(s-k)\frac{z^k}{k!}, \tag{1.119}$$

for $|z| < \pi$, with η the Dirichlet eta function. Thus, the pressure is given by

$$\begin{aligned} P(\mu,T) &= 8\frac{(k_BT)^{d+1}\Omega_{d-1}(d-1)!}{(2\pi\hbar v_F)^d} \\ &\quad \times \sum_{k=0}^{\infty} \frac{\eta(d+1-2k)}{(2k)!}\left(\frac{\mu}{k_BT}\right)^{2k} \\ &= 8\frac{(k_BT)^{d+1}\Omega_{d-1}(d-1)!}{(2\pi\hbar v_F)^d}\left[\eta(d+1)\right. \\ &\quad \left. + \frac{\eta(d-1)}{2}\left(\frac{\mu}{k_BT}\right)^2 + O\left(\frac{\mu}{k_BT}\right)^4\right], \end{aligned} \tag{1.120}$$

and the carrier density is

$$\begin{aligned} n(\mu,T) &= \frac{8\mu(k_BT)^{d-1}\Omega_{d-1}(d-1)!}{(2\pi\hbar v_F)^d} \\ &\quad\times\sum_{k=0}^{\infty}\frac{\eta(d-1-2k)}{(2k+1)!}\left(\frac{\mu}{k_BT}\right)^{2k} \\ &= \frac{8\mu(k_BT)^{d-1}\Omega_{d-1}(d-1)!}{(2\pi\hbar v_F)^d}\Big[\eta(d-1) \\ &\quad+\frac{\eta(d-3)}{6}\left(\frac{\mu}{k_BT}\right)^2+O\left(\frac{\mu}{k_BT}\right)^4\Big]. \end{aligned} \tag{1.121}$$

For instance, for $d=2$, we find

$$P=\frac{(k_BT)^3}{(\hbar v_F)^2}\left[\frac{4\eta(3)}{\pi}+\frac{2\ln(2)}{\pi}\left(\frac{\mu}{k_BT}\right)^2+O\left(\frac{\mu}{k_BT}\right)^4\right], \tag{1.122}$$

and

$$n=\frac{\mu(k_BT)}{(\hbar v_F)^2}\left[\frac{4\ln(2)}{\pi}+\frac{1}{6\pi}\left(\frac{\mu}{k_BT}\right)^2+O\left(\frac{\mu}{k_BT}\right)^6\right]. \tag{1.123}$$

Instead, in the Fermi regime ($\mu\gg k_BT$), an asymptotic expansion of the polylogarithm is given by [41]

$$\mathrm{Li}_s(-e^z)=-2\sum_{k=0}^{\lfloor s/2\rfloor}\frac{\eta(2k)}{(s-2k)!}(z)^{s-2k}+O\big(e^{-z}\big), \tag{1.124}$$

for $\mathrm{Re}\{z\}\gg 1$, while $\mathrm{Li}_s(-\exp(-z))$ is sub-dominant and therefore can be neglected. Thus, we find

$$\begin{aligned} P(\mu,T) &= \frac{8|\mu|^{d+1}\Omega_{d-1}}{(2\pi\hbar v_F)^d} \\ &\quad\times\sum_{k=0}^{\lfloor(d+1)/2\rfloor}\frac{\eta(2k)(d-1)!}{(d+1-2k)!}\left(\frac{k_BT}{\mu}\right)^{2k} \\ &= \frac{8|\mu|^{d+1}\Omega_{d-1}}{(2\pi\hbar v_F)^d}\left[\frac{1}{2(d+1)d}\right. \\ &\quad\left.+\frac{\pi^2}{12}\left(\frac{k_BT}{\mu}\right)^2+O\left(\frac{k_BT}{\mu}\right)^4\right], \end{aligned} \tag{1.125}$$

and the carrier density is

$$\begin{aligned} n(\mu,T) &= \frac{8|\mu|^d \operatorname{sgn}(\mu)\Omega_{d-1}}{(2\pi\hbar v_F)^d} \\ &\quad \times \sum_{k=0}^{\lfloor d/2 \rfloor} \frac{\eta(2k)(d-1)!}{(d-2k)!}\left(\frac{k_BT}{\mu}\right)^{2k} \\ &= \frac{8|\mu|^d \operatorname{sgn}(\mu)\Omega_{d-1}}{(2\pi\hbar v_F)^d}\left[\frac{1}{2d}\right. \\ &\quad \left. + \frac{\pi^2(d-1)}{12}\left(\frac{k_BT}{\mu}\right)^2 + O\left(\frac{k_BT}{\mu}\right)^4\right], \end{aligned} \tag{1.126}$$

Again, for $d = 2$, we have

$$P = \frac{|\mu|^3}{(\hbar v_F)^2}\left[\frac{1}{3\pi} + \frac{\pi}{3}\left(\frac{k_BT}{\mu}\right)^2 + O\left(\frac{k_BT}{\mu}\right)^4\right], \tag{1.127}$$

and

$$n = \frac{\mu^2 \operatorname{sgn}(\mu)}{(\hbar v_F)^2}\left[\frac{1}{\pi} + \frac{\pi}{3}\left(\frac{k_BT}{\mu}\right)^2 + O\left(\frac{k_BT}{\mu}\right)^4\right]. \tag{1.128}$$

Thus, we find the following coefficients

$$\mathcal{C}_0^F = \frac{8|\mu|^{d+1}\Omega_{d-1}}{(2\pi\hbar v_F)^d}\frac{1}{2(d+1)d} \tag{1.129}$$

$$\mathcal{C}_1^F = \frac{8|\mu|^{d+1}\Omega_{d-1}}{(2\pi\hbar v_F)^d}\frac{\pi^2}{12} \tag{1.130}$$

and

$$\mathcal{C}_0^D = 8\frac{(k_BT)^{d+1}\Omega_{d-1}(d-1)!}{(2\pi\hbar v_F)^d}\eta(d+1) \tag{1.131}$$

$$\mathcal{C}_1^D = 8\frac{(k_BT)^{d+1}\Omega_{d-1}(d-1)!}{(2\pi\hbar v_F)^d}\frac{\eta(d-1)}{2}. \tag{1.132}$$

When screening is not negligible, these coefficients get renormalized. For instance, the Dirac coefficients for $d = 2$ and $T \to 0$ become [42]

$$\mathcal{C}_0^D = 8\frac{(k_BT)^3\Omega_1}{(2\pi\hbar v_F)^2}\eta(3)\left(\frac{\alpha(T)}{\alpha_0}\right)^2 \tag{1.133}$$

$$\mathcal{C}_1^D = 8\frac{(k_BT)^3\Omega_1}{(2\pi\hbar v_F)^2}\frac{\eta(1)}{2}\left(\frac{\alpha(T)}{\alpha_0}\right)^2, \tag{1.134}$$

with $\alpha(T)$ given in (1.26).

1.B General Nondimensionalization

A critical aspect of these derivations was the correct choice of nondimensionalization scheme. Depending on the physical regime of interest (Fermi *vs.* Dirac) as well as the relative size of terms (e.g. how large ε is compared to $\sigma_Q\hbar/e^2$), different nondimensionalization choices may be appropriate. To elucidate the relationship between these various schemes a single, general nondimensionalization can be performed. In this section, we will use a unit system in which $\hbar = v_F = k_B = l_{\text{ref}} = e = 1$. Note: we are only nondimensionalizing ($\hbar = 1$, etc), but not normalizing; i.e. we are not requiring that all quantities are unity (unlike the quantities denoted earlier by carets).

For convenience, the main results are collected here:

$$\begin{aligned}
O(\mu) &= \varepsilon^{\frac{1}{2}q-\frac{1}{2}p+\frac{1}{2}m+\frac{1}{2}|m|}\sqrt{\frac{O(\eta)}{O(\sigma_Q)}}\,,\\
O(T) &= \varepsilon^{\frac{1}{2}q-\frac{1}{2}p+\frac{1}{2}|m|}\sqrt{\frac{O(\eta)}{O(\sigma_Q)}}\,,\\
O(P) &= \varepsilon^{\frac{d+1}{2}q-\frac{d+1}{2}p+\frac{d+1}{4}m+\frac{d+1}{4}|m|}\sqrt{\frac{O(\eta)}{O(\sigma_Q)}}^{d+1}\,,\\
O(n) &= \varepsilon^{\frac{d}{2}q-\frac{d}{2}p+\frac{d+1}{4}m+\frac{d+1}{4}|m|}\sqrt{\frac{O(\eta)}{O(\sigma_Q)}}^{d}\,,\\
O(\partial_x) &= \varepsilon^{1+\frac{d+1}{2}q-\frac{d-1}{2}p+\frac{d+1}{4}m+\frac{d+1}{4}|m|}\sqrt{\frac{O(\eta)^{d-1}}{O(\sigma_Q)^{d+1}}}\,,\\
O(d_i) &= \varepsilon^{-\frac{1}{2}-\frac{d+1}{2}q+\frac{d-1}{2}p-\frac{d+1}{4}m-\frac{d+1}{4}|m|}\sqrt{\frac{O(\sigma_Q)^{d+1}}{O(\eta)^{d-1}}}\,,\\
O(u) &= 1\,,\\
O(A) &= \varepsilon^{\frac{-d+1}{2}q+\frac{d-1}{2}p-\frac{d+1}{4}m-\frac{d+1}{4}|m|}\sqrt{\frac{O(\sigma_Q)}{O(\eta)}}^{d-1}\,.
\end{aligned} \tag{1.135}$$

Here, we have defined four parameters [19]: d the spatial dimension, $m \in \mathbb{Z}\setminus\{0\}$, $p \in \mathbb{N} \geq 0$, and $q \in \mathbb{N} \geq 0$.

[19] Note that one combination of parameters is not allowed in this derivation: $m < -1$ and $q = 0$. Owing to the thermodynamic relations, $m < -1$ implies that T_1 will depend on density and pressure of the form $n_{1+|m|}$ and $P_{1+|m|}$. We are able to manipulate the results for $m = -1$ (cf. § 1.C.4) to handle these n_2 and P_2 terms. However, for $m < -1$, these terms cannot be eliminated. If $q > 0$, then μ_1 and T_1 do not appear in our first-order corrections, so this is acceptable; if $q = 0$, we would have these $n_{1+|m|}$ and $P_{1+|m|}$ terms

The parameter m is defined as

$$\varepsilon^m \coloneqq O\left(\frac{\mu}{k_B T}\right)^2, \tag{1.136}$$

and represents the "Dirac" or "Fermi" quality of the system: $m > 0$ corresponds to increasingly strong "Dirac"-character while $m < 0$ is more "Fermi"-like. The parameter p measures the importance of the shear terms η: if $p = 0$, the shear terms enter our first-order correction equations while, for $p > 0$, it enters at the $(p+1)$-order correction equations and thus are not considered in our analysis. Likewise, the parameter q measures the importance of the conductive terms σ_Q: if $q = 0$, the conductive terms enter our first-order correction equations, but they are higher order for $q > 0$.

The KdV-Burgers coefficients specified in §§ 1.E and 1.F and throughout the paper assume $p = q = 0$. When using other choices of p and q, it is important to replace $\eta \to \eta\delta_{p,0}$, $\zeta \to \zeta\delta_{p,0} O(\zeta)/O(\eta)$, and $\sigma_Q \to \sigma\delta_{q,0}$. This ensures that only the relevant dissipative coefficients appear.

Note that we have specified $O(u) = 1$ to allow for large background flows $O(u_0) = 1$. Nevertheless, these results still apply if $u_0 = 0$ (no background flow), in which case $u \sim \varepsilon u_1$ and $O(u) = \varepsilon$. Additionally, these nondimensionalizations assume that $u < 1$ is small enough that $\gamma = 1/\sqrt{1-u^2}$ is order $O(\gamma) = 1$. Finally, note that we have assumed $O(\eta) \geq O(\zeta)$.

1.B.1 Parameter Choice

For concreteness, the main paper utilizes a Dirac regime nondimensionalization of $m = 1$ and $p = q = 0$ with $O(\eta) = 1$ and $O(\sigma_Q) = \varepsilon^{1/2}$.

We also highlight additional terms in the multiple scales expansion arising from the Fermi regime. These come about from a nondimensionalization with $m = -1$ and $p = q = 0$ with $O(\eta) = O(\sigma_Q) = 1$.

The alternate derivation for small ε mentioned in § 1.8 would correspond to $m = p = 1$ and $q = 0$ with $O(\eta) = O(\sigma_Q) = 1$.

It is worth highlighting that different choices of $O(\sigma_Q)$ and $O(\eta)$ do not affect the calculated results or observables (cf. § 1.B.3). Likewise, the parameters m, p, and q have minimal, straightforward effects on the results: p determines whether η and ζ terms appear in $\mathcal{G}'$; q determines if σ_Q appears in $\mathcal{G}'$; and m determines the form of P_1, and thus $\mathcal{F}'$ [20]. Otherwise, the results are independent of the choice of m, p, and q. To wit, these choices do not even affect the ε-order of observable quantities; see § 1.7.

Using the definition of A, it is easy to check that $\kappa \geq 1$ satisfies $O(\kappa) = \varepsilon^{-1/2-q} O(\sigma_Q) O(\alpha) \geq 1$;

which cannot be eliminated.

[20] Furthermore, $m < -1$ precludes the choice of $q = 0$; see footnote 19.

this provides a constraint on the allowed parameters. For $\varepsilon = 0.1$, $q = 0$, $O(\sigma_Q) = \varepsilon^{1/2}$, and $O(\alpha) = 1$ used throughout the main text, we find $O(\kappa) = 1$, consistent with our choice of $\kappa = 1$.

1.B.2 Entropy Divergence

In § 1.7.3, we found that the entropy divergence only depended on the η and ζ terms, to this order. Using our expressions for the generalized nondimensionalization, we can investigate what occurs for different parameter regimes.

Recall that (1.112) showed that

$$\begin{aligned} O(\partial_\nu s^\nu) = \frac{1}{O(T)} O(\partial_x u)^2 [O(\eta) + O(\zeta)] \\ + \frac{O(\sigma_Q)}{O(T)} [O(\partial_x \mu) + O(F^{x\rho} u_\rho)]^2 . \end{aligned} \tag{1.137}$$

Restricting our attention, as usual, to $u < 1$ such that $\gamma = 1/\sqrt{1-u^2} \approx 1$, we see that $O(F_{i\rho} u^\rho) = O(E_x) = O(\partial_x \phi) = O(\partial_x A n)$. Thus, using the results from § 1.B, we have

$$\begin{aligned} O(\partial_\nu s^\nu) = \frac{O(\eta) O(\partial_x)^2 \varepsilon^{2-p}}{O(T)} \Big[\varepsilon^p + \frac{O(\zeta)}{O(\eta)} \varepsilon^p \\ + \varepsilon^q + \varepsilon^{q + \frac{1}{2}m + \frac{1}{2}|m|} + \varepsilon^{q+m+|m|} \Big] . \end{aligned} \tag{1.138}$$

Here, the terms in the square brackets represent the η, ζ, $\sigma_Q E_x^2$, $\sigma_Q E_x \partial_x \mu$, and $\sigma_Q (\partial_x \mu)^2$ terms respectively. Hence, we recognize that increasing p causes the η and ζ terms to be less relevant, while increasing q does the same to the σ_Q terms. Furthermore, the leading factor of μ/T for the σ_Q terms in (1.112) causes these terms to be higher order when $m > 0$ (i.e. when μ/T is small), as expected. Finally, note that 1.135 were defined under the assumption $O(\eta) \geq O(\zeta)$, so $O(\zeta)/O(\eta)$ in (1.138) can be, at most, unity.

1.B.3 Order of Dissipative Coefficients

Notice that we have left $O(\sigma_Q)$ and $O(\eta)$ undetermined. There is some subtlety in choosing these parameters. This most obvious manner to proceed involves using existing theoretical predictions [4] for

their magnitude [21]; for instance, in $d = 2$,

$$\eta \approx \begin{cases} \frac{0.45T^2}{\alpha^2} & \text{Dirac}\,. \\ \frac{3\mu^2|n|}{64\pi\alpha^2 \ln(\alpha^{-1})T^2} & \text{Fermi}\,, \end{cases} \tag{1.139}$$

and

$$\sigma_Q = \begin{cases} \frac{0.12}{\alpha^2} & \text{Dirac}\,, \\ 1 & \text{Fermi}\,, \end{cases} \tag{1.140}$$

with $\alpha \approx 4/\ln\bigl(10^4\,\mathrm{K}/T\bigr)$. Ignoring logarithmic corrections, these will then generate compatibility conditions on the parameters m, p, and q. Nevertheless, such a choice is only valid in the infinitesimal ε limit: we must assume ε is small enough that all the numerical prefactors—like $3/64\pi \approx 0.015$ for η in the Dirac regime—are considered order-1 (i.e. $O\bigl(\varepsilon^0\bigr)$). If ε is large enough that, for instance, $3/64\pi \approx \varepsilon$, then this assumption breaks down.

Alternatively, one could instead calculate the numerical values for σ_Q and η from the existing theories. For instance, in § 1.4, we calculated $\sigma_Q = 0.20$ for our choices of parameters. This value can then be compared to the expected value of ε to determine the correct scaling. Continuing our example, assuming $\varepsilon \approx 0.1$, we found $\sigma_Q \approx \varepsilon^{1/2}$. While this method is somewhat more *ad hoc* than the previously described one, it has the benefit that it is now valid in a neighborhood of the desired ε rather than for solely infinitesimal ε. This is the method used in the main text since we are considering ε small but finite.

1.B.4 Derivation: Dominant Balance

Now, we will derive the results given at the beginning of § 1.B. These results follow from the application of dominant balance.

First, we define a small nondimensional parameter $\varepsilon \ll 1$ as our expansion parameter: that is, all terms will be expanded in integer powers of ε as $y = y_0 + \varepsilon y_1 + \ldots$. Further, we will assume that all leading-order quantities are uniform in space and constant in time (i.e. $y(x,t) = y_0 + \varepsilon y_1(x,t) + \ldots$). This implies that derivatives will always generate one extra factor of ε: $O(\partial_\mu y(x,t)) = O(\partial_\mu \varepsilon y_1(x,t)) = \varepsilon O(\partial_\mu) O(y)$.

Next, we introduce the parameter $m \in \mathbb{Z} \setminus \{0\}$ as

$$\varepsilon^m \coloneqq O\Bigl(\frac{\mu}{T}\Bigr)^2. \tag{1.141}$$

[21] Note that the expression for σ_Q in the Fermi regime lacks numerical factors; see Müller et al. [43] for the exact expression for the (screened) Fermi case.

We require that m be an integer since it enters in an asymptotic expansion of the equation of state $P(\mu, T)$; since our main equations are expanded in integer powers of ε, we must also have this asymptotic expansion in integer powers of ε. Also, notice we used the square of μ/T; it is easily seen that the asymptotic expansion of $P(\mu, T)$ only involves even powers of μ/T since it is an even function of μ/T [22]. Thus, we see that the Dirac regime follows when $m > 0$ and the Fermi case corresponds to $m < 0$; the $m = 0$ case is excluded because then the thermodynamic equation of state (cf. (1.117)) cannot be expanded in a series/asymptotic expansion.

With this definition, we are able to collapse the two different nondimensionalizations of the pressure. From the thermodynamic equation of state (1.117), we see that $O(P) = O(T)^{d+1}$ for Dirac and $O(P) = O(\mu)^{d+1}$ for Fermi. Therefore, we have $O(P) = \varepsilon^{(d+1)m/4+(-d-1)|m|/4} O(T)^{d+1}$ in general. Likewise, the charge density can be nondimensionalized as $O(n) = \varepsilon^{|m|/2} O(P)/O(T) = \varepsilon^{(d+1)m/4+(-d+1)|m|/4} O(T)^{d}$.

Now, we begin using dominant balance to impose restrictions based on our desire that certain terms appear at certain orders. Here, we must use some foresight about which terms the equations will contain. To ensure that we have wavelike solutions, we want the terms appearing in the leading order equations to match those in § 1.6. Since we want the dispersive electromagnetic terms $d_1 d_2 \partial_x^3 n$ to appear at as first-order corrections, this means the nondispersive electromagnetic term $\partial_x n$ must appear at leading order. Thus, the two electromagnetic terms must differ by one factor of ε: this imposes $O(d_i) = \varepsilon^{1/2}/O(\partial_x)$; this is our first assumption. Requiring the nondispersive electromagnetic term to enter at leading order enforces $O(\partial_x P) = O(An\partial_x n)$ yielding our second assumption: $O(A) = \varepsilon^{(-d-1)m/4+(d-3)|m|/4} O(T)^{-d+1}$.

Next, we wish the leading order equations to be satisfied even if $u_0 = 0$. Setting $u_0 = 0$ and performing a dominant balance on the leading charge conservation equation (1.74a) gives $O(\partial_t) = O(u)O(\partial_x)$, our third requirement. Another dominant balance on the leading momentum conservation equation (1.74b) yields $O(u) = 1$, our fourth and final requirement.

Moving onto the shear- and bulk-viscosity terms, we introduce a second parameter $p \in \mathbb{N} \geq 0$. This parameter is defined such that $p = 0$ ensures that the shear/bulk viscosities appear in our first-order correction equations, $p = 1$ would push these terms to second-order corrections, and so on. Since we are only concerned with first-order corrections, this means shear/bulk viscosity is relevant for $p = 0$ and irrelevant for $p > 0$. This is implemented by imposing $O(\varepsilon \partial_x P) = \varepsilon^{-p} O\big(\eta \partial_x^2 n\big)$, yielding $O(\partial_x) = \varepsilon^{p+1} O(P)/O(\eta)$.

Finally, we introduce one more parameter $q \in \mathbb{N} \geq 0$ controlling the order at which the intrinsic conductivity σ_Q appears. Similar to the parameter p, the parameter $q = 0$ yields σ_Q terms at first-order while

[22] Equivalently, Lucas et al. [42] prove $P(\mu, T)$ only involves even powers by recognizing that the equation of state is charge conjugation invariant.

$q > 0$ corresponds to higher-order terms (which will be neglected in this analysis). It is easy to check that of the two σ_Q terms, the electromagnetic term $O(F^{\nu\rho}u_\rho) = O(A\partial_x n)$ is always larger than the thermoelectric term $O(T\partial_x(\mu/T)) \leq O(A\partial_x n)$. Thus, we introduce the parameter q as $O(\varepsilon\partial_t n) = \varepsilon^{-q}O\big(\sigma_Q\partial_x^2 An\big)$. This implies that $O(T) = \varepsilon^{q/2-p/2+|m|/2}\sqrt{O(\eta)/O(\sigma_Q)}$. Using these various relations reproduces the results given at the beginning of § 1.B.

1.C Adiabatic System

Here, we can utilize the same nondimensionalization laid out in § 1.B for the isothermal system. This follows because the derivation in § 1.B.4 required that the leading order equations still be satisfied when $u_0 = 0$. However, it is easy to show that, when $u_0 = 0$, the leading order energy conservation equation (1.156b) is equivalent to the leading order charge conservation equation (1.156a) combined with the isothermal relation between P and n. Thus, the leading order, $u_0 = 0$ adiabatic system is equivalent to the leading order, $u_0 = 0$ isothermal system, and the previous nondimensionalization carries over.

Here, we will redo the multiple scales derivation using the adiabatic assumption. Therefore, we will now include the energy conservation equation (1.10) and allow T to vary dynamically. As we did in § 1.6, we expand all of the dynamic variables (including T) in a perturbation expansion.

1.C.1 Perturbative Thermodynamics

We will be using the thermodynamic relationships of § 1.3.3 to write μ and T in terms of n and P. Expanding the thermodynamic variables and collecting powers of ε yields the following relations for the Dirac regime:

$$P_0 = T_0^{d+1}\mathcal{C}_0\,, \tag{Dirac: C142}$$

$$n_0 = 2T_0^{d-1}\mu_0\mathcal{C}_1\,, \tag{Dirac: C143}$$

$$P_1 = P_0\left[\frac{T_1}{T_0}(d+1) + \frac{\mathcal{C}_1}{\mathcal{C}_0}\left(\frac{\mu_0}{T_0}\right)^2\delta_{m,1}\right], \tag{Dirac: C144}$$

$$n_1 = n_0\left[\frac{\mu_1}{\mu_0} + \frac{T_1}{T_0}(d-1) + 2\frac{\mathcal{C}_2}{\mathcal{C}_1}\left(\frac{\mu_0}{T_0}\right)^2\delta_{m,1}\right], \tag{Dirac: C145}$$

$$P_2 = P_0\Bigg[\frac{T_2}{T_0}(d+1) + \frac{T_1^2}{T_0^2}\frac{(d+1)d}{2} + \frac{\mathcal{C}_1}{\mathcal{C}_0}\left(2\frac{\mu_1}{\mu_0} + (d-1)\frac{T_1}{T_0}\right)\left(\frac{\mu_0}{T_0}\right)^2\delta_{m,1} + \frac{\mathcal{C}_2}{\mathcal{C}_0}\left(\frac{\mu_0}{T_0}\right)^4\delta_{m,1} + \frac{\mathcal{C}_1}{\mathcal{C}_0}\left(\frac{\mu_0}{T_0}\right)^2\delta_{m,2}\Bigg], \tag{Dirac: C146}$$

$$n_2 = n_0\Bigg[\frac{\mu_2}{\mu_0} + \frac{T_2}{T_0}(d-1) + \frac{T_1^2}{T_0^2}\frac{(d-1)(d-2)}{2} + \frac{\mu_1}{\mu_0}\frac{T_1}{T_0}(d-1) + 2\frac{\mathcal{C}_2}{\mathcal{C}_1}\left(3\frac{\mu_1}{\mu_0} + (d-3)\frac{T_1}{T_0}\right)\left(\frac{\mu_0}{T_0}\right)^2\delta_{m,1} + 3\frac{\mathcal{C}_3}{\mathcal{C}_1}\left(\frac{\mu_0}{T_0}\right)^4\delta_{m,1} + 2\frac{\mathcal{C}_2}{\mathcal{C}_1}\left(\frac{\mu_0}{T_0}\right)^2\delta_{m,2}\Bigg] \tag{Dirac: C147}$$

Similarly, for the Fermi regime, we find

$$P_0 = |\mu_0|^{d+1}\mathcal{C}_0\,, \tag{Fermi: C148}$$

$$n_0 = |\mu_0|^d \operatorname{sgn}(\mu_0)\mathcal{C}_0(d+1)\,, \tag{Fermi: C149}$$

$$P_1 = P_0\left[\frac{\mu_1}{\mu_0}(d+1) + \frac{\mathcal{C}_1}{\mathcal{C}_0}\left(\frac{T_0}{\mu_0}\right)^2\delta_{m,-1}\right], \tag{Fermi: C150}$$

$$n_1 = n_0\left[\frac{\mu_1}{\mu_0}d + \frac{\mathcal{C}_1}{\mathcal{C}_0}\frac{d-1}{d+1}\left(\frac{T_0}{\mu_0}\right)^2\delta_{m,-1}\right], \tag{Fermi: C151}$$

$$P_2 = P_0\Bigg[\frac{\mu_2}{\mu_0}(d+1) + \frac{\mu_1^2}{\mu_0^2}\frac{(d+1)d}{2} + \frac{\mathcal{C}_1}{\mathcal{C}_0}\left(2\frac{T_1}{T_0} + (d-1)\frac{\mu_1}{\mu_0}\right)\left(\frac{T_0}{\mu_0}\right)^2\delta_{m,-1} + \frac{\mathcal{C}_2}{\mathcal{C}_0}\left(\frac{T_0}{\mu_0}\right)^4\delta_{m,-1} + \frac{\mathcal{C}_1}{\mathcal{C}_0}\left(\frac{T_0}{\mu_0}\right)^2\delta_{m,-2}\Bigg], \tag{Fermi: C152}$$

$$n_2 = n_0\Bigg[\frac{\mu_2}{\mu_0}d + \frac{\mu_1^2}{\mu_0^2}\frac{d(d-1)}{2} + \frac{\mathcal{C}_1}{\mathcal{C}_0}\frac{d-1}{d+1}\left(2\frac{T_1}{T_0} + (d-2)\frac{\mu_1}{\mu_0}\right)\left(\frac{T_0}{\mu_0}\right)^2\delta_{m,-1} + \frac{\mathcal{C}_2}{\mathcal{C}_0}\frac{d-3}{d+1}\left(\frac{T_0}{\mu_0}\right)^4\delta_{m,-1} + \frac{\mathcal{C}_1}{\mathcal{C}_0}\frac{d-1}{d+1}\left(\frac{T_0}{\mu_0}\right)^2\delta_{m,-2}\Bigg] \tag{Fermi: C153}$$

In the Dirac regime, we can invert these relations to write μ and T in terms of P and n, treating

these as the independent variables at each order. However, in the Fermi regime, this perturbation expansion introduces a peculiarity. The P_0 and n_0 equations do not contain T_0; therefore, rather than giving the value of T_0, these equations provide a constraint on P_0 and n_0:

$$P_0 = \frac{|n_0|^{(d+1)/d}}{|\mathcal{C}_0|^{1/d}(d+1)^{(d+1)/d}} \operatorname{sgn} C_0 \,. \qquad \text{(Fermi: C154)}$$

Similarly, the $P_1(x,t)$ and $n_1(x,t)$ equations only depend on a single dynamical variable $\mu_1(x,t)$ (but not $T_1(x,t)$); therefore, these also give a restriction on P_1 and n_1 to ensure that $T_0(x,t) = T_0$ is independent of x and t:

$$\frac{P_1}{P_0} = \frac{n_1}{n_0}\frac{d+1}{d} + \frac{\mathcal{C}_1}{\mathcal{C}_0}\frac{1}{d}\left(\frac{T_0}{\mu_0}\right)^2 \delta_{m,-1} \,. \tag{1.155}$$

This requirement will be utilized later.

1.C.2 Conservation Equations

If we again restrict to 1D motion and collect terms by powers of ε we get the following equations: Leading Order:

$$\frac{\partial n_1}{\partial t_0} + \gamma^2 n_0 u_0 \frac{\partial u_1}{\partial t_0} + u_0 \frac{\partial n_1}{\partial x} + n_0 \gamma^2 \frac{\partial u_1}{\partial x} = 0 \,, \tag{1.156a}$$

$$\gamma^2 \frac{\partial \varepsilon_1}{\partial t_0} + \gamma^2 u_0^2 \frac{\partial P_1}{\partial t_0} + 2u_0(\varepsilon_0 + P_0)\gamma^4 \frac{\partial u_1}{\partial t_0} + (1+u_0^2)(\varepsilon_0 + P_0)\gamma^4 \frac{\partial u_1}{\partial x} + u_0 \gamma^2 \frac{\partial}{\partial x}(\varepsilon_1 + P_1) + A n_0 u_0 \gamma^2 \frac{\partial n_1}{\partial x} + A n_0^2 u_0^2 \gamma^4 \frac{\partial u_1}{\partial x} = 0 \,, \tag{1.156b}$$

$$\gamma^3(\varepsilon_0 + P_0)\frac{\partial u_1}{\partial t_0} + \gamma u_0 \frac{\partial P_1}{\partial t_0} + u_0 \gamma^3 (\varepsilon_0 + P_0)\frac{\partial u_1}{\partial x} + \gamma \frac{\partial P_1}{\partial x} + A n_0 \gamma \frac{\partial n_1}{\partial x} + A n_0^2 u_0 \gamma^3 \frac{\partial u_1}{\partial x} = 0 \,, \tag{1.156c}$$

First-Order Correction:

$$\frac{\partial n_2}{\partial t_0} + \gamma^2 n_0 u_0 \frac{\partial u_2}{\partial t_0} + u_0 \frac{\partial n_2}{\partial x} + n_0 \gamma^2 \frac{\partial u_2}{\partial x} = \text{RHS} \,, \tag{1.157a}$$

$$\gamma^2 \frac{\partial \varepsilon_2}{\partial t_0} + \gamma^2 u_0^2 \frac{\partial P_2}{\partial t_0} + 2u_0(\varepsilon_0 + P_0)\gamma^4 \frac{\partial u_2}{\partial t_0} + (1+u_0^2)(\varepsilon_0 + P_0)\gamma^4 \frac{\partial u_2}{\partial x} + u_0 \gamma^2 \frac{\partial}{\partial x}(\varepsilon_2 + P_2) + A n_0 u_0 \gamma \frac{\partial n_2}{\partial x} = \text{RHS} \,, \tag{1.157b}$$

$$\gamma^3(\varepsilon_0 + P_0)\frac{\partial u_2}{\partial t_0} + \gamma u_0 \frac{\partial P_2}{\partial t_0} + u_0 \gamma^3 (\varepsilon_0 + P_0)\frac{\partial u_2}{\partial x} + \gamma \frac{\partial P_2}{\partial x} + A n_0 \frac{\partial n_2}{\partial x} = \text{RHS} \,. \tag{1.157c}$$

Again, we have used the electrostatic coupling A according to (1.28). See § 1.D for the terms on the right-hand side.

1.C.3 Leading Order Equations

Using $\varepsilon = Pd$ and combining equations like

$$\begin{aligned}\left(\frac{\partial}{\partial t_0} + u_0\frac{\partial}{\partial x}\right)\Bigg\{ & Adn_0\gamma^2\frac{\partial}{\partial x}\big[(1.156\text{a})\big] \\ & + \left(u_0\frac{\partial}{\partial t_0} + \frac{\partial}{\partial x}\right)\big[(1.156\text{b})\big] \\ & - \gamma\left((d+u_0^2)\frac{\partial}{\partial t_0} + u_0(d+1)\frac{\partial}{\partial x}\right)\big[(1.156\text{c})\big]\Bigg\}\end{aligned}$$

gives

$$\begin{aligned}0 = \gamma^2\left(\frac{\partial}{\partial t_0} + u_0\frac{\partial}{\partial x}\right)\Bigg\{ & \gamma^2(d+1)P_0(u_0^2-d)\frac{\partial^2 u_1}{\partial t_0^2} \\ & - 2\gamma^2(d+1)P_0u_0(d-1)\frac{\partial^2 u_1}{\partial t_0\partial x} \\ & + \left[Adn_0^2 + \gamma^2(d+1)P_0(1-du_0^2)\right]\frac{\partial^2 u_1}{\partial x^2}\Bigg\}.\end{aligned} \tag{1.158}$$

This wave equation has solutions $f(x+v_0t_0) + g(x-v_0t_0)$ with v_0 given by

$$v_0^{(\pm)} = -\frac{u_0(d-1)}{d-u_0^2} \pm \frac{\sqrt{d}}{(d-u_0^2)\gamma^2}\sqrt{1+\frac{An_0^2\gamma^2(d-u_0^2)}{P_0(d+1)}}\,. \tag{1.159}$$

We will take the $(+)$ sign so that $v_0 = v_0^{(+)}$; the other can be recovered by taking $u_0 \to -u_0$ and $v_0 \to -v_0$. Further, we restrict to unidirectional solutions $u_1(x,t_0,t_1) = f(x \pm v_0t_0, t_1)$ for a definite choice of $\pm$; here, we choose $(+)$ as well—the other propagation direction can be recovered by taking $v_0 \to -v_0$.

For stationary perturbations ($v_0 = 0$), we can solve for u_0:

$$u_0 = \pm\sqrt{\frac{(1/d) + [An_0^2/P_0(d+1)]}{1+[An_0^2/P_0(d+1)]}}\,. \tag{1.160}$$

For reference, the velocity of propagation in the absence of a background flow ($u_0 = 0$) is

$$v_0 = \pm\frac{1}{\sqrt{d}}\sqrt{1+\frac{Adn_0^2}{(d+1)P_0}}\,. \tag{1.161}$$

In general, n_1, u_1, and P_1 have traveling wave solutions; neglecting solutions of the form $f(x-$

$u_0 t_0, t_1)$ that are simply advected by the background current, we find solutions given by

$$n_1(x, t_0, t_1) = n_1(x + v_0 t_0, t_1) + F_1(t_1)\,, \tag{1.162a}$$

$$\begin{aligned} u_1(x, t_0, t_1) = &-\frac{(u_0 + v_0)}{n_0 \gamma^2 (1 + u_0 v_0)} n_1(x + v_0 t_0, t_1) \\ &+ F_2(t_1)\,, \end{aligned} \tag{1.162b}$$

$$\frac{P_1(x, t_0, t_1)}{P_0} = \frac{d+1}{d} \frac{n_1(x + v_0 t_0, t_1)}{n_0} + F_3(t_1)\,. \tag{1.162c}$$

Here, we have arbitrary functions $F_1(t_1)$, $F_2(t_2)$, and $F_3(t_2)$; by imposing boundary conditions $n_1 = 0$ at $x = \pm\infty$, we set $F_1 = 0$. We will allow $U_1(t_2) \coloneqq F_2(t_2)$ to remain arbitrary; this uniform background current can be superimposed on the soliton solution as in § 1.5 if desired [23]. In the Dirac regime, we can impose $P_1 = 0$ at $x = \pm\infty$ to set $F_3 = 0$; however, for the Fermi regime, requiring that $T_0(x, t) = T_0$ independent of (x, t) restricts the relationship between P_1 and n_1. Hence, we will write F_3 as

$$F_3(t_1) = \delta_{m,-1} \frac{1}{d} \frac{\mathcal{C}_1}{\mathcal{C}_0} \left(\frac{T_0}{\mu_0} \right)^2 . \tag{1.163}$$

1.C.4 First-Order Corrections

Now considering the first-order corrections, preventing secular growth of the higher-order terms (i.e. n_2, u_2, etc) requires imposing a compatibility condition on the lower-order terms (i.e. n_1, u_1, etc). We can manipulate the system as

$$\begin{aligned} \left(\frac{\partial}{\partial t_0} + u_0 \frac{\partial}{\partial x} \right) \Bigg\{ & A d n_0 \gamma^2 \frac{\partial}{\partial x} \big[(1.157\text{a}) \big] \\ & + \left(u_0 \frac{\partial}{\partial t_0} + \frac{\partial}{\partial x} \right) \big[(1.157\text{b}) \big] \\ & - \gamma \left[(d + u_0^2) \frac{\partial}{\partial t_0} + u_0 (d+1) \frac{\partial}{\partial x} \right] \big[(1.157\text{c}) \big] \Bigg\} \end{aligned}$$

[23] Note that it is possible to generate a stationary soliton by appropriate choice of F_1 or F_3 instead, though the resulting coefficients will be different.

$$
\begin{aligned}
&+\delta_{m,-1}\gamma\frac{1}{2}\frac{\mathcal{C}_0}{\mathcal{C}_1}\frac{\sigma_Q(d+1)}{n_0}\frac{\mu_0^3}{T_0^2}\left(\frac{\partial}{\partial x}+u_0\frac{\partial}{\partial t_0}\right)^2\Bigg(\\
&\quad-\left(\frac{\partial}{\partial x}+u_0\frac{\partial}{\partial t_0}\right)\big[(1.157\text{b})\big]\\
&\quad+\gamma\left[(d+u_0^2)\frac{\partial}{\partial t_0}+u_0(d+1)\frac{\partial}{\partial x}\right]\big[(1.157\text{c})\big]\\
&\quad+\frac{Adn_0^2}{P_0(d+1)}\frac{\partial}{\partial x}\big\{\gamma u_0\big[(1.157\text{c})\big]-\big[(1.157\text{b})\big]\big\}\Bigg)
\end{aligned}
$$

to obtain

$$
\begin{aligned}
&\gamma^4P_0(d+1)(d-u_0^2)\Bigg[\left(\frac{\partial}{\partial t_0}+u_0\frac{\partial}{\partial x}\right)\\
&\quad-\delta_{m,1}\gamma\frac{1}{2}\frac{\mathcal{C}_0}{\mathcal{C}_1}\frac{\sigma_Q(d+1)}{n_0}\frac{\mu_0^3}{T_0^2}\left(\frac{\partial}{\partial x}+u_0\frac{\partial}{\partial t_0}\right)^2\Bigg]\\
&\quad\times\left(v_0^{(+)}\frac{\partial}{\partial x}-\frac{\partial}{\partial t_0}\right)\left(v_0^{(-)}\frac{\partial}{\partial x}-\frac{\partial}{\partial t_0}\right)u_2\\
&=\text{LOT}\,,
\end{aligned}
\tag{1.164}
$$

where LOT represents lower-order terms (i.e. n_1, u_1, etc).

It is instructive here to change variables to $\chi_0^{(\pm)}=x+v_0^{(\pm)}t_0$. Then, the equation becomes

$$
\begin{aligned}
&\gamma^4P_0(d+1)\big(d-u_0^2\big)\Big(v_0^{(+)}-v_0^{(-)}\Big)^2\\
&\quad\times\left\{\left[\sum_{\pm}\Big(u_0+v_0^{(\pm)}\Big)\frac{\partial}{\partial\chi_0^{(\pm)}}\right]\right.\\
&\quad\left.-\delta_{m,-1}\gamma\frac{3\sigma_Q}{\pi^2n_0d}\frac{\mu_0^3}{T_0^2}\left[\sum_{\pm}\Big(1+u_0v_0^{(\pm)}\Big)\frac{\partial}{\partial\chi_0^{(\pm)}}\right]^2\right\}\\
&\quad\times\frac{\partial}{\partial\chi_0^{(-)}}\frac{\partial}{\partial\chi_0^{(+)}}u_2\\
&=\text{LOT}
\end{aligned}
\tag{1.165}
$$

This is where we encounter an apparent problem. Upon inserting our solutions for the lower-order terms, we find the right-hand side depends on products and derivatives of $f\Big(\chi_0^{(+)}\Big)$. This implies that the LOT is solely a function of $\chi_0^{(+)}$.

However, we see that functions of the form $f(\chi^{(+)})$ are also solutions to the homogeneous equation in (1.164) due to the presence of the $\partial_{\chi_0^{(-)}}$ operator.

So, products and derivatives of $f(\chi_0^{(+)})$ appear as inhomogeneous forcing terms that give rise to secular terms. For instance, terms proportional to $f^{(4)}\Big(\chi_0^{(+)}\Big)$ give rise to solutions of the form

$\chi_0^{(-)} f^{(3)}\left(\chi_0^{(+)}\right)$. This grows unbounded in $\chi_0^{(-)}$—and hence, in time t. This will eventually cause $|u_2| > |u_1|$, invalidating the perturbation expansion. Thus, unless LOT vanishes identically, it will give rise to $\chi_0^{(\pm)}$-secular terms in u_2—i.e. solutions growing unbounded in t_0 or x.

Hence, we require the right-hand side to vanish and we are left with the desired compatibility equation:

$$\begin{aligned} 0 = (u_0 + v_0) &\frac{\partial^2}{\partial {\chi_0^{(+)}}^2} (\mathrm{KdVB}[n_1]) \\ &- \delta_{m,-1} \gamma \frac{1}{2} \frac{\mathcal{C}_0}{\mathcal{C}_1} \frac{\sigma_Q (d+1)(1+u_0 v_0)^2}{n_0} \frac{\mu_0^3}{T_0^2} \\ &\times \frac{\partial^3}{\partial {\chi_0^{(+)}}^3} \left. (\mathrm{KdVB}[n_1]) \right|_{\sigma_Q = 0} . \end{aligned} \tag{1.166}$$

Here, $(\mathrm{KdVB}[n_1])$ represents the Korteweg-de Vries-Burgers equation, discussed earlier, acting on n_1:

$$\begin{aligned} \mathcal{A}' \frac{\partial n_1}{\partial t_1} + \mathcal{F}' \frac{\partial n_1}{\partial \chi_0^{(+)}} + \mathcal{B}' n_1 \frac{\partial n_1}{\partial \chi_0^{(+)}} \\ + \mathcal{C}' \frac{\partial^3 n_1}{\partial {\chi_0^{(+)}}^3} - \mathcal{G}' \frac{\partial^2 n_1}{\partial {\chi_0^{(+)}}^2} n_1 = 0 \,; \end{aligned} \tag{1.167}$$

see § 1.F for the functional form of the coefficients. Likewise, $(\left.\mathrm{KdVB}[n_1]\right|_{\sigma_Q=0})$ represents the Korteweg-de Vries-Burgers equation without σ_Q terms.

It is interesting to note the similarities and differences between the adiabatic KdV-Burgers coefficients (§ 1.F) and the isothermal coefficients (§ 1.E). For most of the coefficients ($\mathcal{A}'$, $\mathcal{B}'$, and $\mathcal{C}'$), the adiabatic coefficients are identical to the isothermal Fermi ($m = -1$) coefficients. The $(1 + u_0 v_0)\mathcal{C}_1/\mathcal{C}_0$ term in $\mathcal{F}'$ differs slightly between the adiabatic Fermi case (coefficient $(d+1)/d^2$) and isothermal Fermi case (coefficient $(d-1)/d^2$); the adiabatic Dirac case is completely absent ($\delta_{m,-1}$) compared to the isothermal Dirac case. Interestingly, the adiabatic η and ζ terms in $\mathcal{G}'$ matches the isothermal Fermi terms, while the adiabatic σ_Q term matches the isothermal *Dirac* one.

1.C.5 Solving the Compatibility Equation

In the Fermi regime ($m = -1$), the compatibility equation (1.166) no longer has the simple, decaying soliton solution derived in § 1.5.6. This can certainly be solved numerically. Additionally, we can generate an approximate solution if we assume that $O(\sigma_Q) \ll 1$, (but $\gg \varepsilon$ to prevent them from falling to the next order in our perturbation expansion) and use the same trick as we did in § 1.5.6. Namely, we

factor out a small parameter $\delta \sim O(\sigma_Q)$ from $\sigma_Q = \delta\tilde{\sigma}_Q$. Then, $O(\tilde{\sigma}_Q) = 1$, and we can expand in factors of δ.

Then, another short multiple scales expansion for n_1 can be done in $\delta = O(\mathcal{G}/\mathcal{A})$. To be consistent with our original perturbation series, we require that $\varepsilon \ll \delta \ll 1$. As usual, we expand n_1 as $n_1 = n_1^{(0)} + \delta n_1^{(1)}$ and $\partial_{t_1} = \partial_{\tau_0} + \delta\partial_{\tau_1}$. Then, to leading order, we have

$$(u_0 + v_0)\partial^2_{\chi_0^{(+)}} \left(\mathrm{KdVB}[n_1^{(0)}]\right)\Big|_{\tilde{\sigma}_Q=0} = 0\,. \tag{1.168}$$

This is satisfied by the KdVB equation,

$$\begin{aligned}\mathcal{L}_0 n_1^{(0)} \coloneqq{}& \mathcal{A}'\partial_{\tau_0} n_1^{(0)} + \mathcal{F}'\partial_{\chi_0^{(+)}} n_1^{(0)} + \frac{\mathcal{B}'}{2}\partial_{\chi_0^{(+)}}\left(n_1^{(0)}\right)^2 \\ &+ \mathcal{C}'\partial^3_{\chi_0^{(+)}} n_1^{(0)} - \mathcal{G}'\Big|_{\tilde{\sigma}_Q=0}\partial^2_{\chi_0^{(+)}} n_1^{(0)} \\ ={}& 0\,.\end{aligned} \tag{1.169}$$

Now, we further assume that η and ζ are small; specifically, we assume $O(\eta) \ll 1, \varepsilon \ll O(\delta) \ll O(\zeta)$. Then, the solution was found in § 1.5.6 upon replacing $\mathcal{G}'$ with $\mathcal{G}'\big|_{\tilde{\sigma}_Q=0}$:

$$\begin{aligned}n_1^{(0)}\left(\chi_0^{(+)}, \tau_0\right) = c_1(\tau_0)\,\mathrm{sgn}(\mathcal{B}'\mathcal{C}')\,\mathrm{sech}^2\Bigg(&\sqrt{\frac{c_1|\mathcal{B}'|}{12|\mathcal{C}'|}} \\ &\times\left[\chi_0^{(+)} - \left(\frac{c_1|\mathcal{B}'|}{3|\mathcal{A}'|}\,\mathrm{sgn}(\mathcal{A}'\mathcal{C}') + \frac{\mathcal{F}'}{\mathcal{A}'}\right)\tau_0\right]\Bigg),\end{aligned} \tag{1.170}$$

where

$$c_1(\tau_0) = \frac{c_1(0)}{1 + \tau_0/\tau_d^{(0)}} \tag{1.171}$$

with

$$\tau_d^{(0)} = \frac{45\mathcal{A}'|\mathcal{C}'|}{4c_1(0)|\mathcal{B}'|\,\mathcal{G}'\big|_{\tilde{\sigma}_Q=0}}\,. \tag{1.172}$$

As mentioned above, we have assumed $O(\delta) \ll O\Big(\mathcal{G}'/\mathcal{A}'\big|_{\tilde{\sigma}_Q=0}\Big) \ll 1$, so $1/\tau_d^{(0)} \ll 1$.

At the next order in δ, we must allow the constant $c_1(0)$ to become time-dependent on a slow

time-scale $c_1(0) = c_1(0, \tau_1)$. Now, our equation is

$$\begin{aligned}
&(u_0 + v_0)\partial^2_{\chi_0^{(+)}}\Big(\mathcal{A}'\partial_{\tau_0} n_1^{(1)} + \mathcal{F}'\partial_{\chi_0^{(+)}} n_1^{(1)} \\
&\quad + \mathcal{B}'\partial_{\chi_0^{(+)}}\Big(n_1^{(0)} n_1^{(1)}\Big) + \mathcal{C}'\partial^3_{\chi_0^{(+)}} n_1^{(1)}\Big) \\
&= (u_0 + v_0)\partial^2_{\chi_0^{(+)}}\Big(-\partial_{t_1}\mathcal{A}' n_1^{(0)} + \partial^4_{\chi_0^{(+)}}\mathcal{G}' n_1^{(0)}\Big) \\
&\quad - \delta_{m,-1}\gamma\frac{1}{2}\frac{\mathcal{C}_0}{\mathcal{C}_1}\frac{\sigma_Q(d+1)(1+u_0v_0)^2}{n_0}\frac{\mu_0^3}{T_0^2} \\
&\quad \times \partial {\chi_0^{(+)}}^3\,(\mathrm{KdVB}[n_1^{(0)}])\Big|_{\tilde{\sigma}_Q=0} \\
&= (u_0 + v_0)\partial^2_{\chi_0^{(+)}}\Big(-\partial_{t_1}\mathcal{A}' n_1^{(0)} + \partial^2_{\chi_0^{(+)}}\mathcal{G}' n_1^{(0)}\Big)\,.
\end{aligned} \tag{1.173}$$

In the last line, we used the fact that $n_1^{(0)}$ satisfies the $\mathrm{KdVB}\big|_{\tilde{\sigma}_Q=0}$ equation to simplify the right-hand side. Integrating twice and dropping constants of integration (we want $n_1^{(0)} = n_1^{(1)} = 0$ to be a solution) gives

$$\begin{aligned}
\mathcal{L}_1 n_1^{(1)} &\coloneqq \mathcal{A}'\partial_{\tau_0} n_1^{(1)} + \mathcal{F}'\partial_{\chi_0^{(+)}} n_1^{(1)} + \mathcal{B}'\partial_{\chi_0^{(+)}}\Big(n_1^{(0)} n_1^{(1)}\Big) \\
&\quad + \mathcal{C}'\partial^3_{\chi_0^{(+)}} n_1^{(1)} \\
&= -\partial_{t_1}\mathcal{A}' n_1^{(0)} + \partial^2_{\chi_0^{(+)}}\mathcal{G}' n_1^{(0)}\,.
\end{aligned} \tag{1.174}$$

As before, we note that $\mathcal{L}_0$ and $-\mathcal{L}_1$ are adjoints:

$$\int \mathrm{d}\chi_0^{(+)}\Big(n_1^{(1)}\mathcal{L}_0 n_1^{(0)} + n_1^{(0)}\mathcal{L}_1 n_1^{(1)}\Big) = 0\,. \tag{1.175}$$

Thus, we get the compatibility condition

$$(u_0 + v_0)\int n_1^{(0)}\Big(\mathcal{A}'\partial_{\tau_1} n_1^{(0)} - \mathcal{G}'\partial_x^2 n_1^{(0)}\Big)\,\mathrm{d}\chi_0^{(+)} = 0\,, \tag{1.176}$$

which yields the equation

$$\partial_{\tau_1} c_1(0, \tau_1) = -\frac{c_1(0,\tau_1)^2 |\mathcal{B}'|\tilde{\mathcal{G}}'}{|\mathcal{C}'|\mathcal{A}'}\frac{4}{45}\,. \tag{1.177}$$

Then, solving this equation and converting back to time t_1 gives

$$c_1(0, t_1) = \frac{c_1(0,0)}{1 + t_1/t_d^{(1)}} \tag{1.178}$$

with

$$t_d^{(1)} = \frac{45\mathcal{A}'|\mathcal{C}'|}{4c_1(0,0)|\mathcal{B}'|\mathcal{G}'}\,, \tag{1.179}$$

with $c_1(0,0)$ the initial value of the parameter $c_1(t_0,t_1)$. Combined with the result for $c_1(t_0,t_1)$ ((1.171) and (1.172)),

$$c_1(t_0,t_1) = \frac{c_1(0,t_1)}{1+t_0/t_d^{(0)}} \tag{1.180}$$

with

$$t_d^{(0)} = \frac{45\mathcal{A}'|\mathcal{C}'|}{4c_1(0,t_1)|\mathcal{B}'|\,\mathcal{G}'\big|_{\sigma_Q=0}}\,, \tag{1.181}$$

we now have a complete solution.

1.D Full Equations

All quantities are expressed in normalized, nondimensional form according to the procedures laid out in § 1.4 and § 1.B. The energy conservation equations ((1.182b) and (1.183b)) are only used for the adiabatic setup.

Leading Order:

$$\frac{\partial n_1}{\partial t_0} + \gamma^2 n_0 u_0 \frac{\partial u_1}{\partial t_0} + u_0 \frac{\partial n_1}{\partial x} + n_0 \gamma^2 \frac{\partial u_1}{\partial x} = 0\,, \tag{1.182a}$$

$$\gamma^2 \frac{\partial \varepsilon_1}{\partial t_0} + \gamma^2 u_0^2 \frac{\partial P_1}{\partial t_0} + 2u_0(\varepsilon_0+P_0)\gamma^4 \frac{\partial u_1}{\partial t_0} + (1+u_0^2)(\varepsilon_0+P_0)\gamma^4 \frac{\partial u_1}{\partial x} + u_0\gamma^2 \frac{\partial}{\partial x}(\varepsilon_1+P_1) + An_0u_0\gamma^2 \frac{\partial n_1}{\partial x} + An_0^2u_0^2\gamma^4 \frac{\partial u_1}{\partial x} = 0\,, \tag{1.182b}$$

$$\gamma^3(\varepsilon_0+P_0)\frac{\partial u_1}{\partial t_0} + \gamma u_0 \frac{\partial P_1}{\partial t_0} + u_0\gamma^3(\varepsilon_0+P_0)\frac{\partial u_1}{\partial x} + \gamma \frac{\partial P_1}{\partial x} + An_0\gamma \frac{\partial n_1}{\partial x} + An_0^2u_0\gamma^3 \frac{\partial u_1}{\partial x} = 0\,. \tag{1.182c}$$

First-Order Corrections:

$$
\begin{aligned}
&\frac{\partial n_2}{\partial t_0} + \gamma^2 n_0 u_0 \frac{\partial u_2}{\partial t_0} + u_0 \frac{\partial n_2}{\partial x} + n_0 \gamma^2 \frac{\partial u_2}{\partial x} = \\
&\quad - \frac{\partial n_1}{\partial t_1} - n_0 u_0 \gamma^2 \frac{\partial u_1}{\partial t_1} - u_0 u_1 \gamma^2 \frac{\partial n_1}{\partial t_0} - \gamma^2 \big[\gamma^2 (1 + 2u_0^2) n_0 u_1 + u_0 n_1\big] \frac{\partial u_1}{\partial t_0} \\
&\quad - \gamma^2 \big[u_0 \gamma^2 (2 + u_0^2) n_0 u_1 + n_1 + n_0 u_0 u_1\big] \frac{\partial u_1}{\partial x} - \gamma^2 u_1 \frac{\partial n_1}{\partial x} \\
&\quad + \gamma u_0 A \sigma_Q \frac{\partial^2 n_1}{\partial t_0 \partial x} + \gamma A \sigma_Q \frac{\partial^2 n_1}{\partial x^2} + \gamma^3 u_0 A \sigma_Q n_0 \left(\frac{\partial^2 u_1}{\partial x^2} + u_0 \frac{\partial^2 u_1}{\partial t_0 \partial x} \right) \\
&\quad + \Theta(-m) \gamma \sigma_Q \left[\left(u_0^2 \frac{\partial^2 \mu_1}{\partial t_0^2} + 2u_0 \frac{\partial^2 \mu_1}{\partial t_0 \partial x} + \frac{\partial^2 \mu_1}{\partial x^2} \right) - \frac{\mu_0}{T_0} \left(u_0^2 \frac{\partial^2 T_1}{\partial t_0^2} + 2u_0 \frac{\partial^2 T_1}{\partial t_0 \partial x} + \frac{\partial^2 T_1}{\partial x^2} \right) \right],
\end{aligned}
\tag{1.183a}
$$

$$
\begin{aligned}
&\gamma^2 \frac{\partial \varepsilon_2}{\partial t_0} + \gamma^2 u_0^2 \frac{\partial P_2}{\partial t_0} + 2u_0 (\varepsilon_0 + P_0) \gamma^4 \frac{\partial u_2}{\partial t_0} + (1 + u_0^2)(\varepsilon_0 + P_0) \gamma^4 \frac{\partial u_2}{\partial x} + u_0 \gamma^2 \frac{\partial}{\partial x} (\varepsilon_2 + P_2) \\
&\quad + A n_0 u_0 \gamma^2 \frac{\partial n_2}{\partial x} + A n_0^2 u_0^2 \gamma^4 \frac{\partial u_2}{\partial x} = \\
&\quad - 2(\varepsilon_0 + P_0) u_0 \gamma^4 \frac{\partial u_1}{\partial t_1} - \gamma^2 \frac{\partial \varepsilon_1}{\partial t_1} - \gamma^2 u_0^2 \frac{\partial P_1}{\partial t_1} - 2(\varepsilon_0 + P_0) \gamma^6 (1 + 3u_0^2) u_1 \frac{\partial u_1}{\partial t_0} - 2(\varepsilon_1 + P_1) \gamma^4 u_0 \frac{\partial u_1}{\partial t_0} \\
&\quad - 2u_0 u_1 \gamma^4 \frac{\partial}{\partial t_0} (\varepsilon_1 + P_1) - 2(3 + u_0^2) u_0 u_1 \gamma^6 (\varepsilon_0 + P_0) \frac{\partial u_1}{\partial x} - \gamma^4 (1 + u_0^2)(\varepsilon_1 + P_1) \frac{\partial u_1}{\partial x} \\
&\quad - (1 + u_0^2) u_1 \gamma^4 \frac{\partial}{\partial x} (\varepsilon_1 + P_1) + \gamma^5 u_0 \left[\zeta + 2\eta \left(1 - \frac{1}{d} \right) \right] \left(u_0^2 \frac{\partial^2 u_1}{\partial t_0^2} + 2u_0 \frac{\partial^2 u_1}{\partial t_0 \partial x} + \frac{\partial^2 u_1}{\partial x^2} \right) \\
&\quad - A n_0 u_1 \gamma^4 \frac{\partial n_1}{\partial x} - A u_0 n_1 \gamma^2 \frac{\partial n_1}{\partial x} - A n_0 u_0 \gamma^2 \frac{d_1 d_2}{3} \frac{\partial^3 n_1}{\partial x^3} - 2A n_0^2 u_0 (1 + u_0^2) u_1 \gamma^6 \frac{\partial u_1}{\partial x} \\
&\quad - 2A n_0 u_0^2 n_1 \gamma^4 \frac{\partial u_1}{\partial x} - A n_0^2 u_0^2 \gamma^4 \frac{d_1 d_2}{3} \frac{\partial^3 u_1}{\partial x^3} - A n_0 u_0^2 u_1 \gamma^4 \frac{\partial n_1}{\partial x},
\end{aligned}
\tag{1.183b}
$$

$$
\begin{aligned}
&\gamma^3 (\varepsilon_0 + P_0) \frac{\partial u_2}{\partial t_0} + \gamma u_0 \frac{\partial P_2}{\partial t_0} + u_0 \gamma^3 (\varepsilon_0 + P_0) \frac{\partial u_2}{\partial x} + \gamma \frac{\partial P_2}{\partial x} + A n_0 \gamma \frac{\partial n_2}{\partial x} + A n_0^2 u_0 \gamma^3 \frac{\partial u_2}{\partial x} = \\
&\quad - (\varepsilon_0 + P_0) \gamma^3 \frac{\partial u_1}{\partial t_1} - u_0 \gamma \frac{\partial P_1}{\partial t_1} - \gamma^3 \big[2u_0 u_1 \gamma^2 (\varepsilon_0 + P_0) + (\varepsilon_1 + P_1)\big] \frac{\partial u_1}{\partial t_0} - u_1 \gamma \frac{\partial P_1}{\partial t_0} \\
&\quad - \gamma^3 \big[u_0 (\varepsilon_1 + P_1) + (1 + u_0^2) u_1 \gamma^2 (\varepsilon_0 + P_0)\big] \frac{\partial u_1}{\partial x} - A n_1 \gamma \frac{\partial n_1}{\partial x} - A n_0 \gamma \frac{d_1 d_2}{3} \frac{\partial^3 n_1}{\partial x^3} \\
&\quad - A n_0^2 (1 + u_0^2) u_1 \gamma^5 \frac{\partial u_1}{\partial x} - A n_0^2 u_0 \gamma^3 \frac{d_1 d_2}{3} \frac{\partial^3 u_1}{\partial x^3} - 2A n_0 u_0 n_1 \gamma^3 \frac{\partial u_1}{\partial x} \\
&\quad + \gamma^4 \left[\zeta + 2\eta \left(1 - \frac{1}{d} \right) \right] \left(u_0^2 \frac{\partial^2 u_1}{\partial t_0^2} + 2u_0 \frac{\partial^2 u_1}{\partial t_0 \partial x} + \frac{\partial^2 u_1}{\partial x^2} \right).
\end{aligned}
\tag{1.183c}
$$

1.E Isothermal KdV-Burgers

All quantities are expressed in dimensional form; to get the dimensionless expressions, simply set $v_F = \hbar = l_{\text{ref}} = k_B = e = 1$ and remove all factors of ε. See § 1.A for the values of $\mathcal{C}_0$ and $\mathcal{C}_1$ and § 1.B for

the O expressions. The KdV-Burgers equation is given by

$$\frac{\mathcal{A}'}{v_F}\frac{\partial n_1}{\partial t_1}+\mathcal{F}'\frac{\partial n_1}{\partial x}+\mathcal{B}'\frac{l_{\rm ref}^d}{O\big(nl_{\rm ref}^d\big)}n_1\frac{\partial n_1}{\partial x}+\mathcal{C}'\frac{l_{\rm ref}^2}{O(\partial_x l_{\rm ref})^2}\frac{\partial^3 n_1}{\partial x^3}=\mathcal{G}'\frac{l_{\rm ref}}{O(\partial_x l_{\rm ref})}\frac{\partial^2 n_1}{\partial x^2}\,, \tag{1.184}$$

with

$$\mathcal{A}'=2\gamma^2\frac{u_0+v_0}{v_F^2+u_0v_0}\frac{P_0l_{\rm ref}d}{n_0\hbar v_F^3}\big\{v_0\big[v_F^2(d+1)-u_0^2K_0\big]+u_0v_F^2(d+1-K_0)\big\}\,, \tag{1.185}$$

$$\begin{aligned}\mathcal{B}'=-\gamma^2\frac{u_0+v_0}{v_F^2+u_0v_0}\frac{P_0l_{\rm ref}^{1-d}}{n_0^2d\hbar v_F^4}\big\{&d^2v_F^2(u_0+v_0)^2[4(d+1)-K_0(d+3)]\\&+(v_F^2+u_0v_0)^2[(d+1)\Theta(-m)-K_0d^2]\big\}O\big(nl_{\rm ref}^d\big)\,,\end{aligned} \tag{1.186}$$

$$\mathcal{C}'=-\frac{n_0}{\varepsilon l_{\rm ref}\hbar}Ad\frac{d_1d_2}{3}\frac{u_0+v_0}{v_F^2+u_0v_0}O(\partial_x l_{\rm ref})^2\,, \tag{1.187}$$

$$\begin{aligned}\mathcal{F}'=\gamma^2\frac{P_0l_{\rm ref}d}{\varepsilon n_0\hbar v_F^4}\frac{u_0+v_0}{v_F^2+u_0v_0}\Bigg\{&2U_1\gamma^2(d+1-K_0)(u_0+v_0)(v_F^2+u_0v_0)\\&+\frac{\mathcal{C}_1}{\mathcal{C}_0}\bigg(\frac{\mu_0}{k_BT_0}\bigg)^{2m}\bigg[v_F^2(u_0+v_0)^2(d+1)\bigg(\frac{1}{d}\delta_{m,-1}+\delta_{m,1}\bigg)\\&-(v_F^2+u_0v_0)^2\bigg(\frac{d-1}{d^2}\delta_{m,-1}+2\delta_{m,1}\bigg)\bigg]\Bigg\}\,,\end{aligned} \tag{1.188}$$

$$\begin{aligned}\mathcal{G}'=\frac{\gamma^3(v_F^2+u_0v_0)}{\varepsilon n_0\hbar v_F^{10}}\Bigg\{&\frac{\sigma_Q}{e^2}\gamma^2\bigg(\frac{P_0}{n_0}\bigg)^2(u_0+v_0)(v_F^2+u_0v_0)(d+1)\\&\times\big[v_0\big(v_F^2(d+1)-u_0^2K_0\big)+u_0v_F^2(d+1-K_0)\big]\\&\times\Bigg[\frac{d(u_0+v_0)^2}{(v_F^2+u_0v_0)^2}+\underbrace{\Theta(-m)-K_0\frac{d}{d+1}}_{=0}\Bigg]+v_F^6d(u_0+v_0)^2\bigg[\zeta+2\eta\bigg(1-\frac{1}{d}\bigg)\bigg]\Bigg\}O(\partial_x l_{\rm ref})\,,\end{aligned} \tag{1.189}$$

and

$$v_0^{(\pm)}=v_F^2\frac{-u_0(d+1-K_0)\pm\frac{1}{\gamma}\sqrt{[K_0(d+1)v_F^2]/\gamma^2+(An_0^2/P_0)[v_F^2(d+1)-u_0^2K_0]}}{v_F^2(d+1)-u_0^2K_0}\,. \tag{1.190}$$

If we impose $v_0=0$, then the coefficients take the form given in (1.60). If instead we impose

$u_0 = U_1 = 0$, they take the form

$$\mathcal{A}' = 2\frac{P_0(d+1)v_0^2 l_{\rm ref} d}{n_0 \hbar v_F^3}\,, \tag{1.191}$$

$$\mathcal{B}' = -v_0 \frac{P_0 l_{\rm ref}^{1-d}}{n_0^2 d \hbar v_F^4}\left\{d^2 v_0^2[4(d+1) - K_0(d+3)] + v_F^2\left[(d+1)\Theta(-m) - K_0 d^2\right]\right\} O\big(n l_{\rm ref}^d\big)\,, \tag{1.192}$$

$$\mathcal{C}' = -\frac{n_0}{\varepsilon l_{\rm ref} \hbar v_F^2} A d \frac{d_1 d_2}{3} v_0 O(\partial_x l_{\rm ref})^2\,, \tag{1.193}$$

$$\mathcal{F}' = \frac{P_0 l_{\rm ref} d}{\varepsilon n_0 \hbar v_F^4} v_0 \frac{\mathcal{C}_1}{\mathcal{C}_0}\left(\frac{\mu_0}{k_B T_0}\right)^{2m}\left[v_0^2(d+1)\left(\frac{1}{d}\delta_{m,-1} + \delta_{m,1}\right) - v_F^2\left(\frac{d-1}{d^2}\delta_{m,-1} + 2\delta_{m,1}\right)\right], \tag{1.194}$$

$$\mathcal{G}' = \frac{1}{\varepsilon n_0 \hbar v_F^4}\left\{\frac{\sigma_Q}{e^2}\left(\frac{P_0}{n_0}\right)^2 v_0^2 (d+1)^2\left[\frac{v_0^2 d}{v_F^2} + \underbrace{\Theta(-m) - K_0\frac{d}{d+1}}_{=0}\right] + v_0^2 v_F^2 d\left[\zeta + 2\eta\left(1 - \frac{1}{d}\right)\right]\right\} O(\partial_x l_{\rm ref})\,, \tag{1.195}$$

with

$$v_0 = \pm\frac{v_F}{\sqrt{d+1}}\sqrt{K_0 + \frac{A n_0^2}{P_0}}\,. \tag{1.196}$$

1.F Adiabatic KdV-Burgers

All quantities are expressed in dimensional form; to get the dimensionless expressions, simply set $v_F = \hbar = l_{\rm ref} = k_B = e = 1$ and remove all factors of ε. See § 1.A for the values of $\mathcal{C}_0$ and $\mathcal{C}_1$ and § 1.B for the O expressions. The KdV-Burgers equation is given by

$$\frac{\mathcal{A}'}{v_F}\frac{\partial n_1}{\partial t_1} + \mathcal{F}'\frac{\partial n_1}{\partial x} + \mathcal{B}'\frac{l_{\rm ref}^d}{O(n) l_{\rm ref}^d} n_1 \frac{\partial n_1}{\partial x} + \mathcal{C}'\frac{l_{\rm ref}^2}{O(\partial_x l_{\rm ref})^2}\frac{\partial^3 n_1}{\partial x^3} = \mathcal{G}'\frac{l_{\rm ref}}{O(\partial_x l_{\rm ref})}\frac{\partial^2 n_1}{\partial x^2}\,, \tag{1.197}$$

with

$$\mathcal{A}' = 2\gamma^2 \frac{u_0+v_0}{v_F^2+u_0v_0} \frac{P_0(d+1)l_{\rm ref}}{n_0\hbar v_F^3} \big[v_0\big(v_F^2 d - u_0^2\big) + u_0 v_F^2(d-1)\big]\,, \tag{1.198}$$

$$\mathcal{B}' = -\gamma^2 \frac{u_0+v_0}{v_F^2+u_0v_0} \frac{P_0(d+1)l_{\rm ref}^{1-d}}{n_0^2\hbar v_F^4} \frac{d-1}{d} \big[3dv_F^2(u_0+v_0)^2 - (v_F^2+u_0v_0)^2\big] O\big(nl_{\rm ref}^d\big)\,, \tag{1.199}$$

$$\mathcal{C}' = -\frac{n_0}{\varepsilon l_{\rm ref}\hbar} Ad \frac{d_1 d_2}{3} \frac{u_0+v_0}{v_F^2+u_0v_0} O(\partial_x l_{\rm ref})^2\,, \tag{1.200}$$

$$\begin{aligned}\mathcal{F}' = \gamma^2 \frac{P_0(d+1)l_{\rm ref}}{\varepsilon n_0\hbar v_F^4} \frac{u_0+v_0}{v_F^2+u_0v_0} \Big\{ & 2U_1\gamma^2(d-1)(u_0+v_0)(v_F^2+u_0v_0) \\ & + \delta_{m,-1} \frac{1}{d} \frac{\mathcal{C}_1}{\mathcal{C}_0} \left(\frac{k_B T_0}{\mu_0}\right)^2 \big[dv_F^2(u_0+v_0)^2 - (v_F^2+u_0v_0)^2\big] \Big\}\,,\end{aligned} \tag{1.201}$$

$$\mathcal{G}' = \frac{d\gamma(v_F^2+u_0v_0)}{\varepsilon n_0\hbar v_F^4} \left\{ \frac{\sigma_Q}{e^2} \frac{A^2 n_0^2 v_F^2}{v_F^2+u_0v_0} + \gamma^2(u_0+v_0)^2 \left[\zeta + 2\eta\left(1-\frac{1}{d}\right)\right] \right\} O(\partial_x l_{\rm ref})\,, \tag{1.202}$$

and

$$v_0^{(\pm)} = -\frac{u_0 v_F^2(d-1)}{v_F^2 d - u_0^2} \pm \frac{v_F^2\sqrt{d}}{(v_F^2 d - u_0^2)\gamma^2} \sqrt{v_F^2 + \frac{An_0^2\gamma^2(v_F^2 d - u_0^2)}{P_0(d+1)}}\,. \tag{1.203}$$

If we impose $v_0 = 0$, then the coefficients take the form given in (1.60). If instead we impose $u_0 = U_1 = 0$, they take the form

$$\mathcal{A}' = 2\frac{P_0(d+1)v_0^2 l_{\rm ref} d}{n_0\hbar v_F^3}\,, \tag{1.204}$$

$$\mathcal{B}' = -\frac{P_0(d+1)l_{\rm ref}^{1-d}}{n_0^2\hbar v_F^4} \frac{d-1}{d} v_0\big(3dv_0^2 - v_F^2\big) O\big(nl_{\rm ref}^d\big)\,, \tag{1.205}$$

$$\mathcal{C}' = -\frac{n_0}{\varepsilon l_{\rm ref}\hbar v_F^2} Ad \frac{d_1 d_2}{3} v_0 O(\partial_x l_{\rm ref})^2\,, \tag{1.206}$$

$$\mathcal{F}' = \delta_{m,-1} \frac{An_0 v_0 l_{\rm ref}}{\varepsilon\hbar v_F^2} \frac{\mathcal{C}_1}{\mathcal{C}_0} \left(\frac{k_B T_0}{\mu_0}\right)^2\,, \tag{1.207}$$

$$\mathcal{G}' = \frac{d}{\varepsilon n_0\hbar v_F^2} \left\{ \frac{\sigma_Q}{e^2} A^2 n_0^2 + v_0^2 \left[\zeta + 2\eta\left(1-\frac{1}{d}\right)\right] \right\} O(\partial_x l_{\rm ref})\,, \tag{1.208}$$

with

$$v_0 = \pm\frac{v_F}{\sqrt{d}} \sqrt{1 + \frac{Adn_0^2}{(d+1)P_0}}\,. \tag{1.209}$$

Chapter 2

Wind-induced changes to surface gravity wave shape in deep to intermediate water

2.1 Abstract

Wave shape (i.e. skewness or asymmetry) plays an important role in beach morphology evolution, remote sensing and ship safety. The wind's influence on ocean waves has been extensively studied theoretically in the context of growth, but most theories are phase averaged and cannot predict wave shape. Most laboratory and numerical studies similarly focus on wave growth. A few laboratory experiments have demonstrated that wind can change wave shape, and two-phase numerical simulations have also noted wind-induced wave-shape changes. However, the wind's effect on wave shape is poorly understood, and no theory for it exists. For weakly nonlinear waves, wave-shape parameters are the phase of the first harmonic relative to the primary frequency (or harmonic phase HP, zero for a Stokes wave) and relative amplitude of the first harmonic to the primary wave. Here, surface pressure profiles (denoted Jeffreys, Miles and generalized Miles) are prescribed based on wind–wave generation theories. Theoretical solutions are derived for quasi-periodic progressive waves and the wind-induced changes to the HP, relative harmonic amplitude, as well as the already known phase speed changes and growth rates. The wave-shape parameters depend upon the chosen surface pressure profile, pressure magnitude and phase relative to

the wave profile and non-dimensional depth. Wave asymmetry is linked to the non-dimensional growth rate. Atmospheric large eddy simulations constrain pressure profile parameters. The HP predictions are qualitatively consistent with laboratory observations. This theory, together with the HP and relative harmonic amplitude observables, can provide insight into the actual wave surface pressure profile.

2.2 Introduction

The shape of surface gravity waves plays a role in many physical phenomena. Wave shape is described by the third-order statistical moments, skewness and asymmetry [e.g. 44, 45]. Wave skewness represents a wave's vertical asymmetry, while wave asymmetry corresponds to its horizontal asymmetry. These two parameters are integral in determining sediment transport direction (onshore *vs.* offshore) and magnitude [e.g. 46–48], which play key roles in beach morphodynamics [e.g. 49, 50]. Wave shape is also pertinent in remote sensing, where wave skewness modulates the returned waveform in radar altimetry [e.g. 51–53] and wave asymmetry affects the thermal emissions measured in polarimetric radiometry [e.g. 54–56]. Additionally, these wave-shape parameters play a role in determining ship response to wave impacts [e.g. 57, 58]. Waves propagating on a flat bottom are ordinarily symmetric, although a number of processes can create asymmetry. While some wave asymmetry-inducing phenomena, such as wave shoaling [e.g. 59, 60] and vertically sheared currents [e.g. 61, 62], are well understood, the wind's effect on wave shape is still poorly understood.

The influence of wind on ocean waves has been extensively studied, although primarily in the context of wave growth. An initial investigation by Jeffreys [63] was based on a sheltering hypothesis, where separated airflow resulted in reduced pressure on the wave's leeward side, causing wave growth. While conceptually simple, this mechanism has largely fallen out of favour because such separation only seems to occur near breaking [64] or for steep waves under strong winds [e.g. 65, 66]. Nevertheless, Jeffreys's theory has inspired some recent work; Belcher and Hunt [67] developed a fully turbulent model wherein the sheltering effect causes a thickening of the boundary layer and wave growth, even without separation. Later treatments utilized different physical mechanisms such as resonant forcing by incoherent, turbulent eddies [68], vortex forcing from vertically sheared airflow [e.g. 69, 70] and non-separated sheltering [e.g. 67]. Janssen [71] provides an extensive overview of the relevant developments in wind–wave generation theory. When deriving energy and momentum fluxes from air to water, these seminal theories of wave growth [e.g. 67, 68, 70] utilized a phase-averaging technique, which removes wave-shape information. Thus, although these wind–wave interaction theories focused on the wave growth rate, no theoretical work has investigated

the effect of wind on wave shape in a physically consistent manner.

Measurements and numerical simulations have also been used to investigate the dependence of wave growth on wind speed. Field measurements [e.g. 72–74] and laboratory experiments [e.g. 75–77] have been used to parameterize how quickly intermediate- and deep-water waves grow under various wind conditions, including short fetch [e.g. 78] and strong wind conditions [e.g. 79]. Note that direct measurements of wave surface pressure (related to growth) are notoriously difficult [e.g. 80]. Similarly, numerical simulations have also been used to predict wind-induced growth rates. Early numerical atmospheric models used the Reynolds-averaged Navier–Stokes equations [e.g. 81, 82] to calculate the energy loss of the wind field. However, these early simulations could only approximate turbulence through a Reynolds-averaging process. Recent studies have analysed the turbulence behaviour in detail. Particle image velocimetry and laser-induced fluorescence have been used for turbulence measurements in laboratory experiments and have revealed turbulent structures above the waves [e.g. 83–85]. This turbulent behaviour has also been captured through direct numerical simulations of the governing equations [e.g. 86–88] and by parameterizing subgrid-scale processes in large eddy simulations [LES, e.g. 89–91]. When solving for the atmospheric dynamics, many of these simulations prescribed a static sinusoidal wave shape while focusing on the evolution of the wind field, as well as energy and momentum transfers. Therefore, any wind-induced changes to wave shape were not captured.

While there has been much research regarding wind-induced wave growth, wave shape has seen relatively little work. Coupled air–water simulations [e.g. 92, 93] and two-phase (air and water) simulations [e.g. 94, 95] have begun incorporating dynamically evolving waves into their analyses. These directly model the evolution of both the air and wave fields in a coupled manner in contrast to simulations prescribing a fixed wave shape. Furthermore, some also qualitatively consider how wave shape evolves under the influence of wind [e.g. 96–98]. However, theses analyses are focused on other parameters and do not quantify precisely how the wave shape changes. Additionally, there have been a small number of field measurements [e.g. 99] and laboratory experiments [100, 101] that have directly investigated how wind affects wave shape. It was found that the skewness and asymmetry depended on wind speed for mechanically generated waves in relatively deep [100] or intermediate and shallow [101] water. In particular, the wave asymmetry [100], skewness [99] and energy ratio of the first harmonic (frequency $2f$) to the primary wave (frequency f) [101] all increased with wind speed. It would be beneficial to develop a theory that explains these experimental findings.

In this paper, we develop a theory coupling wind to dynamically evolving intermediate- and

deep-water waves ($kh \geq 1$ with k the wavenumber and h the water depth). We consider the fluid domain beneath a periodic, progressive wave that is forced by a prescribed, wave-dependent surface pressure profile. That is, the atmosphere is not treated dynamically. Determining the wind's effect on wave shape requires a nonlinear theory. As the surface boundary conditions for gravity waves are nonlinear, the equations are solved using a multiple-scale perturbation analysis where the wave steepness $\varepsilon \coloneqq a_1 k$ (with a_1 the primary wave's amplitude) is small and new, slower time scales are introduced over which the nonlinearities act [see, for example, 102]. This formalism has been used to derive the canonical Stokes waves, which are periodic, progressive waves of permanent form in intermediate and deep water [103]. By introducing a surface pressure-forcing term, we will derive solutions of the form

$$\eta = a_1 \exp(\mathrm{i}(kx - \omega t)) + a_2 \exp(\mathrm{i}[2(kx - \omega t) + \beta]) + \ldots, \tag{2.1}$$

with the real part implied. Here, η is the wave height, ω is the complex wave frequency, and $a_1 k = \varepsilon$ and $a_2 k = O(\varepsilon^2)$ are the non-dimensional amplitudes of the primary wave and first harmonic, respectively. We have defined a new parameter, the 'harmonic phase' (or HP) β, which is analogous to the biphase, a statistical tool [59]. Both wave skewness and asymmetry depend on the HP β and relative harmonic amplitude $a_2/(a_1^2 k)$. For example, both skewness and asymmetry are zero for linear waves with $a_2/(a_1^2 k) = 0$. For deep-water ($kh \gg 1$) Stokes waves without wind forcing, $a_2/(a_1^2 k) = 1/2$ gives non-zero skewness, but $\beta = 0$ yields no phase difference between the primary wave and first harmonic in (2.1). Indeed, unforced Stokes waves are exactly symmetric at all orders [104].

Three surface pressure profiles, derived from the theories of Jeffreys [63] and Miles [69], are included in the perturbation expansion. Using the method of multiple scales, Stokes wave-like solutions are derived, giving the wave-shape (via $a_2/(a_1^2 k)$ and β) dependence on the wind-induced surface pressure profile. Additionally, wave growth will result from the fact that $\mathrm{Im}\{\omega\}$ is no longer zero [e.g. 69]. These solutions reduce to unforced Stokes waves when the pressure forcing vanishes.

In § 2.3, we set up the equations and define the different pressure profiles used. Section 2.4 begins the general derivation covering a range of realistic pressure magnitudes, which is continued in § 2.A. As a key aspect to the derivation, the non-dimensional pressure p' is included in the leading-order equations ($p' = O(\varepsilon)$), which is the most general approach by allowing the substitution of $p' \to \varepsilon p'$ or $p' \to \varepsilon^2 p'$, generating weaker $p' = O(\varepsilon^2)$ and $p' = O(\varepsilon^3)$ solutions (cf. § 2.A.6). Section 2.5 details the results of this analysis. In § 2.6, we clarify the solutions' time scale validity, relate the pressure parameters to LES simulations, compare our results to laboratory observations and compare the surface pressure form with

existing data. Section 2.A extends the general derivation to higher orders in ε to demonstrate a weak amplitude dependence of the shape parameters.

2.3 Theoretical background

2.3.1 Governing equations

Here, we specify the equations governing the water dynamics. Homogeneous, incompressible fluids satisfy the incompressible continuity equation,

$$\boldsymbol{\nabla} \cdot \mathbf{u} = 0, \tag{2.2}$$

within the fluid. We assume irrotational flow and write the water velocity $\mathbf{u}$ in terms of a velocity potential ϕ as $\mathbf{u} = \boldsymbol{\nabla}\phi$. We define a coordinate system with $z = 0$ at the initial mean water level, positive z upward and gravity pointing in the $-z$ direction. We assume planar wave propagation in the $+x$ direction and uniform in the y direction. Then, the incompressibility condition becomes Laplace's equation,

$$\frac{\partial^2 \phi}{\partial x^2} + \frac{\partial^2 \phi}{\partial z^2} = 0. \tag{2.3}$$

Assuming uniform water depth with a flat bottom located at $z = -h$, we impose a no-flow bottom boundary condition

$$\frac{\partial \phi}{\partial z} = 0 \quad \text{at} \quad z = -h. \tag{2.4}$$

Finally, the standard surface boundary conditions [e.g. 105] are the kinematic boundary condition

$$\frac{\partial \phi}{\partial z} = \frac{\partial \eta}{\partial t} + \frac{\partial \phi}{\partial x}\frac{\partial \eta}{\partial x} \quad \text{at} \quad z = \eta, \tag{2.5}$$

and the dynamic boundary condition

$$0 = \frac{p}{\rho_w} + g\eta + \frac{\partial \phi}{\partial t} + \frac{1}{2}\left(\frac{\partial \phi}{\partial x}^2 + \frac{\partial \phi}{\partial z}^2\right) \quad \text{at} \quad z = \eta. \tag{2.6}$$

Here, g is the acceleration due to gravity, ρ_w the water density, $\eta(x,t)$ the surface profile and $p(x,t)$ the surface pressure evaluated at $z = \eta$. Note that we have absorbed the Bernoulli constant from (2.6) into ϕ using its gauge freedom $\phi \to \phi + f(t)$ for arbitrary $f(t)$. In § 2.3.3 we specify the surface pressure profiles.

2.3.2 Assumptions

Our analysis is characterized by a number of non-dimensional parameters. The wave slope $\varepsilon \coloneqq a_1 k$, assumed small, will order our perturbation expansion. Additionally, we will restrict our attention to intermediate and deep water by requiring that the non-dimensional depth $kh \gtrapprox 1$ so that the Ursell parameter is small, $\varepsilon/(kh)^3 \ll 1$. An additional parameter is the non-dimensional surface pressure magnitude induced by the wind discussed in §§ 2.3.3 and 2.3.4. We seek waves with wavelength $\lambda \coloneqq 2\pi/k$ travelling in the x direction that are periodic in x and quasi-periodic in t

$$\eta(x,t) = \eta(x+\lambda,t) = \eta(\theta,t) \quad \text{and} \quad \phi(x,z,t) = \phi(x+\lambda,z,t) = \phi(\theta,z,t), \tag{2.7}$$

with θ defined for right-propagating waves ($\mathrm{Re}\{\omega(t)\} > 0$) as

$$\theta \coloneqq kx - \int \mathrm{Re}\{\omega(t)\}\,\mathrm{d}t\,, \tag{2.8}$$

which is analogous to the standard $kx - \mathrm{Re}\{\omega\}t$, but allows for a complex, time dependent frequency $\omega(t)$. Additionally, we neglect surface tension σ by restricting to wavelengths $\lambda \gg 2\,\mathrm{cm}$, implying a large Bond number ($\rho g/k^2\sigma \gg 1$). Furthermore, we assume no mean Eulerian current. Finally, we seek a solution of a single primary wave and its bound harmonics. Including additional primary waves permits us to study the wind's effect on sideband instabilities [e.g. 106] but is beyond the scope of this work.

In the dynamic boundary condition (2.6), we incorporated the normal stress (surface pressure) but neglected the shear stress as it is usually significantly smaller than the normal stress [e.g. 90, 107, 108]. Additionally, we note that surface shear stresses cause a slight thickening of the boundary layer, which is equivalent to a pressure phase shift on the remainder of the water column [109]. Therefore, we can include the effect of shear stresses through a phase shift in the pressure relative to the wave profile. Hence, in this investigation we only consider pressures acting normal to the wave surface.

The irrotational assumption was motivated by our assumption that vorticity-generating wind shear stresses are small. Additionally, any such vorticity is constrained to a thin boundary layer just below the wave surface [109]. Finally, viscous forces vanish—necessary for Bernoulli's equation (2.6)—for any flow that is both irrotational and incompressible (with constant viscosity; e.g. Fang [110]). Thus, we will assume irrotational, inviscid flow throughout the fluid interior.

2.3.3 Surface pressure profiles

Here, we define the surface pressure profiles used in the analysis. The Jeffreys [63] theory yields a ('Jeffreys') surface pressure profile,

$$p_J(x,t) = s\rho_a U^2 \frac{\partial \eta(x,t)}{\partial x}, \tag{2.9}$$

with ρ_a the air density, U a characteristic wind speed and s an empirical, unitless constant. Although the Miles mechanism is now favoured for gently sloping waves or weak winds [66], the Jeffreys mechanism is still relevant for steep, strongly forced waves [e.g. 65]. The simple, analytic form of the Jeffreys forcing also lends itself well to theoretical treatments. Indeed, many treatments [e.g. 111–113] approximate the Miles forcing by a wave slope coherent pressure $p \propto \partial\eta/\partial x$ equivalent to our Jeffreys-type forcing (2.9).

The Miles [69] theory of wind–wave growth gives a ('Miles') surface pressure profile of the form

$$p_M(x,t) = \left(\tilde{\alpha} + \mathrm{i}\tilde{\beta}\right)\rho_a U^2 k \eta_a(x,t), \tag{2.10}$$

with $\tilde{\alpha}$ and $\tilde{\beta}$ empirical, unitless constants. Additionally, η_a the analytic representation of η, where the analytic representation of a real function $f(x)$ is $f(x) + \mathrm{i}\hat{f}(x)$ with $\hat{f}(x)$ the Hilbert transform of $f(x)$ (for our purposes, only two representations will be relevant: the analytic representation of $\cos(x)$ is $\exp(\mathrm{i}x)$ and that of $\sin(x)$ is $-\mathrm{i}\exp(\mathrm{i}x)$). This theory was developed for a linear, sinusoidal (i.e. primary) wave without harmonics. Note that (2.10) shifts each harmonic $\exp(\mathrm{i}mkx)$ by the same phase, $\tan^{-1}(\tilde{\beta}/\tilde{\alpha})$, but by a different distance, $m\tan^{-1}(\tilde{\beta}/\tilde{\alpha})/k$, distorting the pressure profile relative to η. This pressure profile gives no wave-shape change at leading order (§ 2.A.5) and, since wind-induced shape changes have been observed experimentally, they will not be discussed further here.

Another suitable generalization, capturing the motivation behind the Miles profile, is specifying the surface pressure as phase shifted relative to η. This prescription is more appropriate for nonlinear waves since all harmonics are shifted the same distance. Thus, we define another ('generalized Miles') surface pressure profile as

$$p_G(x,t) = r\rho_a U^2 k \eta(kx + \psi_P, t), \tag{2.11}$$

with r a new, unitless constant and a new parameter, the 'wind phase' ψ_P, which corresponds to the phase shift between the wave and pressure profile, has been introduced. As the surface pressure is elevated on the wave's windward (relative to the leeward) side, $\psi_P > 0$ corresponds to wind blowing from the left,

assuming $\psi_P \in (-\pi, \pi]$. Note that the wind phase ψ_P is a free parameter for the pressure profile. Although ψ_P likely depends on other factors such as wave age, determining such a relationship is outside the scope of this work. For a single primary wave, we treat ψ_P as a fixed parameter (for a given wind speed) which is assumed known—possibly from experiments or simulations (cf. § 2.6.2).

To facilitate comparison, the various pressure profiles are written in a common form. Inspired by similarities in (2.9)–(2.11), we define a non-negative pressure magnitude constant, P, which implicitly encodes the wind speed. For instance, (2.9)–(2.11) suggest

$$P \propto \rho_a U^2, \tag{2.12}$$

although this form serves only as motivation, and the particular U dependence will be immaterial to our analysis. Since the definition of $\varepsilon \coloneqq a_1 k$ implies $k|\eta| = O(\varepsilon)$, we see from the various definitions (2.9)–(2.11) that

$$O(|p|) = O(\varepsilon P). \tag{2.13}$$

We will define P_J for the Jeffreys profile such that

$$p_J(x,t) = \pm P_J \frac{\partial \eta(x,t)}{\partial x}, \tag{2.14}$$

with the plus sign for wind blowing from the left. Likewise, we will rewrite the generalized Miles profile as

$$p_G(x,t) = P_G k \eta(kx + \psi_P, t). \tag{2.15}$$

The constant P is subscripted to denote Jeffreys (P_J) or generalized Miles (P_G) when the distinction is relevant. In § 2.4, these two surface pressure profiles, (2.14) and (2.15), are expanded in a Fourier series to yield simpler equations. Expanding an arbitrary function $f(x)$ in a Fourier series as the real part of $f(x) = \sum_{m=0} \hat{f}_m \exp(\mathrm{i}mkx)$ with $m \in \mathbb{N}$ yields

$$\hat{p}_{J,m}(t) = \pm \mathrm{i} k m P_J \hat{\eta}_m(t), \tag{2.16}$$

$$\hat{p}_{G,m}(t) = k P_G \exp(\mathrm{i} m \psi_P) \hat{\eta}_m(t). \tag{2.17}$$

Therefore, we will generically write

$$\hat{p}_m(t) = k \hat{P}_m \hat{\eta}_m(t), \tag{2.18}$$

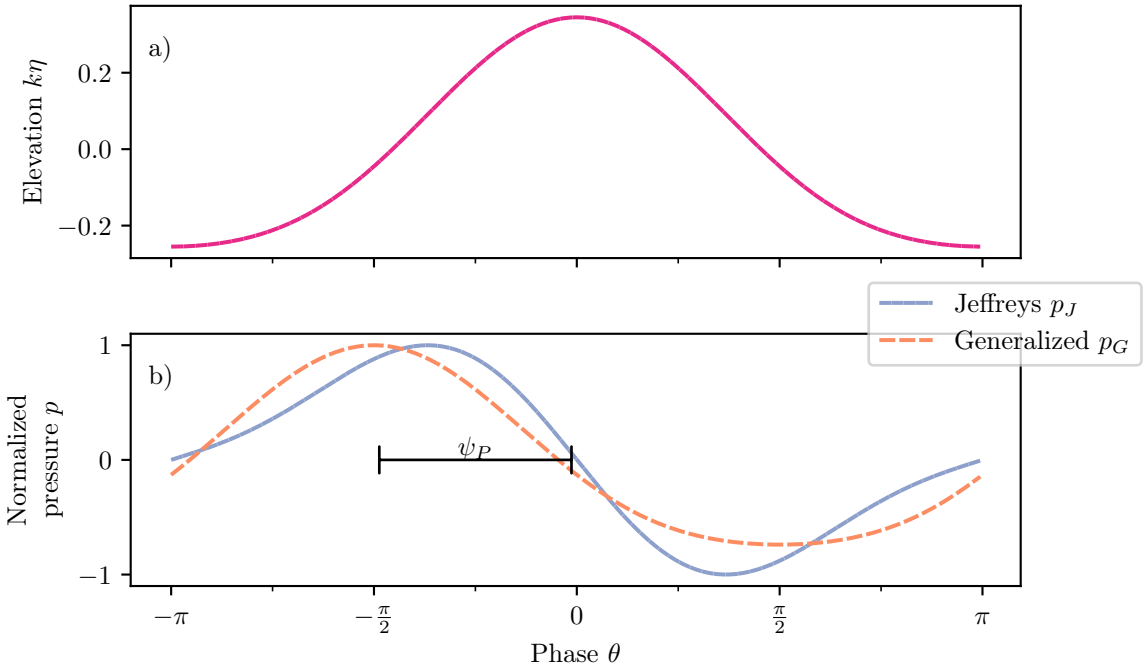

Figure 2.1. (a) Non-dimensional, right-propagating Stokes wave $k\eta$ (2.19) as a function of phase $\theta = kx - \omega t$ with $\varepsilon = 0.2$. (b) Normalized surface pressure profiles $p(\theta)$ as described in (2.14) and (2.15); see legend. The maximum pressure magnitude is normalized to unity (arbitrary units), and a value of $\psi_P = \pi/2$ was chosen to facilitate comparison with the Jeffreys profile with ψ_P positive corresponding to wind blowing to the right.

with $\hat{P}_m = mP_J \exp(\mathrm{i}\psi_P)$ and $\psi_P = \pm\pi/2$ for Jeffreys and $\hat{P}_m = P_G \exp(\mathrm{i}m\psi_P)$ for generalized Miles profiles. Although we highlight these two forcing profiles, we stress the derivation's generality. The results apply to any pressure profile (2.18) that results from a convolution of $\eta(x,t)$ with a time-independent function $f(x)$, each yielding a specific $\hat{P}_m$. For example, $\hat{P}_m$ could be chosen to match numerical simulations (cf. § 2.6.4).

To make these definitions concrete and contrast the different forcing types, a deep-water, second-order Stokes wave

$$k\eta(\theta) = \varepsilon\cos(\theta) + \frac{1}{2}\varepsilon^2\cos(2\theta) \tag{2.19}$$

is shown for $\varepsilon = 0.2$ in figure 2.1(a) with phase $\theta = kx - \omega t$. The Stokes wave profile is used to compute both (unity normalized) surface pressure profiles (figure 2.1(b)). These two pressure profiles, (2.14) and (2.15), are largely similar to each other, although differences arise due to the Stokes wave harmonics. The derivative in the Jeffreys profile (blue figure 2.1(b)) multiplies each Fourier harmonic by its wavenumber,

mk, enhancing higher frequencies. In contrast, the wind phase ψ_P, measured left from $\theta = 0$ to the pressure maximum, shifts the entire pressure waveform relative to the surface waveform η for the generalized Miles profile (orange, figure 2.1(b)). The LES numerical simulations of Hara and Sullivan [90] and Husain et al. [108] show $\psi_P \approx 3\pi/4$ for a variety of wind speeds (§ 2.6.2). However, in figure 2.1(b), $\psi_P = \pi/2$ is chosen for the generalized Miles profiles to facilitate comparison with the Jeffreys case (for which $\psi_P = \pm\pi/2$).

2.3.4 Determination of pressure magnitude P

We will use existing experimental data to determine the magnitude of P in various contexts. Assuming a logarithmic wind profile, Miles [69] derived the wave-energy growth rate γ, normalized by the (unforced, linear, deep-water) wave frequency f_0^∞, for the pressure profile p_M (2.15)

$$\frac{\gamma}{f_0^\infty} = 2\pi\tilde{\beta}\frac{\rho_a}{\rho_w}\frac{U^2}{(c_0^\infty)^2} = 2\pi\frac{P_G}{\rho_w(c_0^\infty)^2}\sin(\psi_P), \tag{2.20}$$

where, $c_0^\infty = \sqrt{g/k}$ is the unforced, linear, deep-water phase speed, ρ_w is the water density and (2.12) is used to define P_G. Using the value $\psi_P = 3\pi/4$ from Hara and Sullivan [90] and Husain et al. [108] gives $P_G k/(\rho_w g) = 0.23(\gamma/f_0^\infty)$.

Furthermore, we use empirical data relating wind speed U to growth rate to constrain the P_G pressure magnitude constant in deep water. Figure 2.2 shows the energy growth rate γ/f_0^∞ as a function of inverse wave age, u_*/c_0^∞ with u_* the friction velocity. The empirical observations of γ/f_0^∞ versus u_*/c_0^∞ in deep water collapse onto a curve permitting a conversion from u_*/c_0^∞ to γ/f_0^∞ and yielding $P_G k/(\rho_w g)$ (2.20).

Here, we consider $|p|k/(\rho_w g) = O(\varepsilon)$ to $O(\varepsilon^3)$, or $Pk/(\rho_w g) = O(1)$ to $O(\varepsilon^2)$—cf. (2.13). If we assume $\varepsilon \approx 0.1$, $\psi_P \approx 3\pi/4$, and $\rho_a/\rho_w = 1.225 \times 10^{-3}$, then (2.20) shows we are considering growth rates $\gamma/f_0^\infty \approx 4 \times 10^{-2}$ to 4. Referring to figure 2.2, we see these reside mostly in the laboratory measurement regime, corresponding to $u_*/c_0^\infty \approx 5 \times 10^{-1}$ to 5. We can approximate U_{10} using logarithmic boundary layer theory [e.g. 115]

$$u_* = \frac{\kappa U_{10}}{\ln[(10\,\mathrm{m})/z_0]}, \tag{2.21}$$

with $\kappa \approx 0.4$ the von Kármán constant and $z_0 \approx 1.4 \times 10^{-5}$ the surface roughness parameter for 2 m long, 0.1 m high deep-water waves, as one might have in a wave tank [116]. Substituting these values, we find

$$U_{10} \approx 34u_*, \tag{2.22}$$

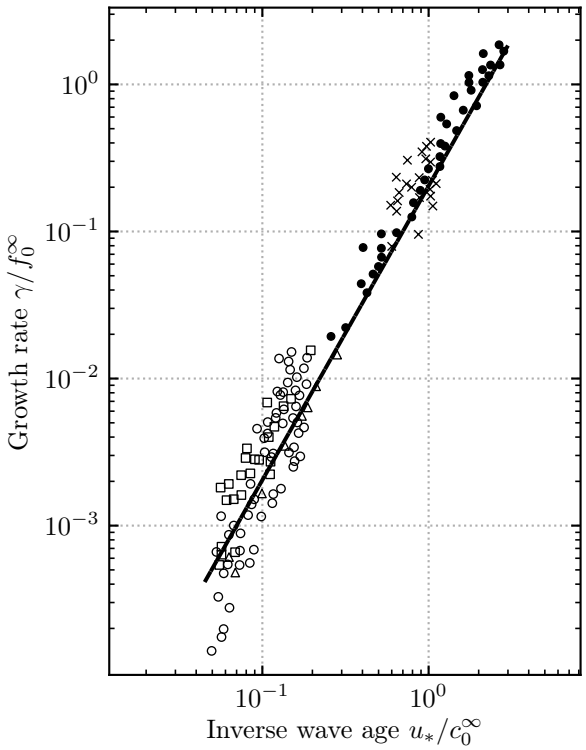

Figure 2.2. Non-dimensional, deep-water wave-energy growth rate γ/f_0^∞ versus inverse wave age, u_*/c_0^∞ with u_* the wind's friction velocity and $c_0^\infty = \sqrt{g/k}$ the unforced, linear, deep-water phase speed. The filled symbols represent laboratory measurements while the hollow symbols represent field measurements [from 114]. The solid line represents the fit parameterized by Banner and Song [111].

yielding $U_{10}/c_0^\infty \approx 1\times10^1$ to 1×10^2, or $U_{10} \approx 3\times10^1\,\mathrm{m\,s^{-1}}$ to $3\times10^2\,\mathrm{m\,s^{-1}}$ assuming a deep-water dispersion relation.

It is interesting to examine the pressure-forcing magnitudes used previously. Phillips [68] modelled wave growth using a different mechanism, but the pressure forcing was included at the same order as η. That is, $|p|k/(\rho_w g) = O(\varepsilon)$, or $Pk/(\rho_w g) = O(1)$, implying $\gamma/f_0^\infty = O(1)$. Referring to figure 2.2, this corresponded to strongly forced waves and a fast wind ($u_*/c_0^\infty = O(1)$). Other theoretical works have used $|p|k/(\rho_w g) = O\big(\varepsilon^2\big)$ [e.g. 106, 113, 117] or $|p|k/(\rho_w g) = O\big(\varepsilon^3\big)$ [e.g. 118–120], corresponding to $Pk/(\rho_w g) = O(\varepsilon)$ and $Pk/(\rho_w g) = O\big(\varepsilon^2\big)$, respectively. Thus, the choices of $Pk/(\rho_w g) = O(1)$ to $O\big(\varepsilon^2\big)$ are all relevant in the literature.

2.3.5 Multiple-scale expansion

As mentioned in § 2.3.2, we will utilize an asymptotic expansion in the small wave slope $\varepsilon \coloneqq a_1 k$ to prevent secular terms in this singular perturbation expansion. While nonlinear wave theories often use an ordinary Stokes expansion (i.e. a Poincaré–Lindstedt, or strained coordinate, expansion), this does not permit the complex frequencies required for wave growth. Instead, we employ the method of multiple scales and replace t by a series of slower time scales depending on ε such that $t_0 = t$, $t_1 = t/\varepsilon$, etc, yielding

$$\frac{\partial}{\partial t} = \frac{\partial}{\partial t_0} + \varepsilon\frac{\partial}{\partial t_1} + \dots . \tag{2.23}$$

Additional time scales t_2 and t_3, inversely proportional to ε^2 and ε^3 respectively, are required in the $O\big(\varepsilon^4\big)$ derivation of § 2.A. This is exclusively a temporal multiple-scale expansion. While a spatial multiple-scale analysis would also permit the study of surface pressure effects on modulational instabilities [106], we solely focus on the wind-induced shape change of a single wave.

As discussed in § 2.3.4, the non-dimensional pressure forcing can have magnitudes ranging from $Pk/(\rho_w g) = O(1)$ to $O\big(\varepsilon^2\big)$. Writing $Pk/(\rho_w g) = O(\varepsilon^n)$ for $n = 0$ to 2, we will show that the derivation must be solved to $O\big(\varepsilon^{n+2}\big)$ to demonstrate shape change. Many theoretical treatments using $Pk/(\rho_w g) = O\big(\varepsilon^2\big)$ only utilize $O\big(\varepsilon^3\big)$ equations like the nonlinear Schröedinger (NLS) equation [e.g. 119, 120] or Davey–Stewartson equation [e.g. 118]. Therefore, no shape change would be derived without going to higher order. In contrast, both Brunetti et al. [113] and Brunetti and Kasparian [106] coupled a moderately strong wind $Pk/(\rho_w g) = O(\varepsilon)$ to a slowly varying wave train and derived an $O\big(\varepsilon^3\big)$ forced NLS equation. Although solved at sufficiently high order to show wind-induced shape changes, neither

reported results for the first harmonic. Instead, these focused on wind-forced wave packet evolution, with Brunetti et al. [113] finding various envelope solitons for the primary wave and Brunetti and Kasparian [106] deriving an enhancement of the primary wave's modulational instability.

In §§ 2.A and 2.4, we include the pressure in the leading-order equations, i.e. $Pk/(\rho_w g) = O(1)$, which is the most general case. The leading-order contributions to the shape parameters β and $a_2/(a_1^2 k)$ are found at $O(\varepsilon^2)$, while the higher-order corrections occur at $O(\varepsilon^4)$ (§ 2.A). From the full $O(\varepsilon^4)$ solution, shape changes for $Pk/(\rho_w g) = O(\varepsilon)$ or $Pk/(\rho_w g) = O(\varepsilon^2)$ can be found by substituting $P \to \varepsilon P$ or $P \to \varepsilon^2 P$, respectively (cf. § 2.A.6).

2.3.6 Non-dimensionalization

Non-dimensional systems are useful in perturbation expansions. Here, a standard non-dimensionalization [e.g. 121] is performed by defining new non-dimensional, order-unity primed variables

$$\left.\begin{array}{lll} x = \dfrac{x'}{k}, & z = \dfrac{z'}{k}, & \eta = \varepsilon\dfrac{\eta'}{k}, \\ t = \dfrac{t'}{\sqrt{gk}}, & h = \dfrac{h'}{k}, & \Phi = \varepsilon\Phi'\sqrt{\dfrac{g}{k^3}}, \end{array}\right\} \tag{2.24}$$

Notice the ε factor in the equations for η and ϕ since these are assumed small. Unlike in the standard Stokes wave problem, the surface pressure must also be non-dimensionalized. As shown in (2.13), $O(|p|) = \varepsilon O(P)$. Thus, we find p and P (as well as their Fourier transforms) are non-dimensionalized by

$$(p, \hat{p}) = O\left(\frac{\varepsilon P k}{\rho_w g}\right)\frac{\rho_w g}{k}(p', \hat{p}'), \tag{2.25}$$

$$(P, \hat{P}_m) = O\left(\frac{P k}{\rho_w g}\right)\frac{\rho_w g}{k}(P', \hat{P}'_m), \tag{2.26}$$

with $p'(x,t)$ and P' (as well as their Fourier transforms) now order unity and dimensionless. For the remainder of the paper, primes will be dropped and all variables will be assumed non-dimensional and order unity, except where explicitly stated.

2.4 Derivation of wave-shape parameters

We now couple a prescribed surface pressure profile (2.18) to the nonlinear wave problem (2.3)–(2.6) to derive the wind's effect on wave shape. In this section, we will ultimately find an expression for the

non-dimensional surface profile of the form

$$\eta = \varepsilon A_1(t_1, \ldots)\exp(\mathrm{i}(x - \omega_0 t_0)) + \varepsilon^2 A_2(t_1, \ldots)\exp(\mathrm{i}[2(x - \omega_0 t_0) + \beta]) + \ldots, \tag{2.27}$$

where the real part is implied and ω_0 is the leading-order approximation to ω defined in (2.8). Note that we are not assuming this as a functional form for η, but are only giving a preview of our final result. A comparison of non-dimensional (2.27) with dimensional (2.1) shows we will have (ignoring the time dependence; cf. § 2.A.4) $a_1 = \varepsilon A_1$, $a_2 = \varepsilon^2 A_2/k$, etc, so $A_2/A_1^2 = a_2/(a_1^2 k)$. Both the HP β and a_2/a_1^2 encode information about the wave shape. We take the ratio a_2/a_1^2 because we will find that $a_2 \propto \exp(2\,\mathrm{Im}\{\omega_0\}t_0)$ while $a_1 \propto \exp(\mathrm{Im}\{\omega_0\}t_0)$. As we are mainly interested in the shape, the growth is removed by using the ratio a_2/a_1^2.

Now, expanding our non-dimensional variables in an asymptotic series of ε, we have

$$\eta = \sum_{n=1}^{\infty} \varepsilon^n \eta_n(x, t_0, t_1, \ldots), \tag{2.28}$$

$$\phi = \sum_{n=1}^{\infty} \varepsilon^n \phi_n(x, z, t_0, t_1, \ldots), \tag{2.29}$$

$$p = \sum_{n=1}^{\infty} \varepsilon^n p_n(x, t_0, t_1, \ldots). \tag{2.30}$$

Choosing $Pk/(\rho_w g) = O(1)$ gives $p_1 \neq 0$. Laplace's equation (2.3) and the bottom boundary condition (2.4) are linear and—unlike when spatial multiple scales are employed [e.g. 121]—can be satisfied identically. Laplace's equation is solved via a Fourier transform and, with the bottom boundary condition, has solution (real part implied)

$$\phi_n(x, z, t_0, t_1, \ldots) = \hat{\phi}_{n,0}(t_0, t_1, \ldots) + \frac{\cosh[m(z+h)]}{\sinh(mh)}\exp(\mathrm{i}mx)\hat{\phi}_{n,m}(t_0, t_1, \ldots), \tag{2.31}$$

with arbitrary $m \in \mathbb{N}_{>0}$ and arbitrary functions $\hat{\phi}_{n,0}(t_0, t_1, \ldots)$ and $\hat{\phi}_{n,m}(t_0, t_1, \ldots)$. Note that we imposed the no-mean-current condition by choosing $\langle u \rangle = \langle \partial_x \phi \rangle = 0$ at each order n, with $\langle \cdot \rangle$ the spatial average over one wavelength. Furthermore, to express the surface pressure profile p_n in terms of the surface height

η_n (cf. (2.18)), all variables are written as Fourier series

$$\eta_n(x,t_0,t_1,\ldots) = \sum_{m=0}^{m=n} \exp(\mathrm{i}mx)\hat{\eta}_{n,m}(t_0,t_1,\ldots), \tag{2.32}$$

$$\phi_n(x,z,t_0,t_1,\ldots) = \sum_{m=1}^{m=n} \exp(\mathrm{i}mx)\hat{\phi}_{n,m}(t_0,t_1,\ldots)\frac{\cosh(m(z+h))}{\sinh(mh)} + \hat{\phi}_{n,0}(t_0,t_1,\ldots), \tag{2.33}$$

$$p_n(x,t_0,t_1,\ldots) = \sum_{m=0}^{m=n} \exp(\mathrm{i}mx)\hat{p}_{m,n}(t_0,t_1,\ldots). \tag{2.34}$$

Aside from the pressure expansion, this follows the standard Stokes expansion methodology [e.g. 102]. Other texts, such as Mei et al. [121], treat the Stokes expansion using both slow time and spatial scales, but such spatial expansions are outside the scope of this paper (cf. § 2.3.2). Recall that we previously related (cf. (2.18)) the Fourier transform of the surface pressure to the surface profile,

$$\hat{p}_{m,n}(t_0,t_1,\ldots) = \hat{P}_m\hat{\eta}_{m,n}(t_0,t_1,\ldots). \tag{2.35}$$

Thus, p has higher-order corrections because η has higher-order Stokes-like corrections.

We now expand the kinematic (2.5) and dynamic (2.6) boundary conditions in ε and collect terms order by order.

$O(\varepsilon)$:

$$\frac{\partial\eta_1}{\partial t_0} - \frac{\partial\phi_1}{\partial z} = 0 \tag{2.36}$$

$$\eta_1 + \frac{\partial\phi_1}{\partial t_0} + p_1 = 0, \tag{2.37}$$

$O(\varepsilon^2)$:

$$\frac{\partial\phi_2}{\partial z} - \frac{\partial\eta_2}{\partial t_0} = \frac{\partial\eta_1}{\partial t_1} + \frac{\partial\eta_1}{\partial x}\frac{\partial\phi_1}{\partial x} - \eta_1\frac{\partial^2\phi_1}{\partial z^2}, \tag{2.38}$$

$$\eta_2 + \frac{\partial\phi_2}{\partial t_0} + p_2 = -\frac{\partial\phi_1}{\partial t_1} - \eta_1\frac{\partial\phi_1}{\partial z t_0} - \frac{1}{2}\left(\frac{\partial\phi_1}{\partial x}\right)^2 - \frac{1}{2}\left(\frac{\partial\phi_1}{\partial z}\right)^2, \tag{2.39}$$

$O(\varepsilon^3)$:

$$\begin{aligned}\frac{\partial\phi_3}{\partial z}-\frac{\partial\eta_3}{\partial t_0}&=\frac{\partial\eta_2}{\partial t_1}+\frac{\partial\eta_1}{\partial t_2}+\frac{\partial\eta_2}{\partial x}\frac{\partial\phi_1}{\partial x}+\frac{\partial\eta_1}{\partial x}\frac{\partial\phi_2}{\partial x}+\eta_1\frac{\partial\eta_1}{\partial x}\frac{\partial^2\phi_1}{\partial z\partial x}-\eta_1\frac{\partial^2\phi_2}{\partial z^2}\\&\quad-\frac{1}{2}\eta_1^2\frac{\partial^3\phi_1}{\partial z^3}-\eta_2\frac{\partial^2\phi_1}{\partial z^2},\end{aligned}\tag{2.40}$$

$$\begin{aligned}\eta_3+\frac{\partial\phi_3}{\partial t_0}+p_3&=-\frac{\partial\phi_1}{\partial t_2}-\frac{\partial\phi_2}{\partial t_1}-\frac{1}{2}\eta_1^2\frac{\partial^3\phi_1}{\partial z^2\partial t_0}-\eta_1\frac{\partial^2\phi_2}{\partial z\partial t_0}-\eta_2\frac{\partial^2\phi_1}{\partial z\partial t_0}\\&\quad-\eta_1\frac{\partial^2\phi_1}{\partial z\partial t_1}-\frac{\partial\phi_1}{\partial x}\frac{\partial\phi_2}{\partial x}-\eta_1\frac{\partial\phi_1}{\partial x}\frac{\partial^2\phi_1}{\partial x\partial z}-\frac{\partial\phi_1}{\partial z}\frac{\partial\phi_2}{\partial z}-\eta_1\frac{\partial\phi_1}{\partial z}\frac{\partial^2\phi_1}{\partial z^2},\end{aligned}\tag{2.41}$$

$O(\varepsilon^4)$:

$$\begin{aligned}\frac{\partial\phi_4}{\partial z}-\frac{\partial\eta_4}{\partial t_0}&=-\frac{\partial\eta_1}{\partial t_3}-\frac{\partial\eta_2}{\partial t_2}-\frac{\partial\eta_3}{\partial t_1}-\frac{\partial\eta_1}{\partial x}\frac{\partial\phi_3}{\partial x}-\frac{\partial\eta_2}{\partial x}\frac{\partial\phi_2}{\partial x}-\frac{\partial\eta_3}{\partial x}\frac{\partial\phi_1}{\partial x}+\eta_3\frac{\partial^2\phi_1}{\partial z^2}\\&\quad-\left(\frac{\partial\eta_1}{\partial x}\frac{\partial^2\phi_1}{\partial x\partial z}-\frac{\partial^2\phi_2}{\partial z^2}\right)\eta_2-\left(\frac{\partial\eta_1}{\partial x}\frac{\partial^2\phi_2}{\partial x\partial z}+\frac{\partial\eta_2}{\partial x}\frac{\partial^2\phi_1}{\partial x\partial z}-\frac{\partial^2\phi_3}{\partial z^2}\right)\eta_1+\frac{\partial^3\phi_1}{\partial z^3}\eta_1\eta_2\\&\quad-\left(\frac{1}{2}\frac{\partial\eta_1}{\partial x}\frac{\partial^2\phi_1}{\partial x\partial z}-\frac{1}{2}\frac{\partial^3\phi_2}{\partial z^3}\eta_1^2-\frac{1}{6}\frac{\partial^4\phi_1}{\partial z^4}\eta_1^3\right),\end{aligned}\tag{2.42}$$

$$\begin{aligned}\eta_4+\frac{\partial\phi_4}{\partial t_0}+p_4&=-\frac{\partial\phi_1}{\partial t_3}-\frac{\partial\phi_2}{\partial t_2}-\frac{\partial\phi_3}{\partial t_1}-\frac{\partial\phi_1}{\partial x}\frac{\partial\phi_3}{\partial x}-\frac{1}{2}\left(\frac{\partial\phi_2}{\partial x}\right)^2-\frac{\partial\phi_1}{\partial z}\frac{\partial\phi_3}{\partial z}\\&\quad-\frac{1}{2}\left(\frac{\partial\phi_2}{\partial z}\right)^2-\frac{\partial^2\phi_1}{\partial t_0\partial z}\eta_3-\left(\frac{\partial^2\phi_1}{\partial t_1\partial z}+\frac{\partial^2\phi_2}{\partial t_0\partial z}+\frac{\partial\phi_1}{\partial x}\frac{\partial^2\phi_1}{\partial x\partial z}+\frac{\partial\phi_1}{\partial z}\frac{\partial^2\phi_1}{\partial z^2}\right)\eta_2\\&\quad-\left(\frac{\partial^2\phi_1}{\partial t_2\partial z}+\frac{\partial^2\phi_2}{\partial t_1\partial z}+\frac{\partial^2\phi_3}{\partial t_0\partial z}+\frac{\partial\phi_1}{\partial x}\frac{\partial^2\phi_2}{\partial x\partial z}+\frac{\partial\phi_2}{\partial x}\frac{\partial^2\phi_1}{\partial x\partial z}+\frac{\partial\phi_1}{\partial z}\frac{\partial^2\phi_2}{\partial z^2}+\frac{\partial\phi_2}{\partial z}\frac{\partial^2\phi_1}{\partial z^2}\right)\eta_1\\&\quad-\frac{\partial^2\phi_1}{\partial t_0\partial z}\eta_1\eta_2-\left(\frac{1}{2}\frac{\partial^2\phi_1}{\partial t_1\partial z}+\frac{1}{2}\frac{\partial^2\phi_2}{\partial t_0\partial z}+\frac{1}{2}\frac{\partial\phi_1}{\partial x}\frac{\partial^2\phi_1}{\partial x\partial z}+\frac{1}{2}\left(\frac{\partial^2\phi_1}{\partial x\partial z}\right)^2+\frac{1}{2}\frac{\partial\phi_1}{\partial z}\frac{\partial^3\phi_1}{\partial z^3}\right.\\&\quad\left.+\frac{1}{2}\left(\frac{\partial^2\phi_1}{\partial z^2}\right)^2\right)\eta_1^2-\frac{1}{6}\frac{\partial^2\phi_1}{\partial t_0\partial z}\eta_1^3.\end{aligned}\tag{2.43}$$

We solve these equations to $O(\varepsilon^2)$ here and $O(\varepsilon^4)$ in § 2.A.

2.4.1 The $O(\varepsilon)$ equations

Proceeding to first order in ε, the linearized boundary conditions are

$$\frac{\partial\phi_1}{\partial z}-\frac{\partial\eta_1}{\partial t_0}=0,\tag{2.44}$$

$$\frac{\partial\phi_1}{\partial t_0}+\eta_1+p_1=0.\tag{2.45}$$

Inserting the Fourier transforms (2.32)–(2.34) and the pressure profile (2.18) gives

$m = 1$ Fourier component:

$$\hat{\phi}_{1,1} - \frac{\partial \hat{\eta}_{1,1}}{\partial t_0} = 0, \tag{2.46}$$

$$\frac{\partial \hat{\phi}_{1,1}}{\partial t_0} \coth(h) + \hat{\eta}_{1,1} + \hat{P}_1 \hat{\eta}_{1,1} = 0, \tag{2.47}$$

$m = 0$ Fourier component:

$$-\frac{\partial \hat{\eta}_{1,0}}{\partial t_0} = 0, \tag{2.48}$$

$$\frac{\partial \hat{\phi}_{1,0}}{\partial t_0} + \hat{\eta}_{1,0} + \hat{P}_0 \hat{\eta}_{1,0} = 0. \tag{2.49}$$

The $m = 0$ Fourier equations are solved by $\hat{\eta}_{1,0} = \hat{\phi}_{1,0} = 0$ when placing the initial mean water level $\langle \eta \rangle$ at $z = 0$. Combining the $m = 1$ equations (2.46) and (2.47) to eliminate $\hat{\eta}_{1,1}$ gives

$$\frac{\partial^2 \hat{\phi}_{1,1}}{\partial t_0^2} \coth(h) + \left(1 + \hat{P}_1\right) \hat{\phi}_{1,1} = 0. \tag{2.50}$$

This is the usual, finite-depth, linear operator on $\hat{\phi}_{1,1}$ modified by the presence of $\hat{P}_1$, showing that $\hat{\phi}_{1,1}(t_0, t_1, \ldots)$ is harmonic. Using a bit of foresight to define the constants, we write

$$\hat{\phi}_{1,1} = -\mathrm{i}\omega_0 A_1(t_1) \exp(-\mathrm{i}\omega_0 t_0), \tag{2.51}$$

giving

$$\phi_1 = -\mathrm{i}\omega_0 A_1(t_1) \exp(\mathrm{i}(x - \omega_0 t_0)) \frac{\cosh(z + h)}{\sinh(h)}, \tag{2.52}$$

where

$$\omega_0 = \pm \sqrt{\tanh(h)\left(1 + \hat{P}_1\right)}. \tag{2.53}$$

We choose the (+) sign, corresponding to waves propagating to the right. While $A_1(t_1)$ and $\exp(-\mathrm{i}\omega_0 t_0)$ always appear together and could be simply left as a single, t_0-dependent variable $A(t_0, t_1) \in \mathbb{C}$, we find it instructive to explicitly write the t_0-dependence. Inserting this into the surface boundary conditions gives

equations for η_1,

$$\frac{\partial \hat{\eta}_1}{\partial t_0} = -\mathrm{i}\omega_0 A_1(t_1)\exp(-\mathrm{i}\omega_0 t_0), \tag{2.54}$$

$$\hat{\eta}_1 + \hat{P}_1\hat{\eta}_1 = \coth(h)\omega_0^2 A_1(t_1)\exp(-\mathrm{i}\omega_0 t_0). \tag{2.55}$$

This gives

$$\eta_1 = A_1(t_1)\exp(\mathrm{i}(x-\omega_0 t_0)). \tag{2.56}$$

It is instructive to consider the real and imaginary parts of ω_0

$$\mathrm{Re}\{\omega_0\} = \sqrt{\frac{\tanh(h)}{2}}\sqrt{1+\mathrm{Re}\Big\{\hat{P}_1\Big\}+\sqrt{1+\Big|\hat{P}_1\Big|^2+2\,\mathrm{Re}\Big\{\hat{P}_1\Big\}}}, \tag{2.57}$$

$$\mathrm{Im}\{\omega_0\} = \mathrm{sgn}\left(\mathrm{Im}\Big\{\hat{P}_1\Big\}\right)\sqrt{\frac{\tanh(h)}{2}}\sqrt{-1-\mathrm{Re}\Big\{\hat{P}_1\Big\}+\sqrt{1+\Big|\hat{P}_1\Big|^2+2\,\mathrm{Re}\Big\{\hat{P}_1\Big\}}}. \tag{2.58}$$

Notice that the pressure causes growth ($\mathrm{Im}\{\omega_0\} > 0$) for wind in the direction of the waves ($\mathrm{Im}\{\hat{P}_1\} > 0$) and decay ($\mathrm{Im}\{\omega_0\} < 0$) for opposing wind ($\mathrm{Im}\{\hat{P}_1\} < 0$). Likewise, observe that an applied pressure, $\hat{P}_1 \neq 0$, modifies the dispersion relation (2.57). This phenomenon was also derived by Jeffreys [63] and Miles [69] for $Pk/(\rho_w g) = O(\varepsilon)$, which we can reproduce by substituting $\hat{P}_1 \to \varepsilon\hat{P}_1$ in (2.57) and (2.58).

2.4.2 The $O(\varepsilon^2)$ equations

Proceeding to second order, the kinematic and dynamic boundary conditions are

$$\frac{\partial \phi_2}{\partial z} - \frac{\partial \eta_2}{\partial t_0} = \frac{\partial \eta_1}{\partial t_1} + \frac{\partial \eta_1}{\partial x}\frac{\partial \phi_1}{\partial x} - \eta_1\frac{\partial^2 \phi_1}{\partial z^2}, \tag{2.59}$$

$$\frac{\partial \phi_2}{\partial t_0} + \eta_2 + p_2 = -\frac{\partial \phi_1}{\partial t_1} - \eta_1\frac{\partial^2 \phi_1}{\partial z \partial t_0} - \frac{1}{2}\left(\frac{\partial \phi_1}{\partial x}\right)^2 - \frac{1}{2}\left(\frac{\partial \phi_1}{\partial z}\right)^2. \tag{2.60}$$

By inserting the Fourier transforms (2.32)–(2.34), we can express p_2 using (2.35). Inserting the first-order solutions (2.52) and (2.56) and collecting harmonics yields

$m = 1$ Fourier component:

$$\hat{\phi}_{2,1} - \frac{\partial \hat{\eta}_{2,1}}{\partial t_0} = \frac{\partial A_1}{\partial t_1}\exp(-\mathrm{i}\omega_0 t_0), \tag{2.61}$$

$$\frac{\partial \hat{\phi}_{2,1}}{\partial t_0}\coth(h) + (1+\hat{P}_1)\hat{\eta}_{2,1} = \mathrm{i}\omega_0\frac{\partial A_1}{\partial t_1}\exp(-\mathrm{i}\omega_0 t_0)\coth(h), \tag{2.62}$$

$m = 2$ Fourier component:

$$2\hat{\phi}_{2,2} - \frac{\partial \hat{\eta}_{2,2}}{\partial t_0} = \mathrm{i}\omega_0 A_1^2 \exp(-2\mathrm{i}\omega_0 t_0)\coth(h), \tag{2.63}$$

$$\frac{\partial \hat{\phi}_{2,2}}{\partial t_0}\coth(2h) + (1+\hat{P}_2)\hat{\eta}_{2,2} = \frac{1}{4}\omega_0^2 A_1^2 \exp(-2\mathrm{i}\omega_0 t_0)\big(2 - \operatorname{csch}^2(h)\big), \tag{2.64}$$

$m = 0$ Fourier component:

$$-\frac{\partial \hat{\eta}_{2,0}}{\partial t_0} = 0, \tag{2.65}$$

$$\frac{\partial \hat{\phi}_{2,0}}{\partial t_0} + \hat{\eta}_{2,0} = \frac{1}{4}\Big(2\,\mathrm{Re}\big\{\omega_0^2\big\} - |\omega_0|^2\big(2 + \operatorname{csch}^2(h)\big)\Big)|A_1|^2|\exp(-\mathrm{i}\omega_0 t_0)|^2. \tag{2.66}$$

Eliminating the various $\hat{\eta}_{2,m}$ to get equations solely in terms of $\hat{\phi}_{2,m}$ gives

$m = 1$ Fourier component:

$$\frac{\partial^2 \hat{\phi}_{2,1}}{\partial t_0^2}\coth(h) + (1+\hat{P}_1)\hat{\phi}_{2,1} = 2\Big(1+\hat{P}_1\Big)\frac{\partial A_1}{\partial t_1}\exp(-\mathrm{i}\omega_0 t_0), \tag{2.67}$$

$m = 2$ Fourier component:

$$\begin{aligned}\frac{\partial^2 \hat{\phi}_{2,2}}{\partial t_0^2}\coth(2h) + 2(1+\hat{P}_2)\hat{\phi}_{2,2} = -\mathrm{i}\frac{1}{2}\omega_0 A_1^2\Big\{&\big[2 - \operatorname{csch}^2(h)\big]\omega_0^2 \\ &- 2\Big(1+\hat{P}_2\Big)\coth(h)\Big\}\exp(2\mathrm{i}\omega_0 t_0),\end{aligned} \tag{2.68}$$

$m = 0$ Fourier component:

$$\frac{\partial^2 \hat{\phi}_{2,0}}{\partial t_0^2} = \frac{1}{2}\Big(2\,\mathrm{Re}\big\{\omega_0^2\big\} - |\omega_0|^2\big(2 + \operatorname{csch}^2(h)\big)\Big)|A_1|^2\exp(2\,\mathrm{Im}\{\omega_0\}t_0)\,\mathrm{Im}\{\omega_0\}. \tag{2.69}$$

Preventing secular terms in $\hat{\phi}_{2,1}$ requires that $\partial_{t_1} A_1 = 0$. This is consistent with standard, unforced Stokes waves: Stokes corrections to the unforced wave frequency first occur at $O\big(\varepsilon^2\big)$, meaning we would only expect A_1 to have a t_2-dependence (which we also observe, cf. § 2.A.1). Solving (2.67)–(2.69) for $\hat{\phi}_{2,m}$ and transforming back to ϕ_2 via (2.31) gives

$$\begin{aligned}\phi_2 = \mathrm{i}\frac{\omega_0}{4}A_1^2\coth(h)&\frac{\big(2 - \operatorname{csch}^2(h)\big)\omega_0^2 - 2\Big[1+\hat{P}_2\Big]\coth(h)}{\big(2 + \operatorname{csch}^2(h)\big)\omega_0^2 - \Big[1+\hat{P}_2\Big]\coth(h)}\exp(2\mathrm{i}(x - \omega_0 t_0))\frac{\cosh[2(z+h)]}{\sinh(2h)} \\ &+ \frac{1}{8\,\mathrm{Im}\{\omega_0\}}\Big(2\,\mathrm{Re}\big\{\omega_0^2\big\} - |\omega_0|^2\big(2 + \operatorname{csch}^2(h)\big)\Big)|A_1|^2(\exp(2\,\mathrm{Im}\{\omega_0\}t_0) - 1).\end{aligned} \tag{2.70}$$

We have included a constant term -1 in $\exp(2\,\mathrm{Im}\{\omega_0\}t_0) - 1$ so that ϕ_2 remains finite if $P \to 0$ (i.e. $\mathrm{Im}\{\omega_0\} \to 0$). We have also dropped the homogeneous solution, which would only amount to redefining the linear solution, A_1.

The surface boundary conditions are now solely equations for $\hat{\eta}_{2,m}$

$$\frac{\partial\hat{\eta}_{2,2}}{\partial t_0} = -\mathrm{i}\frac{1}{2}\omega_0^3 A_1^2 \exp(-2\mathrm{i}\omega_0 t_0)\frac{\big(2+3\,\mathrm{csch}^2(h)\big)\coth(h)}{\big(2+\mathrm{csch}^2(h)\big)\omega_0^2 - \Big[1+\hat{P}_2\Big]\coth(h)} \tag{2.71}$$

$$\Big[1+\hat{P}_2\Big]\hat{\eta}_{2,2} = \frac{1}{4}\Big[1+\hat{P}_2\Big]A^2\exp(-2\mathrm{i}\omega_0 t_0)\frac{(2+3\,\mathrm{csch}^2(h))\coth(h)\omega_0^2}{\big(2+\mathrm{csch}^2(h)\big)\omega_0^2 - \Big[1+\hat{P}_2\Big]\coth(h)}, \tag{2.72}$$

and $\hat{\eta}_{2,0} = \hat{\eta}_{2,1} = 0$. These have the solution

$$\eta_2 = \frac{1}{4}A_1^2\exp(2\mathrm{i}(x-\omega_0 t_0))\big(2+3\,\mathrm{csch}^2(h)\big)\coth(h)\left(1-\coth^2(h)\left[\frac{\hat{P}_2-\hat{P}_1}{1+\hat{P}_1}\right]\right)^{-1} \tag{2.73}$$

Note that we chose $\hat{\eta}_{2,0} = 0$ since we imposed $\overline{\eta} = 0$ at $t = 0$ with our choice of the mean water level as our initial datum in § 2.3.1. It is interesting to note that, when $\overline{\eta} = 0$ initially, it remains zero for all times. This implies that the mean water level does not change over time. Another choice of datum occasionally used [e.g. 122] is the mean energy level (MEL), defined such that $\overline{\partial_t\phi} = 0$ [e.g. 123]. However, even if we chose $\overline{\partial_t\phi} = 0$ initially by adding a constant A to η_2 and a term $-At_0$ to ϕ_2, (2.70) shows that the MEL would still vary with time.

Redimensionalizing, we find

$$\eta = \varepsilon\frac{A_1}{k}\exp(\mathrm{i}(x-\omega_0 t_0)) + \varepsilon^2\frac{A_1^2}{k}\exp(2\mathrm{i}(x-\omega_0 t_0))C_{2,2} + O\big(\varepsilon^3\big), \tag{2.74}$$

where the complex $C_{2,2}$ is the pressure-induced (or wind-induced) correction to the first harmonic

$$C_{2,2} \coloneqq \frac{1}{4}\big(2+3\,\mathrm{csch}^2(h)\big)\coth(h)\left(1-\coth^2(h)\left[\frac{\hat{P}_2-\hat{P}_1}{1+\hat{P}_1}\right]\right)^{-1}. \tag{2.75}$$

Note that $A_1^2|C_{2,2}|/k$ is the quantity denoted A_2 in (2.27).

We have now found the primary wave $\hat{\eta}_{m=1} = \varepsilon\hat{\eta}_{1,m} + O\big(\varepsilon^3\big)$ and first harmonic $\hat{\eta}_{m=2} = \varepsilon^2\hat{\eta}_{2,2} + O\big(\varepsilon^3\big)$. Therefore, the amplitudes of the primary wave and first harmonic are respectively

$$a_1 \coloneqq |\hat{\eta}_{m=1}| = \varepsilon\frac{|A_1(t_2)|}{k}\exp(\mathrm{Im}\{\omega_0\}t_0) + O\big(\varepsilon^3\big), \tag{2.76}$$

$$a_2 \coloneqq |\hat{\eta}_{m=2}| = \varepsilon^2\frac{\big|A_1^2(t_2)\big|}{k}\exp(2\,\mathrm{Im}\{\omega_0\}t_0)|C_{2,2}| + O\big(\varepsilon^3\big). \tag{2.77}$$

Hence, in order to cancel the t_0-dependence, we define the relative harmonic amplitude shape parameter as

$$\frac{a_2}{a_1^2 k} \coloneqq \left| \frac{\hat{\eta}_{m=2}}{\hat{\eta}_{m=1}^2 k} \right|. \tag{2.78}$$

With this definition, (2.74) becomes

$$\eta = a_1 \exp(\mathrm{i}(x - \mathrm{Re}\{\omega_0\}t_0)) + a_2 \exp(\mathrm{i}[2(x - \mathrm{Re}\{\omega_0\}t_0) + \beta]) + O\big(\varepsilon^3\big), \tag{2.79}$$

where we have absorbed the complex phase of A_1 into $\exp(\mathrm{i}x)$ (redefining the $x = 0$ location) and defined the harmonic phase β as the complex angle of $\hat{\eta}_{m=2}/\hat{\eta}_{m=1}^2$

$$\beta \coloneqq \tan^{-1}\left(\frac{\mathrm{Im}\{\hat{\eta}_{m=2}/\hat{\eta}_{m=1}^2\}}{\mathrm{Re}\{\hat{\eta}_{m=2}/\hat{\eta}_{m=1}^2\}} \right). \tag{2.80}$$

In general, both β and $a_2/(a_1^2 k)$ will have an expansion in ε since $\hat{\eta}_{m=2}$ will have higher-order corrections. For instance, the HP β has expansion $\beta = \beta_0 + \varepsilon\beta_1 + \ldots$. Inserting our solution (2.74) into (2.80) gives β_0, which is just the complex angle of $C_{2,2}$ at this order

$$\begin{aligned} \beta_0 &= \tan^{-1}\left(\frac{\mathrm{Im}\Big\{\Big[\frac{\hat{P}_2 - \hat{P}_1}{1+\hat{P}_1}\Big]\Big\}}{\tanh^2(h) - \mathrm{Re}\Big\{\Big[\frac{\hat{P}_2 - \hat{P}_1}{1+\hat{P}_1}\Big]\Big\}} \right) \\ &= \tan^{-1}\left(\frac{\mathrm{Im}\Big\{\Big[\hat{P}_2 - \hat{P}_1\Big]\Big(1 + \hat{P}_1^*\Big)\Big\}}{\Big|1 + \hat{P}_1\Big|^2 \tanh^2(h) - \mathrm{Re}\Big\{\Big[\hat{P}_2 - \hat{P}_1\Big]\Big(1 + \hat{P}_1^*\Big)\Big\}} \right), \end{aligned} \tag{2.81}$$

with an asterisk representing the complex conjugate. Similarly, using (2.78) shows that the leading-order term of $a_2/(a_1^2 k)$ is just $|C_{2,2}|$

$$\frac{a_2}{a_1^2 k} = |C_{2,2}| = \frac{2 + 3\,\mathrm{csch}^2(h)}{4} \coth(h) \left| 1 - \coth^2(h) \left[\frac{\hat{P}_2 - \hat{P}_1}{1 + \hat{P}_1} \right] \right|^{-1}. \tag{2.82}$$

Without wind ($\hat{P}_1 = \hat{P}_2 = 0$), $C_{2,2}$ is real and equals $(2 + 3\,\mathrm{csch}^2(h))\coth(h)/4$, or $1/2$ in deep water. Thus, $\hat{P}_1 = \hat{P}_2 = 0$ reproduces the usual Stokes waves values of $a_2/(a_1^2 k) = 1/2$ in deep water and $\beta = 0$.

Asymmetry and skewness are common shape parameters that depend on β and $a_2/(a_1^2 k)$. The

skewness S and asymmetry A are defined as

$$\mathrm{S} \coloneqq \frac{\langle \eta^3 \rangle}{\langle \eta^2 \rangle^{3/2}}, \tag{2.83}$$

$$\mathrm{A} \coloneqq \frac{\langle \mathcal{H}\{\eta\}^3 \rangle}{\langle \eta^2 \rangle^{3/2}}, \tag{2.84}$$

with $\langle \cdot \rangle$ the spatial average over one wavelength and $\mathcal{H}\{\cdot\}$ the Hilbert transform (in x). The average of any Fourier component $\exp(\mathrm{i}mx)$ over a wavelength is zero for all $m \neq 0 \in \mathbb{N}$. Therefore, only combinations wherein the x-dependence cancels will contribute. Inserting our solution for η (2.79) into the skewness and asymmetry definitions (2.83) and (2.84) yields

$$\mathrm{S} = \frac{3}{\sqrt{2}}\varepsilon |A_1| \exp(\mathrm{Im}\{\omega_0\}t_0)\frac{a_2}{a_1^2 k}\cos(\beta_0) + O\big(\varepsilon^2\big), \tag{2.85}$$

$$\mathrm{A} = -\frac{3}{\sqrt{2}}\varepsilon |A_1| \exp(\mathrm{Im}\{\omega_0\}t_0)\frac{a_2}{a_1^2 k}\sin(\beta_0) + O\big(\varepsilon^2\big). \tag{2.86}$$

By solving the kinematic and dynamic boundary conditions to $O\big(\varepsilon^2\big)$, we have generated the leading-order terms for β and $a_2/(a_1^2 k)$. We continue this analysis by solving to $O\big(\varepsilon^4\big)$ in § 2.A, deriving the first non-trivial correction to β (2.164), $a_2/(a_1^2 k)$ (2.163) and the complex frequency ω (2.170). Additionally, going to $O\big(\varepsilon^4\big)$ also extends our solutions to weaker wind conditions. As outlined in § 2.3.5, we can substitute $P \to \varepsilon P$ or $P \to \varepsilon^2 P$ to generate shape parameters for weaker winds $Pk/(\rho_w g) = O(\varepsilon)$ or $Pk/(\rho_w g) = O\big(\varepsilon^2\big)$, respectively (§ 2.A.6). In this way, we find the shape parameters' dependence on our non-dimensional parameters (kh, ε, P and ψ_P) and demonstrate weak time and amplitude dependence over a range of wind conditions from strong $Pk/(\rho_w g) = O(1)$ to relatively weak $Pk/(\rho_w g) = O\big(\varepsilon^2\big)$.

2.5 Results

Now, we present the main results of this theory. The harmonic phase β, harmonic magnitudes a_1 and a_2, and complex frequency ω depend on the four non-dimensional parameters: the wave steepness $\varepsilon \coloneqq a_1 k$, water depth kh, pressure magnitude constant $Pk/(\rho_w g)$ and wind phase ψ_P. To reduce the non-dimensional parameter range, we keep a fixed $\varepsilon = 0.2$. Recall (§ 2.3.2) the requirement of $\varepsilon/(kh)^3 \leq 1$, such that the expansion remains properly ordered, implies $kh \geq 0.5$, although we keep $kh \geq 1$. Note that taking kh to ∞ yields solutions on infinite depth. The pressure magnitude constant P is P_J or P_G, corresponding to the choice of pressure profile. For both solutions, taking $P \to 0$ recovers the unforced

Stokes wave.

For the remainder of the paper, we will revert to dimensional variables. In particular, the pressure constant P is dimensional again and not necessarily order unity. Replacing the multiple time scales with the true time t in our solution (2.79), we obtain a surface height profile η of the form

$$k\eta = (a_1 k)\exp(\mathrm{i}\theta) + (a_1 k)^2 \frac{a_2}{a_1^2 k}\exp(\mathrm{i}(2\theta+\beta)) + \ldots, \tag{2.87}$$

with the real part implied and θ defined in (2.8). Note that the growth of the harmonics means that these solutions are only valid for finite time (cf. § 2.6.1).

2.5.1 Harmonic phase, relative harmonic amplitude and wave shape

The wave shape is a function of the harmonic phase β, quantifying the relative phase shift between the primary wave and first harmonic, and the relative harmonic ratio $a_2/(a_1^2 k)$. The solutions for these parameters are extended to $O(\varepsilon^2)$ in § 2.A.3, applying to all pressure profiles satisfying (2.18) with magnitude $Pk/(\rho_w g) = O(1)$ to $O(\varepsilon^2)$. We now specialize these results to the two pressure profiles of interest.

The full, $O(\varepsilon^2)$-accurate Jeffreys harmonic phase β_J (2.164) is depicted in figures 2.3(*a*,*4a*,*5a*). To develop a better understanding of its functional dependence, we can consider simpler, limiting cases. For very small wave steepnesses, $\varepsilon \lll 1$, the leading-order correction (2.81) is

$$\beta_J = \pm\tan^{-1}\left(\frac{Pk/(\rho_w g)}{\tanh^2(kh) - \operatorname{sech}^2(kh)P^2k^2/(\rho_w^2 g^2)}\right) + O(\varepsilon), \tag{2.88}$$

with the $\pm$ corresponding to the sign of $\psi_P = \pm\pi/2$ in the pressure profile. If, instead of assuming $\varepsilon \lll 1$, we expand (2.164) considering a weak pressure forcing $Pk/(\rho_w g) \ll 1$, we find

$$\beta_J = \pm\frac{Pk}{\rho_w g}\coth^2(kh) + O(\varepsilon^3). \tag{2.89}$$

The full, $O(\varepsilon^2)$-accurate generalized Miles β_G (2.164) is also depicted in figures 2.3(*a*,*4a*,*5a*). For very

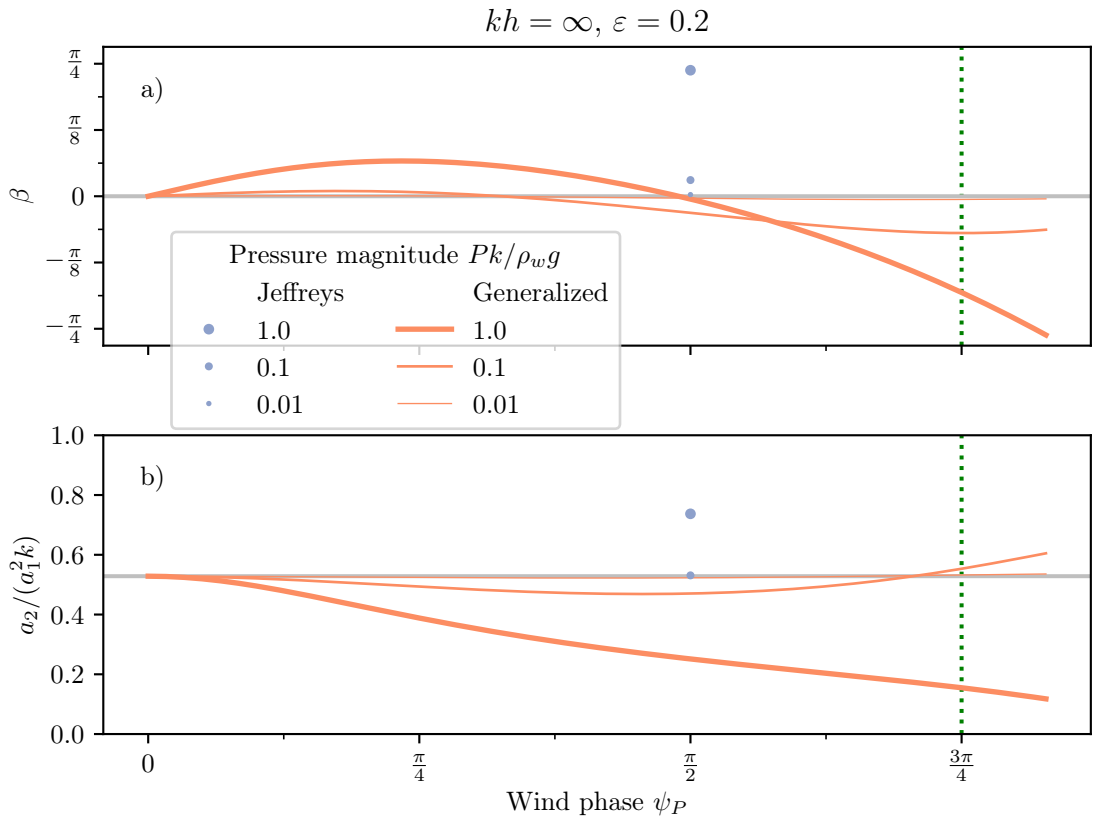

Figure 2.3. (a) Harmonic phase β (2.80) and (b) relative harmonic amplitude $a_2/(a_1^2 k)$ (2.78) versus wind phase ψ_P. Results are shown for Jeffreys and generalized Miles profiles with $kh = \infty$, $\varepsilon = 0.2$ and pressure magnitude constants $Pk/(\rho_w g) = 0.01$, 0.1 and 1, as indicated in the legend. The Jeffreys β_J is only shown at $\psi_P = \pi/2$ as that is its implied ψ_P. All results are plotted using the full, $O(\varepsilon^2)$-accurate expressions (2.163) and (2.164). The grey lines are the results for a fourth-order unforced Stokes wave, and the green dotted line represents $\psi_P = 3\pi/4$ used in many of the other plots and supported by numerical simulations from Hara and Sullivan [90] and Husain et al. [108].

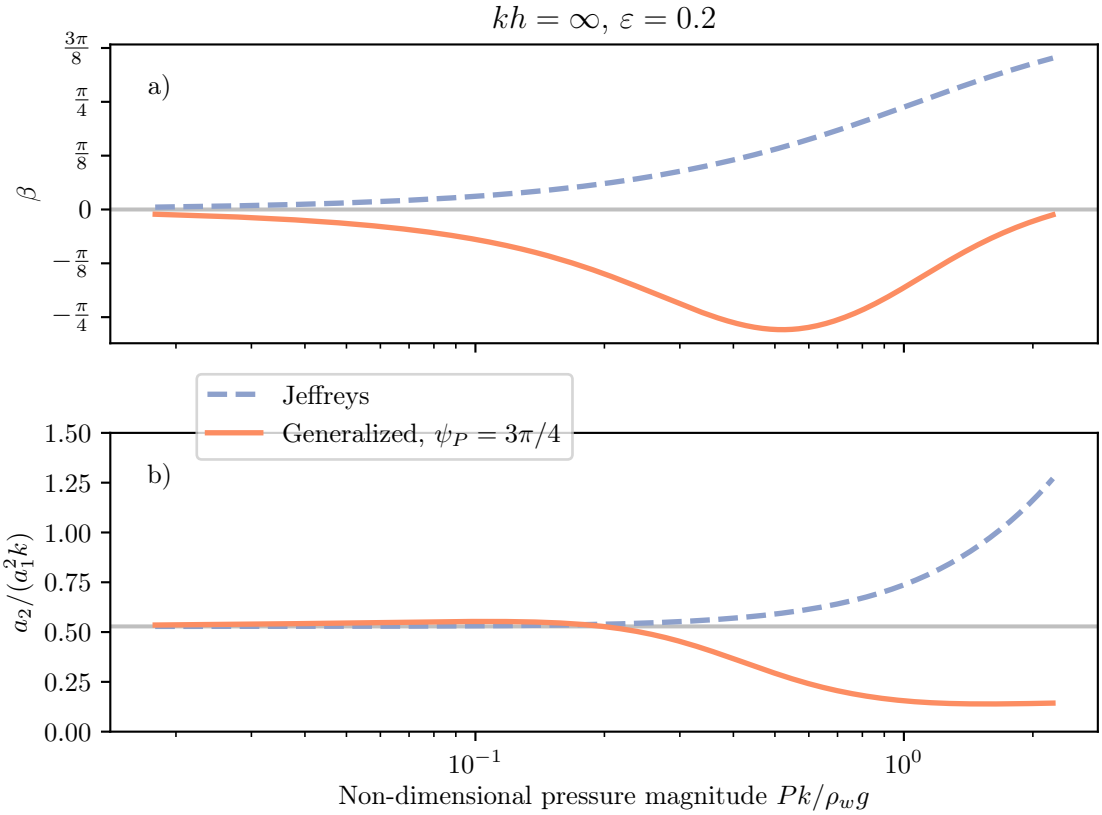

Figure 2.4. (a) Harmonic phase β (2.80) and (b) relative harmonic amplitude $a_2/(a_1^2 k)$ (2.78) versus non-dimensional pressure magnitude constant $Pk/(\rho_w g)$. Results are shown for Jeffreys and generalized Miles profiles, as indicated in the legend, with $kh = \infty$, $\varepsilon = 0.2$ and $\psi_P = 3\pi/4$ (for generalized Miles). All results are plotted using the full, $O(\varepsilon^2)$-accurate expressions (2.163) and (2.164), which include the $Pk/(\rho_w g) \ll 1$ limits for β (2.89) and (2.91), as well as for $a_2/(a_1^2 k)$ (2.93) and (2.95). The grey lines are the results for a fourth-order unforced Stokes wave.

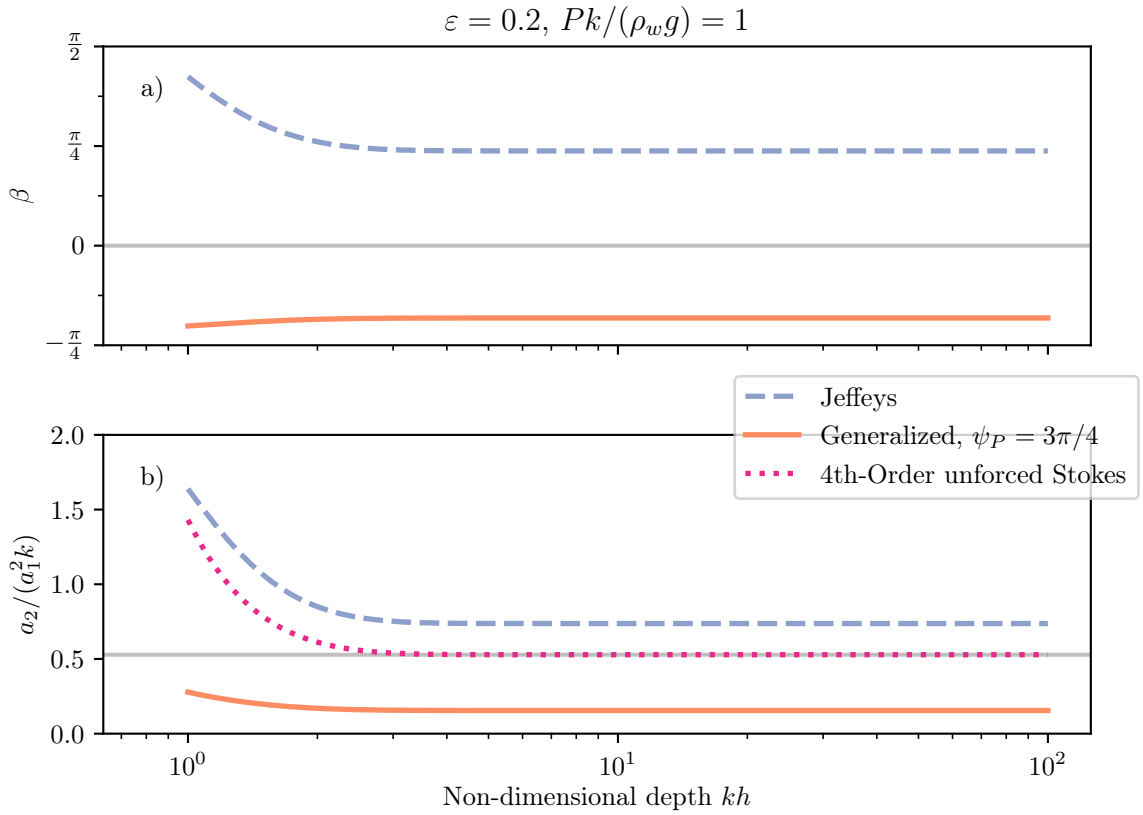

Figure 2.5. (a) Harmonic phase β (2.80) and (b) relative harmonic amplitude $a_2/(a_1^2 k)$ (2.78) versus non-dimensional depth kh. Results are shown for Jeffreys and generalized Miles profiles, as well as unforced (i.e. no wind) Stokes waves, with $\varepsilon = 0.2$, pressure magnitude constant $Pk/(\rho_w g) = 1$ and $\psi_P = 3\pi/4$ (for generalized Miles). All results are plotted using the full, $O(\varepsilon^2)$-accurate expressions (2.163) and (2.164). The grey lines are the results for a fourth-order unforced Stokes wave with $kh = \infty$.

small $\varepsilon \lll 1$, we have the approximation

$$\beta_G = \tan^{-1}\Bigg(\Bigg[2\cos(\psi_P) - 1 + \frac{Pk}{\rho_w g}\Bigg]\frac{Pk}{\rho_w g}\sin(\psi_P)\Bigg[-\left(\frac{Pk}{\rho_w g}\right)^2\cos(\psi_P) - 1 \\ - \frac{Pk}{\rho_w g}(\cos(2\psi_P) + \cos(\psi_P)) + \left(1 + 2\frac{Pk}{\rho_w g}\cos(\psi_P) + \left(\frac{Pk}{\rho_w g}\right)^2\right)\big(2 - \operatorname{sech}^2(kh)\big)\Bigg]^{-1}\Bigg) \\ + O(\varepsilon). \tag{2.90}$$

Instead of requiring $\varepsilon \lll 1$, we can expand (2.164) while considering a weak pressure forcing $Pk/(\rho_w g) \ll 1$ to find

$$\beta_G = \frac{Pk}{\rho_w g}(\sin(2\psi_P) - \sin(\psi_P))\coth^2(kh) + \frac{1}{2}\left(\frac{Pk}{\rho_w g}\right)^2\coth^4(kh)\Big(\sin(4\psi_P) \\ - 4\sin(3\psi_P) + 3\sin(2\psi_P) + 2\operatorname{sech}^2(kh)[\sin(3\psi_P) - \sin(2\psi_P)]\Big) + O\big(\varepsilon^3\big). \tag{2.91}$$

Next, we consider the relative harmonic amplitude, $a_2/(a_1^2 k)$. The full, $O\big(\varepsilon^2\big)$-accurate Jeffreys relative harmonic amplitude (2.163) is shown in figures 2.3(b,$4b$,$5b$), but we can approximate it for very small $\varepsilon \lll 1$ as (2.82)

$$\left(\frac{a_2}{a_1^2 k}\right)_J = \frac{2 + 3\operatorname{csch}^2(kh)}{4}\coth(kh)\sqrt{\frac{1 + P^2k^2/(\rho_w^2 g^2)}{1 + P^2k^2/(\rho_w^2 g^2)\operatorname{csch}^4(kh)}}. \tag{2.92}$$

Inserting a weak wind $Pk/(\rho_w g) \ll 1$ in (2.163) instead of requiring $\varepsilon \lll 1$ yields

$$\left(\frac{a_2}{a_1^2 k}\right)_J = \frac{2 + 3\operatorname{csch}^2(kh)}{4}\coth(kh)\left(1 + \frac{1 - \operatorname{csch}^4(kh)}{2}\left(\frac{Pk}{\rho_w g}\right)^2\right) + (a_1 k)^2\mathcal{A} + O\big(\varepsilon^3\big), \tag{2.93}$$

with $\mathcal{A}$ only a function of kh and defined in (2.161). We now have the direct appearance of the amplitude $a_1 k$ with an implicit time dependence due to growth. The full, $O\big(\varepsilon^2\big)$-accurate generalized Miles $a_2/(a_1^2 k)_G$ (2.163) is also plotted in figures 2.3(b,$4b$,$5b$). We can simplify $a_2/(a_1^2 k)_G$ by assuming a very small wave steepness $\varepsilon \lll 1$

$$\left(\frac{a_2}{a_1^2 k}\right)_G = \frac{2 + 3\operatorname{csch}^2(kh)}{4}\coth(kh)\left|1 - \coth^2(kh)\frac{[\exp(\mathrm{i}\psi_P) - 1]Pk/(\rho_w g)}{\exp(-\mathrm{i}\psi_P) + Pk/(\rho_w g)}\right|^{-1} + O(\varepsilon). \tag{2.94}$$

Instead of assuming very small ε, we can approximate (2.163) by assuming $Pk/(\rho_w g) \ll 1$ to give

$$\left(\frac{a_2}{a_1^2 k}\right)_G = \frac{2+3\,\mathrm{csch}^2(kh)}{4}\coth(kh)\Bigg(1+\frac{Pk}{\rho_w g}[\cos(2\psi_P)-\cos(\psi_P)]\coth^2(kh) \\ +\frac{1}{2}\left(\frac{Pk}{\rho_w g}\right)^2(\cos(\psi_P)-1)\Big\{3\coth^2(kh)\cos(3\psi_P)-4\cos(2\psi_P) \\ -4\cos(\psi_P)-3-\mathrm{csch}^2(kh)\Big\}\coth^2(kh)\Bigg)+(a_1k)^2\mathcal{A}+O\big(\varepsilon^3\big). \tag{2.95}$$

Note that we see a weak amplitude dependence (i.e. $a_1 k$ terms) appearing in some of these results, such as (2.93) and (2.95). This amplitude dependence is implicitly present in figures 2.3–2.5 since they show the full, $O\big(\varepsilon^2\big)$ results (2.163) and (2.164) which encode this dependence. However, we do not show the β and $a_2/(a_1^2 k)$ dependence on ε as these effects are $O\big(\varepsilon^2\big)$, or approximately 4 % of the leading-order effects in figures 2.3–2.5.

Figure 2.3 shows the influence of wind phase ψ_P on β and $a_2/(a_1^2 k)$ for both the Jeffreys and generalized Miles profiles with $kh = \infty$ and $\varepsilon = 0.2$ for a range of pressure magnitudes $Pk/(\rho_w g) = 0.01$, 0.1 and 1. For the strongest pressure forcing $Pk/(\rho_w g) = 1$, both the Jeffreys and generalized Miles profiles induce a harmonic phase magnitude $|\beta|$ up to $\pi/4$ (figure 2.3a). The Jeffreys value of $\beta_J = \pi/4$ is placed at $\psi_P = \pi/2$ to correspond with its restriction that $\psi_P = \pm\pi/2$. The generalized Miles HP β increases from zero at $\psi_P = 0$ (figure 2.3a) to roughly $\pi/16$ for the largest pressure, before decreasing to approximately $-\pi/4$ and passing through zero near $\psi_P = \pi/2$. The weaker pressure forcings show a much reduced β range, cross $\beta = 0$ at somewhat smaller values of ψ_P and yield much smaller β for large wind phase angles. The angle $\psi_P = 3\pi/4$ is denoted by a dashed line in figure 2.3, and this ψ_P is utilized hereafter, as suggested by Hara and Sullivan [90] and Husain et al. [108].

The relative harmonic amplitude shows opposing behaviour for the two forcing types in figure 2.3(b). The Jeffreys $a_2/(a_1^2 k)_J = 0.7$ for the strongest wind is enhanced relative to the deep-water Stokes value $a_2/(a_1^2 k) = 1/2$, while the generalized Miles value is suppressed $a_2(a_1^2 k)_G \leq 1/2$ for most values of ψ_P. As in figure 2.3(a), the weaker pressure magnitudes give correspondingly smaller changes to $a_2/(a_1^2 k)$, although the small $Pk/(\rho_w g)$ do slightly enhance $a_2/(a_1^2 k)$ for large ψ_P. It is worth noting that the strongest pressure $Pk/(\rho_w g) = 1$ suppresses the first harmonic a_2 as $\psi_P \to \pi$, making the wave more linear. However, as discussed in § 2.6.2, $\psi_P \approx \pi$ is usually observed for very weak winds. As the $Pk/(\rho_w g) = 0.1$ and 0.01 lines in figure 2.3(b) show, weaker winds show no such linearization. Note that figure 2.3 only depicts $\psi_P \geq 0$ since β (2.81) is antisymmetric and $a_2/(a_1^2 k)$ (2.82) is symmetric about $\psi_P = 0$. This is seen by

noticing $\psi_P \to -\psi_P \implies \hat{P}_m \to \hat{P}_m^*$.

The wave-shape parameters show a particularly rich dependence on the pressure magnitude $Pk/(\rho_w g)$ (figure 2.4). While both Jeffreys and generalized Miles yield non-zero harmonic phase β for small pressures (figure 2.4a), they have opposite responses for large $Pk/(\rho_w g)$. The Jeffreys profile increases steadily, reaching $3\pi/8$ for $Pk/(\rho_w g) = 3$. Instead, the generalized Miles profile first decreases, reaching a minimum of approximately $-\pi/4$ at $Pk/(\rho_w g) = 0.6$ and then increasing to small, positive values. The relative harmonic amplitude shows (figure 2.4b) virtually no change from the deep-water Stokes value of 1/2 until $Pk/(\rho_w g) = 0.3$. Then, the Jeffreys profile increases rapidly, attaining $a_2/(a_1^2 k)_J = 1.7$ for $Pk/(\rho_w g) = 3$. Contrarily, the generalized Miles profile decreases and asymptotes to $a_2/(a_1^2 k)_G \approx 0.2$.

Finally, the non-dimensional depth kh also modulates the wind's effect on wave shape. For the chosen values of $Pk/(\rho_w g) = 1$ and $\psi_P = 3\pi/4$, the generalized Miles $\beta_G \approx -\pi/4$ while Jeffreys $\beta_J \approx +\pi/4$ for large kh (figure 2.5a). However, as kh decreases, both values grow in magnitude with β_J increasing faster, nearly reaching $\beta_J = \pi/2$ at $kh = 1$. Thus, the shallower depth kh strongly enhances the effect of wind on β. The wind's influence on $a_2/(a_1^2 k)$ is less pronounced. Notice that the unforced Stokes wave also has a depth dependence for $a_2/(a_1^2 k)$ (dashed line in figure 2.5b). Although the relative harmonic amplitude is enhanced for small kh in all three cases (Jeffreys, generalized and unforced Stokes), both pressure profiles grow slower than the unforced Stokes wave. That is, the pressure forcing appears to counteract shoaling-induced $a_2/(a_1^2 k)$ enhancement to some extent. Figure 2.5(b) also highlights the importance of restricting to $kh \geq 1$. As kh decreases, a_2 becomes large compared to a_1 and the perturbation expansion could become disordered. This figure highlights a trend where Jeffreys and generalized Miles profiles exhibit opposite responses to the wind: namely, Jeffreys yields positive β and an enhanced $a_2/(a_1^2 k)$, while generalized Miles gives a negative β and a suppressed $a_2/(a_1^2 k)$. This difference is also apparent in figure 2.4, wherein β and $a_2/(a_1^2 k)$ increase with increasing pressure magnitude for Jeffreys, while they decrease (at least initially) for the generalized Miles profile. This can be attributed to different choices of ψ_P ($\psi_P = \pi/2$ for Jeffreys, but $\psi_P = 3\pi/4$ for generalized Miles), as well as different effects on higher harmonics, including the derivative in the Jeffreys profile enhancing higher harmonics.

Both the harmonic phase and the relative harmonic amplitude determine the wave shape. We consider their combined influence by plotting the surface profile under the action of the generalized Miles pressure profile, with $\varepsilon = 0.2$ to emphasize the pressure-induced shape changes. Figure 2.6(a) shows how the surface profile η versus phase θ varies with $Pk/(\rho_w g) = 0$, 0.1 and 0.2 for wind blowing to the right. The $Pk/(\rho_w g) = 0$ profile has skewness (2.85) $S = 0.6$ and asymmetry (2.86) $A = 0$, as

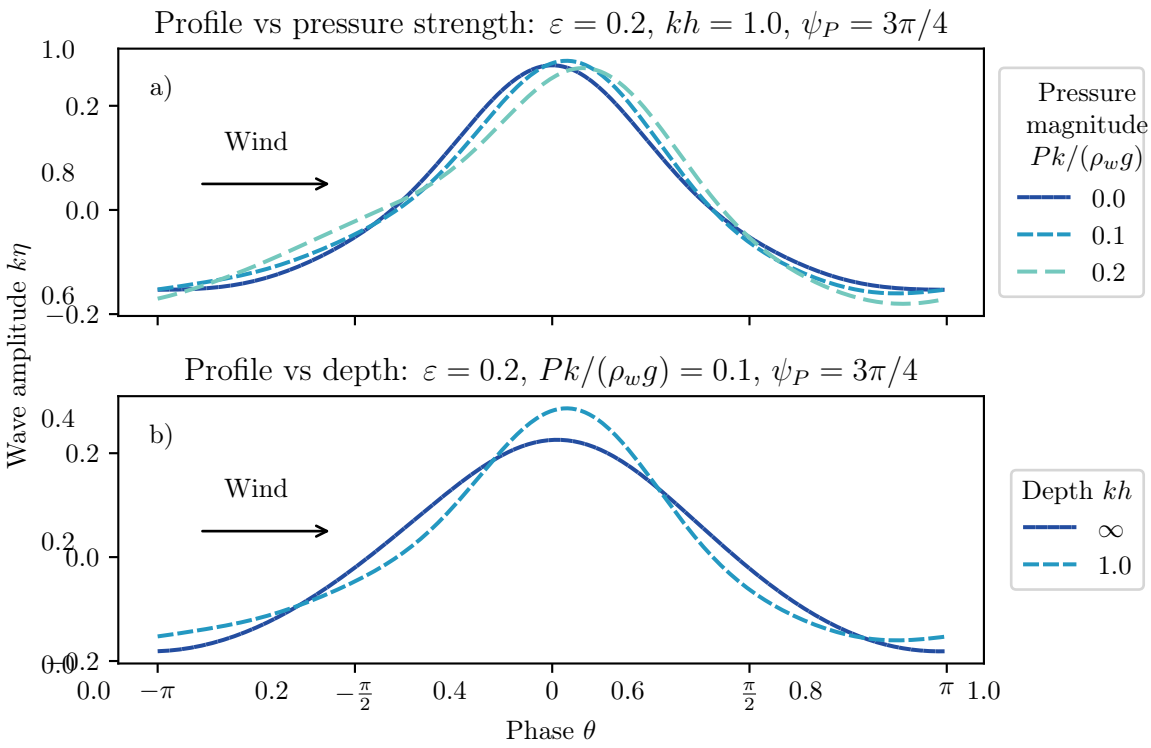

Figure 2.6. Wave profile $k\eta$ versus phase θ for $\varepsilon = 0.2$, $\psi_P = 3\pi/4$ and the generalized Miles pressure profile for (a) $kh = 1.0$ and variable $Pk/(\rho_w g)$ (see legend) and (b) $Pk/(\rho_w g) = 0.1$ and variable kh (see legend).

expected for a $kh = 1$ Stokes wave. The $Pk/(\rho_w g) = 0.1$ profile deviates only slightly from the unforced profile. However, the $Pk/(\rho_w g) = 0.2$ profile shows a noticeable horizontal asymmetry, with both skewness $S = 0.4$ and asymmetry $A = 0.3$ that are fundamentally different from a Stokes wave. This follows from figure 2.4(a) with $kh = \infty$ since $Pk/(\rho_w g) = 0.1$ generates a somewhat small $\beta_G \approx -12°$, while $\beta_G \approx -27°$ is significantly larger for $Pk/(\rho_w g) = 0.2$. Instead, (2.91) can be used when $kh = 1$ to calculate $\beta_G \approx -19°$ for $Pk/(\rho_w g) = 0.1$ and $\beta_G \approx -45°$ for $Pk/(\rho_w g) = 0.2$. Note that the larger pressure magnitudes cause the crest to shrink. This is to be expected, since the magnitude of the first harmonic $a_2/a_1^2 k$ decreases as $Pk/(\rho_w g)$ increases for the generalized Miles profile (figure 2.3b). We can also see that increasing the depth kh decreases the influence of wind on asymmetry (figure 2.6b). The $kh = \infty$ profile ($S = 0.2$, $A = 0.04$) is less asymmetric than the $kh = 1$ profile, in agreement with figure 2.5.

2.5.2 Phase speed and growth rate

In addition to influencing wave shape, the pressure-forcing terms also affect the phase speed, as predicted by Jeffreys [63] and Miles [69]. We normalize the phase speed $c = \mathrm{Re}\{\omega\}/k$ by the unforced, linear phase speed $c_0 = \sqrt{g \tanh(kh)/k}$. The complete fractional phase speed change $\Delta c/c_0$ is given in (2.171). If we consider very small waves $\varepsilon \lll 1$, then (2.171) simplifies considerably

$$\begin{aligned}\frac{\Delta c}{c_0} &= \frac{|c| - |c|\big|_{P=0}}{c_0} \\ &= \frac{1}{\sqrt{2}}\sqrt{1 + \frac{Pk}{\rho_w g}\cos(\psi_P) + \sqrt{1 + \left(\frac{Pk}{\rho_w g}\right)^2 + 2\frac{Pk}{\rho_w g}\cos(\psi_P)}} - 1 + O(\varepsilon^2),\end{aligned} \tag{2.96}$$

with $\psi_P = \pm\pi/2$ for the Jeffreys profile. If, instead of very small waves, we assume the forcing is weak, $Pk/(\rho_w g) \ll 1$, we find

$$\begin{aligned}\frac{\Delta c}{c_0} = \frac{1}{2}\frac{Pk}{\rho_w g}\cos(\psi_P) - \frac{1}{8}\left(\frac{Pk}{\rho_w g}\right)^2 \cos(2\psi_P) \\ + \frac{8\cosh^4(kh) - 8\cosh^2(kh) + 9}{16\sinh^4(kh)}\left((a_1 k)^2 - (a_1 k)^2\Big|_{P=0}\right) + O(\varepsilon^3),\end{aligned} \tag{2.97}$$

For these limiting cases, we find that both surface pressure profiles generate the same change to the phase speed. This is unsurprising since, at leading order, both pressure profiles are equivalent (if $\psi_P = \pm\pi/2$). The a_1^2 term is the amplitude dispersion due to nonlinearity described by Stokes [103].

As shown in § 2.4, the different harmonics grow at different rates. Here, we will discuss the growth rate of the primary wave. It is conventional to describe the energy growth rate, $\gamma \coloneqq \partial_t E/E$, rather than

the amplitude growth rate, $\partial_t \eta/\eta = \mathrm{Im}\{\omega\}$. However, since $E \propto \eta^2$, they are related as $\gamma = 2\,\mathrm{Im}\{\omega\}$. The complete non-dimensional growth rate γ/f_0 is given in (2.172). For very small waves, $\varepsilon \lll 1$, (2.172) simplifies to

$$\begin{aligned}\frac{\gamma}{f_0} &= \frac{4\pi\,\mathrm{Im}\{\omega\}}{c_0 k} = 2\sqrt{2}\pi\,\mathrm{sgn}\left(\frac{Pk}{\rho_w g}\sin(\psi_P)\right) \\ &\quad\times\sqrt{-1 - P\cos(\psi_P)k/(\rho_w g) + \sqrt{1 + P^2k^2/(\rho_w^2 g^2) + 2P\cos(\psi_P)k/(\rho_w g)}} + O\big(\varepsilon^2\big),\end{aligned} \tag{2.98}$$

with $f_0 = \mathrm{Re}\{\omega_0\}/(2\pi) = c_0 k/(2\pi)$ the unforced, linear wave frequency. Instead of assuming very small waves, if we consider weak wind forcing $Pk/(\rho_w g) \ll 1$, we find

$$\frac{\gamma}{f_0} = 2\pi\frac{Pk}{\rho_w g}\sin(\psi_P) - \frac{\pi}{2}\left(\frac{Pk}{\rho_w g}\right)^2\sin(2\psi_P) + O\big(\varepsilon^3\big). \tag{2.99}$$

Both Jeffreys [63]—with $\psi_P = \pi/2$—and Miles [69] calculated the growth rate to leading order for weak pressure forcing $Pk/(\rho_w g) = O(\varepsilon)$; (2.99) matches their results. Naturally, if $P \to 0$, we find $\gamma \to 0$, as there is no growth.

Notice that, for both the Jeffreys and generalized Miles profiles, the HP β and growth rate are related for very small waves ($\varepsilon \lll 1$) with weak wind ($Pk/(\rho_w g) \ll 1$) as

$$\begin{aligned}\begin{pmatrix}\beta_{0,J}\\ \beta_{0,G}\end{pmatrix} &= \frac{Pk}{\rho_w g}\begin{pmatrix}\pm 1\\ \sin(2\psi_P) - \sin(\psi_P)\end{pmatrix}\coth^2(kh) + O\left(\varepsilon\frac{Pk}{\rho_w g}\right) \\ &= \frac{1}{2\pi}\frac{\gamma}{f_0}\begin{pmatrix}1\\ (2\cos(\psi_P) - 1)\end{pmatrix}\coth^2(kh) + O\left(\varepsilon\frac{Pk}{\rho_w g}\right).\end{aligned} \tag{2.100}$$

The connection with wave asymmetry (related to β) suggests a deeper link between wave growth and wave shape. This is potentially analogous to shoaling, weakly nonlinear waves that both grow and becomes asymmetric.

2.6 Discussion

2.6.1 Time scale validity

Here, we discuss the time scale validity of our results. As asymptotic expansions must stay ordered to remain consistent, the solution's $O(\varepsilon)$ term must be larger than the $O\big(\varepsilon^2\big)$ term as $\varepsilon \to 0$. However, as

shown in (2.76) and (2.77), the $O(\varepsilon^2)$ first harmonic grows faster than the $O(\varepsilon)$ primary wave, resulting in a disordered expansion in finite time. As the first harmonic grows faster than the primary wave by a factor of $\exp(\mathrm{Im}\{\omega_0\}t)$, consistency requires that this exponent remain $O(1)$ as $\varepsilon \to 0$, i.e.

$$t\,\mathrm{Im}\{\omega_0\} = O(1). \tag{2.101}$$

Since $O(\mathrm{Im}\{\omega_0\}) = O(Pk/(\rho_w g))$, redimensionalizing shows our results are restricted to

$$\frac{t}{T_0^\infty} \leq O\left(\frac{Pk}{\rho_w g}\right)^{-1}, \tag{2.102}$$

with the characteristic, unforced, linear, deep-water wave period $T_0^\infty = 2\pi/\sqrt{gk}$. For the case considered here with $Pk/(\rho_w g) = O(1)$, this implies the solution may only be valid for a few characteristic waves periods T_0^∞. However, for weaker winds, the temporal range of validity is extended. For $Pk/(\rho_w g) = O(\varepsilon^2)$, the solution is well ordered for time intervals $O(T_0^\infty/\varepsilon^2)$, assuming the solution is calculated to $O(\varepsilon^3)$ accuracy with a frequency ω accurate to order ε^2.

The shape parameters β and $a_2/(a_1^2 k)$ change very little over time. To leading order, the primary wave (2.76) grows like $\hat{\eta}_{m=1} \propto \exp(\mathrm{Im}\{\omega_0\}t_0)$ while the first harmonic (2.77) goes as $\hat{\eta}_{m=2} \propto \exp(2\,\mathrm{Im}\{\omega_0\}t_0)$. By dividing $\hat{\eta}_{m=2}/(\hat{\eta}_1^2 k)$ in (2.78) and (2.80), our shape parameters β (2.81) and $a_2/(a_1^2 k)$ (2.82) are constant for time intervals of the length $O(T_0^\infty)$. Even the higher-order corrections (§ 2.A) for $a_2/(a_1^2 k)$ (2.163) and β (2.164) show very little temporal variation during the valid time scales where $t\,\mathrm{Im}\{\omega_0\} = O(1)$. In contrast, the skewness (2.85) and asymmetry (2.86) show a stronger time scale dependence, with $\exp(t\,\mathrm{Im}\{\omega_0\})$ appearing at leading order. Nevertheless, our restriction that $t\,\mathrm{Im}\{\omega_0\} = O(1)$ ensures that, over the solution's range of temporal validity, the skewness and asymmetry do not vary substantially.

2.6.2 Using LES to constrain the surface pressure

LES simulations of the airflow over a single, static, sinusoidal (i.e. no harmonics), deep-water wave by Husain et al. [108] [see also 90] allow estimation of the two unknown parameters: pressure magnitude $Pk/(\rho_w g)$ and wind phase ψ_P. The Husain et al. [108] simulations were based on the laboratory experiments of Buckley and Veron [124] and explored a variety of surface roughnesses kz_0, wave steepnesses ε and wind speeds u_*/c_0^∞. We consider the simulation [108] with intermediate surface roughness $kz_0 = 1.35 \times 10^{-3}$, appreciable wave slope $\varepsilon = 0.2$ and young waves $u_*/c_0^\infty = 0.71$ (figure 2.7). The non-dimensional surface

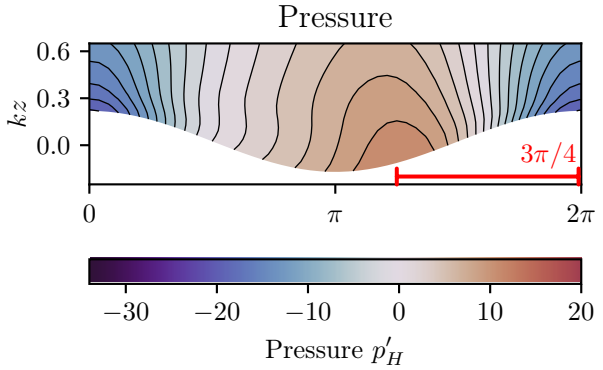

Figure 2.7. LES modelled non-dimensional, perturbation air pressure over a right-propagating linear surface gravity wave as a function of non-dimensional phase kx and height kz. This simulation has non-dimensional surface roughness $kz_0 = 1.35 \times 10^{-3}$, wave steepness $\varepsilon = 0.2$ and inverse wave age $u_*/c_0^\infty = 0.71$. The red line denotes the wind phase ψ_P, as measured from the wave crest to the high pressure location. Reproduced from figure 2b of Husain et al. [108].

perturbation pressure p'_{H} varies over a range of ± 20 with the maximum shifted $\approx 3\pi/4$ windward of the crest (red bar in figure 2.7), yielding our choice of $\psi_P \approx 3\pi/4$. The Husain et al. [108] value of $\psi_P \approx 3\pi/4$ is also qualitatively consistent with the surface pressure and wind phase reported by Donelan et al. [125].

Note that ψ_P appears to be a function of wind speed (or pressure magnitude). Donelan et al. [125], Hara and Sullivan [90] and Husain et al. [108] suggest $\psi_P \approx 3\pi/4$ for inverse wave ages $u_c/c_0 \approx 0.19$ to 0.71. In contrast, numerical simulations find $\psi_P \approx \pi$ for very small inverse wave ages $u_*/c_0 \leq 0.09$ [e.g. 87, 126]. According to figure 2.2, this corresponds to a growth rate $\gamma/f_0^\infty \leq 10^{-3} \lessapprox \varepsilon^4$ for $\varepsilon = 0.2$. Given that our analysis is limited to $Pk/(\rho_w g) = O(\varepsilon^2)$ or stronger (cf. § 2.A.6), these weak winds are outside the scope of our analysis.

In regards to the pressure magnitude, Husain et al. [108] non-dimensionalized pressure with the air density and friction velocity,

$$p'_{\mathrm{H}} = \frac{p}{\rho_a u_*^2}, \tag{2.103}$$

whereas we non-dimensionalized p' by ρ_w, g and k. Thus, converting p'_{H} to p' we find

$$p' = \frac{pk}{\rho_w g} = \frac{p}{\rho_a u_*^2} \frac{u_*^2}{(c_0^\infty)^2} \frac{\rho_a}{\rho_w} = \frac{u_*^2}{(c_0^\infty)^2} \frac{\rho_a}{\rho_w} p'_{\mathrm{H}} \approx 5.0 \times 10^{-4} p'_{\mathrm{H}}. \tag{2.104}$$

With $u_*/c_0^\infty = 0.71$ [108] and $\rho_a/\rho_w \approx 10^{-3}$, $p' \approx 10^{-2}$ and $|p'| \approx 7 \times 10^{-3}$. Using their value of $\varepsilon = 0.2$ then gives $|p|k/(\rho_w g) \approx \varepsilon^3$, or $Pk/(\rho_w g) \approx \varepsilon^2$. Interestingly, the non-dimensional pressure magnitude for this simulation is consistent with that inferred from the u_*/c_0^∞ versus γ/f_0 relationship (figure 2.2), where we see that $u_*/c_0^\infty = 0.7 \implies \gamma/f_0 = 0.1$. Using (2.20) and $\psi_P = 3\pi/4$ gives

$Pk/(\rho_w g) = \gamma/[2\pi f_0 \sin(\psi_P)] = 2 \times 10^{-2}$. That is, $Pk/(\rho_w g) \approx \varepsilon^2$. This can be compared to our results for weak wind $Pk/(\rho_w g) \ll 1$, such as (2.91) and (2.95) truncated to $\varepsilon O(Pk/(\rho_w g)) = O(\varepsilon^3)$. Thus, the results of Husain et al. [108] provide an estimate for ψ_P and a $Pk/(\rho_w g)$ consistent with our theoretical development. However, the appropriate, specific pressure profile (Jeffreys or generalized Miles) remains to be determined; cf. § 2.6.4.

2.6.3 Comparison of theory to laboratory wave-shape observations

Here, we compare our predicted harmonic phase to the laboratory experiments in Leykin et al. [100]. We cannot compare to Feddersen and Veron [101] as their $kh \leq 1.2$, and the u_*/c_0 to γ/f_0 relationship (figure 2.2) needed for determining $Pk/(\rho_w g)$ is for deep water. In Leykin et al. [100], laboratory wind-generated surface gravity waves with $\varepsilon \approx 0.15$ and $kh = 2.5$ had a quasi-linear relationship between the biphase β at the peak frequency (the statistical analogue of our harmonic phase β) and the inverse wave age u_*/c_0 (figure 2.8). For comparison, our pressure magnitude $Pk/(\rho_w g)$ must be converted to an inverse wave age u_*/c_0 (§ 2.3.4). We assume the deep-water relationship between u_*/c_0 and γ/f_0 (figure 2.2) holds for $kh = 2.5$, which is parameterized [111] as (figure 2.2, solid line)

$$\frac{\gamma}{f_0} = 32.5(2\pi)\frac{\rho_a}{\rho_w}\left(\frac{u_*}{c_0}\right)^2. \tag{2.105}$$

Using (2.20), we can relate γ/f_0 to $Pk/(\rho_w g)$ for deep water to give

$$\frac{Pk}{\rho_w g} = \frac{32.5}{\sin(\psi_P)}\frac{\rho_a}{\rho_w}\left(\frac{u_*}{c_0}\right)^2 \tag{2.106}$$

allowing comparison between theory and laboratory observations.

Using (2.106), the measured inverse wave ages $u_*/c_0 = 0.5$ to 1.5 correspond to pressure magnitudes $Pk/(\rho_w g) = 0.01$ to 0.1, or $Pk/(\rho_w g) = O(\varepsilon^2)$ to $O(\varepsilon)$. Therefore, our results for weak forcing $Pk/(\rho_w g) \ll 1$ are applicable here (cf. § 2.A.6). Assuming a generalized Miles pressure profile with $\psi_P = 3\pi/4$, the predicted and measured β are in qualitative agreement (compare red curve to symbols in figure 2.8). We emphasize that (2.106), relying on the conversion between u_*/c_0 and γ/f_0 from figure 2.2, is only approximate and is of questionable applicability for water depth $kh = 2.5$. If the conversion coefficient were a factor of 3 larger, the results would match reasonably well. We also note that the relatively high wind speeds (u_* up to $1.7\,\mathrm{m\,s^{-1}}$) likely caused additional physical processes, such as whitecapping or microbreaking, to occur. Such dissipative processes are not considered in our theoretical treatment.

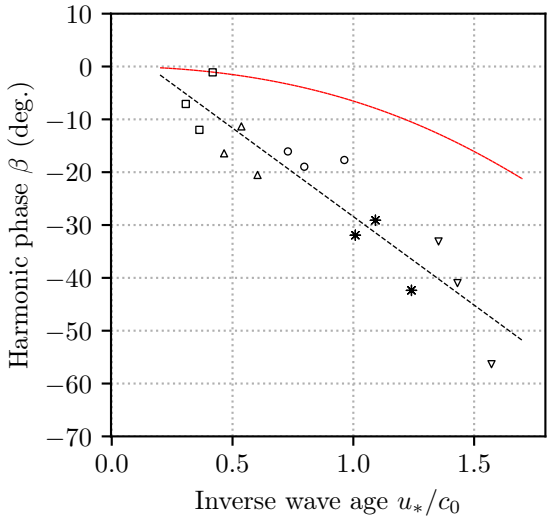

Figure 2.8. Harmonic phase β versus inverse wave age u_*/c_0 (symbols) for the Leykin et al. [100] laboratory experiments. The black, dashed line is the Leykin et al. [100] linear fit. Theoretical HP β (solid red) are given for the generalized Miles pressure profile with $\psi_P = 3\pi/4$, $kh = 2.5$ and $\varepsilon = 0.15$, and conversion of u_*/c_0 to $Pk/(\rho_w g)$ is given by (2.106) (cf. § 2.6.3).

2.6.4 The surface pressure profile

Most theoretical treatments of wind-induced wave growth utilize a linear theory with monochromatic waves [e.g. 67, 69, 127]. In this scenario, for the same ψ_P, the pressure profiles considered are identical at leading order and one need not distinguish between, for instance, the Jeffreys or generalized Miles profiles. However, when considering higher-order corrections to the higher harmonics, differences arise and care must be taken when choosing the pressure profile.

Direct measurements of the surface pressure profile are challenging and rare [125]. However, our theory can offer insight by comparing the profiles' differing effects on wave-shape parameters to simulations and measurements of wind-forced waves, which have found a non-zero β [100, 101]. Both Feddersen and Veron [101] and Leykin et al. [100] measure a harmonic phase $\beta < 0$ for co-aligned wind and waves. However, the Jeffreys profile gives a positive β while the generalized Miles profile with $\psi_P \approx 3\pi/4$ gives a negative β (figures 2.3*a*,*4a*). Additionally, the Jeffreys requirement of $\psi_P = \pm\pi/2$ appears inconsistent with numerical simulations showing $\psi_P \approx 3\pi/4$ [90, 108]. Among the profiles considered here, the generalized Miles case best reproduces the results of wave-shape experiments.

Throughout the derivation, we have maintained a rather general surface pressure profile $p(x,t)$, namely any time-independent convolution with η (i.e. $\hat{p}_m \propto \hat{\eta}_m$, cf. § 2.3.3). Coupled air–water simulations [e.g. 92, 93] offer the possibility of extracting realistic wave shapes and surface pressures, which could

then be compared to our theory. However, LES atmospheric simulations over purely sinusoidal waves yield surface pressure profiles that are not purely sinusoidal (e.g. [90, figure 7] or [108, figure 6]). Although this is counter to our assumption that $\hat{p}_m \propto \hat{\eta}_m$, it could be remedied by extending our small ε theory to allow pressures with Fourier representations $\hat{p}_m = k\hat{P}_m\hat{\eta}_m + k^2 \sum_n \hat{P}_{m,n}\hat{\eta}_n\hat{\eta}_m + \dots$. Additional surface pressure complexity is likely generated if LES atmospheric simulations used a Stokes wave profile instead of a single sinusoid. Finally, allowing the wind, via surface pressure profiles, to affect wave shape, as we have done, likely induces further changes back to the airflow and surface pressure profile. That is, the air and water phases are coupled. Although this study relied on prescribed surface pressures, it lays the groundwork for a weakly nonlinear coupled theory. Future work will attempt to couple the wind and waves directly, providing insight into the surface pressure profile and the related wave shape and growth.

2.7 Summary

Here, we derive a theory for the wind's effect on the shape of surface gravity waves. The influence of the wind on ocean waves has been studied in great detail theoretically, numerically and observationally in the context of wave growth. A few laboratory and numerical experiments have shown that wind can also influence wave shape, although no theory for this effect exists. Two key, weakly nonlinear wave-shape parameters are the harmonic phase β, encoding the relative phase between the primary wave and first harmonic (zero for unforced Stokes waves), and the relative harmonic amplitude $a_2/(a_1^2k)$. These two parameters can also be converted to the more conventional skewness and asymmetry. Motivated by prior wind–wave generation theories, two surface pressure profiles (Jeffreys and generalized Miles) based on convolutions with the wave profile η are prescribed. A multiple-scale perturbation analysis is performed for the small wave steepness $\varepsilon \coloneqq a_1k$. The deep- to intermediate-water theoretical solutions are derived for quasi-periodic progressive waves yielding the wind-induced changes to β and $a_2/(a_1^2k)$ as well as higher-order corrections to the previously known growth and phase speed changes. These parameters are functions of the four non-dimensional parameters: the wave steepness a_1k, depth kh, pressure magnitude $Pk/(\rho_w g)$ and wind phase ψ_P. By substituting the pressure magnitude P with $P \to \varepsilon P$ or $P \to \varepsilon^2 P$, our derivation permits a variety of pressure magnitudes (i.e. wind speeds).

The relative harmonic ratio $a_2/(a_1^2k)$ displays a strong dependence on the forcing type, enhanced for Jeffreys but suppressed for generalized Miles. The harmonic phase β has more complicated behaviour, including a local minimum for the generalized Miles case as a function of the pressure magnitude. Despite restricting our analysis to intermediate and deep water, we find decreasing kh enhances the wind's effect

on wave shape. This suggests pressure forcing could play a larger role in wave shape for shallow-water waves. We also find direct relationships between growth rates and β for the pressure profiles considered. Atmospheric large eddy simulations constrain both the pressure magnitude P and wind phase ψ_P. Using the constrained ψ_P, our HP predictions are qualitatively consistent with laboratory observations. Only the generalized Miles profile could reproduce the observed sign for β, suggesting that generalized Miles surface pressure profiles best represent the actual wave surface pressure profile. Future studies will investigate the shallow-water limit. Other avenues for future work include dynamically coupling the air and wave field. Such an approach would obviate the need to impose a specified pressure profile, increasing the applicability of the theory.

2.8 Acknowledgements

We are grateful to W. R. Young, N. Pizzo and A. B. Villas Bôas for discussions on this work. The computations in this paper were performed by using MAPLE™ [40]. We thank the National Science Foundation (OCE-1558695) and the Mark Walk Wolfinger Surfzone Processes Research Fund for their support of this work. The authors report no conflict of interest. Chapter 2, in full, is a reprint of the material as it appears in Wind-Induced Changes to Surface Gravity Wave Shape in Deep to Intermediate Water in Journal of Fluid Mechanics by T. Zdyrski and F. Feddersen in 2020. The dissertation author was the primary investigator and author of this paper.

2.A Strong forcing: $Pk/(\rho_w g) = O(1)$ continued

2.A.1 The $O(\varepsilon^3)$ equations

In § 2.4, we derived the leading-order contributions to the HP β and relative amplitude $a_2/(a_1^2 k)$. Now, we will extend this derivation to the next non-zero correction. This will reveal a weak amplitude and time dependence to these shape parameters. Furthermore, by finding β and $a_2/(a_1^2 k)$ accurate to $O(\varepsilon^2)$, we can substitute $P \to \varepsilon P$ yielding solutions with $Pk/(\rho_w g) = O(\varepsilon)$, or $P \to \varepsilon^2$ generating $Pk/(\rho_w g) = O(\varepsilon^2)$ results (§ 2.A.6). However, the expressions begin to become unwieldy. Therefore, we will only sketch the

derivation. The third-order equations give

$$\begin{aligned}\frac{\partial\phi_3}{\partial z}-\frac{\partial\eta_3}{\partial t_0}&=\frac{\partial A_1}{\partial t_2}\exp(\mathrm{i}(x-\omega_0 t_0))\\&\quad+A_1|A_1|^2\,\mathrm{KIN}_{3,1}\exp(\mathrm{i}(x-\omega_0 t_0))|\exp(-\mathrm{i}\omega_0 t_0)|^2+A_1^3\,\mathrm{KIN}_{3,3}\exp(3\mathrm{i}(x-\omega_0 t_0)),\end{aligned}\tag{2.107}$$

$$\begin{aligned}\frac{\partial\phi_3}{\partial t_0}+\eta_3+p_3&=\mathrm{i}\omega_0\frac{\partial A_1}{\partial t_2}\exp(\mathrm{i}(x-\omega_0 t_0))\coth(h)\\&\quad+A_1|A_1|^2\,\mathrm{DYN}_{3,1}\exp(\mathrm{i}(x-\omega_0 t_0))|\exp(-\mathrm{i}\omega_0 t_0)|^2+A_1^3\,\mathrm{DYN}_{3,3}\exp(3\mathrm{i}(x-\omega_0 t_0)),\end{aligned}\tag{2.108}$$

with the real part implied. Here, $\mathrm{KIN}_{3,1},\mathrm{KIN}_{3,3},\mathrm{DYN}_{3,1},\mathrm{DYN}_{3,3}\in\mathbb{C}$ are constants that do not depend on A_1, x, t_n or z (these dependencies have been explicitly factored out) and are composed entirely of known quantities from previous orders. In general, $\mathrm{KIN}_{n,m}$ and $\mathrm{DYN}_{n,m}$ are the constants (depending on h, ψ_P and $\hat{P}_m$ only) for the nth order, mth Fourier component (i.e., $\exp(\mathrm{i}mkx)$) term from the kinematic or dynamic boundary condition, respectively. See § 2.B for their expressions.

Once again, inserting our Fourier transforms (2.32)–(2.34), we find

$m=1$ Fourier component:

$$\hat{\phi}_{3,1}-\frac{\partial\hat{\eta}_{3,1}}{\partial t_0}=\frac{\partial A_1}{\partial t_2}\exp(-\mathrm{i}\omega_0 t_0)+A_1|A_1|^2\,\mathrm{KIN}_{3,1}\exp(-\mathrm{i}\omega_0 t_0)|\exp(-\mathrm{i}\omega_0 t_0)|^2,\tag{2.109}$$

$$\begin{aligned}\coth(h)\frac{\partial\hat{\phi}_{3,1}}{\partial t_0}+(1+\hat{P}_1)\hat{\eta}_{3,1}&=\mathrm{i}\omega_0\frac{\partial A_1}{\partial t_2}\exp(-\mathrm{i}\omega_0 t_0)\coth(h)\\&\quad+A_1|A_1|^2\,\mathrm{DYN}_{3,1}\exp(-\mathrm{i}\omega_0 t_0)|\exp(-\mathrm{i}\omega_0 t_0)|^2,\end{aligned}\tag{2.110}$$

$m=3$ Fourier component:

$$3\hat{\phi}_{3,3}-\frac{\partial\hat{\eta}_{3,3}}{\partial t_0}=A_1^3\,\mathrm{KIN}_{3,3}\exp(-3\mathrm{i}\omega_0 t_0),\tag{2.111}$$

$$\coth(3h)\frac{\partial\hat{\phi}_{3,3}}{\partial t_0}+(1+\hat{P}_3)\hat{\eta}_{3,3}=A_1^3\,\mathrm{DYN}_{3,3}\exp(-3\mathrm{i}\omega_0 t_0).\tag{2.112}$$

Eliminating $\hat{\phi}_{3,m}$ gives

$m=1$ Fourier component:

$$\begin{aligned}\coth(h)\frac{\partial^2\hat{\eta}_{3,1}}{\partial t_0^2}+(1+\hat{P}_1)\hat{\eta}_{3,1}&=-\left(-\mathrm{i}\omega_0+\frac{\partial}{\partial t_0}\right)\frac{\partial A_1}{\partial t_2}\exp(-\mathrm{i}\omega_0 t_0)\coth(h)\\&\quad+A_1|A_1|^2[(\mathrm{i}\omega_0-2\,\mathrm{Im}\{\omega_0\})\coth(h)\,\mathrm{KIN}_{3,1}+\mathrm{DYN}_{3,1}]\exp(-\mathrm{i}\omega_0 t_0)|\exp(-\mathrm{i}\omega_0 t_0)|^2,\end{aligned}\tag{2.113}$$

$m=3$ Fourier component:

$$\coth(3h)\frac{\partial^2\hat{\eta}_{3,3}}{\partial t_0^2}+3(1+\hat{P}_3)\hat{\eta}_{3,3}=3A_1^3[\mathrm{i}\omega_0\coth(3h)\,\mathrm{KIN}_{3,3}+\mathrm{DYN}_{3,3}]\exp(-3\mathrm{i}\omega_0 t_0).\tag{2.114}$$

Notice that we did not evaluate the $\partial/\partial t_0$ derivative in the $(\partial/\partial t_0 - \mathrm{i}\omega_0)$ of (2.113). We will discuss this momentarily.

Preventing secular terms requires that coefficients of $\exp(-\mathrm{i}\omega_0 t_0)$ for $m = 1$ vanish. Thus, we require

$$\begin{aligned}\coth(h)&\left(-\mathrm{i}\omega_0 + \frac{\partial}{\partial t_0}\right)\frac{\partial A_1}{\partial t_2}\exp(-\mathrm{i}\omega_0 t_0) \\ &= A_1|A_1|^2\exp(-\mathrm{i}\omega_0 t_0)\exp(2\,\mathrm{Im}\{\omega_0\}t_0)[(\mathrm{i}\omega_0 - 2\,\mathrm{Im}\{\omega_0\})\coth(h)\,\mathrm{KIN}_{3,1} + \mathrm{DYN}_{3,1}].\end{aligned} \tag{2.115}$$

Here, we encounter an issue: given that $A_1(t_2, t_3, \ldots)$ is explicitly not a function of t_0, there is no (non-trivial) way to satisfy the t_0 dependence of this compatibility condition.

We encounter this issue because the growth on the fast time scale affects the period of the slower time scales. This could be dealt with formally if we had allowed the fast time scale t_0 to modulate the slower time scales by defining our multiple-scale expansion with additional, fast time scale dependencies

$$\frac{\mathrm{d}t_0'}{\mathrm{d}t} = 1, .\frac{\mathrm{d}t_1'}{\mathrm{d}t} = \varepsilon\mu_1(t_0'), .\frac{\mathrm{d}t_2'}{\mathrm{d}t} = \varepsilon^2\mu_2(t_0'), \ldots, .\frac{\mathrm{d}t_n'}{\mathrm{d}t} = \varepsilon^n\mu_n(t_0'), \tag{2.116}$$

with the primes to make our new time scales distinct from the originally defined ones. Then, we can choose the form of μ_n to remove secular terms. This modified multiple-scale approach is similar to the one specified in Pedersen [128].

Using this freedom to remove these problematic secularities, we would find that

$$\mu_n(t_0') = \exp(n\,\mathrm{Im}\{\omega_0\}t_0'). \tag{2.117}$$

This method would eliminate the need to be careful about the $(\partial/\partial t_0' - \mathrm{i}\omega_0)\,\partial A_1/\partial t_2'$ term previously mentioned, and would eliminate the $\exp(2\,\mathrm{Im}\{\omega_0\}t_0')$ term we are attempting to deal with currently. Later, to re-express the solution in terms of t, a simple integration yields

$$t_n' = \frac{\varepsilon^n}{n\,\mathrm{Im}\{\omega_0\}}(\exp(n\,\mathrm{Im}\{\omega_0\}t) - 1). \tag{2.118}$$

where we required that $t_n' = 0$ at $t = 0$. Note that t_0' is not a special case; treating n as a continuous variable and taking the limit $n \to 0$ recovers $t_0' = t$.

Note that, since our previous solutions had no t_1 dependence, making this change to t_2 does not alter any of our previous conclusions. Furthermore, we will see that only the even time scales (t_2, t_4, etc)

need this treatment. Since we are only considering time scales up to t_3, we will only make this replacement for t_2.

Making this redefinition, our compatibility conditions becomes

$$\begin{aligned}\coth(h)\left(-\mathrm{i}\omega_0+\frac{\partial}{\partial t_0}\right)\frac{\partial A_1}{\partial t_2'}\exp(-\mathrm{i}\omega_0 t_0)\exp(2\,\mathrm{Im}\{\omega_0\}t_0)\\ =A_1|A_1|^2\exp(-\mathrm{i}\omega_0 t_0)\exp(2\,\mathrm{Im}\{\omega_0\}t_0)[(\mathrm{i}\omega_0-2\,\mathrm{Im}\{\omega_0\})\coth(h)\,\mathrm{KIN}_{3,1}+\mathrm{DYN}_{3,1}],\end{aligned} \tag{2.119}$$

which simplifies to

$$\begin{aligned}\frac{\partial A_1}{\partial t_2'}&=A_1|A_1|^2\frac{(\mathrm{i}\omega_0-2\,\mathrm{Im}\{\omega_0\})\,\mathrm{KIN}_{3,1}+\tanh(h)\,\mathrm{DYN}_{3,1}}{-2\mathrm{i}\omega_0+2\,\mathrm{Im}\{\omega_0\}}\\ &\coloneqq -\mathrm{i}A_1|A_1|^2\,\mathrm{COMB}_{3,1},\end{aligned} \tag{2.120}$$

where we defined

$$\mathrm{COMB}_{3,1}\coloneqq \mathrm{i}\frac{(\mathrm{i}\omega_0-2\,\mathrm{Im}\{\omega_0\})\,\mathrm{KIN}_{3,1}+\tanh(h)\,\mathrm{DYN}_{3,1}}{-2\mathrm{i}\omega_0+2\,\mathrm{Im}\{\omega_0\}}. \tag{2.121}$$

Now, if we assume a solution of the form

$$A_1(t_2')=\rho(t_2')\exp(\mathrm{i}\psi(t_2')), \tag{2.122}$$

with $\rho(t_2'),\psi(t_2')\in\mathbb{R}$, (2.121) yields

$$\frac{\partial\rho}{\partial t_2'}+\mathrm{i}\rho\frac{\partial\psi}{\partial t_2'}=-\mathrm{i}\rho^3\,\mathrm{COMB}_{3,1}\,. \tag{2.123}$$

Collecting real and imaginary parts and solving yields

$$\begin{aligned}A_1(t_2')=A_1'\exp\left[\mathrm{i}\frac{1}{2}\ln\left(1-2|A_1'|^2t_2'\,\mathrm{Im}\{\mathrm{COMB}_{3,1}\}\right)\frac{\mathrm{Re}\{\mathrm{COMB}_{3,1}\}}{\mathrm{Im}\{\mathrm{COMB}_{3,1}\}}\right]\\ \div\sqrt{1-2|A_1'|^2t_2'\,\mathrm{Im}\{\mathrm{COMB}_{3,1}\}},\end{aligned} \tag{2.124}$$

with $A_1'(t_3)\in\mathbb{C}$. Later, converting back to t will give

$$\begin{aligned}A_1(t)=A_1'\exp\left\{\frac{\mathrm{i}}{2}\ln\left[1-\varepsilon^2|A_1'|^2(\exp(2\,\mathrm{Im}\{\omega_0\}t)-1)\frac{\mathrm{Im}\{\mathrm{COMB}_{3,1}\}}{\mathrm{Im}\{\omega_0\}}\right]\frac{\mathrm{Re}\{\mathrm{COMB}_{3,1}\}}{\mathrm{Im}\{\mathrm{COMB}_{3,1}\}}\right\}\\ \div\sqrt{1-\varepsilon^2|A_1'|^2\big(\exp(2\,\mathrm{Im}\{\omega_0\}t)-1\big)\frac{\mathrm{Im}\{\mathrm{COMB}_{3,1}\}}{\mathrm{Im}\{\omega_0\}}}.\end{aligned} \tag{2.125}$$

Note that if $p \to 0$, then $\mathrm{COMB}_{3,1}$ reduces to the real quantity

$$\mathrm{COMB}_{3,1}\Big|_{p=0} = \omega_0 \frac{8\cosh^4(h) - 8\cosh^2(8) + 9}{16\sinh^4(h)}. \tag{2.126}$$

With the compatibility condition solved, the $m = 1$ equation reduces to the homogeneous equation. For simplicity, we will choose $\hat{\eta}_{3,1} = 0$.

Substituting (2.120) and our solution for $\hat{\eta}_{3,1}$ into the surface boundary conditions allows us to solve for $\hat{\phi}_{3,1}$. Assuming a solution of the form

$$\hat{\phi}_{3,1} = C_{3,1} A_1 |A_1|^2 \exp(-\mathrm{i}\omega_0 t_0) \exp(2\,\mathrm{Im}\{\omega_0\} t_0), \tag{2.127}$$

yields

$$C_{3,1} = \frac{-\mathrm{i}\omega_0\,\mathrm{KIN}_{3,1} + \tanh(h)\,\mathrm{DYN}_{3,1}}{-2\mathrm{i}\omega_0 + 2\,\mathrm{Im}\{\omega_0\}}. \tag{2.128}$$

The second harmonic ($m = 3$) equation is solved for $\hat{\eta}_{3,3}$ as usual. Then, substituting this solution into the surface boundary conditions permits solving for $\hat{\phi}_{3,3}$.

Thus, we have the solutions

$$\begin{aligned} \phi_3 = {} & C_{3,1} A_1 |A_1|^2 \exp(2\,\mathrm{Im}\{\omega_0\} t_0) \exp(\mathrm{i}(x - \omega_0 t_0)) \frac{\cosh(z+h)}{\sinh(h)} \\ & + C'_{3,3} A_1^3 \exp(3\mathrm{i}(x - \omega_0 t_0)) \frac{\cosh[3(z+h)]}{\sinh(3h)}, \end{aligned} \tag{2.129}$$

$$\eta_3 = C_{3,3} A_1^3 \exp(3\mathrm{i}(x - \omega_0 t_0)), \tag{2.130}$$

with

$$C_{3,1} = \frac{-\mathrm{i}\omega_0\,\mathrm{KIN}_{3,1} + \tanh(h)\,\mathrm{DYN}_{3,1}}{-2\mathrm{i}\omega_0 + 2\,\mathrm{Im}\{\omega_0\}}, \tag{2.131}$$

$$C'_{3,3} = \frac{\left(1 + \hat{P}_3\right)\mathrm{KIN}_{3,3} - 3\mathrm{i}\omega_0\,\mathrm{DYN}_{3,3}}{-9\omega_0^2 \coth(3h) + 3\left(1 + \hat{P}_3\right)}, \tag{2.132}$$

$$C_{3,3} = 3\frac{\mathrm{i}\omega_0 \coth(3h)\,\mathrm{KIN}_{3,3} + \mathrm{DYN}_{3,3}}{-9\omega_0^2 \coth(3h) + 3\left(1 + \hat{P}_3\right)}. \tag{2.133}$$

With no correction to the first harmonic $\hat{\eta}_{m=2}$, we continue to the next order.

2.A.2 The $O(\varepsilon^4)$ equations

Finally, going to fourth order, we have

$$\begin{aligned}\frac{\partial \phi_4}{\partial z} - \frac{\partial \eta_4}{\partial t_0} &= \frac{\partial A_1}{\partial t_3}\exp(\mathrm{i}(x-\omega_0 t_0)) \\ &\quad + \mathrm{KIN}_{4,0}\,|A_1\exp(-\mathrm{i}\omega_0 t_0)|^4 + \mathrm{KIN}_{4,2}\,A_1^2\exp(2\mathrm{i}(x-\omega_0 t_0))|A_1\exp(-\mathrm{i}\omega_0 t_0)|^2 \\ &\quad + \mathrm{KIN}_{4,4}\,A_1^4\exp(4\mathrm{i}(x-\omega_0 t_0)),\end{aligned} \tag{2.134}$$

$$\begin{aligned}\frac{\partial \phi_4}{\partial t_0} + \eta_4 + p_4 &= \mathrm{i}\omega_0\frac{\partial A_1}{\partial t_3}\exp(\mathrm{i}(x-\omega_0 t_0))\coth(h) \\ &\quad + \mathrm{DYN}_{4,0}\,|A_1\exp(-\mathrm{i}\omega_0 t_0)|^4 + \mathrm{DYN}_{4,2}\,A_1^2\exp(2\mathrm{i}(x-\omega_0 t_0))|A_1\exp(-\mathrm{i}\omega_0 t_0)|^2 \\ &\quad + \mathrm{DYN}_{4,4}\,A_1^4\exp(4\mathrm{i}(x-\omega_0 t_0))\end{aligned} \tag{2.135}$$

Here, $\mathrm{KIN}_{4,0}, \mathrm{KIN}_{4,2}, \mathrm{KIN}_{4,4}, \mathrm{DYN}_{4,0}, \mathrm{DYN}_{4,2}, \mathrm{DYN}_{4,4} \in \mathbb{C}$ are constants that do not depend on A_1, x, t_n or z (these dependencies have been explicitly factored out) and are composed entirely of known quantities from previous orders. See § 2.C for their expressions.

Inserting the Fourier transforms (2.32)–(2.34) gives

$m = 2$ Fourier component:

$$2\hat{\phi}_{4,2} - \frac{\partial \hat{\eta}_{4,2}}{\partial t_0} = A_1^2|A_1|^2\,\mathrm{KIN}_{4,2}\exp(2\mathrm{i}(x-\omega_0 t_0))|\exp(-\mathrm{i}\omega_0 t_0)|^2, \tag{2.136}$$

$$\frac{\partial \hat{\phi}_{4,2}}{\partial t_0}\coth(2h) + (1+\hat{P}_2)\hat{\eta}_{4,2} = A_1^2|A_1|^2\,\mathrm{DYN}_{4,2}\exp(2\mathrm{i}(x-\omega_0 t_0))|\exp(-\mathrm{i}\omega_0 t_0)|^2, \tag{2.137}$$

$m = 4$ Fourier component:

$$4\hat{\phi}_{4,4} - \frac{\partial \hat{\eta}_{4,4}}{\partial t_0} = A_1^4\,\mathrm{KIN}_{4,4}\exp(4\mathrm{i}(x-\omega_0 t_0)), \tag{2.138}$$

$$\frac{\partial \hat{\phi}_{4,4}}{\partial t_0}\coth(4h) + (1+\hat{P}_4)\hat{\eta}_{4,4} = A_1^4\,\mathrm{DYN}_{4,4}\exp(4\mathrm{i}(x-\omega_0 t_0)), \tag{2.139}$$

$m = 0$ Fourier component:

$$-\frac{\partial \hat{\eta}_{4,0}}{\partial t_0} = |A_1|^4\,\mathrm{KIN}_{4,0}\,|\exp(-\mathrm{i}\omega_0 t_0)|^4, \tag{2.140}$$

$$\frac{\partial \hat{\phi}_{4,0}}{\partial t_0} + \hat{\eta}_{4,0} = |A_1|^4\,\mathrm{DYN}_{4,0}\,|\exp(-\mathrm{i}\omega_0 t_0)|^4, \tag{2.141}$$

$m = 1$ Fourier component:

$$\hat{\phi}_{4,1} - \frac{\partial \hat{\eta}_{4,1}}{\partial t_0} = \frac{\partial A_1}{\partial t_3}\exp(-\mathrm{i}\omega_0 t_0), \tag{2.142}$$

$$\frac{\partial \hat{\phi}_{4,1}}{\partial t_0}\coth(h) + (1+\hat{P}_1)\hat{\eta}_{4,1} = \mathrm{i}\omega_0\frac{\partial A_1}{\partial t_3}\exp(-\mathrm{i}\omega_0 t_0)\coth(h). \tag{2.143}$$

Again, eliminating $\hat{\eta}_4$ gives

$m = 2$ Fourier component:

$$\frac{\partial^2 \hat{\phi}_{4,2}}{\partial t_0^2} \coth(2h) + 2(1 + \hat{P}_2)\hat{\phi}_{4,2} = A_1^2 |A_1|^2 \exp(-2\mathrm{i}\omega_0 t_0) \exp(2\,\mathrm{Im}\{\omega_0\} t_0) \times \Big[(1 + \hat{P}_2)\,\mathrm{KIN}_{4,2} + 2(-\mathrm{i}\omega_0 + \mathrm{Im}\{\omega_0\})\,\mathrm{DYN}_{4,2}\Big]. \tag{2.144}$$

$m = 4$ Fourier component:

$$\frac{\partial^2 \hat{\phi}_{4,4}}{\partial t_0^2} \coth(4h) + 4(1 + \hat{P}_4)\hat{\phi}_{4,4} = A_1^4 \exp(-4\mathrm{i}\omega_0 t_0)\Big[(1 + \hat{P}_4)\,\mathrm{KIN}_{4,4} - 4\mathrm{i}\omega_0\,\mathrm{DYN}_{4,4}\Big]. \tag{2.145}$$

$m = 0$ Fourier component:

$$\frac{\partial^2 \hat{\phi}_{4,0}}{\partial t_0^2} = |A_1|^4 \exp(4\,\mathrm{Im}\{\omega_0\} t_0)[\mathrm{KIN}_{4,0} + 4\,\mathrm{Im}\{\omega_0\}\,\mathrm{DYN}_{4,0}]. \tag{2.146}$$

$m = 1$ Fourier component:

$$\frac{\partial^2 \hat{\phi}_{4,1}}{\partial t_0^2} \coth(h) + (1 + \hat{P}_1)\hat{\phi}_{4,1} = 2\Big(1 + \hat{P}_1\Big) \frac{\partial A_1}{\partial t_3} \exp(-\mathrm{i}\omega_0 t_0). \tag{2.147}$$

Preventing secular terms requires that $\partial_{t_3} A_1 = 0$. These can be solved as usual for $\hat{\phi}_{4,m}$. Using the surface boundary conditions, the solutions for $\hat{\eta}_{4,m}$ can then be determined as well.

The only terms worth discussing are the zero modes, $\hat{\phi}_{4,0}$ and $\hat{\eta}_{4,0}$. While $\hat{\eta}_{4,0}$ has physical meaning (this is a component of the setup or setdown), $\hat{\phi}_{4,0}$ has a gauge freedom. We may add a constant term (in x, z and t_0), as well as a term proportional to t_0, without affecting any observables. Using this freedom, we will choose these two free constants such that the $\hat{\eta}_{4,0} \to 0$ and $\hat{\phi}_{4,0} \to 0$ as $P \to 0$.

The solutions at this order are

$$\begin{aligned}\phi_4 = {} & C'_{4,2} A_1^2 |A_1|^2 \exp(2\mathrm{i}(x - \omega_0 t_0)) \exp(2\,\mathrm{Im}\{\omega_0\} t_0) \frac{\cosh[2(z+h)]}{\sinh(2h)} \\ & + C'_{4,4} A_1^4 \exp(4\mathrm{i}(x - \omega_0 t_0)) \frac{\cosh[4(z+h)]}{\sinh(4h)} \\ & + C'_{4,0}\left(|A_1|^4 \exp(4\,\mathrm{Im}\{\omega_0\} t_0) - \left|\tilde{A}_1\right|^4\right) + t_0 C_{4,0} \left|\tilde{A}_1\right|^4,\end{aligned} \tag{2.148}$$

$$\begin{aligned}\eta_4 = {} & C_{4,2} A_1^2 |A_1|^2 \exp(2\mathrm{i}(x - \omega_0 t_0)) \exp(2\,\mathrm{Im}\{\omega_0\} t_0) + C_{4,4} A_1^4 \exp(4\mathrm{i}(x - \omega_0 t_0)) \\ & + C_{4,0}\left(|A_1|^4 \exp(4\,\mathrm{Im}\{\omega_0\} t_0) - \left|\tilde{A}_1\right|^4\right),\end{aligned} \tag{2.149}$$

with

$$C_{4,0} = -\frac{\mathrm{KIN}_{4,0}}{4\,\mathrm{Im}\{\omega_0\}} = 0, \tag{2.150}$$

$$C_{4,2} = \frac{(\mathrm{i}\omega_0 - \mathrm{Im}\{\omega_0\})\coth(2h)\,\mathrm{KIN}_{4,2} + \mathrm{DYN}_{4,2}}{2(-\mathrm{i}\omega_0 + \mathrm{Im}\{\omega_0\})^2\coth(2h) + \left(1+\hat{P}_2\right)}, \tag{2.151}$$

$$C_{4,4} = \frac{\mathrm{i}\omega_0\coth(4h)\,\mathrm{KIN}_{4,4} + \mathrm{DYN}_{4,4}}{-4\omega_0^2\coth(4h) + \left(1+\hat{P}_4\right)}, \tag{2.152}$$

$$C'_{4,0} = \frac{\mathrm{KIN}_{4,0} + 4\,\mathrm{Im}\{\omega_0\}\,\mathrm{DYN}_{4,0}}{16\,\mathrm{Im}\{\omega_0\}^2}, \tag{2.153}$$

$$C'_{4,2} = \frac{\left(1+\hat{P}_2\right)\mathrm{KIN}_{4,2} + 2(-\mathrm{i}\omega_0 + \mathrm{Im}\{\omega_0\})\,\mathrm{DYN}_{4,2}}{4(-\mathrm{i}\omega_0 + \mathrm{Im}\{\omega_0\})^2\coth(2h) + 2\left(1+\hat{P}_2\right)}, \tag{2.154}$$

$$C'_{4,4} = \frac{\left(1+\hat{P}_4\right)\mathrm{KIN}_{4,4} - 4\mathrm{i}\omega_0\,\mathrm{DYN}_{4,4}}{-16\omega_0^2\coth(4h) + 4\left(1+\hat{P}_4\right)}. \tag{2.155}$$

Here, $\tilde{A}_1 \coloneqq A_1\big|_{P=0}$ is the additive 'constant' we were permitted from the $m=0$ equation; note that $\tilde{A}_1$ could still be a function of slower time scales t_1, t'_2, etc. As mentioned previously, a term, linear in t_0, was included in $\hat{\phi}_{4,0}$. This was necessary in order to include the $\tilde{A}_1$ term in $\hat{\eta}_{4,0}$, ensuring that the $C_{4,0}$ setdown term vanishes as $t \to 0$, as required by our choice of $z=0$ datum at the initial mean water level. In addition, note that $\mathrm{KIN}_{4,0} = 0$ (cf. § 2.C) implies the setdown term $C_{4,0}$ is identically zero for all times. For reference, the full solution for η is

$$\begin{aligned}\eta = \mathrm{Re}\Big\{&\varepsilon A_1\exp(\mathrm{i}(x-\omega_0 t_0)) + \varepsilon^2 A_1^2 C_{2,2}\exp(2\mathrm{i}(x-\omega_0 t_0)) + \varepsilon^3 A_1^3 C_{3,3}\exp(3\mathrm{i}(x-\omega_0 t_0))\\ &+ \varepsilon^4\Big(A_1^4 C_{4,4}\exp(4\mathrm{i}(x-\omega_0 t_0)) + A_1^2|A_1|^2\exp(2\,\mathrm{Im}\{\omega_0\}t_0)\exp(2\mathrm{i}(x-\omega_0 t_0))\Big)\Big\}\\ &+ O\big(\varepsilon^5\big),\end{aligned} \tag{2.156}$$

with $A_1(t_2)$ given by (2.124). At this order, we have a correction to the first harmonic $\hat{\eta}_{m=2}$, which will modify our shape parameters.

2.A.3 Shape parameters

Now, we can calculate the shape parameters when pressure enters at leading order. Recall that we are seeking two parameters—the HP β, and the relative harmonic amplitude, $a_2/(a_1^2 k)$ (with a_2 the amplitude of the complete first harmonic, and a_1 the amplitude of the complete primary wave).

The primary wave is simply

$$\eta_{m=1} = \varepsilon A_1 \exp(\mathrm{i}(x - \omega_0 t_0)) + O\big(\varepsilon^5\big), \tag{2.157}$$

with $A_1(t_2')$ given by (2.124).

The first harmonic has two components. We calculated the $O\big(\varepsilon^2\big)$ contribution in (2.73), and the $O\big(\varepsilon^4\big)$ contribution in (2.149). Combining these, we have the first harmonic

$$\begin{aligned}\eta_{m=2} = \varepsilon^2 A_1^2 \exp(2\mathrm{i}(x - \omega_0 t_0)) C_{2,2} + \varepsilon^4 A_1^2 |A_1|^2 \exp(2\mathrm{i}(x - \omega_0 t_0)) \exp(2\,\mathrm{Im}\{\omega_0\} t_0) C_{4,2} \\ + O\big(\varepsilon^5\big)\end{aligned} \tag{2.158}$$

with $C_{2,2}$ defined in (2.75) as

$$C_{2,2} \coloneqq \frac{1}{4}\big(2 + 3\,\mathrm{csch}^2(h)\big)\coth(h)\frac{1 + \hat{P}_1}{1 + \hat{P}_1 - \coth^2(h)\Big[\hat{P}_2 - \hat{P}_1\Big]}, \tag{2.159}$$

and $C_{4,2}$ defined in (2.151) as

$$C_{4,2} = \frac{(\mathrm{i}\omega_0 - \mathrm{Im}\{\omega_0\})\coth(2h)\,\mathrm{KIN}_{4,2} + \mathrm{DYN}_{4,2}}{2(-\mathrm{i}\omega_0 + \mathrm{Im}\{\omega_0\})^2 \coth(2h) + \Big(1 + \hat{P}_2\Big)}. \tag{2.160}$$

See § 2.D for the full expression. Note that if $p \to 0$, then $C_{4,2}$ reduces to the real quantity

$$\begin{aligned}C_{4,2}\Big|_{p=0} \coloneqq \mathcal{A} = \frac{\tanh(h)}{384}\big(272 + 856\,\mathrm{csch}^2(h) + 512\,\mathrm{csch}^4(h) \\ - 558\,\mathrm{csch}^6(h) - 567\,\mathrm{csch}^8(h) - 81\,\mathrm{csch}^{10}(h)\big).\end{aligned} \tag{2.161}$$

To find the relative harmonic amplitude and HP, we will need to calculate the ratio of the first harmonic, $\hat{\eta}_{m=2}$, to the primary wave, $\hat{\eta}_{m=1}$, squared (cf. (2.78) and (2.80)):

$$\frac{\hat{\eta}_{m=2}}{\hat{\eta}_{m=1}^2} = C_{2,2} + \varepsilon^2 |A_1|^2 \exp(2\,\mathrm{Im}\{\omega_0\} t_0) C_{4,2} + O\big(\varepsilon^3\big). \tag{2.162}$$

Now, the relative harmonic amplitude (2.78), $a_2/(a_1^2 k)$, is the magnitude of this quantity,

$$\begin{aligned}\frac{a_2}{a_1^2 k} &= \left| C_{2,2} + \varepsilon^2 |A_1|^2 \exp(2\,\mathrm{Im}\{\omega_0\} t_0) C_{4,2} \right| + O\big(\varepsilon^3\big) \\ &= |C_{2,2}| \left(1 + \varepsilon^2 |A_1|^2 \exp(2\,\mathrm{Im}\{\omega_0\} t_0) \frac{\mathrm{Re}\big\{C_{4,2} C_{2,2}^*\big\}}{|C_{2,2}|^2} \right) + O\big(\varepsilon^3\big),\end{aligned} \tag{2.163}$$

with an asterisk representing the complex conjugate. We can see that the $O\big(\varepsilon^2\big)$ correction grows as a function of the fast time scale, t_0, as well as the slow time scale, t_2' (through its $A_1(t_2)$ dependence).

Likewise, the HP β is the complex angle (2.80) of (2.162)

$$\begin{aligned}\beta &\coloneqq \tan^{-1} \left(\frac{\mathrm{Im}\Big\{ C_{2,2} + \varepsilon^2 |A_1|^2 \exp(2\,\mathrm{Im}\{\omega_0\} t_0) C_{4,2} \Big\}}{\mathrm{Re}\Big\{ C_{2,2} + \varepsilon^2 |A_1|^2 \exp(2\,\mathrm{Im}\{\omega_0\} t_0) C_{4,2} \Big\}} \right) + O\big(\varepsilon^3\big) \\ &\approx \beta_0 + \varepsilon^2 |A_1|^2 \exp(2\,\mathrm{Im}\{\omega_0\} t_0) \frac{\mathrm{Re}\{C_{2,2}\}\,\mathrm{Im}\{C_{4,2}\} - \mathrm{Im}\{C_{2,2}\}\,\mathrm{Re}\{C_{4,2}\}}{\mathrm{Re}\{C_{2,2}\}^2 + \mathrm{Im}\{C_{2,2}\}^2} + O\big(\varepsilon^3\big),\end{aligned} \tag{2.164}$$

with β_0 given in (2.81) by

$$\beta_0 = \tan^{-1} \left(\frac{\mathrm{Im}\Big\{ \Big[\hat{P}_2 - \hat{P}_1 \Big] \Big(1 + \hat{P}_1^* \Big) \Big\}}{\Big| 1 + \hat{P}_1 \Big|^2 \tanh^2(h) - \mathrm{Re}\Big\{ \Big[\hat{P}_2 - \hat{P}_1 \Big] \Big(1 + \hat{P}_1^* \Big) \Big\}} \right). \tag{2.165}$$

Notice that β also has a weak time dependence appearing at $O\big(\varepsilon^2\big)$. Additionally, both β and $a_2/(a_1^2 k)$ display a weak amplitude, $\varepsilon|A_1|$, dependence. Finally, as given in (2.83) and (2.84), the skewness S and asymmetry A of a wave are defined as

$$\mathrm{S} \coloneqq \frac{\langle \eta^3 \rangle}{\langle \eta^2 \rangle^{3/2}}, \tag{2.166}$$

$$\mathrm{A} \coloneqq \frac{\langle \mathcal{H}\{\eta\}^3 \rangle}{\langle \eta^2 \rangle^{3/2}}, \tag{2.167}$$

with $\langle \cdot \rangle$ the spatial average over one wavelength and $\mathcal{H}\{\cdot\}$ the Hilbert transform (in x). In § 2.4, we only calculated the $O(\varepsilon)$ contribution for brevity. Using the full solution (2.156) for η would yield a solution accurate up to and including $O\big(\varepsilon^3\big)$ terms.

2.A.4 Complex frequency

After deriving our solutions (2.157) and (2.158), it is useful to repackage them in a more conventional notation. Therefore, we will gather the entire time dependence into a complex phase $\Theta \in \mathbb{C}$, from which

we can extract a complex, time dependent frequency $\omega(t) \in \mathbb{C}$ giving both propagation and growth. From (2.125), we can write the entire t-dependence of $A_1(t)$ as a complex phase

$$A_1(t) = A_1' \exp\Bigg\{ \mathrm{i}\frac{1}{2}\frac{\mathrm{COMB}_{3,1}}{\mathrm{Im}\{\mathrm{COMB}_{3,1}\}} \ln\Big[1 - \varepsilon^2 |A_1'|^2 (\exp(2\,\mathrm{Im}\{\omega_0\}t) - 1) \times \frac{\mathrm{Im}\{\mathrm{COMB}_{3,1}\}}{\mathrm{Im}\{\omega_0\}}\Big]\Bigg\} + O(\varepsilon^4). \tag{2.168}$$

Therefore, the entire complex phase Θ of the first harmonic $\eta_{m=1} = A_1' \exp(\mathrm{i}\Theta)$ is

$$\Theta \coloneqq kx - \omega_0 t + \mathrm{i}\frac{1}{2}\frac{\mathrm{COMB}_{3,1}}{\mathrm{Im}\{\mathrm{COMB}_{3,1}\}} \ln\Big[1 - \varepsilon^2 |A_1'|^2 (\exp(2\,\mathrm{Im}\{\omega_0\}t) - 1) \times \frac{\mathrm{Im}\{\mathrm{COMB}_{3,1}\}}{\mathrm{Im}\{\omega_0\}}\Big] + O(\varepsilon^4). \tag{2.169}$$

Now, we define the full, complex frequency as

$$\omega \coloneqq -\frac{\partial \Theta}{\partial t} = \omega_0 + \varepsilon^2 |A_1'|^2 \exp(2\,\mathrm{Im}\{\omega_0\}t)\,\mathrm{COMB}_{3,1} + O(\varepsilon^4). \tag{2.170}$$

Notice that the time dependence of ω is a manifestation of the (time-dependent) amplitude dispersion of unforced Stokes waves. Then, the phase speed is the real part of ω,

$$c \coloneqq \mathrm{Re}\{\omega\} = \mathrm{Re}\{\omega_0\} + \varepsilon^2 |A_1'|^2 \exp(2\,\mathrm{Im}\{\omega_0\}t)\,\mathrm{Re}\{\mathrm{COMB}_{3,1}\} + O(\varepsilon^4), \tag{2.171}$$

while the growth rate is the imaginary

$$\gamma \coloneqq \mathrm{Im}\{\omega\} = \mathrm{Im}\{\omega_0\} + \varepsilon^2 |A_1'|^2 \exp(2\,\mathrm{Im}\{\omega_0\}t)\,\mathrm{Im}\{\mathrm{COMB}_{3,1}\} + O(\varepsilon^4). \tag{2.172}$$

It is natural to define the (dimensional) harmonic amplitudes a_n of (2.156) as containing the growth time dependence

$$a_1(t) \coloneqq |\hat{\eta}_{m=1}| = \varepsilon \frac{|A_1'|}{k} \exp(\mathrm{Im}\{\Theta\}) + O(\varepsilon^5), \tag{2.173}$$

$$\begin{aligned} a_2(t) &\coloneqq |\hat{\eta}_{m=2}| = \varepsilon^2 \frac{|A_1'|^2}{k} \exp(2\,\mathrm{Im}\{\Theta\})\Big[1 + \varepsilon^2 |A_1|^2 \exp(2\,\mathrm{Im}\{\omega_0\}t)\Big] + O(\varepsilon^5) \\ &= \varepsilon^2 \frac{|A_1'|^2}{k} \exp(2\,\mathrm{Im}\{\Theta\})\big[1 + (a_1 k)^2\big] + O(\varepsilon^5), \end{aligned} \tag{2.174}$$

where we made the approximation $\mathrm{Im}\{\omega_0\}t_0 \approx \mathrm{Im}\{\Theta\}$ in the final line. This leaves the propagation time

dependence given by the (real) phase

$$\theta \coloneqq \mathrm{Re}\{\Theta\} = kx - \int \mathrm{Re}\{\omega\}\,\mathrm{d}t\,, \tag{2.175}$$

such that the dimensional solution is

$$k\eta = (a_1 k)\exp(\mathrm{i}\theta) + (a_1 k)^2 \frac{a_2}{a_1^2 k}\exp(\mathrm{i}(2\theta+\beta)) + \dots\,. \tag{2.176}$$

2.A.5 Miles profile

The Miles surface pressure defined in (2.10) has a Fourier representation, similar to (2.16) and (2.17), given by

$$\hat{p}_{M,m}(t) = kP_M \exp(\mathrm{i}\,\mathrm{sgn}(m)\psi_P)\hat{\eta}_m(t), \tag{2.177}$$

or $\hat{P}_m = P_M \exp(\mathrm{i}\,\mathrm{sgn}(m)\psi_P)$, with P_M the constant P for the Miles profile. For this profile, the leading-order correction to the first harmonic $C_{2,2}$ (2.74) reduces to the unforced Stokes result ($\hat{P}_1 = \hat{P}_2 = 0$). Indeed, the leading-order HP β_0 (2.81) vanishes for any pressure profile of the form $\hat{P}_2 = \alpha + \hat{P}_1(1+\alpha)$, with $\alpha \in \mathbb{R}$ (Miles is $\alpha = 0$). Thus, the Miles pressure profile has no impact on leading-order wave shape. Note that, for the Miles profile, the higher-order correction $C_{4,2}$ differs from the unforced case, giving a small $O(\varepsilon^2)$ change to the shape parameters. Given that leading-order wind-induced shape changes have been measured [e.g. 100, 101], the Miles profile appears to be an inappropriate pressure profile.

2.A.6 Weaker wind forcing

In §§ 2.A.1 and 2.A.2 we performed the derivation up to $O(\varepsilon^4)$ with a strong pressure forcing $Pk/(\rho_w g) = O(1)$. This yielded expressions (2.163), (2.164) and (2.170) for $a_2/(a_1^2 k)$ β, and $\omega \in \mathbb{C}$ accurate to $O(\varepsilon^3)$. However, it is occasionally useful to consider weaker winds, such as $Pk/(\rho_w g) = O(\varepsilon)$ or $O(\varepsilon^2)$, as discussed in § 2.3.4. These results can be generated by substituting $P \to \varepsilon P$ or $P \to \varepsilon^2 P$, respectively, into (2.163), (2.164) and (2.170) and dropping terms $O(\varepsilon^3)$ or higher. We have also performed the derivation assuming *a priori* that $Pk/(\rho_w g) = O(\varepsilon^2)$ (not included here), which gives identical results to $O(\varepsilon^2)$ to the more general solution (§§ 2.A and 2.4) after converting back to the true time t. This further confirms the wide parameter range of the $Pk/(\rho_w g) = O(1)$ derivation (§§ 2.A and 2.4).

2.B The $O(\varepsilon^3)$ coefficients

Here, we give the full expressions for third-order coefficients, $\mathrm{KIN}_{3,m}$ and $\mathrm{DYN}_{3,m}$, defined in (2.107) and (2.108) as the coefficients of the lower-order terms' m-th harmonics in the kinematic and dynamic boundary conditions, respectively. Recall that $\hat{P}_m$ was defined in (2.18) as the pressure's Fourier coefficient multiplying the m-th harmonic of the wave profile: $\hat{p}_m(t) = k\hat{P}_m\hat{\eta}_m(t)$. The expressions are given as Maple code, and we represent the pressure Fourier coefficients $\hat{P}_1$, $\hat{P}_2$, and $\hat{P}_3$ as P1, P2, and P3, respectively. Likewise, we represent ω by omega, h by h and i by I.

$\mathrm{KIN}_{3,1}$ =

```
1/4*I*(((3/4+(P1-1/4*P2))*cosh(h)^4+(-1/4+(-1/2*P1+1/4*P2))*cosh(h)^2+1/4*P1
    +1/4)*abs(1+P1)+1/2*((P2+1)*cosh(h)^4+(P1+1)*cosh(h)^2-1/2*P1-1/2)*(P1+1)
    )^3/((1/2+(P1-1/2*P2))*cosh(h)^2-1/2*P1-1/2)/omega/sinh(h)/cosh(h)
```

$\mathrm{KIN}_{3,3}$ =

```
3/8*I*(3*cosh(h)^2-1)*(cosh(h)^2*P2+cosh(h)^2+2*P1+2)*omega^2/(2*cosh(h)^2*
    P1-cosh(h)^2*P2+cosh(h)^2-P1-1)/sinh(h)^2
```

$\mathrm{DYN}_{3,1}$ =

```
-(((P1+1)*cosh(h)^4+(-3/4*P1+1/4*P2-1/2)*cosh(h)^2-1/8*P1-1/8)*P1*abs(1+P1)
    +1/2*(((P1+1/4*P2^2-3/4)*abs(P1)^2+(P1^2^2+(-3/2*P2^2-1/2)*P1-5/4*P2-5/4)
    *P1)*cosh(h)^2-5/2*(P1+1)^2*P1)*(cosh(h)+1)*(cosh(h)-1))*abs(A1)^2^2/sinh
    (h)^2/P1/(2*cosh(h)^2*P1-cosh(h)^2*P2+cosh(h)^2-P1-1)
```

$\mathrm{DYN}_{3,3}$ =

```
-1/8*(4*cosh(h)^4*P1-7*cosh(h)^4*P2-3*cosh(h)^4-18*cosh(h)^2*P1+9*cosh(h)^2*
    P2-9*cosh(h)^2+15*P1+15)*(P1+1)^2*epsilon^3*A1^3/(2*cosh(h)^2*P1-cosh(h)
    ^2*P2+cosh(h)^2-P1-1)/sinh(h)^2
```

Recall that $\mathrm{COMB}_{3,1}$ is defined in (2.121) as the combination of $\mathrm{KIN}_{3,1}$ and $\mathrm{DYN}_{3,1}$ formed by eliminating $\hat{\phi}_{3,1}$. This grouping appears often in the 4th-order coefficients and governs the higher-order corrections to the phase speed (2.171) and growth rate (2.172). Therefore, we give its expression here and represent it in Maple code by C3.

$\mathrm{COMB}_{3,1}$ =

```
1/6*(1/2*P1*(8*cosh(h)^4*P1-2*cosh(h)^4*P2+6*cosh(h)^4-6*cosh(h)^2*P1+2*cosh
    (h)^2*P2-4*cosh(h)^2+P1+1)*abs(1+P1)+1/4*(((-8*P1+2*P2)^2-6)*abs(P1)
    ^2+(4*P1^3-2*P1^2*P2)^2-2*P1^2-4*P1)*cosh(h)^4-5/2*((-2/5+(-3/5*P1+1/5*P2
    ))*abs(P1)^2+(P1*(P1-3/5*P2)+4/5*P1-2/5*P2)*P1)*cosh(h)^2+2*(P1^2-1/8*abs
    (P1)^2+7/8*P1)*(P1+1))^3*(P1+1)/((1+(-P2+2*P1))*cosh(h)^2-P1-1)/cosh(h)/
    P1/omega/(P1-1/3*abs(1+P1)+1)/sinh(h)
```

2.C The $O(\varepsilon^4)$ coefficients

Here, we give the full expressions for fourth-order coefficients, $\mathrm{KIN}_{4,m}$ and $\mathrm{DYN}_{4,m}$, defined in (2.134) and (2.135) as the coefficients of the lower-order terms' m-th harmonics in the kinematic and dynamic boundary conditions, respectively.

$\mathrm{KIN}_{4,2} =$

```
1/2*(P1+1)*(-2*(cosh(h)^2+1/2)*(1/2*I*sinh(h)*C3*((2/3+(P1-1/3*P3))*cosh(h)
    ^2-2/3+(-3/4*P1+1/12*P3))*cosh(h)*omega+I*((2/3+(P1-1/3*P3))*(9/8+(P1
    +1/8*P2))*cosh(h)^4-13/8*(29/39+(P1-10/39*P3))*(P1+1)*cosh(h)^2+3/4*(P1
    +1)*(31/36+(P1-5/36*P3)))^3)*P1*abs(1+P1)+3*I*sinh(h)*(P1+1)*(cosh(h)
    ^2+1/2)*C3*P1*((2/3+(P1-1/3*P3))*cosh(h)^2-2/3+(-3/4*P1+1/12*P3))*cosh(h)
    *omega+I^3*(((25/36+(P1^2+(-5/18*P3-1/12*P2)*P1+1/18*P2*P3)+(59/36*P1
    -2/9*P3-1/36*P2))*abs(P1)^2-1/2*(-5/9+(P1^2+(2/3*P3-2*P2)*P1+7/6*P2*P3)*
    P1^3+(-1/3*P1^2+(55/18*P3-8/3*P2)*P1+19/18*P2*P3)^2+(-16/9*P1+41/18*P3
    -7/9*P2))*P1)*cosh(h)^6+(-17/12*(10/17+(P1^2+(-23/102*P3-4/17*P2)*P1
    +5/102*P2*P3)^2+(157/102*P1-3/17*P3-19/102*P2))*abs(P1)^2+25/8*P1*(-8/75+
    P1*(P1^2+(-18/25*P2-4/15*P3)*P1+11/75*P2*P3)^3+(39/25*P1^2+(-64/225*P3
    -89/75*P2)*P1+28/225*P2*P3)^2+(107/225*P1-1/25*P3-22/45*P2)))*cosh(h)
    ^4+(23/48*(16/23+(P1^2+(-5/69*P3-6/23*P2)*P1+2/69*P2*P3)^2+(5/3*P1-1/23*
    P3-16/69*P2))*abs(P1)^2-73/16*(104/219+(P1^2+(-18/73*P2-17/73*P3)*P1
    +2/73*P2*P3)*P1^3+(529/219*P1^2+(-283/657*P3-32/73*P2)*P1+16/657*P2*P3)
    ^2+(1244/657*P1-44/219*P3-128/657*P2))*P1)*cosh(h)^2+3/32*(P1+1)
    *((25/27+(P1-2/27*P3))*abs(P1)^2+20*(239/270+P1*(P1-29/180*P3)^2+(17/9*P1
    -89/540*P3))*P1)))/omega/sinh(h)^2/((1/2+(P1-1/2*P2))*cosh(h)^2-1/2*P1
```

−1/2)/P1/(−3∗P1+abs(1+P1)−3)/((2/3+(P1−1/3∗P3))∗cosh(h)^2−2/3+(−3/4∗P1
+1/12∗P3))

$KIN_{4,4}$ =

1/4∗I∗((8/9+(P1^3+(−4/3∗P2+5/9∗P3)∗P1^2+2/3∗(2/3∗P3+P2)∗P2∗P1−4/9∗P2^2∗P3)
^3+(20/9∗P1^2+(−8/9∗P2+14/9∗P3)∗P1+2/9∗P2∗(−2∗P3+P2))^2+(23/9∗P1−4/9∗P2
+5/9∗P3))∗cosh(h)^8+(−5/9+(−59/12∗P1^3+(85/12∗P2+11/12∗P3)∗P1^2−49/24∗P2
∗(146/147∗P3+P2)∗P1+31/72∗P2^2∗P3)^3+(−27/4∗P1^2+(145/18∗P2−7/36∗P3)∗P1
−29/18∗P2∗(P2+21/29∗P3))^2+(−203/72∗P1+11/6∗P2−49/72∗P3))∗cosh(h)
^6+(11/6+(81/8∗P1^3+(−33/4∗P2−185/72∗P3)∗P1^2+P2∗(P2+59/36∗P3)∗P1−1/9∗P2
^2∗P3)^3+(176/9∗P1^2+(−\463/36∗P2−7/2∗P3)∗P1+8/9∗P2∗(P2+51/32∗P3))
^2+(91/8∗P1−29/6∗P2−25/24∗P3))∗cosh(h)^4−361/48∗(P1+1)∗(530/1083+(P1
^2+(−129/361∗P2−73/361∗P3)∗P1+53/1083∗P2∗P3)^2+(520/361∗P1−334/1083∗P2
−166/1083∗P3))∗cosh(h)^2+57/32∗(P1+1)^2∗(436/513+(P1−77/513∗P3)))^3∗cosh(
h)∗omega/sinh(h)^3/((2/3+(P1−1/3∗P3))∗cosh(h)^2−2/3+(−3/4∗P1+1/12∗P3))
/((1/2+(P1−1/2∗P2))∗cosh(h)^2−1/2∗P1−1/2)^2

$KIN_{4,0}$ =

0

$DYN_{4,2}$ =

−1/4∗((−C3∗sinh(h)∗((P2+1)∗cosh(h)^4+(P1+1)∗cosh(h)^2−1/2∗P1−1/2)∗P1∗((2/3+(
P1−1/3∗P3))∗cosh(h)^2−2/3+(−3/4∗P1+1/12∗P3))∗cosh(h)∗omega−1/6∗(((7/6+((
P2+1/3∗P3)∗P1−1/6∗P2∗P3)^2+(4/3∗P1+5/6∗P2+1/6∗P3))∗abs(P1)^2+15∗P1
∗(59/45+P1∗(P1^2+(−1/2∗P2+4/15∗P3)∗P1+7/15∗P2∗P3)^3+(83/30∗P1^2+(−7/15∗P2
+46/45∗P3)∗P1+41/90∗P2∗P3)^2+(1/45∗P2+67/90∗P3+139/45∗P1)))∗cosh(h)
^8+(7/2∗(5/21+(P1^2+(−13/28∗P2−17/42∗P3)∗P1+3/28∗P2∗P3)^2+(95/84∗P1−5/14∗
P2−\25/84∗P3))∗abs(P1)^2−165/4∗P1∗(2/9+P1∗(P1^2+(−8/55∗P3−93/110∗P2)∗P1
+7/30∗P2∗P3)^3+(127/66∗P1^2+(−78/55∗P2−23/990∗P3)∗P1+37/165∗P2∗P3)
^2+(52/45∗P1−32/55∗P2+56/495∗P3)))∗cosh(h)^6+(−11/2∗(7/11+(P1^2+(−2/11∗P2
−5/22∗P3)∗P1+1/22∗P2∗P3)^2+(35/22∗P1−3/22∗P2−2/11∗P3))∗abs(P1)^2+63∗P1
∗(2/7+(P1^2+(−16/63∗P3−13/28∗P2)∗P1+5/84∗P2∗P3)∗P1^3+(79/36∗P1
^2+(−215/252∗P2−3/7∗P3)∗P1+1/18∗P2∗P3)^2+(187/126∗P1−11/28∗P2−5/28∗P3)))∗

cosh(h)^4+(2*(73/96+(P1^2+(−3/16*P2−7/96*P3)*P1+1/48*P2*P3)^2+(167/96*P1
−1/6*P2−5/96*P3))*abs(P1)^2−747/16*P1*(1538/2241+(P1^2+(−18/83*P3−6/83*P2
)*P1+2/249*P2*P3)*P1^3+(1993/747*P1^2+(−32/249*P2−947/2241*P3)*P1
+16/2241*P2*P3)^2+(5278/2241*P1−128/2241*P2−463/2241*P3)))*cosh(h)
^2−1/48*((P3^2+1)*abs(P1)^2+(−486*P1^3+72*P1^2*P3)^2+(−900*P1^2+73*P1*P3)
−413*P1)*(P1+1))^3)*abs(1+P1)−3*(P1+1)*(−C3*sinh(h)*((P2+1)*cosh(h)^4+(P1
+1)*cosh(h)^2−1/2*P1−1/2)*P1*((2/3+(P1−1/3*P3))*cosh(h)^2−2/3+(−3/4*P1
+1/12*P3))*cosh(h)*omega−1/3^3*(((3/2+(P1+1/2*P2))*(7/6+(P1+1/6*P3))*abs(
P1)^2+(11/6+P1*(P1^2+(7/6*P3−17/4*P2)*P1+13/6*P2*P3)^3+(11/12*P1
^2+(−35/6*P2+14/3*P3)*P1+9/4*P2*P3)^2+(−3/2*P2+43/12*P3+5/3*P1))*P1)*cosh
(h)^8+(1/2*(−2/3+(P1^2+(−5/4*P3−1/2*P2)*P1+1/12*P2*P3)^2+(1/4*P1−5/12*P2
−7/6*P3))*abs(P1)^2−49/4*P1*(1/21+(P1^2+(−67/294*P3−51/49*P2)*P1+85/294*
P2*P3)*P1^3+(71/42*P1^2+(−521/294*P2−17/147*P3)*P1+2/7*P2*P3)^2+(109/147*
P1−36/49*P2+16/147*P3)))*cosh(h)^6+(−35/16*(4/5+(P1^2+4/105*P2*P3−5/21*P1
*P3)^2+(37/21*P1+4/105*P2−1/5*P3))*abs(P1)^2+425/16*(148/425+P1*(P1
^2+(−111/425*P3−162/425*P2)*P1+24/425*P2*P3)^3+(967/425*P1^2+(−12/17*P2
−569/1275*P3)*P1+4/75*P2*P3)^2+(122/75*P1−418/1275*P2−16/85*P3))*P1)*cosh
(h)^4+(17/32*(15/17+(P1^2+(10/51*P3−6/17*P2)*P1+2/51*P2*P3)^2+(94/51*P1
−16/51*P2+4/17*P3))*abs(P1)^2−597/32*(1274/1791+P1*(P1^2+(−328/1791*P3
−18/199*P2)*P1+2/199*P2*P3)^3+(4832/1791*P1^2+(−32/199*P2−72/199*P3)*P1
+16/1791*P2*P3)^2+(1439/597*P1−\128/1791*P2−322/1791*P3))*P1)*cosh(h)
^2+3/16*((7/9+(P1−2/9*P3))*abs(P1)^2+18*P1*(293/324+P1*(P1−5/36*P3)
^2+(23/12*P1−49/324*P3)))*(P1+1))))/(cosh(h)+1)/sinh(h)/(−3*P1+abs(1+P1)
−3)/((1/2+(P1−1/2*P2))*cosh(h)^2−1/2*P1−1/2)/(cosh(h)−1)/P1/((2/3+(P1
−1/3*P3))*cosh(h)^2−2/3+(−3/4*P1+1/12*P3))/cosh(h)

$\mathrm{DYN}_{4,4}$ =

1/8*((4/9+(P1^3+(7/9*P3−19/6*P2)*P1^2+19/12*(2/3*P3+P2)*P2*P1−29/36*P2^2*P3)
^3+(11/18*P1^2+(−19/9*P2+47/18*P3)*P1+7/9*P2*(−5/7*P3+P2))^2+(−\5/9*P2
+37/36*P3+31/36*P1))*cosh(h)^10+(−5/9+(−115/12*P1^3+(46/3*P2+53/36*P3)*P1
^2−14/3*P2*(P2+20/21*P3)*P1+4/3*P2^2*P3)^3+(−215/18*P1^2+(152/9*P2−3/2*P3
)*P1−10/3*P2*(8/15*P3+P2))^2+(−17/4*P1+38/9*P2−59/36*P3))*cosh(h)

^8+(145/36+(581/24*P1^3+(−1067/48*P2−439/72*P3)*P1^2+347/96*P2*(P2
+482/347*P3)*P1−47/96*P2^2*P3)^3+(6379/144*P1^2+(−773/24*P2−1033/144*P3)*
P1+25/8*P2*(97/75*P3+P2))+(7087/288*P1−263/24*P2−451/288*P3))*cosh(h)
^6+(−671/72+(−2257/96*P1^3+(363/32*P2+1447/288*P3)*P1^2−1/2*P2*(P2
+499/144*P3)*P1+1/18*P2^2*P3)^3+(−15599/288*P1^2+(5747/288*P2+2395/288*P3
)*P1−4/9*P2*(467/128*P3+P2))^2+(−1441/36*P1+157/18*P2+241/72*P3))*cosh(h)
^4+26/3*(1753/2496+(P1^2+(−129/832*P2−103/624*P3)*P1+7/312*P2*P3)
^2+(4193/2496*P1−331/2496*P2−89/624*P3))*(P1+1)*cosh(h)^2−105/128*(P1+1)
^2*(788/945+(P1−157/945*P3)))^3*(P1+1)/cosh(h)/((2/3+(P1−1/3*P3))*cosh(h)
^2−2/3+(−3/4*P1+1/12*P3))/((1/2+(P1−1/2*P2))*cosh(h)^2−1/2*P1−1/2)^2/sinh
(h)^3

$\mathrm{DYN}_{4,0}$ =

−I/C3*((−13/6*I*((−3/13^2*C3^2*abs(P1)^4+P1*((P1+1)*abs(C3)^2−C3^2*(P1
+19/13))*abs(P1)^2+P1^2*((3/13*P1^2^2+19/13*P1+16/13)*abs(C3)^2−C3^2*(P1
+16/13)))*cosh(h)^2−3/13*(P1^2+abs(P1)^2+2*P1)*(−C3^2*abs(P1)^2+((P1+1)*
abs(C3)^2−C3^2)*P1))*P1*cosh(h)*((P1−1/2*P2+1/2)*cosh(h)^2−1/2*P1−1/2)*
sinh(h)*((2*abs(P1)^2*P2+P1*(−abs(P2)^2+P2))*cosh(h)^2−P2*(abs(P1)^2+P1))
*omega+19/24*I*(P1+1)*P1*((100/19*(67/100+(P1−33/100*P2))*P2^3*abs(P1)
^6+146/19*P1*(−65/146*(101/130+(P1−29/130*P2))*abs(P2)^2+(411/292+P1*(P1
−91/146*P2)^2+(218/73*P1−351/292*P2))*P2)^2*abs(P1)^4+26/19*P1
^2*(−\34/13*(147/68+P1*(P1−11/34*P2)^2+(61/17*P1−3/4*P2))*abs(P2)^2+P2
(87/13+P1^2(P1−8/13*P2)^3+11*P1*(P1−96/143*P2)^2+(252/13*P1−123/13*P2))
)*abs(P1)^2+P1^3*(−7/19*(100/7+P1^2*(P1−1/2*P2)^3+171/14*P1*(P1−58/171*P2
)^2+(193/7*P1−40/7*P2))*abs(P2)^2+(32/19+P1^2*(P1−25/38*P2)^3+245/38*P1*(
P1−188/245*P2)^2+(154/19*P1−100/19*P2))*P2))*cosh(h)^8+(−260/19*(97/130+(
P1−33/130*P2))*P2^3*abs(P1)^6−425/19*P1*(((−167/850*P1+79/1700*P2)
^2−3/20)*abs(P2)^2+(3267/1700+P1*(P1−253/850*P2)^2+(284/85*P1−1219/1700*
P2))*P2)^2*abs(P1)^4−59/19*P1^2*(−229/118*(420/229+P1*(P1−64/229*P2)
^2+(728/229*P1−143/229*P2))*abs(P2)^2+(2017/118+P1^2*(P1−39/118*P2)
^3+893/59*P1*(P1−260/893*P2)^2+(2001/59*P1−399/59*P2))*P2)*abs(P1)
^2−45/19*P1^3*(−14/45*(78/7+P1^2*(P1−17/56*P2)^3+87/8*P1*(P1−54/203*P2)

```
^2+(157/7*P1-4*P2))*abs(P2)^2+(376/45+P1^2*(P1-61/180*P2)^3+1721/180*P1*(
P1-500/1721*P2)^2+(323/18*P1-52/15*P2))*P2))*cosh(h)^6+(315/38*(517/630+(
P1-113/630*P2))*P2^3*abs(P1)^6+261/19*P1*(-25/522*(43/50+(P1-7/50*P2))*
abs(P2)^2+(206/87+P1*(P1-20/261*P2)^2+(962/261*P1-103/261*P2))*P2)^2*abs(
P1)^4+67/38*P1^2*(-127/134*(223/127+P1*(P1+10/127*P2)^2+(364/127*P1
-4/127*P2))*abs(P2)^2+P2*(3379/134+P1^2*(P1-11/134*P2)^3+1176/67*P1*(P1
-4/49*P2)^2+(2961/67*P1-253/67*P2)))*abs(P1)^2+107/76*P1
^3*(-27/107*(68/9+P1^2*(P1-1/9*P2)^3+205/27*(P1+4/205*P2)*P1+389/27*P1)*
abs(P2)^2+P2*(1400/107+P1^2*(P1-8/107*P2)^3+1230/107*P1*(P1-53/615*P2)
^2+(2629/107*P1-204/107*P2))))*cosh(h)^4+(12/19*P2^3*(31/48+(P1-17/48*P2)
)*abs(P1)^6+179/76*P1*((-19/179^2*P1-19/179)*abs(P2)^2+(193/179+P1*(P1
-60/179*P2)^2+(423/179*P1-111/179*P2))*P2)^2*abs(P1)^4+5/76*P1^2*((-12^3*
P1^2-158/5^2*P1-98/5)*abs(P2)^2+(47+P1^2*(P1-3/5*P2)^3+62*P1*(P1-63/155*
P2)^2+(591/5*P1-174/5*P2))*P2)*abs(P1)^2+1/19*P1^3*((-1/4^4*P1^3-63/4^3*
P1^2-71/2^2*P1-20)*abs(P2)^2+(18+P1^2*(P1-3/4*P2)^3+32*P1*(P1-33/64*P2)
^2+(213/4*P1-20*P2))*P2))*cosh(h)^2-7/76*(P1+1)*(abs(P1)^2+P1)*(89/14*abs
(P1)^4^2+(233/14*P1^2^2+411/14*P1)*abs(P1)^2+P1^2*(P1^2^2+261/14*P1+24))*
P2)*C3^3)*abs(1+P1)+1/12*I*P1*sinh(h)*cosh(h)*(P1+1)*(2*P1*cosh(h)^2-P2*
cosh(h)^2+cosh(h)^2-P1-1)*(abs(P1)^2+P1)*(2*abs(P1)^2*cosh(h)^2*P2-abs(P2
)^2*cosh(h)^2*P1-abs(P1)^2*P2+P2*P1*
cosh(h)^2-P1*P2)*(-13*C3^2*abs(P1)^2*cosh(h)^2-3*C3^2*cosh(h)^2*P1^2+3*abs(
P1)^2*abs(C3)^2*cosh(h)^2+13*abs(C3)^2*cosh(h)^2*P1^2+10*C3^2*abs(P1)
^2-16*C3^2*cosh(h)^2*P1+16*abs(C3)^2*cosh(h)^2*P1-10*abs(C3)^2*P1^2+10*C3
^2*P1-10*abs(C3)^2*P1)*omega-67/24*I*(P1+1)*(abs(P1)^2+P1)*C3
*((26/67*(19/26+(P1-7/26*P2))*P2^3*abs(P1)^6+146/67*P1*(-8/73*(25/32+(P1
-7/32*P2))*abs(P2)^2+(245/292+P1*(P1-34/73*P2)^2+(143/73*P1-171/292*P2))*
P2)^2*abs(P1)^4+100/67*P1^2*(-91/100*(94/91+P1*(P1-22/91*P2)^2+(192/91*P1
-29/91*P2))*abs(P2)^2+(77/50+P1^2*(P1-13/20*P2)^3+109/25*P1*(P1-61/109*P2
)^2+(126/25*P1-193/100*P2))*P2)*abs(P1)^2+P1^3*(-33/67*(100/33+P1^2*(P1
-29/66*P2)^3+117/22*P1*(P1-34/117*P2)^2+(82/11*P1-40/33*P2))*abs(P2)^2+P2
*(32/67+P1^2*(P1-101/134*P2)^3+411/134*P1*(P1-98/137*P2)^2+(174/67*P1
```

```
−100/67*P2))))*cosh(h)^8+(−59/67*(45/59+(P1−14/59*P2))*P2^3*abs(P1)
^6−425/67*P1*(−39/850*(61/78+(P1−17/78*P2))*abs(P2)^2+(1721/1700+P1*(P1
−229/850*P2)^2+(893/425*P1−609/1700*P2))*P2)^2*abs(P1)^4−260/67*P1
^2*((−253/520*P1*(P1−64/253*P2)^3+(−P1+81/520*P2)^2−25/52)*abs(P2)
^2+(323/104+P1^2*(P1−167/520*P2)^3+71/13*P1*(P1−91/355*P2)^2+(2001/260*P1
−157/130*P2))*P2)*abs(P1)^2−194/67*P1^3*(−33/97*(26/11+P1^2*(P1−79/264*P2
)^3+1219/264*(P1−286/1219*P2)*P1^2+(133/22*P1−28/33*P2))*abs(P2)
^2+(188/97+P1^2*(P1−255/776*P2)^3+3267/776*P1*(P1−280/1089*P2)
^2+(2017/388*P1−78/97*P2))*P2))*cosh(h)^6+(1/2*(107/134+(P1−27/134*P2))*
P2^3*abs(P1)^6+261/67*P1*(−11/1044*(8/11+(P1−3/11*P2))*abs(P2)
^2+(205/174+P1*(P1−127/1044*P2)^2+(196/87*P1−205/1044*P2))*P2)^2*abs(P1)
^4+315/134*P1^2*(−8/63*(53/40+P1*(P1+1/8*P2)^2+(12/5*P1+1/20*P2))*abs(P2)
^2+P2*(2629/630+P1^2*(P1−5/63*P2)^3+1924/315*P1*(−7/74*P2+P1)^2+(47/5*P1
−389/630*P2)))*abs(P1)^2+517/268*P1^3*(−113/517*(204/113+P1^2*(P1−7/113*
P2)^3+412/113*P1*(P1−1/103*P2)^2+506/113*P1)*abs(P2)^2+(1400/517+P1^2*(P1
−43/517*P2)^3+2472/517*P1*(P1−223/2472*P2)^2+(3379/517*P1−204/517*P2))*P2
))*cosh(h)^4+(5/268*(4/5+(P1−1/5*P2))*P2^3*abs(P1)^6+179/268*P1
*((−3/179^2*P1−3/179)*abs(P2)^2+(128/179+P1*(P1−60/179*P2)^2+(310/179*P1
−63/179*P2))*P2)^2*abs(P1)^4+12/67*P1^2*((−5/4^3*P1^2−21/8^2*P1−11/8)*abs
(P2)^2+P2*(71/16+P1^2*(P1−19/48*P2)^3+141/16*P1*(P1−158/423*P2)
^2+(197/16*P1−71/24*P2)))*abs(P1)^2+31/268*P1^3*((−17/31^4*P1^3−111/31^3*
P1^2−174/31^2*P1−80/31)*abs(P2)^2+P2*(72/31+P1^2*(P1−19/31*P2)^3+193/31*
P1*(P1−98/193*P2)^2+(235/31*P1−80/31*P2))))*cosh(h)^2−89/536*(P1+1)*(abs(
P1)^2+P1)*(14/89*abs(P1)^4^2+(233/89*P1^2^2+261/89*P1)*abs(P1)^2+P1^2*(P1
^2^2+411/89*P1+336/89))*P2)^3)/(P1+1)/cosh(h)/((2*abs(P1)^2*P2+P1*(−abs(
P2)^2+P2))*cosh(h)^2−P2*(abs(P1)^2+P1))/(−1/3*P1*(13*abs(P1)^2+3*P1^2+16*
P1)*abs(1+P1)+1/3*(abs(P1)^2+P1)*(3*abs(P1)^2+13*P1^2+16*P1))/P1/(cosh(h)
+1)/((1+(2*P1−P2))*cosh(h)^2−P1−1)/sinh(h)/(cosh(h)−1)
```

2.D The full $C_{4,2}$ expression

Here, we give the full expression for $C_{4,2}$, defined in (2.151) as the coefficient of the $O(\varepsilon^4)$ correction to the $m = 2$ harmonic of η.

$C_{4,2} =$

```
−8*((−1/72*P1*C3*sinh(h)*cosh(h)*(12*P1*cosh(h)^2−4*cosh(h)^2*P3+8*cosh(h)
    ^2−9*P1+P3−8)*(6*cosh(h)^4*P1+cosh(h)^4*P2+7*cosh(h)^4+P1*cosh(h)^2+cosh(
    h)^2−2*P1−2)*omega−4/3^3*((1/8*(8/9+(P1^2+(1/12*P2−2/9*P3)*P1+1/36*P2*P3)
    ^2+(67/36*P1+1/9*P2−7/36*P3))*abs(P1)^2+(145/144+(P1^2+(−5/24*P3+1/16*P2)
    *P1+1/24*P2*P3)*P1^3+(143/48*P1^2+(17/96*P2−29/72*P3)*P1+13/288*P2*P3)
    ^2+(17/144*P2−55/288*P3+859/288*P1))*P1)*cosh(h)^8+(−1/6*(25/32+(P1
    ^2+(−5/64*P2−1/6*P3)*P1+5/192*P2*P3)^2+(337/192*P1−5/96*P2−9/64*P3))*abs(
    P1)^2−53/32*P1*(37/53+(P1^2+(−34/159*P3−49/212*P2)*P1+41/636*P2*P3)*P1
    ^3+(563/212*P1^2+(−43/106*P2−725/1908*P3)*P1+32/477*P2*P3)^2+(2243/954*P1
    −82/477*P2−\26/159*P3)))*cosh(h)^6+(13/384*(8/13+(P1^2+(−6/13*P2+2/39*P3)
    *P1+1/39*P2*P3)^2+(62/39*P1−17/39*P2+1/13*P3))*abs(P1)^2+59/64*(30/59+P1
    *(P1^2+(−21/118*P3−45/118*P2)*P1+8/177*P2*P3)^3+(877/354*P1^2+(−130/177*
    P2−164/531*P3)*P1+49/1062*P2*P3)^2+(1054/531*P1−187/531*P2−23/177*P3))*P1
    )*cosh(h)^4−19/128*(P1+1)*(−3/19*(25/27+(P1−2/27*P3))*abs(P1)
    ^2+(113/171+(P1−11/57*P3)*P1^2+(94/57*P1−31/171*P3))*P1)*cosh(h)^2−3/64*(
    P1+1)^2*(1/8*abs(P1)^2+(35/36+(P1−11/72*P3))*P1)))*abs(1+P1)+1/288*C3*
    sinh(h)*cosh(h)*(P1+1)*(12*P1*cosh(h)^2−4*cosh(h)^2*P3+8*cosh(h)^2−9*P1+
    P3−8)*(4*cosh(h)^4*abs(P1)^2+36*cosh(h)^4*P1^2+12*cosh(h)^4*P1*P2+52*cosh
    (h)^4*P1+12*cosh(h)^2*P1^2+12*cosh(h)^2*P1−abs(P1)^2−15*P1^2−16*P1)*omega
    −1/12*(P1+1)^3*((−12*(8/9+(P1^2+(1/12*P2−2/9*P3)*P1+1/36*P2*P3)^2+(67/36*
    P1+1/9*P2−7/36*P3))*abs(P1)^2+P1*(−25/3+(P1−1/3*P3)*(P1+5/2*P2)*P1
    ^3+(−41/6*P1^2+(19/6*P2+7/6*P3)*P1−7/6*P2*P3)^2+(1/3*P2+7/6*P3−95/6*P1)))
    *cosh(h)^8+(17*(151/204+(P1^2+(−7/68*P2−19/102*P3)*P1+1/34*P2*P3)
    ^2+(349/204*P1−5/68*P2−8/51*P3))*abs(P1)^2+17/4*(106/51+(P1^2+(−19/51*P3
    −36/17*P2)*P1+31/51*P2*P3)*P1^3+(230/51*P1^2+(−206/51*P2−15/17*P3)*P1
    +37/51*P2*P3)^2+(93/17*P1−92/51*P2−20/51*P3))*P1)*cosh(h)
```

^6+(−19/4∗(34/57+(P1^2+(−15/38∗P2−5/114∗P3)∗P1+2/57∗P2∗P3)^2+(89/57∗P1
−41/114∗P2−1/114∗P3))∗abs(P1)^2−131/8∗(200/393+(P1^2+(−40/131∗P3−54/131∗
P2)∗P1+7/131∗P2∗P3)∗P1^3+(337/131∗P1^2+(−116/131∗P2−224/393∗P3)∗P1
+25/393∗P2∗P3)^2+(814/393∗P1−182/393∗P2−100/393∗P3))∗P1)∗cosh(h)^4+99/8∗(
P1+1)∗(−29/198∗(80/87+(P1−7/87∗P3))∗abs(P1)^2+P1∗(71/99+P1∗(P1−4/27∗P3)
^2+(1013/594∗P1−3/22∗P3)))∗cosh(h)^2−9/8∗(P1+1)∗(−7/12∗((P1−4/63∗P3)
+59/63)∗abs(P1)^2+(P1∗(P1−1/36∗P3)^2+(25/18∗P1+1/108∗P3)+23/54)∗P1)))∗
cosh(h)/((1+(2∗P1−P2))∗cosh(h)^2−P1−1)/sinh(h)/(cosh(h)+1)/((1/18∗(−54∗P1
^2+4∗P1∗P2−2∗abs(P1)^2−52∗P1)∗cosh(h)^2+3/2∗P1^2+1/18∗abs(P1)^2+14/9∗P1)∗
abs(1+P1)+1/6∗(P1+1)∗(6∗cosh(h)^2∗abs(P1)^2+18∗cosh(h)^2∗P1^2−4∗cosh(h)
^2∗P1∗P2+20∗cosh(h)^2∗P1−3∗abs(P1)^2−9∗P1^2−12∗P1))/(cosh(h)−1)/((8+(12∗
P1−4∗P3))∗cosh(h)^2−8+(−9∗P1+P3))

Chapter 3

Wind-induced changes to surface gravity wave shape in shallow water

3.1 Abstract

Wave shape (e.g. wave skewness and asymmetry) impacts sediment transport, remote sensing and ship safety. Previous work showed that wind affects wave shape in intermediate and deep water. Here, we investigate the effect of wind on wave shape in shallow water through a wind-induced surface pressure for different wind speeds and directions to provide the first theoretical description of wind-induced shape changes. A multiple-scale analysis of long waves propagating over a shallow, flat bottom and forced by a Jeffreys-type surface pressure yields a forward or backward Korteweg–de Vries (KdV)–Burgers equation for the wave profile, depending on the wind direction. The evolution of a symmetric, solitary-wave initial condition is calculated numerically. The resulting wave grows (decays) for onshore (offshore) wind and becomes asymmetric, with the rear face showing the largest shape changes. The wave profile's deviation from a reference solitary wave is primarily a bound wave and trailing, dispersive, decaying tail. The onshore wind increases the wave's energy and skewness with time while decreasing the wave's asymmetry, with the opposite holding for offshore wind. The corresponding wind speeds are shown to be physically realistic, and the shape changes are explained as slow growth followed by rapid evolution according to the unforced KdV equation.

3.2 Introduction

The study of wind and ocean wave interactions began with Jeffreys [63] and continues to be an active field of research [e.g. 125, 129, 130]. Many theoretical studies [e.g. 63, 68, 69] focus on calculating wind-induced growth rates and often employ phase-averaging techniques. However, experimental [e.g. 100, 101] and theoretical [e.g. 131] studies have shown wind can also influence wave shape, quantified by third-order shape statistics such as skewness and asymmetry, corresponding to vertical and horizontal asymmetry, respectively. Furthermore, while many numerical studies on coupled wind and waves employ sinusoidal water waves and therefore neglect wind-induced shape changes [e.g. 90, 108], some recent numerical studies have incorporated wind-induced changes to the wave field using coupled air–water simulations [e.g. 92, 93] or direct numerical simulations of two-fluid flows [e.g. 88, 132]. Wave shape influences sediment transport, affecting beach morphodynamics [e.g. 46, 49], while wave skewness affects radar altimetry signals [e.g. 52] and asymmetry influences ship responses to wave impacts [e.g. 57].

Waves in shallow water, where $kh \ll 1$ (with h the water depth, $k = 2\pi/\lambda$ the wavenumber and λ the wavelength), differ qualitatively from those in intermediate ($kh \sim 1$) to deep ($kh \gg 1$) water. For waves with small amplitudes $a_0 \ll h$, leveraging the small parameters $a_0/h \sim (kh)^2 \ll 1$ yields the Boussinesq equations with weak dispersion and nonlinearity. When dispersion balances nonlinear focusing, a special class of waves, known as solitary waves, are formed and appear in environments ranging from nonlinear optical pulses [e.g. 133] to astrophysical dusty plasmas [e.g. 134]. These well-understood waves are often used to study fluid dynamical [e.g. 135–138] and engineering [e.g. 139–141] contexts owing to their simplicity. One of the simplest equations displaying solitary waves is the Korteweg–de Vries (KdV) equation, which incorporates dispersion and nonlinearity. When augmented with a dissipative term, this becomes the KdV–Burgers equation, with applications to damped internal tides [e.g. 142], electron waves in graphene [e.g. 143] and viscous flow in blood vessels [e.g. 144]. While field observations [e.g. 145] have investigated the wind-induced growth of shallow-water waves, the interaction of wind and shallow-water waves has not yet been formulated into a simple equation such as the KdV–Burgers equation.

The influence of wind on wave shape has been previously investigated in intermediate and deep water [131]. However, the coupling between wind and wave shape has not yet been investigated in shallow water. To investigate wind and surface wave interactions in shallow water over a flat bottom, we introduce a wind-induced pressure term to the Boussinesq equations in § 3.3. The resulting KdV–Burgers equation governs a solitary wave's evolution, which we solve numerically to yield the wave's energy, skewness and asymmetry in § 3.4. We calculate the wind speed, discuss the asymmetry and compare our results to

intermediate- and deep-water waves in § 3.5.

3.3 Derivation of the KdV–Burgers equation

3.3.1 Governing equations

We treat the flow as irrotational and inviscid and neglect surface tension. Furthermore, we restrict ourselves to planar wave propagation in the $+x$ direction. Finally, we choose a coordinate system with $z = 0$ at the mean water level and a horizontal, flat bottom located at $z = -h$. Then, the incompressibility condition and standard boundary conditions are

$$0 = \phi_{xx} + \phi_{zz} \qquad \text{on} \quad -h < z < \eta, \tag{3.1}$$

$$0 = \phi_z \qquad \text{on} \quad z = -h, \tag{3.2}$$

$$\phi_z = \eta_t + \phi_x \eta_x \qquad \text{on} \quad z = \eta, \tag{3.3}$$

$$0 = \frac{p}{\rho_w} + g\eta + \phi_t + \frac{1}{2}\left[\phi_x^2 + \phi_z^2\right] \quad \text{on} \quad z = \eta. \tag{3.4}$$

Here, $\eta(x,t)$ is the wave profile, $\phi(x,z,t)$ is the flow's velocity potential related to the velocity $\mathbf{u} = \boldsymbol{\nabla}\phi$, $p(x,t)$ is the surface pressure, g is the gravitational acceleration and ρ_w is the water density. We used the ϕ gauge freedom to absorb the Bernoulli 'constant' $C(t)$ in the dynamic boundary condition. We seek a solitary, progressive wave which decays at infinity, $\eta(\mathbf{x},t) \to 0$ as $|\mathbf{x}| \to \infty$, with similar conditions on $\mathbf{u}$. We choose a coordinate system where the average bottom horizontal velocity vanishes,

$$\overline{\frac{\partial \phi}{\partial x}} = 0 \quad \text{on} \quad z = -h, \tag{3.5}$$

with the overline a spatial average $\overline{f} \coloneqq \lim_{L\to\infty} \int_{-L}^{L} f \,\mathrm{d}x \,/(2L)$. Additionally, we assume the surface pressure $p(x,t)$ is a Jeffreys-type forcing [63],

$$p(x,t) = P\frac{\partial \eta(x,t)}{\partial x}. \tag{3.6}$$

Here, P is proportional to $(U-c)^2$, with c the wave's nonlinear phase speed and U the wind speed (cf. § 3.5.1). Note that $P > 0$ corresponds to ('onshore') wind in the same direction as the wave while $P < 0$ denotes ('offshore') wind opposite the wave. We use a Jeffreys forcing for its analytic simplicity and clear demonstration of wind–wave coupling. Jeffrey's separated sheltering mechanism is likely only relevant in

special situations (e.g. near breaking, [64], or for steep waves under strong winds, [65, 66]). Additionally, numerical simulations of sinusoidal waves suggest the peak surface pressure is shifted approximately 135° from the wave peak, while Jeffreys would give a 90° shift [108]. However, a fully dynamic coupling between wind and waves — necessary for an accurate surface pressure over a non-sinusoidal, dynamic water surface — is outside the scope of this paper. Furthermore, the applicability of Jeffreys forcing to extreme waves means our theory could apply to the wind forcing of rogue waves in shallow water [146].

3.3.2 Non-dimensionalization

We non-dimensionalize our system with the known characteristic scales: the horizontal length scale L over which η changes rapidly, expressed as an effective wavenumber $k_E \coloneqq 2\pi/L$; the (initial) wave amplitude $a_0 = H_0/2$ (i.e. half the wave height H_0); the depth h; the gravitational acceleration g; and the wind speed U, expressed as a pressure magnitude $P \propto \rho_a(U-c)^2$, with $\rho_a \approx 1.225 \times 10^{-3}\rho_w$ the density of air. Denoting non-dimensional variables with primes, we have

$$\begin{aligned} x &= \frac{x'}{k_E} = h\frac{x'}{\sqrt{\mu_E}}, & t &= \frac{t'}{k_E c_0} = \frac{t'}{\sqrt{\mu_E}}\sqrt{\frac{h}{g}}, & \eta &= a_0\eta' = h\varepsilon\eta', \\ z &= hz', & P &= \varepsilon P'\frac{\rho_w g}{k_E} = \frac{\varepsilon}{\sqrt{\mu_E}}P'\rho_w c_0^2, & \phi &= \phi'\frac{a_0}{k_E}\sqrt{\frac{g}{h}} = \frac{\phi'\varepsilon}{\sqrt{\mu_E}}c_0 h, \end{aligned} \tag{3.7}$$

with linear, shallow-water phase speed $c_0 = \sqrt{gh}$. Our system's dynamics is controlled by three small, non-dimensional parameters: $\varepsilon \coloneqq a_0/h$, $\mu_E \coloneqq (k_E h)^2$ and $Pk_E/(\rho_w g)$. We will later require $O(\varepsilon) = O(\mu_E) = O(Pk_E/(\rho_w g))$. Now, our non-dimensional equations take the form

$$0 = \mu_E\phi'_{x'x'} + \phi'_{z'z'} \qquad \text{on} \quad -1 < z' < \varepsilon\eta', \tag{3.8}$$

$$0 = \phi'_{z'} \qquad \text{on} \quad z' = -1, \tag{3.9}$$

$$\phi'_{z'} = \mu_E\eta'_{t'} + \varepsilon\mu_E\phi'_{x'}\eta'_{x'} \qquad \text{on} \quad z' = \varepsilon\eta', \tag{3.10}$$

$$0 = \varepsilon P'\eta'_{x'} + \eta' + \phi'_{t'} + \frac{1}{2}\left(\varepsilon\phi'^{,2}_{x'} + \frac{\varepsilon}{\mu_E}\phi'^{,2}_{z'}\right) \qquad \text{on} \quad z' = \varepsilon\eta'. \tag{3.11}$$

We will drop the primes throughout the remainder of this section for readability.

3.3.3 Boussinesq equations, multiple-scale expansion, KdV equation and initial condition

Here, we modify the Boussinesq equation's derivation provided by Mei et al. [121] or Ablowitz [102] by including the surface pressure forcing in (3.4). Taylor expanding the velocity potential ϕ about the bottom, $z = -1$, and applying Laplace's equation (3.8) and the bottom boundary condition (3.9) yields an expansion of ϕ in terms of $\mu_E \ll 1$ and the velocity potential at the bottom, $\varphi \coloneqq \phi\big|_{z=-1}$. This ϕ expansion can be substituted into the two remaining boundary equations, (3.10) and (3.11), to give the Boussinesq equations with a pressure forcing term,

$$\partial_t \eta + \partial_x^2 \varphi + \varepsilon \partial_x(\eta \partial_x \varphi) - \frac{1}{6}\mu_E \partial_x^4 \varphi = O\big(\mu_E^2\big), \tag{3.12}$$

$$\partial_t \varphi + \varepsilon P \partial_x \eta + \eta - \frac{1}{2}\mu_E \partial_t \partial_x^2 \varphi + \frac{1}{2}\varepsilon (\partial_x \varphi)^2 = O\big(\mu_E^2\big). \tag{3.13}$$

Further, we will now assume $O(\varepsilon) = O(\mu_E) \ll 1$.

We now expand t using multiple time scales $t_n = \varepsilon^n t$ for $n = 0, 1$, so all time derivatives become $\partial_t \to \partial_{t_0} + \varepsilon \partial_{t_1}$. Then, we write η and φ as asymptotic series of ε,

$$\eta(x,t) = \sum_{k=0}^{\infty} \varepsilon^k \eta_k(x, t_0, t_1) \quad \text{and} \quad \varphi(x,t) = \sum_{k=0}^{\infty} \varepsilon^k \varphi_k(x, t_0, t_1,). \tag{3.14}$$

Now, we will reduce the Boussinesq equations, (3.12) and (3.13), to the KdV equation following a similar method to Mei et al. [121] and Ablowitz [102]. Collecting order-one terms $O\big(\varepsilon^0\big)$ from (3.12) and (3.13) gives a wave equation for η_0 and ϕ_0. The right-moving solutions are

$$\varphi_0 = f_0(x - t_0, t_1) \quad \text{and} \quad \eta_0 = f_0'(x - t_0, 1) \quad \text{with} \quad f_0' \coloneqq \left.\frac{\partial f_0(\theta, t_1)}{\partial \theta}\right|_{\theta = x - t_0}. \tag{3.15}$$

Continuing to the next order of perturbation theory, we retain terms of $O(\varepsilon)$,

$$\frac{\partial \eta_1}{\partial t_0} + \frac{\partial^2 \varphi_1}{\partial x^2} = -\frac{\partial \eta_0}{\partial t_1} - \frac{\partial}{\partial x}\left(\eta_0 \frac{\partial \varphi_0}{\partial x}\right) + \frac{1}{6}\frac{\mu_E}{\varepsilon}\frac{\partial^4 \varphi_0}{\partial x^4}, \tag{3.16}$$

$$\eta_1 + \frac{\partial \varphi_1}{\partial t_0} = -P\frac{\partial \eta_0}{\partial x} - \frac{\partial \varphi_0}{\partial t_1} + \frac{1}{2}\frac{\mu_E}{\varepsilon}\frac{\partial^3 \varphi_0}{\partial t_0 \partial^2 x} - \frac{1}{2}\left(\frac{\partial \varphi_0}{\partial x}\right)^2. \tag{3.17}$$

Inserting our leading-order solutions for η_0 and φ_0, eliminating η_1 and preventing resonant forcing of φ_1

gives the KdV–Burgers equation,

$$\frac{\partial \eta_0}{\partial t_1} + \frac{3}{2}\eta_0 \frac{\partial \eta_0}{\partial x} + \frac{1}{6}\frac{\mu_E}{\varepsilon}\frac{\partial^3 \eta_0}{\partial x^3} = -P\frac{1}{2}\frac{\partial^2 \eta_0}{\partial x^2}. \tag{3.18}$$

Note that (3.18) has a rescaling symmetry, with $\mu_E \to \lambda^2 \mu_E$ equivalent to taking $(x, t_0, t_1, P) \to (x, t_0, t_1, P)/\lambda$. Therefore, we fix the length scale (equivalently, k_E) by choosing $\mu_E = 6\varepsilon$. Note that incorporating slowly varying bottom bathymetry $\partial_x h = O(\varepsilon)$ can yield an equation of the form (3.18) with spatially varying coefficients [e.g. 147, 148], although such an analysis is outside the scope of this study.

For offshore wind, the pressure term $P\partial_x^2 \eta_0$ acts as a positive viscosity causing damping, and (3.18) is the (forward) KdV–Burgers equation with $P < 0$. However, for onshore wind, the viscosity is negative and causes wave growth, yielding the backward KdV–Burgers equation with $P > 0$. The backward KdV–Burgers equation is ill posed in the sense of Hadamard because the solution is highly sensitive to changes in the initial condition [149]. While a finite-time singularity (i.e. wave breaking) is likely, the multiple-scale expansion used to derive (3.18) is only valid for time intervals of $O(1/\varepsilon)$, and we limit our analysis to short times removing the need to regularize the solution.

The solitary-wave solutions of the unforced ($P = 0$) KdV equation exist due to a balance of dispersion $\partial_x^3 \eta_0$ with focusing nonlinearity $\eta_0 \partial_x \eta_0$ and have the form [e.g. 121]

$$\eta_0 = H_0 \operatorname{sech}^2\left(\frac{x}{\Delta}\right) \quad \text{with} \quad \Delta = \sqrt{\frac{8}{H_0}}, \tag{3.19}$$

in a co-moving frame with $H_0 > 0$ an order-one parameter. For reference, unforced solitary waves travel relative to the laboratory frame with non-dimensional, nonlinear phase speed [e.g. 121]

$$c = 1 + \varepsilon\frac{H_0}{2} \tag{3.20}$$

We use (3.19) for our initial condition and choose $H_0 = 2$ so the initial, dimensional amplitude a_0 is half the wave height (cf. § 3.3.2). Note that the unforced KdV equation also has periodic solutions known as cnoidal waves. For a fixed height, these cnoidal waves have a smaller characteristic wavelength $1/k_E$ than solitary waves and can be studied by choosing larger $\mu_E > 6\varepsilon$ (cf. § 3.5.3). However, wind-induced shape changes are more readily understood when considering solitary waves owing to their reduced number of free parameters (i.e. μ_E). Furthermore, since solitary waves are well understood and highly relevant to fluid dynamical systems [e.g. 136–139], we will restrict our analysis to solitary waves for brevity and clarity.

The wind-forcing term $P\partial_x^2\eta_0$ in (3.18) disrupts the solitary wave's balance of dispersion and nonlinearity, inducing growth/decay and shape changes. The KdV–Burgers equation has no known solitary-wave solutions, so we will solve it numerically.

3.3.4 Numerics and shape statistics

To solve (3.18) numerically, we will use the Dedalus spectral solver [150] which implements a generalized tau method with a Chebyshev basis. Since the onshore wind, $P > 0$ case is ill posed, we require an implicit solver, so time stepping is done with coupled four-stage, third-order Diagonally Implicit Runge–Kutta and Explicit Runge–Kutta schemes. The spatial domain has a length of $L = 80$, and we require $\eta_0 = 0$ at $x' = -40$ and $\eta_0 = \partial_x\eta_0 = 0$ at $x' = 40$. We employ $N_c = 1600$ Chebyshev coefficients and zero padding with a scaling factor of 3/2 to prevent aliasing of nonlinear terms. This corresponds to $N_x = 2400$ spatial points with spacing $\Delta x = 7.7 \times 10^{-5}$ to 7.9×10^{-2} for an average spacing of $\Delta x = 0.05$. The simulation runs from $t_1 = 0$ to $t_1 = T = 10$, since the multiple-scale expansion of § 3.3.3 is only accurate for times of $O(1/\varepsilon)$. Adaptive time stepping is employed such that the Courant–Friedrichs–Lewy number is $(\Delta t)\max(\eta_0)/(\Delta x) = 1$. For the unforced case, this corresponds to $\Delta t \approx 7.86 \times 10^{-3}$, increases to 1.04×10^{-2} for $P = -0.25$ and decreases to 4.73×10^{-4} for $P = 0.25$. We found that linearly ramping up P from 0 at $t_1 = 0$ to its full value at $t_1 = \varepsilon$, or full, dimensional time $T_0 = 1/(\sqrt{gh}k_E)$ (i.e. the time required to cross the inverse, effective wavenumber $1/k_E$, or 'wave-crossing time') did not qualitatively modify the results, so we do not utilize such a ramp-up here. The spectral solver results in high numerical accuracy, with the normalized root-mean-square difference between the unforced ($P = 0$) profile η_0 at $t_1' = 10$ and the initial condition $\eta_0^{(0)}$ is 2×10^{-13}, and the normalized wave height change is $1 - [\max(\eta_0) - \min(\eta_0)]/\left[\max(\eta_0^{(0)}) - \min(\eta_0^{(0)})\right] = -1 \times 10^{-13}$.

We quantify the wave shape with the wave's energy E, skewness S and asymmetry A,

$$E \coloneqq \langle\eta_0^2\rangle, \quad \mathrm{S} \coloneqq \frac{\langle\eta_0^3\rangle}{\langle\eta_0^2\rangle^{3/2}} \quad \text{and} \quad \mathrm{A} \coloneqq \frac{\langle\mathcal{H}\{\eta_0^3\}\rangle}{\langle\eta_0^2\rangle^{3/2}}, \quad \text{with} \quad \langle f\rangle \coloneqq \frac{1}{L}\int_{-L/2}^{L/2} f\,\mathrm{d}x\,. \tag{3.21a–c}$$

Here, $\mathcal{H}(f)$ is the Hilbert transform of f, defined as the imaginary part of $\mathcal{F}^{-1}(\mathcal{F}(f)2U)$ with U the unit step function and $\mathcal{F}$ the Fourier transform. Since these definitions depend on the domain size L, we normalize the energy E and skewness S by their initial values.

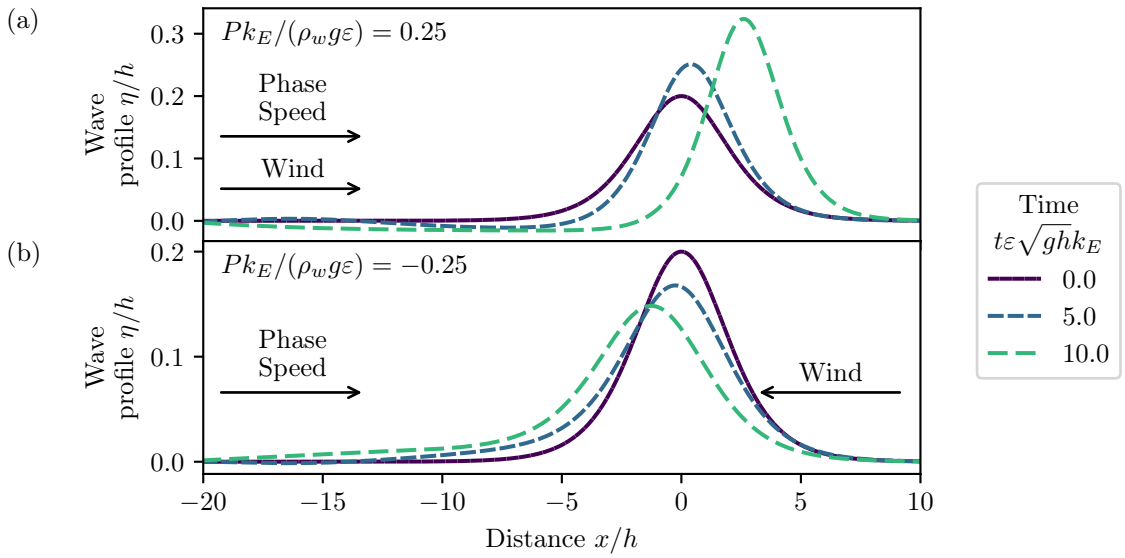

Figure 3.1. Solitary-wave evolution under (a) onshore and (b) offshore wind-induced surface pressure in the frame of the unforced solitary wave. Non-dimensional wave height η/h versus non-dimensional distance x/h for $\varepsilon = 0.1$, $\mu_E = 0.6$, $|Pk_E/(\rho_w g\varepsilon)| = 0.25$ and non-dimensional slow times $t_1' = t\varepsilon\sqrt{gh}k_E = 0$, 5 and 10, as indicated in the legend. Only a subset of the full spatial domain is shown. The arrows denote the wave propagation (phase speed) and wind direction.

3.4 Results

We study the pressure magnitude's effect on solitary-wave evolution and shape by varying the KdV–Burgers equation's (3.18) one free parameter, $Pk_E/(\rho_w g\varepsilon)$, with emphasis on the contrast between onshore ($P > 0$) and offshore wind ($P < 0$). We revert to denoting non-dimensional variables with primes and dimensional ones without.

The wave profile η/h snapshots in figure 3.1 qualitatively show how the wave shape evolves over non-dimensional slow time $t_1' = t\varepsilon\sqrt{gh}k_E$ in the unforced solitary wave's frame. The onshore wind generates wave growth, apparent at the wave crest (figure 3.1a), whereas the offshore wind causes decay (figure 3.1b). The wind also changes the phase speed, with the wave's acceleration (deceleration) under an onshore (offshore) wind visible by the advancing (receding) of the crest. This is expected due to the (unforced) solitary wave's nonlinear phase speed (3.20) dependence on the wave height H.

In shallow water, wave growth/decay and phase speed changes are well-known wind effects [e.g. 69, 145], but wind-induced wave shape changes [131] have not been previously studied for shallow-water systems. Such changes are visible in figure 3.1 where, despite the wave starting from a symmetric, solitary-wave initial condition, the wind induces a horizontal asymmetry in the wave shape, particularly on the rear face

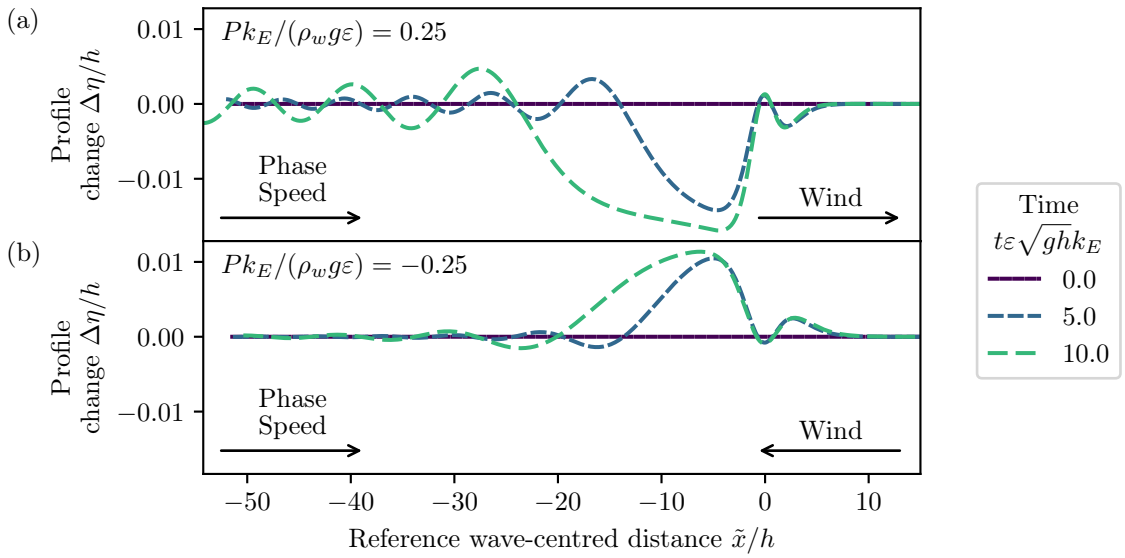

Figure 3.2. The non-dimensional profile change $\Delta\eta/h$ between the surface profile and reference solitary wave (3.19) under (a) onshore and (b) offshore Jeffreys forcing versus non-dimensional reference wave-centred distance $\tilde{x}/h$. Results are shown for $\varepsilon = 0.1$, $\mu_E = 0.6$, $|Pk_E/(\rho_w g\varepsilon)| = 0.25$ and non-dimensional slow times $t_1' = t\varepsilon\sqrt{gh}k_E = 0$, 5 and 10, as indicated in the legend. Only a subset of the full spatial domain is shown. The arrows denote the direction of wave propagation (phase speed) or wind direction.

($x < 0$) of the wave. The offshore wind (figure 3.1b) raises the rear base of the wave (near $x/h = -5$) relative to its initial profile (purple line), but the onshore wind (figure 3.1a) depresses the rear face and forms a small depression below the still water level at $t\varepsilon\sqrt{gh}k_E = 5$ (blue line) which widens and deepens at $t\varepsilon\sqrt{gh}k_E = 10$ (green line). Finally, the onshore wind (figure 3.1a) increases the maximum wave-slope magnitude with time while the offshore wind (figure 3.1b) decreases it, although the windward side of the wave becomes steeper than the leeward side for both winds (up to 8 % steeper for the time period shown). Although the equation is ill posed in the sense of Hadamard, the smooth solutions show that our solution is acceptable up to the current time and thus we are justified in neglecting a regularization scheme.

To further examine the wind-induced wave asymmetry, we fit η to a reference solitary-wave profile η_{ref} (3.19) by minimizing the L_1 difference, yielding the reference height $H_{\text{ref}}(t_1)$ and peak location $x_{\text{ref}}(t_1)$. The profile change is defined as $\Delta\eta(x) \coloneqq \eta - \eta_{\text{ref}}$ and is shown as a function of the reference wave-centred distance $\tilde{x} \coloneqq x - x_{\text{ref}}$ in figure 3.2. Notice that the profile change begins near the front face of the wave and has extrema for negative $\tilde{x}'$ but with opposite signs for onshore and offshore winds. Additionally, the magnitude of the extrema decay with distance in the $-\tilde{x}$ direction. Finally, note that the onshore (offshore) wind generates a small peak (trough) at $\tilde{x} = 0$ and two small troughs (peaks) near $\tilde{x}/h = \pm 3$, with the

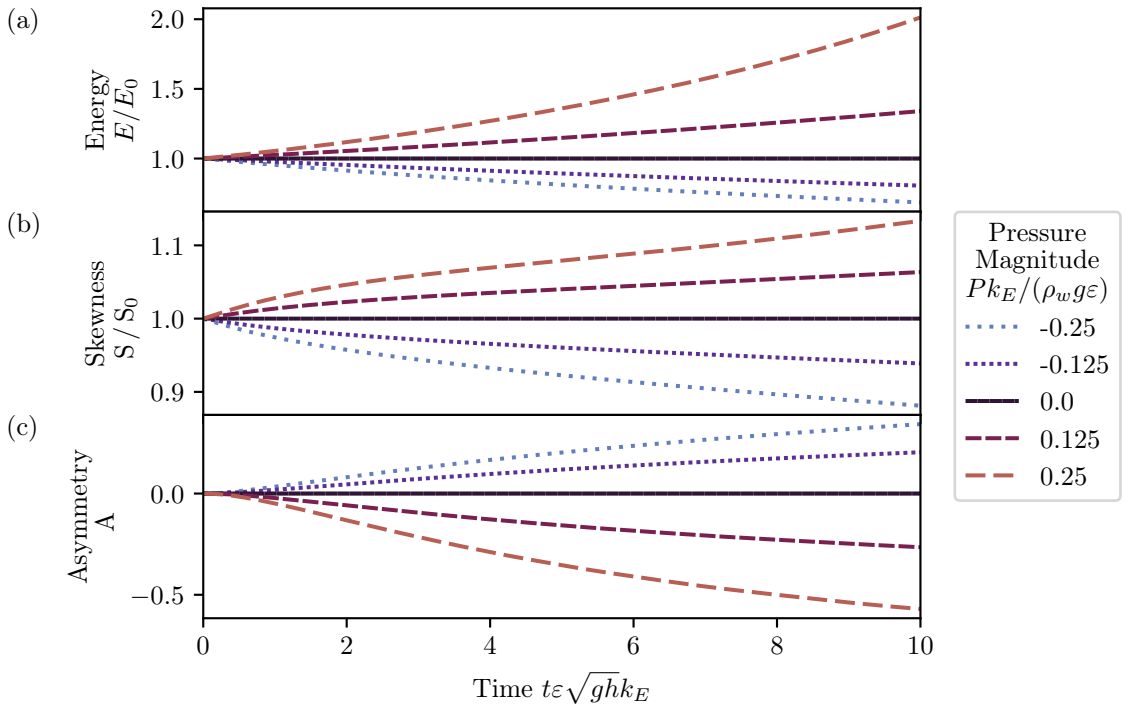

Figure 3.3. Solitary-wave shape statistics under onshore and offshore Jeffreys forcing versus non-dimensional slow time $t_1' = t\varepsilon\sqrt{gh}k_E = 0$–$10$. The (a) energy (normalized by the initial energy), (b) skewness (normalized by the initial skewness) and (c) asymmetry are defined in (3.21a–c). Results are shown for $\varepsilon = 0.1$, $\mu_E = 0.6$ and pressure magnitude $|Pk_E/(\rho_w g\varepsilon)|$ up to 0.25, as indicated in the legend. The solid black line is the unforced case, $P = 0$, and shows no growth or asymmetry and a constant skewness.

$\tilde{x} < 0$ extrema larger than the $\tilde{x} > 0$ one. This is analogous to a dispersive tail, well known in KdV-type systems [e.g. 136], and its appearance here helps explain the pressure-induced shape change (cf. § 3.5.2).

The effect of wind on wave shape is quantified by the time evolution of wave shape statistics — energy, skewness and asymmetry — for onshore and offshore wind (figure 3.3). We plot all cases for initial steepness $\varepsilon = 0.1$ up to slow time $t\varepsilon\sqrt{gh}k_E = 10$, corresponding to $10/\varepsilon = 100$ wave-crossing times, $T_0 = 1/(\sqrt{gh}k_E)$. The unforced case ($P = 0$) displays constant shape statistics and zero asymmetry, as expected. The normalized energy E/E_0 shows different growth/decay rates: the onshore wind ($P > 0$) causes accelerating wave growth while the offshore wind ($P < 0$) causes slowing wave decay (figure 3.3a). The energy of the unforced wave is virtually unchanged, with a normalized energy change of $1 - E/E_0 = -1 \times 10^{-13}$ at $t_1' = 10$. The onshore (offshore) wind causes the wave to become more (less) skewed over time, with the normalized skewness nearly symmetric about unity with respect to $\pm P$. Finally, the onshore wind causes a backwards tilt and negative asymmetry while the offshore wind increases the asymmetry and

causes a forward tilt, which was also seen in figure 3.1. Notice that |A| is larger for onshore winds than offshore winds. Since the definitions of the skewness and asymmetry are insensitive to waveform scaling $\eta \to \lambda\eta$, this effect is not simply caused by the wave's growth/decay. Instead, the onshore wind generates a larger dispersive tail (figure 3.2), which is the asymmetric wave component.

3.5 Discussion

3.5.1 Wind speed estimation

We now relate the non-dimensional pressure magnitude $Pk_E/(\rho_w g) = O(\varepsilon)$ to the wind speed. First, we need a relationship between the surface pressure and wave energy E (3.21*a*–*c*), which we can approximate using the standard procedure [e.g. 121] of multiplying the (non-dimensional, denoted by primes) KdV–Burgers equation (3.18) by η_0' and integrating from $x' = -\infty$ to ∞ to obtain

$$\frac{\partial}{\partial t_1'} \int_{-\infty}^{\infty} {\eta'}_0^2 \, \mathrm{d}x' = \int_{-\infty}^{\infty} P' \left(\frac{\partial \eta_0'}{\partial x'} \right)^2 \mathrm{d}x' \,. \tag{3.22}$$

The left integral is the non-dimensional energy (3.21*a*–*c*), so re-dimensionalizing and converting back to the full time t gives the energy growth rate γ,

$$\frac{\gamma}{c_0 k_E} \coloneqq \frac{1}{c_0 k_E E} \frac{\partial E}{\partial t} = \frac{P k_E}{\rho_w g} \frac{\langle (\partial_x \eta)^2 \rangle}{\langle (k_E \eta)^2 \rangle} = \frac{1}{5} \frac{P k_E}{\rho_w g}, \tag{3.23}$$

with $\langle (\partial_x \eta)^2 \rangle / \langle (k_E \eta)^2 \rangle = 1/5$ evaluated with the initial, solitary-wave profile (3.19) and the linear, shallow-water phase speed $c_0 = \sqrt{gh}$ coming from the re-dimensionalization of $t' = t c_0 k_E$ (3.7). Alternatively, a secondary multiple-scale approximation of the forward KdV–Burgers equation has been used previously to derive the energy growth rate for solitary waves as [143]

$$E \propto \frac{1}{(1 - \gamma t)^2} \quad \text{with} \quad \gamma \coloneqq b \left[\frac{P k_E}{\rho_w g} \right] c_0 k_E, \tag{3.24}$$

with analytically derived $b = 2/15$. Numerically fitting (3.24) to our calculated energy instead yields $b = 0.10081 \pm 0.00003$, similar to the analytic approximation. Note that the exponential energy growth (3.23) correctly approximates (3.24) for small times $\gamma t \ll 1$, and both expressions are consistent with the observed accelerating (decelerating) energy change for $P > 0$ ($P < 0$) in figure 3.3.

Next, Jeffreys's ([1925]) theory relates the growth rate of periodic waves to the wind speed $U_{\lambda/2}$,

measured at a height equal to half the wavelength $z = \lambda/2$, as

$$\frac{\gamma}{ck} = S_{\lambda/2}\frac{\rho_a}{\rho_w}\left(\frac{U_{\lambda/2}}{c} - 1\right)\left|\frac{U_{\lambda/2}}{c} - 1\right|, \tag{3.25}$$

with $S_{\lambda/2}$ a small, non-dimensional sheltering parameter potentially dependent on ε, μ_E and $U_{\lambda/2}/c$. For simplicity, we approximate the nonlinear phase speed c (given non-dimensionally in (3.20)) by its leading-order term $c_0 = \sqrt{gh}$, yielding an error of only 10 % in the subsequent calculations. Combining this approximation of (3.25) with (3.23) gives

$$U_{\lambda/2} = c_0\left(1 \pm \sqrt{\frac{1}{5}\left|\frac{Pk_E}{\rho_w g}\right|\frac{\rho_w}{\rho_a}\frac{1}{S_{\lambda/2}}}\right). \tag{3.26}$$

Here, the $\pm$ corresponds to onshore $(+)$ or offshore $(-)$ winds. Note that changing the wind direction (i.e. $\pm$ sign) while holding the surface pressure magnitude $|Pk_E/(\rho_w g)|$ constant means onshore wind speeds $\left|U_{\lambda/2}\right|$ will be larger than offshore wind speeds.

We can evaluate (3.26) for the parameters of § 3.4: $\varepsilon = 0.1$, $\mu_E = 0.6$ and $Pk/(\rho_w g\varepsilon) = 0.25$. Donelan et al. [125] parameterized $S_{\lambda/2}$ for periodic shallow-water waves with a dependence on airflow separation: $S_{\lambda/2} = 4.91\varepsilon\sqrt{\mu}$ for our non-separated flow (according to their criterion), with $\mu \coloneqq (kh)^2$. Assuming this holds approximately for solitary waves, we choose $\lambda = 2\pi/k_E = 20\,\mathrm{m}$ to calculate the wind speed at $z = \lambda/2 = 10\,\mathrm{m}$. This choice corresponds to a depth of $h = 2.5\,\mathrm{m}$ and initial wave height $H_0 = 0.5\,\mathrm{m}$ and yields a wind speed of $U_{10} = 22\,\mathrm{m\,s^{-1}}$, a physically realistic wind speed for strongly forced shallow-water waves. Weaker wind speeds will induce smaller surface pressures and thus take longer to change the wave shape.

3.5.2 Physical mechanism of asymmetry generation

Our initial, symmetric solitary waves (3.19) are permanent-form solutions of the unforced KdV equation. More generally, any initial solitary wave which does not exactly solve the KdV equation will evolve into a solitary wave and a trailing, dispersive tail according to the inverse scattering transform [e.g. 121]. In our system, the pressure continually perturbs the system away from the unforced KdV soliton solution resulting in a trailing, bound, dispersive tail (figure 3.2), which is responsible for the wave asymmetry. To see this, consider an initial, symmetric profile η. The pressure forcing term $P\partial_x^2\eta$ preserves the initial symmetry and induces a symmetric bound wave after a short time $\Delta t_1' \ll 1$. This is apparent when considering the non-dimensional KdV–Burgers equation (3.18) in the unforced solitary wave's frame

(figure 3.1) at the initial time,

$$\left.\frac{\partial \eta_0'}{\partial t_1}\right|_{t_1'=0} = -P' \frac{\partial^2}{\partial x^2}\left[\operatorname{sech}^2\left(\frac{x'}{2}\right)\right] \tag{3.27}$$

$$\implies \eta_0'(x', \Delta t_1') = (2 - P'\Delta t_1')\operatorname{sech}^2\left(\frac{x'}{2}\right) + P'\Delta t_1' \frac{3}{2}\operatorname{sech}^4\left(\frac{x'}{2}\right). \tag{3.28}$$

The $P'\Delta t_1'$ terms generate a small bound wave with a peak (trough) at $x' = 0$ and troughs (peaks) symmetrically in front and behind the wave peak for onshore (offshore) wind. As time increases, the continual pressure forcing causes the bound wave to grow and lengthen behind the wave, as is apparent in figure 3.2 (e.g. $\tilde{x}/h = -20$ to 3 for $P' = 0.25$ and $t_1' = 10$).

The small numerical value $|P'| = 0.25 \ll 1$ used in § 3.4 allows us to consider the wave's evolution as two steps with time scale separation. First, the pressure generates a bound wave (3.28) on the slow time scale, and then the wave evolves a dispersive tail on the fast time scale according to the inverse scattering transform of the unforced KdV equation. The dispersive tail in figure 3.2 (e.g. located left of $\tilde{x}/h = -20$ for $P' = 0.25$ and $t_1' = 10$) is analogous to the ubiquitous dispersive tails in prior studies on shallow-water solitary waves, such as figures 8(b) and 8(c) of Hammack and Segur [136]. However, unlike dispersive tails generated from initial conditions which fail to satisfy the KdV equation, our tail is continually forced and lengthened by the wind forcing. Finally, interactions with the trailing, dispersive tail are responsible for lengthening the bound wave (3.28) behind, rather than ahead, of the solitary wave. Hence, the disturbance induced by the pressure forcing (3.28) has two effects on the wave. First, the wind slowly generates a bound wave which changes the height and width of the initial solitary wave, which is reflected in the growth (decay) and narrowing (widening) under onshore (offshore) winds in figure 3.1. Second, it quickly generates an asymmetric, dispersive tail behind the wave (figure 3.2), producing a greater shape change on the wave's rear face (figure 3.1). Finally, the different wind directions (i.e. pressure forcing signs) change the sign of the bound wave and dispersive tail and, hence, the sign of the asymmetry in figure 3.3.

3.5.3 Comparison to intermediate and deep water

Zdyrski and Feddersen [131] investigated the effect of wind on Stokes-like waves in intermediate to deep water. This study, with wind coupled to waves in shallow water, finds qualitative agreement with those intermediate- and deep-water results. The shallow-water asymmetry magnitude increases as the pressure magnitude P increases (figure 3.3), and figure 4(a) of Zdyrski and Feddersen [131] displayed a similar trend for the corresponding Jeffreys pressure profile, with positive (negative) pressure increasing

(decreasing) the asymmetry. Although Zdyrski and Feddersen [131] compared their theoretical predictions to limited experimental results with $kh > 1$, there are no appropriate experiments on wind-induced changes to wave shape in shallow water for comparison with our results. In addition to the Jeffreys pressure profile employed here, Zdyrski and Feddersen [131] also utilized a generalized Miles profile, only applicable to periodic waves, wherein the pressure was proportional to η shifted by a distance parameter ψ_P/k. Future investigations could couple a higher-order Zakharov equation [e.g. 151] to a Jeffreys-type pressure forcing or to an atmospheric large eddy simulation, as was done for deep water by Hao and Shen [93]. Although this analysis focuses on solitary waves, we also investigated the effect of wind on periodic waves using the cnoidal-wave KdV solutions as initial conditions. Wind-forced cnoidal waves displayed qualitatively similar shape changes with stronger onshore (offshore) wind causing the energy and skewness to increase (decrease) while the asymmetry decreased (increased) with time. Furthermore, results were qualitatively similar across multiple classes of cnoidal waves with different values of μ_E, implying that these results apply rather generally.

3.6 Conclusion

Prior results [131] in intermediate and deep water demonstrated that wind, acting through a wave-dependent surface pressure, can generate shape changes that become more pronounced in shallower water. Here, we produced a novel analysis of wind-induced wave shape changes in shallow water using a multiple-scale analysis to couple weak wind with small, shallow-water waves, i.e. $a_0/h \sim (k_E h)^2 \sim Pk/(\rho_w g) \ll 1$. This analysis produced a KdV–Burgers equation governing the wave profile η, which we then solved numerically with a symmetric, solitary-wave initial condition. The deviations between the numerical results and a reference solitary wave had the form of a bound, dispersive tail, with differing signs for onshore and offshore wind. The tail's presence and shape are the result of a symmetric, pressure-induced shape change evolving under the inverse scattering transform. We also estimated the energy, skewness and asymmetry as functions of time and pressure magnitude. For onshore wind (positive P), the wave's energy and skewness increased with time while asymmetry decreased, while offshore wind produced the opposite effects. Furthermore, these effects were enhanced for strong pressures, and they reduced to the unforced case for $P = 0$. The shape statistics found here show qualitative agreement with the results in intermediate and deep water. Finally, the wind speeds corresponding to these pressure differences were calculated and found to be physically realistic.

3.7 Acknowledgements

We are grateful to D.G. Grimes and M.S. Spydell for discussions on this work. Additionally, we thank the anonymous reviewers for their suggestions and comments. We thank the National Science Foundation (OCE-1558695) and the Mark Walk Wolfinger Surfzone Processes Research Fund for their support of this work. The authors report no conflict of interest. Chapter 3, in full, is a reprint of the material as it appears in Wind-Induced Changes to Surface Gravity Wave Shape in Shallow Water in Journal of Fluid Mechanics by T. Zdyrski and F. Feddersen in 2021. The dissertation author was the primary investigator and author of this paper.

Chapter 4

Wind-induced changes to shoaling surface gravity wave shape

4.1 Abstract

Unforced shoaling waves experience growth and changes to wave shape, and wind-forced waves on a flat-bottom likewise experience growth/decay and changes to wave shape. However, the combination of shoaling and wind-forcing, particularly relevant in the near shore environment, has rarely been investigated. Here, we consider small-amplitude, shallow-water solitary waves propagating up a gentle, planar bathymetry forced by a weak, Jeffreys-type wind-induced surface pressure. We derive a variable-coefficient Korteweg–de Vries–Burgers equation governing the surface profile's evolution and solve it numerically using a Runge-Kutta third-order finite difference solver. The simulations run until convective pre-breaking, and we find that offshore winds weakly enhance the ratio of pre-breaking height to depth as well as pre-breaking slope. Onshore winds have a strong impact on narrowing the wave peak, and wind also modulates the rear shelf formed behind the wave. Furthermore, wind strongly affects the width of the pre-breaking zone, with larger effects for smaller beach slopes. After converting our pressure magnitudes to physically realistic wind speeds, we observe qualitative agreement with prior laboratory and numerical experiments.

4.2 Introduction

Wind couples to surface gravity waves leading to wave growth and decay as well as changes to wave shape. However, many aspects of wind-wave coupling are not yet fully understood. Since the sheltering theory of wind-wave coupling by Jeffreys [63], a variety of mechanisms for wind-wave interactions have been put forward, often with a focus on calculating growth rates [e.g. 68, 69]. Furthermore, these theories have been tested by many studies in the laboratory [e.g. 76, 85, 152, 153] and the field [e.g. 74, 125]. Similarly, numerical studies have modeled the airflow above waves using methods such as large eddy simulations [e.g. 89, 90, 108] or modeled the combined air and water domain using Reynolds-averaged Navier Stokes (RANS) solvers [e.g. 95] or direct numerical simulations [e.g. 88, 132].

While wave growth rates and airflow structure have received much attention, wind-induced wave shape changes have been less studied. Unforced, weakly nonlinear waves on flat bottoms (e.g. Stokes, cnoidal, and solitary waves) are horizontally symmetric about the peak (i.e. zero asymmetry) but are not vertically symmetric (i.e. non-zero skewness, [e.g. 104, 154]). Laboratory experiments of wind blowing over periodic waves have demonstrated that wave asymmetry increases with onshore wind speed in intermediate-water [e.g. 100] and deep-water [e.g. 101]. Theoretical studies have likewise shown that wind-induced surface pressure induces wave shape changes in both deep [131] and shallow [155] water. However, the influence of wind on wave shape has not yet been investigated for waves on a sloping bottom.

In contrast, the shoaling of unforced waves up a beach is a relatively well-studied phenomenon that causes wave growth and shape change. Field observations have revealed the importance of nonlinearity in wave shoaling and its relation to skewness and asymmetry [e.g. 59, 156]. Additionally, laboratory experiments of waves shoaling on planar beach slopes yield how the wave height and wave shape evolve with distance up the beach [e.g. 157–159]. Furthermore, numerical studies have investigated wave shoaling all the way to wave breaking. A variety of methods have been utilized, including pseudo-spectral models [e.g. 160], fully nonlinear potential flow boundary element method solvers [e.g. 161, 162], large eddy simulation volume of fluid methods [e.g. 162] and two-phase direct numerical simulations of both the air and water [e.g. 163]. Theoretical [e.g. 164] and numerical [e.g. 162] investigations of wave breaking have shown that convective wave breaking depends on the surface water velocity u and the phase speed c and occurs when the Froude number $\mathrm{Fr} \coloneqq u/c$ is approximately unity. The type of wave breaking (e.g. spilling, plunging, surging, etc.) is related to the beach slope β, initial wave height H_0 and initial wave width L_0 through the Iribarren number $\mathrm{ir} \coloneqq \beta/\sqrt{H_0/L_0}$ [e.g. 165, 166].

There have been extremely few studies looking at the combined effects of wind and shoaling of

surface gravity waves. Experimental studies have found that onshore wind increases the surfzone width [e.g. 167] and decreases the wave height-to-water depth ratio at breaking [e.g. 168], with offshore wind having the opposite effect. Additionally, numerical studies using two-phase RANS solvers of wind-forced solitary [e.g. 97] and periodic [e.g. 98] breaking waves have demonstrated that increasingly onshore winds enhance the wave height at all points prior to breaking. Furthermore, only Feddersen and Veron [101] have investigated the combined influence of wind and shoaling on wave shape, demonstrating that onshore winds enhance the shoaling-induced asymmetry while offshore winds reduce it. Nevertheless, a theoretical description of wind-induced changes to wave shoaling (e.g. wave shape, breaking location, etc.) has not yet been developed.

Therefore, this study will derive a simplified, theoretical model for wind-forced shoaling waves that takes the form of a variable-coefficient Korteweg–de Vries (KdV)–Burgers equation. The standard KdV equation describes unidirectional wave propagation with weak nonlinearity and dispersion in shallow, flat-bottomed domains [e.g. 136]. It has localized solutions which propagate without changing shape by balancing nonlinearity and dispersion known as solitary waves [e.g. 121]. Furthermore, arbitrary disturbances will decay into a number of discrete solitary waves as well as an oscillatory, dispersive tail [e.g. 136]. When the bottom bathymetry is allowed to vary, the coefficients of the KdV equation are no longer constant and the system is described by a variable-coefficient KdV (vKdV) equation [e.g. 169, 170]. The deformation of solitary waves propagating on a sloping-bottom vKdV system has been studied both analytically [e.g. 137] and numerically [e.g. 160] with solitary wave initial conditions becoming deformed and gaining a rear "shelf" for small enough slopes [e.g. 137]. Alternatively, if the flat-bottomed KdV equation is augmented with a wind-induced surface pressure forcing, the KdV–Burgers equation results [131]. These waves gain a dispersive tail similar to KdV non-solitary waves, but these tails grow continually and change polarity depending on the wind direction [131].

In this work, we begin by applying a wind-induced pressure forcing over a sloping bathymetry to derive a vKdV–Burgers equation and determining a convective pre-breaking condition in § 4.3. We will then solve the resulting vKdV–Burgers equation numerically using a third-order Runge-Kutta solver and investigate the changes to wave shape and pre-breaking location in § 4.4. Finally, we discuss the relationship between pressure and wind speed as well as the connection of our findings to previous laboratory and numerical studies in § 4.5.

4.3 vKdV–Burgers equation derivation and model setup

4.3.1 Governing equations

We derive a vKdV–Burgers equation for wind-forced shoaling waves by considering incompressible, irrotational, inviscid flows and neglecting surface tension. We restrict our attention to planar, two-dimensional waves propagating in the $+x$-direction. Additionally, we choose the $+z$-direction to be vertically upwards with the $z = 0$ datum at the mean water level and impose a bottom bathymetry at $z = -h(x)$. The standard incompressibility, bottom boundary, kinematic boundary and dynamic boundary conditions are

$$0 = \frac{\partial^2 \phi}{\partial x^2} + \frac{\partial^2 \phi}{\partial z^2} \qquad \text{on} \quad -h < z < \eta\,, \tag{4.1}$$

$$\frac{\partial \phi}{\partial z} = -\frac{\partial h}{\partial x}\frac{\partial \phi}{\partial x} \qquad \text{on} \quad z = -h, \tag{4.2}$$

$$\frac{\partial \phi}{\partial z} = \frac{\partial \eta}{\partial t} + \frac{\partial \phi}{\partial x}\frac{\partial \eta}{\partial x} \qquad \text{on} \quad z = \eta\,, \tag{4.3}$$

$$0 = \frac{p}{\rho_w} + g\eta + \frac{\partial \phi}{\partial t} + \frac{1}{2}\left[\left(\frac{\partial \phi}{\partial x}\right)^2 + \left(\frac{\partial \phi}{\partial z}\right)^2\right] \qquad \text{on} \quad z = \eta\,. \tag{4.4}$$

We have introduced the wave profile $\eta(x,t)$, the velocity potential $\phi(x,z,t)$ derived from the water velocity $\mathbf{u} = \boldsymbol{\nabla}\phi$, the surface pressure $p(x,t)$, the gravitational acceleration g and the water density ρ_w which is much larger than the air density $\rho_a \approx 1.225 \times 10^{-3}\rho_w$. Additionally, we removed the Bernoulli constant from the dynamic boundary condition by using the ϕ gauge freedom. Next, to examine the wind's effect on shoaling waves, we impose the analytically-simple Jeffreys-type surface pressure $p(x,t)$ forcing [63]:

$$p(x,t) = P\frac{\partial \eta(x,t)}{\partial x}\,. \tag{4.5}$$

The pressure constant $P \propto \rho_a(U-c)^2$ depends on the wave phase speed c and wind speed U (cf. § 4.5.1). For a wave propagating towards the shore, onshore winds yield $P > 0$ while offshore winds give $P < 0$. The application of a Jeffreys-type forcing to the flat-bottom KdV equation was discussed in Zdyrski and Feddersen [155].

4.3.2 Model domain and model parameters

The model domain (figure 4.1) consists of an initial flat section 20 units long at a depth of $h_0 = 1$ and transitions smoothly at $x = 0$ into a planar beach region with constant slope β and characteristic

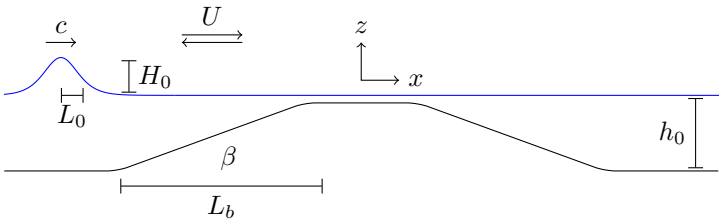

Figure 4.1. A schematic showing the (periodic) simulation domain and relevant length scales. The blue line represents the water surface and wave profile η, and the solid black line is the bottom bathymetry $h(x)$. The solitary wave initial condition has an effective half-width L_0 and height H_0 and begins with its peak on the far left side, in the middle of flat region of depth h_0. The initial wave then propagates to the right with phase speed c up the beach with slope β until it reaches pre-breaking (cf. § 4.3.6). The positive/negative wind speed U corresponds to an onshore/offshore wind forcing.

beach width $L_b \coloneqq h_0/\beta$, as defined by Knowles and Yeh [160]. The bathymetry then smoothly transitions to a flat plateau 40 units long at a depth of $h = 0.1$ followed by a downward slope with slope $-\beta$. Finally, there is another flat section at a depth of $h_0 = 1$ before the domain wraps periodically.

The initial condition will be a KdV solitary wave with height H_0 and width L_0 following Knowles and Yeh [160], and L_0 will be specified later. The solitary wave begins centered on the left boundary, in between the two flat, deep, 20 unit-long sections. From the defined dimensional quantities, we specify four non-dimensional parameters,

$$\varepsilon_0 \coloneqq \frac{H_0}{h_0}, \qquad \mu_0 \coloneqq \left(\frac{h_0}{L_0}\right)^2, \qquad P_0 \coloneqq \frac{P}{\rho_w g L_0}, \qquad \gamma_0 \coloneqq \frac{L_0}{L_b}. \tag{4.5a–d}$$

Here, ε_0 is the non-dimensional initial wave height, μ_0 is the square reciprocal of the non-dimensional initial wave width, P_0 is the non-dimensional pressure magnitude (normalized by the initial wave width), and γ_0 is ratio of the initial wave width to the beach width. Note that the wave-to-beach width parameter γ_0 is related to the beach slope β as $\gamma_0 = \beta/\sqrt{\mu_0}$. Together, these four non-dimensional parameters control the system's dynamics.

4.3.3 Non-dimensionalization

We non-dimensionalize our system's variables using the characteristic scales described in § 4.3.2: the initial depth h_0; the initial wave's height H_0; the initial wave's horizontal length scale L_0; the gravitational acceleration g; and the pressure magnitude P. Using primes for non-dimensional variables, we normalize

as Zdyrski and Feddersen [155] did and define

$$
\begin{aligned}
x &= L_0 x' = h_0 \frac{x'}{\sqrt{\mu_0}}\,, & h &= h' h_0\,, \\
z &= h_0 z'\,, & \eta &= H_0 \eta' = h_0 \varepsilon_0 \eta'\,, \\
t &= \frac{t' L_0}{\sqrt{g h_0}} = \frac{t'}{\sqrt{\mu_0}} \sqrt{\frac{h_0}{g}}\,, & \phi &= \phi' H_0 L_0 \sqrt{\frac{g}{h_0}} = \frac{\phi' \varepsilon_0}{\sqrt{\mu_0}} \sqrt{g h_0^3}\,.
\end{aligned}
\tag{4.6}
$$

We will later assuming the non-dimensional parameters ε_0, μ_0, γ_0 and P_0 are small to leverage a perturbative analysis. For the constant slope β beach profile, the spatial derivative of the bathymetry is also small $\partial_{x'} h' = \beta/\sqrt{\mu_0} = \gamma_0 \ll 1$ (the factor of $\sqrt{\mu_0}$ comes from the different non-dimensionalizations of h and x). However, perturbation analyses is simplest when all non-dimensional variables are $O(1)$. Therefore, we leverage the two, horizontal length scales L_0 and L_b (cf. § 4.3.2) to define a non-dimensional, stretched bathymetry $\tilde{h}'$ that depends on $x/L_b = \gamma_0 x'$ as $\tilde{h}'(\gamma_0 x') = h'(x')$. Then, denoting derivatives with respect to $\gamma_0 x'$ using an overdot, the derivative of $\tilde{h}$ is $\dot{\tilde{h}}' \coloneqq \partial_{\gamma_0 x'} \tilde{h}'(\gamma_0 x') = O(1)$, and the small slope becomes explicit as $\partial_{x'} h' = \gamma_0 \dot{\tilde{h}}'$.

Now, the non-dimensional equations take the form

$$
0 = \mu_0 \frac{\partial^2 \phi'}{\partial x'^2} + \frac{\partial^2 \phi'}{\partial z'^2} \qquad \text{on} \quad -1 < z' < \varepsilon_0 \eta'\,, \tag{4.7}
$$

$$
\frac{\partial \phi'}{\partial z'} = -\mu_0 \gamma_0 \dot{\tilde{h}}' \frac{\partial \phi'}{\partial x'} \qquad \text{on} \quad z' = -\tilde{h}'(\gamma_0 x')\,, \tag{4.8}
$$

$$
\frac{\partial \phi'}{\partial z'} = \mu_0 \frac{\partial \eta'}{\partial t'} + \varepsilon_0 \mu_0 \frac{\partial \phi'}{\partial x'} \frac{\partial \eta'}{\partial x'} \qquad \text{on} \quad z' = \varepsilon_0 \eta'\,, \tag{4.9}
$$

$$
0 = \varepsilon_0 P_0 \frac{\partial \eta'}{\partial x'} + \eta' + \frac{\partial \phi'}{\partial t'} + \frac{1}{2} \left[\varepsilon_0 \left(\frac{\partial \phi'}{\partial x'} \right)^2 + \frac{\varepsilon_0}{\mu_0} \left(\frac{\partial \phi'}{\partial z'} \right)^2 \right] \qquad \text{on} \quad z' = \varepsilon_0 \eta'\,. \tag{4.10}
$$

For the remainder of § 4.3, we remove the primes for clarity.

4.3.4 Boussinesq equations, multiple-scale expansion and vKdV–Burgers equation

We follow the conventional Boussinesq equation derivation presented in, e.g., Mei et al. [121] or Ablowitz [102]. The two modifications we include are the weakly sloping bottom, similar to the treatment in Johnson [169] and Mei et al. [121], and the inclusion of a pressure forcing like that of Zdyrski and Feddersen [155]. For the sake of brevity, we only detail the relevant differences here. First, we expand the

velocity potential in a Taylor series about the bottom $z = -h(x)$ as

$$\phi(x,z,t) = \sum_{n=0}^{\infty} \Big[z + \tilde{h}(\gamma_0 x)\Big]^n \phi_n(x,t)\,. \tag{4.11}$$

Substituting this expansion into the incompressibility equation (4.7) and bottom boundary condition (4.8) and assuming $\mu_0 \ll 1$ gives ϕ as a function of the velocity potential evaluated at the bottom $\varphi \coloneqq \phi_0$. If we further assume that the bottom is very weakly sloping $\gamma_0 \sim \mu_0 \ll 1$, this simplifies to

$$\phi = \varphi - \mu_0 \frac{1}{2}(z+\tilde{h})^2 \partial_x^2 \varphi + O\big(\mu_0^2, \gamma_0^2, \gamma_0\mu_0\big)\,. \tag{4.12}$$

Note that the assumption $\gamma_0 \sim \mu_0 \ll 1$ implies a moderate slope $\beta = \gamma_0\sqrt{\mu_0} \sim \mu_0^{3/2}$ and is used by several other authors [e.g. 137, 160, 169]. For reference, if $\mu_0 = \gamma_0 = 0.1$, then this implies a physically realistic $\beta = 0.03$. Svendsen and Hansen [170] compares this moderate slope to other theoretical derivations using larger or smaller slopes.

Substituting this ϕ expansion (4.12) into the kinematic and dynamic boundary conditions (4.9) and (4.10) yields Boussinesq-type equations with a pressure forcing term,

$$\partial_t \eta + \Big(\tilde{h} + \varepsilon_0\eta\Big)\partial_x^2\varphi \;+ \Big(\gamma_0\dot{\tilde{h}} + \varepsilon_0\partial_x\eta\Big)\partial_x\varphi - \mu_0\frac{1}{6}\tilde{h}^3\partial_x^4\varphi = O\big(\mu_0^2, \gamma_0^2, \gamma_0\mu_0\big)\,, \tag{4.13}$$

$$P_0\partial_x\eta + \eta + \partial_t\varphi - \frac{1}{2}\mu_0\tilde{h}^2\partial_x^2\partial_t\varphi + \frac{1}{2}\varepsilon_0(\partial_x\varphi)^2 = O\big(\mu_0^2, \gamma_0^2, \gamma_0\mu_0\big)\,. \tag{4.14}$$

Note that replacing $\tilde{h}$ with the total depth $h_{\text{total}} = \tilde{h} + \varepsilon_0\eta$ shows that these are equivalent to the flat-bottomed Boussinesq equations with $h_{\text{total}} = 1 + \varepsilon_0\eta$. In other words, any sloping-bottom terms $\dot{\tilde{h}}$ only appear in the combination $\partial_x h_{\text{total}} = \gamma_0\dot{\tilde{h}} + \varepsilon_0\partial_x\eta$. This is expected since the only sloping-bottom term $\mu_0\gamma_0\dot{\tilde{h}}\partial_x\phi$ in the governing equations (4.7)–(4.10) was dropped when we neglected terms of $O\big(\mu_0^2, \gamma_0^2, \gamma_0\mu_0\big)$.

Since the bathymetry varies on the slow scale x/γ_0, we expand our system in multiple spatial scales $x_n = \gamma_0^n x$ for $n = 0, 1, 2, \ldots$, so the derivatives become

$$\frac{\partial}{\partial x} \to \frac{\partial}{\partial x_0} + \gamma_0\frac{\partial}{\partial x_1} + \ldots\,, \tag{4.15}$$

and the bathymetry is a function of the long spatial scale $\tilde{h} = \tilde{h}(x_1)$. Then, we expand η and φ in

asymptotic series of ε_0

$$\eta(x,t) \to \sum_{k=0}^{\infty} \varepsilon_0^k \eta_k(t, x_0, x_1, \ldots)\,, \qquad \varphi(x,t) \to \sum_{k=0}^{\infty} \varepsilon_0^k \varphi_k(t, x_0, x_1, \ldots)\,. \tag{4.15a,b}$$

Similar to Johnson [169], we replace x_0 and t with left- and right-moving coordinates translating with speed $\tilde{c}(x_1)$ dependent on the stretched coordinate x_1:

$$\xi_+ = -t + \int^{x_0} \frac{\mathrm{d}x_0'}{\tilde{c}(\gamma_0 x_0')}\,, \qquad \xi_- = t + \int^{x_0} \frac{\mathrm{d}x_0'}{\tilde{c}(\gamma_0 x_0')}\,. \tag{4.16}$$

Then, we replace the derivatives ∂_t and ∂_{x_0} with

$$\frac{\partial}{\partial t} = \frac{\partial}{\partial \xi_-} - \frac{\partial}{\partial \xi_+}\,, \qquad \frac{\partial}{\partial x_0} = \frac{1}{\tilde{c}}\left(\frac{\partial}{\partial \xi_-} + \frac{\partial}{\partial \xi_+}\right). \tag{4.17}$$

Now, we will assume that $\varepsilon_0 \sim P_0 \sim \mu_0 \ll 1$ and follow the standard multiple-scale technique [e.g. 102, 121]. The order-one terms $O\big(\varepsilon_0^0\big)$ from (4.13) and (4.14) yield wave equations for ϕ_0 and η_0

$$\frac{\partial^2 \phi_0}{\partial \eta_+ \partial \eta_-} = 0\,, \qquad \frac{\partial^2 \eta_0}{\partial \eta_+ \partial \eta_-} = 0\,, \tag{4.17a,b}$$

with right-moving solutions

$$\varphi_0 = f_0(\xi_+, x_1) \quad \text{and} \quad \eta_0 = \partial_{\xi_+} f_0(\xi_+, x_1)\,, \tag{4.18}$$

propagating with the slowly varying, linear shallow-water phase speed $\tilde{c}(x_1) = \sqrt{\tilde{h}(x_1)}$. Continuing to $O(\varepsilon_0)$ of the asymptotic expansion gives

$$\begin{aligned} -\frac{\partial \eta_1}{\partial \xi_+} + \frac{\partial \eta_1}{\partial \xi_-} + \frac{\partial^2 \varphi_1}{\partial \xi_+^2} + 2\frac{\partial^2 \varphi_1}{\partial \xi_+ \partial \xi_-} + \frac{\partial^2 \varphi_1}{\partial \xi_-^2} &= -2\frac{\gamma_0}{\varepsilon_0}\tilde{c}\frac{\partial^2 \varphi_0}{\partial \xi_+ \partial x_1} + \frac{\partial \tilde{c}}{\partial x_1}\frac{\partial \varphi_0}{\partial \xi_+} \\ &\quad - \frac{1}{\tilde{c}^2}\eta_0 \frac{\partial^2 \varphi_0}{\partial \xi_+^2} - \frac{\gamma_0}{\varepsilon_0}\frac{\dot{\tilde{h}}}{\tilde{c}}\frac{\partial \varphi_0}{\partial \xi_+} - \frac{1}{\tilde{c}^2}\frac{\partial \eta_0}{\partial \xi_+}\frac{\partial \varphi_0}{\partial \xi_+} + \frac{\mu_0}{\varepsilon_0}\tilde{h}\frac{1}{6}\frac{\partial^4 \varphi_0}{\partial \xi_+^4}\,, \end{aligned} \tag{4.19}$$

$$\eta_1 - \frac{\partial \varphi_1}{\partial \xi_+} + \frac{\partial \varphi_1}{\partial \xi_-} = -\frac{\alpha}{\varepsilon_0}p_0 - \frac{1}{2}\frac{\mu_0}{\varepsilon_0}\tilde{h}\frac{\partial^3 \varphi_0}{\partial^3 \xi_+} - \frac{1}{2\tilde{c}^2}\left(\frac{\partial \varphi_0}{\partial \xi_+}\right)^2. \tag{4.20}$$

Eliminating η_1 from these equations gives

$$4\frac{\partial^2 \phi_1}{\partial \xi_+ \partial \xi_-} = -2\frac{\gamma_0}{\varepsilon_0}\tilde{c}\frac{\partial \eta_0}{\partial x_1} - \frac{\gamma_0}{\varepsilon_0}\frac{\partial \tilde{c}}{\partial x_1}\eta_0 - 3\frac{1}{\tilde{c}^2}\eta_0\frac{\partial \eta_0}{\partial \xi_+} - \frac{1}{3}\frac{\mu_0}{\varepsilon_0}\tilde{c}^2\frac{\partial^3 \eta_0}{\partial \xi_+^3} - \frac{1}{\tilde{c}}\frac{P_0}{\varepsilon_0}\frac{\partial^2 \eta_0}{\partial \xi_+^2}\,. \tag{4.21}$$

The left-hand operator $\partial^2/\partial\xi_-\partial\xi_+$ is the same as the $O(1)$ differential operator (4.17*a,b*). Therefore, the right-hand side must vanish to prevent ϕ_1 from developing secular terms. Thus, the right-hand side becomes the variable-coefficient Korteweg–de Vries–Burgers (vKdV–Burgers) equation

$$\frac{\gamma_0}{\varepsilon_0}\tilde{c}\frac{\partial\eta_0}{\partial x_1} + \frac{1}{2}\frac{\gamma_0}{\varepsilon_0}\frac{\partial\tilde{c}}{\partial x_1}\eta_0 + \frac{3}{2}\frac{1}{\tilde{c}^2}\eta_0\frac{\partial\eta_0}{\partial\xi_+} + \frac{1}{6}\frac{\mu_0}{\varepsilon_0}\tilde{c}^2\frac{\partial^3\eta_0}{\partial\xi_+^3} + \frac{1}{2\tilde{c}}\frac{P_0}{\varepsilon_0}\frac{\partial^2\eta_0}{\partial\xi_+^2} = 0\,. \tag{4.22}$$

Finally, multiplying (4.22) by ε, adding the $O(1)$ differential equation $\partial_{\xi_-}\eta_0 = 0$ derived from (4.17*a,b*), and transforming back to the original, non-dimensional variables x and t yields

$$\frac{\partial\eta_0}{\partial t} + c\frac{\partial\eta_0}{\partial x} + \frac{1}{2}\frac{\partial c}{\partial x}\eta_0 + \frac{3}{2}\varepsilon_0\frac{1}{c}\eta_0\frac{\partial\eta_0}{\partial x} + \frac{1}{6}\mu_0 c^5\frac{\partial^3\eta_0}{\partial x^3} + \frac{1}{2}P_0 c\frac{\partial^2\eta_0}{\partial x^2} = 0\,. \tag{4.23}$$

The pressure term $P_0\partial_x^2\eta_0$ functions as a damping, positive viscosity for offshore $P_0 < 0$ wind, making (4.23) a (forward) vKdV–Burgers equation. Conversely, onshore $P_0 > 0$ wind causes a growth-inducing, negative viscosity giving the backward vKdV–Burgers equation. The backward, constant-coefficient KdV–Burgers equation is ill posed in the sense of Hadamard [149]. Though it is possible the backward vKdV–Burgers equation is also ill posed for certain bathymetries $\tilde{h}$, this is irrelevant here owing to the finite time it takes the wave to reach the beach.

4.3.5 Initial conditions

Our initial condition will be the solitary-wave solutions of the unforced ($P_0 = 0$), flat-bottom KdV equation. These waves balance the KdV equation's nonlinearity $\eta_0\partial_x\eta_0$ and dispersion $\partial_x^3\eta_0$ terms, propagate without changing shape and require that the height H_0 and width L_0 satisfy $H_0L_0^2 =$ constant. Therefore, we now fix the previously unspecified L_0 by choosing $\mu_0 = (3/4)\varepsilon_0$ so L_0 acts like an effective half-width for the solitary wave initial condition [e.g. 121]

$$\eta_0 = \operatorname{sech}^2(x)\,, \tag{4.24}$$

While the unforced KdV equation also possesses periodic solutions called cnoidal waves, we only consider solitary waves here.

4.3.6 Convective breaking criterion

The asymptotic assumptions used to derive the vKdV–Burgers equation (4.23) fail when the wave gets too large. Therefore, we require a condition to determine when the simulations should stop. We use a convective "pre-breaking" condition similar to that derived by Brun and Kalisch [164] for solitary waves on a flat-bottom depending on the wave velocity profile $u(x,t)$ at the surface and the phase speed c. They utilized the local Froude number $\mathrm{Fr} \coloneqq \varepsilon_0 u(x,t)/c$, with the ε_0 coming from non-dimensionalization, and defined convective breaking to occur wherever $\max_x(\mathrm{Fr}) = 1$, where $\max_x$ represents the maximum over x. However, when the Froude number approaches the breaking value of unity, our weakly-nonlinear asymptotic assumption used to derive the vKdV–Burgers equation are violated. Thus, we instead stop our simulations at the smaller pre-breaking Froude number $\mathrm{Fr}_{\mathrm{pb}} \coloneqq 1/3$ and define the pre-breaking time t_{pb} as the first time this condition is met:

$$\max_x(\mathrm{Fr}) \coloneqq \max_x\left(\varepsilon_0 \frac{u(x)}{c_{\mathrm{adi}}}\right) = \mathrm{Fr}_{\mathrm{pb}} \coloneqq \frac{1}{3}\,. \tag{4.25}$$

Likewise, we define x_{pb} as the location on the wave where $\mathrm{Fr} = \mathrm{Fr}_{\mathrm{pb}}$, which will be very near the wave peak. To calculate Fr, we need to estimate $u(x,t)$ and c.

As the solitary wave propagates on a slope, the wave evolves over time and the phase speed c can be ambiguous. One option is to use the adiabatic approximation derived by [137] for unforced solitary waves on very gentle slopes:

$$c_{\mathrm{adi}} = \sqrt{h(x_{\mathrm{peak}})}\left(1 + \frac{\varepsilon_0}{2}\frac{\eta(x_{\mathrm{peak}})}{h(x_{\mathrm{peak}})}\right), \tag{4.26}$$

with x_{peak} the location of the wave peak. Alternatively, Derakhti et al. [162] used large eddy simulations to numerically investigate unforced solitary wave breaking on slopes ranging from $\beta = 0.2$ to 0.005 for two different forms of c. They found wave breaking at $\max_x(\mathrm{Fr}) = 0.85$ when using the speed of the numerically-tracked wave peak c_{peak}. However, they also found that the shallow-water approximation $c_{\mathrm{shallow}} = \sqrt{h(x_{\mathrm{peak}}) + \varepsilon_0\eta(x_{\mathrm{peak}})}$ (equivalent to c_{adi} to $O(\varepsilon_0^2)$) was within 15 % of c_{peak} near breaking. Therefore, we will use (4.26) owing to its simplicity and theoretical foundation. Finally, though these studies all considered unforced solitary waves, our results will show that c_{adi} varies approximately 3 % across pressure magnitudes P_0 for our simulations, so this is a valid approximation.

We now derive the wave velocity profile $u(x,z,t) = \boldsymbol{\nabla}\phi$ by modifying the example of Brun and Kalisch [164] to include sloping bathymetry and pressure forcing. We begin by combining the vKdV–Burgers

equation (4.23) and kinematic boundary condition (4.13) to eliminate $\partial_t \eta$ and yield

$$\begin{aligned}\tilde{c}^2 \frac{\partial^2 \varphi}{\partial x^2} - \tilde{c} \frac{\partial \eta}{\partial x} + \varepsilon_0 \left(\eta \frac{\partial^2 \varphi}{\partial x^2} + \frac{\partial \eta}{\partial x} \frac{\partial \varphi}{\partial x} - \frac{3}{2} \frac{1}{\tilde{c}} \eta \frac{\partial \eta}{\partial x} \right) - P_0 \frac{1}{2} \tilde{c} \frac{\partial^2 \eta}{\partial x^2} \\ - \mu_0 \left(\frac{1}{6} \tilde{c}^6 \frac{\partial^4 \varphi}{\partial x^4} + \frac{1}{6} \tilde{c}^5 \frac{\partial^3 \eta}{\partial x^3} \right) + \gamma_0 \left(2\tilde{c} \frac{\partial \tilde{c}}{\partial x_1} \frac{\partial \varphi}{\partial x} - \frac{1}{2} \eta \frac{\partial \tilde{c}}{\partial x_1} \right) = 0 \,.\end{aligned} \tag{4.27}$$

Assuming an ansatz

$$\frac{\partial \varphi}{\partial x} = \frac{1}{\tilde{c}} \eta + \varepsilon_0 A(x,t) + \gamma_0 B(x,t) + \mu_0 C(x,t) + P_0 D(x,t) \tag{4.28}$$

$$\implies \frac{\partial^2 \varphi}{\partial x^2} = \frac{1}{\tilde{c}} \frac{\partial \eta}{\partial x} + \varepsilon_0 \frac{\partial A}{\partial x} + \gamma_0 \left(\frac{\partial B}{\partial x} - \frac{1}{\tilde{c}^2} \eta \frac{\partial \tilde{c}}{\partial x_1} \right) + \mu_0 \frac{\partial C}{\partial x} + P_0 \frac{\partial D}{\partial x} \,, \tag{4.29}$$

we insert (4.28) and (4.29) into (4.27), drop terms of $O(\varepsilon^2)$ and solve for A, B, C, and D by using the independence of ε_0, γ_0, μ_0 and P_0:

$$A = -\frac{1}{4\tilde{c}^3} \eta^2 \,, \qquad B = -\frac{\tilde{c}'}{2\tilde{c}^2} \int_{+\infty}^{x} \eta(x') \, \mathrm{d}x' \,, \qquad C = \frac{\tilde{c}^3}{3} \frac{\partial^2 \eta}{\partial x^2} \,, \qquad D = \frac{1}{2\tilde{c}} \frac{\partial \eta}{\partial x} \,. \tag{4.29a–d}$$

Note that A represents the nonlinear contribution, B the effect of shoaling, C the dispersive effect, and D the pressure forcing. Finally, the Taylor expansion of $\phi(x,z)$ (4.12) gives the fluid velocity at the surface $u(x,t,z=\varepsilon_0\eta) = \partial_x \phi$ as

$$\begin{aligned}u(x,t) &= \partial_x \varphi - \mu_0 \frac{1}{2} \tilde{c}^4 \partial_x^3 \varphi \\ &= \frac{1}{\tilde{c}} \eta - \varepsilon_0 \frac{1}{4\tilde{c}^3} \eta^2 + P_0 \frac{1}{2\tilde{c}} \frac{\partial \eta}{\partial x} - \mu_0 \frac{\tilde{c}^3}{6} \frac{\partial^2 \eta}{\partial x^2} - \gamma_0 \frac{\tilde{c}'}{2\tilde{c}^2} \int_{\infty}^{x} \eta(x') \, \mathrm{d}x' \,.\end{aligned} \tag{4.30}$$

Therefore, the Froude number is calculated as

$$\mathrm{Fr} := \frac{\varepsilon u(x,t)}{\sqrt{h(x_{\mathrm{peak}})}} \left(1 + \frac{\varepsilon_0}{2} \frac{\eta(x_{\mathrm{peak}})}{h(x_{\mathrm{peak}})} \right)^{-1} , \tag{4.31}$$

with $u(x,t)$ given by (4.30), and (4.25) defines our pre-breaking condition.

4.3.7 Numerics

The vKdV–Burgers equation (4.23) lacks analytic, solitary-wave-type solutions, so we solve it numerically using a third-order explicit Runge-Kutta adaptive time-stepper with the error controlled by a second-order Runge-Kutta method as implemented in SciPy [171]. We discretize the spatial domain using

Table 4.1. Range of non-dimensional parameters simulated.

Parameter	Range
ε_0	0.2
μ_0	0.15
$\lvert P/(\rho_w g L_0 \varepsilon_0)\rvert$	0.003125, 0.00625, 0.0125, 0.025, 0.05
β	0.01, 0.015, 0.02, 0.025

a fourth-order finite difference method on a periodic domain with grid spacing $\mathrm{d}x = 0.05$. We employ adaptive time stepping to keep the relative error below 10^{-6} and the absolute error below 10^{-3} at each step. For all cases, the average time-step is $\Delta t \approx 2 \times 10^{-3}$. The pressure is initially turned off until the solitary wave is one unit (i.e. a half-width L_0) away from the start of the beach slope. The pressure is linearly ramped up to its full value over the time it takes the wave to cross a full-width $2L_0$. For numerical stability, we included a biviscosity $\nu_{\mathrm{bi}}\partial_x^4\eta_0$ with $\nu_{\mathrm{bi}} = 1 \times 10^{-5}$.

We validated the solver against the unforced, flat-bottom analytical solution and had a normalized root-mean-square error of 3.9×10^{-4} after non-dimensional time $t = 100$ (longer than the longest simulation) as well as a normalized wave height change of $1 - [\max(\eta_0) - \min(\eta_0)]/\left[\max(\eta_0^{(0)}) - \min(\eta_0^{(0)})\right] = 2.4 \times 10^{-4}$. Furthermore, the results were qualitatively consistent with the simulations of Knowles and Yeh [160] of an unforced solitary wave shoaling on a slope. Finally, the simulation reproduced the finding of Knowles and Yeh [160] that small waves ($\varepsilon_0 \ll 1$) on weak slopes ($\gamma_0 \ll 1$) yield Green's Law for the wave height $H(x) \coloneqq \max_t(\eta) \propto h(x)^{1/4}$ (with $\max_t$ the maximum over time t), while moderate waves ($\varepsilon_0 < 1$) on very weak slopes ($\gamma_0 \lll 1$) give Miles' adiabatic law $H(x) \propto h(x)^{-1}$ [172].

The vKdV–Burgers equation (4.22) is determined by two non-dimensional parameter combinations: the pressure term P_0/ε_0 and the shoaling term γ_0/ε_0. Recall that the dispersive term μ_0/ε_0 is a redundancy which we fixed by specifying L_0 (cf. § 4.3.5). We investigate this two-dimensional parameter space by choosing $\varepsilon_0 = 0.2$ and $\mu_0 = 0.15$ and varying the beach slope $\beta = 0.01$ to 0.025 and pressure $P = 0.003125$ to 0.05 (cf. § 4.5.1 for a discussion of the size of P). This yields a total of 20 simulations (table 4.1). Note that (4.22) demonstrates changing $\varepsilon_0 \to \lambda\varepsilon_0$ is equivalent to $\gamma_0 \to \gamma_0/\lambda$ in the wave's co-moving reference frame. Therefore, solutions for waves with different initial heights ε_0 can be generated from our solutions to the vKdV–Burgers equation in the lab frame (4.23) by scaling the height, boosting, and adjusting γ_0. We also note that the asymptotic expansion assumed $P_0 \sim \varepsilon_0$, or $P/(\rho_w g L_0 \varepsilon_0) \sim 1$, but the pressure values we are using (table 4.1) are smaller than unity. Nevertheless, multiple-scale expansions are often accurate outside their parameters' validity ranges, and this constraint would be satisfied asymptotically for smaller values of ε_0.

4.3.8 Shape statistics

When stopping the simulations at t_{pb} (§ 4.3.6), we are interested in determining the wave location x_{pb} at pre-breaking. To estimate how x_{pb} changes, we first calculate the shoreline x_{shore} as the location where the bathymetry would intersect $z = 0$ if it had a constant slope β without our shallow plateau. Then, we calculate the pre-breaking zone width as $x_{\text{pz}} \coloneqq x_{\text{pb}} - x_{\text{shore}}$. For a given beach slope β, we will analyze the change in pre-breaking zone width relative to the unforced case $\Delta x_{\text{pz}} \coloneqq x_{\text{pz}} - x_{\text{pz}}\big|_{P=0}$ normalized by the unforced pre-breaking zone width $x_{\text{pz}}\big|_{P=0}$. This global statistic $\Delta x_{\text{pb}}/(x_{\text{pb}}\big|_{P=0})$ determines the variance in pre-breaking locations as a fractional change of the pre-breaking zone width.

Additionally, we will investigate four more shape statistics that vary as the wave propagates. The first three are local shape parameters defined at each location x. First, we directly examine the maximum Froude number $\max_t(\text{Fr})$ expressed in (4.31). Second, we investigate the maximum height relative to the local water depth $\max_t(\eta)/h(x)$ at each location x. Third, we consider the maximum slope $\max_t(|\partial\eta/\partial x|)$. Both the relative height and maximum slope contribute to the convective breaking criterion (4.25). Finally, we introduce a global shape parameter, the full width of the wave at half of the wave's maximum (FWHM) $L_W(t)$ normalized by the local water depth $h(x)$. For our unforced KdV solitary wave initial condition (4.24), the FWHM divided by the initial depth is $L_W/h_0 = 2\cosh^{-1}(\sqrt{2})/\sqrt{\mu_0}$. We seek to compare this global shape parameter defined at each point in time t with the local parameters defined at each point in space. Therefore, we define $L_W(x) = L_W(t_{\text{peak}}(x))$ at the time $t_{\text{peak}}(x)$ when the wave peak passed location x.

4.4 Results

Now, we use the results of the numerical simulations to investigate the effect of wind on solitary wave shoaling. We will present shape statistics (§ 4.3.8) for the 20 different runs (table 4.1) to detail the wave shape changes and pre-breaking behavior across the parameter space. For the remainder of the paper, we will utilize dimensional variables for easier comparison to experiments and observations.

4.4.1 Profiles of shoaling solitary waves with wind

First, we qualitatively investigate the effect of varying pressures P and bathymetric slopes β on solitary-wave shoaling by examining the wave profile η/h_0, normalized by the initial depth h_0, at three different times t (figure 4.2) corresponding to when the solitary wave first feels the slope ($t = 0$), the time

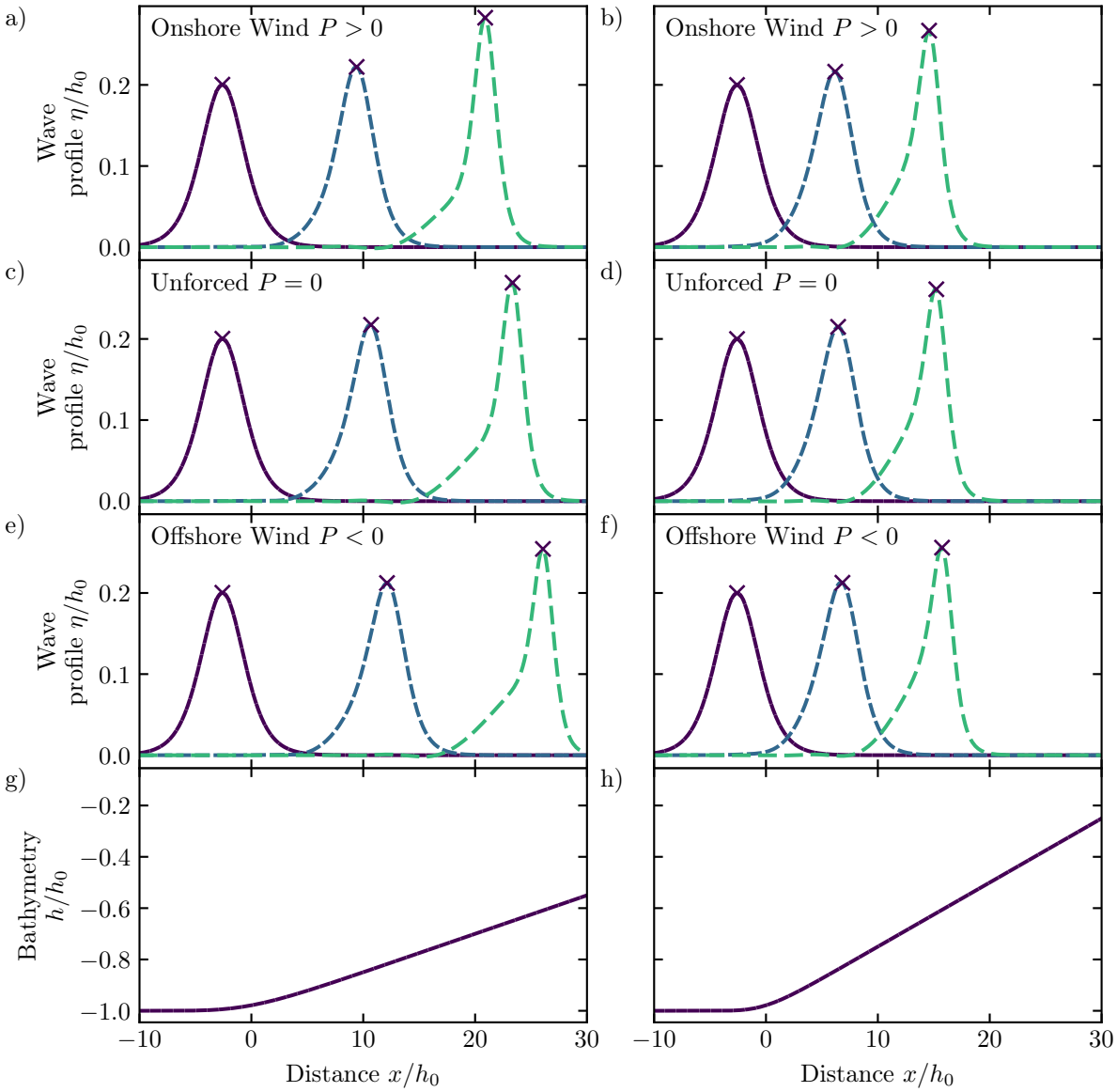

Figure 4.2. Shoaling solitary-wave η evolution under (a,b) onshore $P > 0$, (c,d) unforced $P = 0$ and (e,f) offshore $P < 0$ wind-induced surface pressure versus non-dimensional distance x/h_0 as the wave propagates up the (g,h) planar bathymetry. The profile times shown depend on the Froude number (4.31) and therefore vary between the panels. The first profile (purple) occurs when the peak is located at $x = -L_0$ where the pressure begins turning on, and the time is defined so $t = 0$ here. The last profile (green) occurs when the convective pre-breaking condition $\max_x(\mathrm{Fr}) = \mathrm{Fr}_{\mathrm{pb}} = 1/3$ is met (cf. § 4.3.6), and the middle profile (blue) occurs at a time halfway between the first and last profiles. Both columns have $\varepsilon_0 = 0.2$ and $\mu_0 = 0.15$, and the left-column forced cases (a,e) have $|P/(\rho_w g L_0 \varepsilon_0)| = 0.05$ and $\beta = 0.015$ while the right-column forced cases (b,f) use $|P/(\rho_w g L_0 \varepsilon_0)| = 0.025$ and $\beta = 0.25$. The x's denote the locations with the highest Froude number (4.31), and the x's on the last profiles (green) are the pre-breaking locations x_{pb}. We only display a subset of the full spatial domain.

of pre-breaking ($t = t_{\text{pb}}$) and half-way between ($t = t_{\text{pb}}/2$). We note that these $t = 0$ wave profiles (purple in figure 4.2) are nearly identical to the $\text{sech}^2(x/L_0)$ initial condition (4.24) since the waves have only propagated over a flat bottom (figures 4.2*g*,*h*) and the pressure has not yet been turned on. Halfway to pre-breaking ($t = t_{\text{pb}}/2$, blue), the solitary wave has grown through shoaling with a steeper front face ($+x$ side) and increased asymmetry for all P and β. At the time of pre-breaking ($t = t_{\text{pb}}$, green) the solitary wave has increased in height, steepened, and gained a substantial rear shelf for all P and β. Onshore wind ($P > 0$) reinforces the shoaling-based wave growth and yields relatively narrow peak widths for both β (figures 4.2*a*,*b*). In contrast, offshore wind ($P < 0$) reduces the wave shoaling but results in wider peak widths (figures 4.2*a*,*b*). These differences in wave-shoaling result in the offshore-forced ($P < 0$) solitary wave reaching pre-breaking (x_{pb}, x's in figure 4.2) farther onshore (shallower water) than the onshore-forced ($P > 0$) solitary wave. Similarly, the larger beach slope ($\beta = 0.025$, figures 4.2*b*,*d*,*f*) causes waves to reach x_{pb} in less horizontal distance, though they pre-break in shallow water than the milder beach slope ($\beta = 0.015$) waves. At $t = t_{\text{pb}}$, the rear shelf is wider and extends higher up the rear face for offshore winds ($\approx 0.1h_0$ in figure 4.2*e*) than for onshore winds ($\approx 0.07h_0$ in figure 4.2*a*). As the control case, the unforced ($P = 0$) solitary wave has x_{pb} located between the onshore and offshore wind cases with an intermediate rear shelf. Finally, the milder slope ($\beta = 0.015$) has a sharper, more pronounced rear shelf while the steeper slope ($\beta = 0.025$) has a more gently sloping rear shelf.

We next investigate the impact of onshore (figures 4.3*a*,*c*,*e*) and offshore (figures 4.3*b*,*d*,*f*) wind on shoaling waves' slopes $\partial_x\eta$ and wave velocity profiles $u/\sqrt{gh_0}$. The wave slope (figures 4.3*c*,*d*) highlights the shoaling- and wind-induced shape changes by accentuating the front-rear asymmetry. At $t = 0$ (purple figures 4.3*a*,*b*), the wave slope has odd-parity about the peak. However, as the wave propagates onshore, both the front and rear face steepen, though the front face steepens more dramatically. The influence of the wind is most noticeable in three aspects: the offshore-forced wave ($P = -0.05$, figure 4.3*b*) is 10 % smaller than the onshore forced wave ($P = 0.05$, figure 4.3*a*); the offshore-forced rear-face wave slope (figure 4.3*d*) is 15 % smaller than the onshore-forced wave slope (figure 4.3*c*), though the front-face slope is only 2 % smaller; and the trailing shelf's slope extends further behind the offshore-forced wave ($\approx 8h_0$, figure 4.3*d*) than the onshore-forced wave ($\approx 5h_0$, figure 4.3*c*). The wave velocity profile $u/\sqrt{gh_0}$ ((4.30), figures 4.3*e*,*f*) nearly mirrors the wave profile (figures 4.3*a*,*b*), as is expected given that $u \propto \eta$ to leading order (4.30). Finally, the phase speed c_{adi} (red, (4.26)) decreases as the wave shoals which enhances convective pre-breaking, though it only varies 3 % between onshore and offshore wind. Note, in figures 4.3(*e*,*f*), c_{adi} is multiplied by $\text{Fr}_{\text{pb}} = 1/3$ so that the intersection of the red curve with the wave

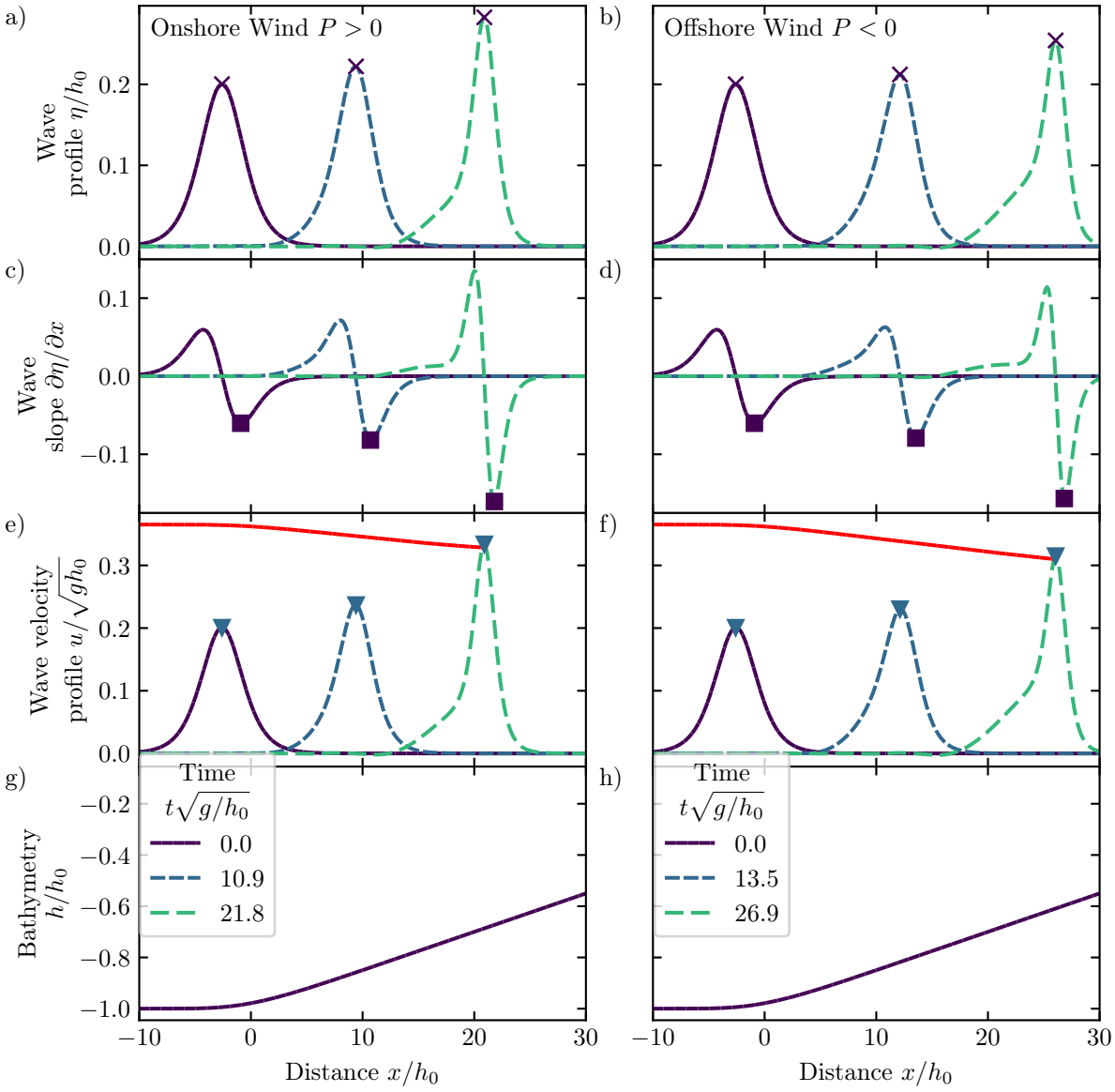

Figure 4.3. Shoaling solitary-wave (a,b) non-dimensional profile η/h_0, (c,d) slope $\partial\eta/\partial x$ (e,f) and non-dimensional wave velocity profile $u/\sqrt{gh_0}$ under (a,c,e) onshore and (b,d,f) offshore wind-induced surface pressure as the wave propagates up the (g,h) planar bathymetry. Values are shown versus non-dimensional distance x/h_0 for $\varepsilon_0 = 0.2$, $\mu_0 = 0.15$, $|P/(\rho_w g L_0 \varepsilon_0)| = 0.05$, $\beta = 0.015$ and non-dimensional times $t\sqrt{gh}/L_0$ indicated in the legends. The red lines in (e,f) represent the phase speed c_{adi} (4.26) at each location multiplied by the pre-breaking Froude number $\text{Fr}_{\text{pb}} = 1/3$. The x's denote the locations with the highest Froude number, and the x's on the last (green) profiles are the pre-breaking locations x_{pb}. The squares are the locations of the maximum slope magnitude $|\partial\eta/\partial x|$, and the upside-down triangles represent the locations of the maximum wave velocity profile. We only display a subset of the full spatial domain.

velocity profile occurs at x_{pb}, the location of pre-breaking.

4.4.2 Shape statistics with shoaling and variations of pre-breaking zone width with wind

Building on the previous qualitative descriptions of the wave profile, slope, and wave velocity profile, we also quantify the change in the shoaling wave's shape parameters for onshore and offshore P (figure 4.4). First, we consider the maximum Froude number $\max_t(\mathrm{Fr})$ as a function of non-dimensional position x/h_0 (figure 4.4a). In the flat region ($x < 0$), the maximum Froude number is $\max_t(\mathrm{Fr}) = 0.1818$, and it increases as the waves shoal to the pre-breaking value $\max_t(\mathrm{Fr}) = \mathrm{Fr}_{\mathrm{pb}} = 1/3$ (light gray line). The wind has a significant impact on the location of pre-breaking x_{pb}, with onshore wind (red) causing the Froude number to increase faster and x_{pb} to occur farther offshore than offshore wind (blue) does. This can also be seen in figures 4.3(e,f), where the maximum velocities $u/\sqrt{gh_0}$ (upside-down triangles), which are proportional to $\max_t(\mathrm{Fr})$, are growing faster for the onshore wind (figure 4.3e) than the offshore wind (figure 4.3f). Notably, at a fixed location x/h_0, the $\max_x(\mathrm{Fr})$ varies substantially (e.g. 0.25 to 0.30 at $x/h_0 = 20$). In addition, we consider the maximum height at a fixed location $\max_t(\eta)$ normalized by the local water depth $h(x)$ (figure 4.4b). For all pressures P, the solitary wave increases in height, but the onshore wind enhances this growth while the offshore wind partially suppresses it. Again, this is apparent in the evolution of the maximums $\eta(x_{\mathrm{peak}})/h_0$ in figure 4.2, which are closely approximated by the x's (since $x_{\mathrm{peak}} \approx x_{\mathrm{pb}}$). Since $\mathrm{Fr} \propto \eta$ to leading order, the relative height at pre-breaking is approximately 0.41 for all P (figure 4.4b) with offshore-forced wave slightly larger (1 %) than onshore-forced waves.

Figure 4.4(c) shows the evolution of the maximum wave slope magnitude $\max_t |\partial_x \eta|$, corresponding to the front face's slope (figures 4.3c,d). Like the relative height (figure 4.4b), the steepness is enhanced by onshore wind $P > 0$, suppressed for offshore wind $P < 0$, and approaches nearly the same pre-breaking value of 0.14 for all wind speeds, being only 1 % larger for offshore winds than onshore winds. Finally, we examine the FWHM L_W, normalized by the local water depth $h(x)$ (figure 4.4d). While $L_W/h(x)$ decreases from its initial value of 4.55 for all pressure magnitudes, there is significant variation in the pre-breaking value. For our parameters, $L_W/h(x)$ changes nearly 16 % more for onshore wind ($P = 0.05$) than offshore wind ($P = -0.05$) from start to pre-breaking. Figures 4.3(a,b) show that the rear shelf does not rise to half the wave height, so the FWHM does not incorporate the shelf's width. Instead, the onshore-forced narrowing is occurring in the top region above the shelf. Hence, while the relative height and slope at pre-breaking are largely similar for all the wind speeds, the FWHM at pre-breaking is strongly

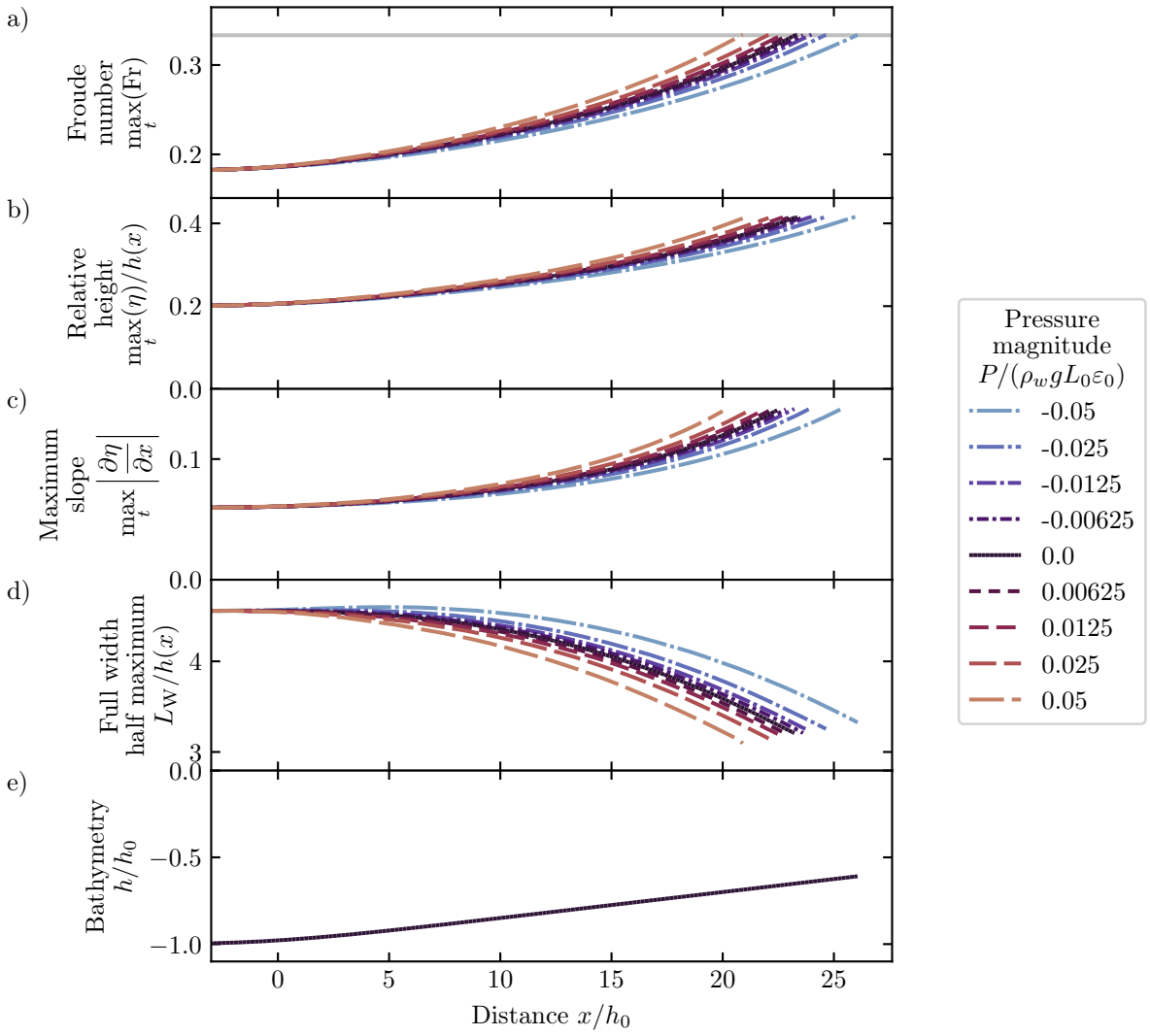

Figure 4.4. Shoaling solitary-wave shape statistics under onshore and offshore pressure forcing versus non-dimensional distance x/h_0. The (a) Froude number $\max_t(\mathrm{Fr})$ (4.31), (b) maximum height normalized by the local water depth $\max_t(\eta)/h(x)$, (c) maximum slope $\max_t(|\partial\eta/\partial x|)$ and (d) full width at half maximum normalized by the local water depth $L_W/h(x)$ (cf. § 4.3.8) are displayed at each location along the (g) planar bathymetry. Results are shown for $\varepsilon_0 = 0.2$, $\mu_0 = 0.15$, $\beta = 0.015$ and pressure magnitude $|P/(\rho_w g L_0 \varepsilon_0)|$ up to 0.05, as indicated in the legend. The solid black line is the unforced case, $P = 0$. The light gray line on (a) represents the convective pre-breaking Froude number $\mathrm{Fr}_{\mathrm{pb}} = 1/3$ at which the simulations were stopped.

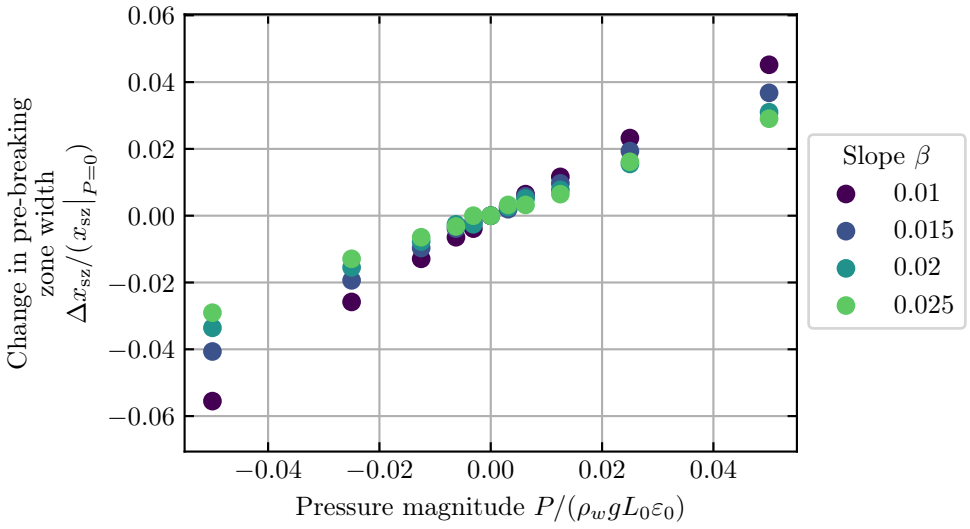

Figure 4.5. The fractional change in pre-breaking zone width Δx_{pz} compared to the unforced case $x_{\text{pz}}|_{P=0}$ (cf. § 4.3.8) versus the non-dimensional pressure magnitude $P/(\rho_w g L_0 \varepsilon_0)$. The results are shown for beach slopes $\beta = 0.01$–0.025 as indicated in the legend.

affected by the wind speed indicating wind effects on shoaling shape.

We also investigate the change in the pre-breaking zone width Δx_{pz} (§ 4.3.8) as a function of pressure $P/(\rho_w g L_0 \varepsilon_0)$ for four different values of the beach slope β (figure 4.5). First, Δx_{pz} is linearly related to the pressure magnitude, and the wind has a larger effect on Δx_{pz} for smaller beach slopes, with $P/(\rho_w g L_0 \varepsilon_0) = -0.05$ changing the pre-breaking zone width by approximately 5 % for the smallest slope $\beta = 0.01$. This is because the wind has more time to affect the wave before it reaches pre-breaking. This wind-induced change in pre-breaking location is visible in figure 4.2, where the breakpoint x_{pb} (x's on green profiles) occurs closer to the shoreline ($+x$ direction) for offshore winds $P < 0$. Additionally, we note that for the smallest slope $\beta = 0.01$, the change in pre-breaking zone width appears asymmetric with respect to pressure, with offshore $P/(\rho_w g L_0 \varepsilon_0) = -0.05$ yielding a 23 % larger change than onshore $P/(\rho_w g L_0 \varepsilon_0) = 0.05$.

4.4.3 Normalized pre-breaking wave shape changes induced by wind and shoaling

As figure 4.4 quantified the shape statistics at pre-breaking for all x, we now directly investigate the effect of pressure P and shoaling β on pre-breaking wave shape by normalizing each pre-breaking wave

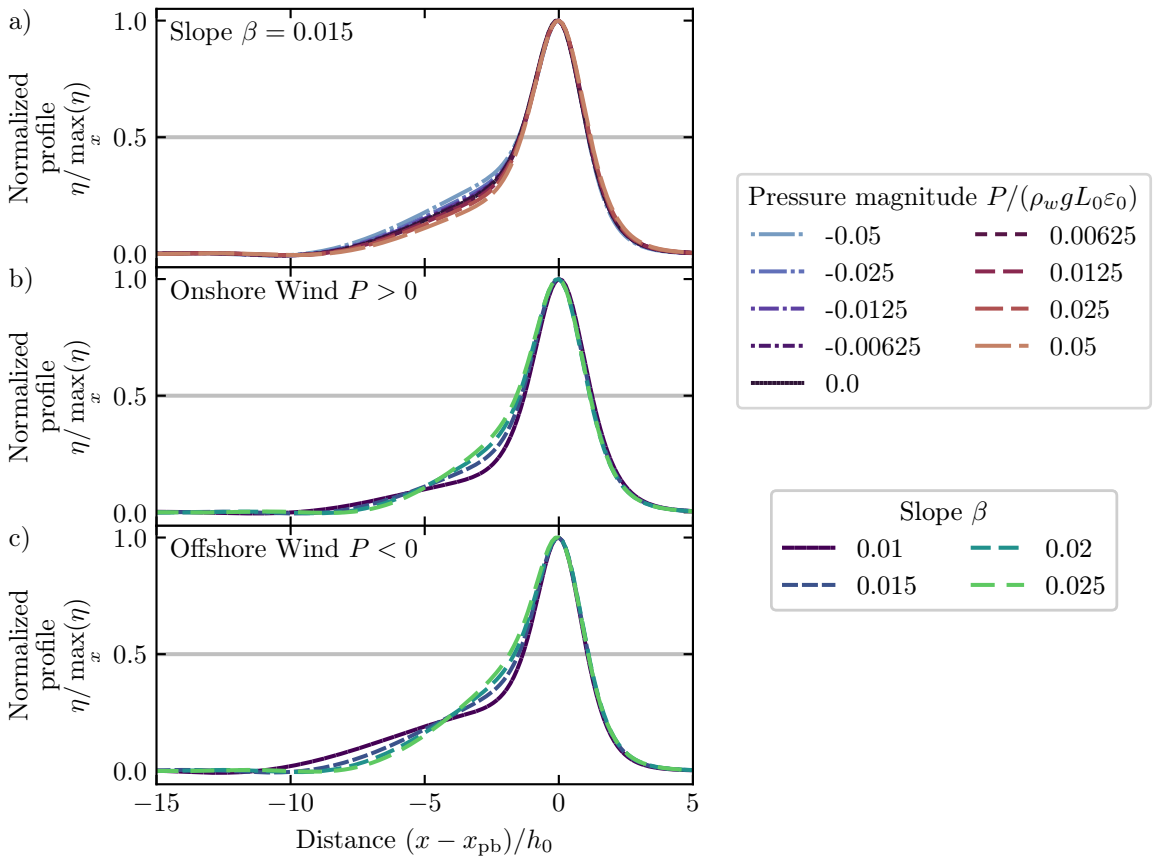

Figure 4.6. Pre-breaking wave profile $\eta(x, t_{\mathrm{pb}})/\max_x(\eta)$ normalized by the maximum height versus non-dimensional position $(x - x_{\mathrm{pb}})/h_0$ relative to the pre-breaking location x_{pb}. All profiles occur at pre-breaking $\max_x(\mathrm{Fr}) = \mathrm{Fr}_{\mathrm{pb}} = 1/3$ (cf. § 4.3.6) and display different values of the (a) pressure magnitude $P/(\rho_w g L_0 \varepsilon_0)$ and the (b,c) bottom slope β, as indicated in the legend. Results are shown for $\varepsilon_0 = 0.2$, $\mu_0 = 0.15$ and (a) slope $\beta = 0.015$, (b) onshore $P/(\rho_w g L_0 \varepsilon_0) = 0.05$ or (c) offshore $P/(\rho_w g L_0 \varepsilon_0) = -0.05$ pressure magnitude. The light gray line shows where the FWHM is measured.

profile η by its maximum height $\max_x(\eta)$ and aligning the pre-breaking locations x_{pb}/h_0 (figure 4.6). For a fixed slope (figure 4.6a), the front wave faces at pre-breaking are qualitatively very similar and match an unforced solitary wave of the same height. However, wind strongly affects the rear shelfs observed in figure 4.2. The offshore winds (blue) cause the shelf to be thicker and extend higher up the rear wave face than the offshore wind (reds) do, though the shelf intersects $z = 0$ at $(x - x_{\mathrm{pb}})/h_0 = -10$ for all wind speeds.

We also consider the wave shape at breaking for different values of the beach slope β with a fixed onshore (figure 4.6b) or offshore (figure 4.6c) wind. Furthermore, the rear face shows that bottom slope β impacts the rear shelf differently than pressure $P/(\rho_w g L_0 \varepsilon_0)$ does. While the shelf intersected $z = 0$ at the same location for all wind speeds (figure 4.6a), increasing β causes the intersection point (i.e. the base of the shelf) to move forward and closer to the peak. Finally, the offshore wind (figure 4.6c) causes a noticeably larger shelf than the onshore wind (figure 4.6b) for the weakest slope $\beta = 0.01$ (purple), with a similar pattern observed in figure 4.3(a) ($\beta = 0.015$) compared to figure 4.3(b) ($\beta = 0.025$). However, this difference is much smaller for the steeper (green) slopes, implying that stronger shoaling partially suppresses the wind-induced shape change because there is less time for pressure to act prior to pre-breaking.

4.5 Discussion

4.5.1 Wind Speed

Our derivation in § 4.3 coupled wind to the wave's motion through the use of a surface pressure (4.5). The resulting vKdV–Burgers equation (4.23) had a wind-induced term dependent on the pressure magnitude constant $P/(\rho_w g L_0 \varepsilon_0)$. We analyzed the evolution and pre-breaking of solitary waves parameterized by different values of P (§ 4.4). While the usage of P was the most natural since it is the physical coupling between wind and waves (in the absence of viscous tangential stress), measuring the surface pressure is challenging in field observations or lab experiments [e.g. 85, 125]. Therefore, we also consider the evolution and pre-breaking of the shoaling solitary waves as a function of the wind speed U. Zdyrski and Feddersen [155] did this by considering a surface pressure acting on a flat-bottom KdV solitary wave initial condition (equivalent to our (4.24)) with dimensional form

$$\eta = \varepsilon h \operatorname{sech}^2\left(\sqrt{\frac{3\varepsilon}{4}}\frac{x}{h}\right)^2, \tag{4.32}$$

Table 4.2. Wind speeds as functions of pressure $P/(\rho_w g L\varepsilon)$ and local depth h for solitary waves (4.32) with $\varepsilon = 0.2$. U_{onshore} corresponds to $P > 0$ and U_{offshore} to $P < 0$. The conversion from $P/(\rho_w g L\varepsilon)$ to U is given in (4.33).

$\lvert P/(\rho_w g L\varepsilon)\rvert$	h[m]	U_{onshore}[m s^{-1}]	U_{offshore}[m s^{-1}]	h[m]	U_{onshore}[m s^{-1}]	U_{offshore}[m s^{-1}]
0	2.5	4.9	4.9	1	3.1	3.1
0.0031	2.5	8.7	1.2	1	5.5	0.73
0.0063	2.5	10	−0.41	1	6.5	−0.26
0.013	2.5	13	−2.6	1	7.9	−1.7
0.025	2.5	16	−5.8	1	9.9	−3.6
0.050	2.5	20	−10	1	13	−6.5

with non-dimensional height $\varepsilon = H/h$ and width $L = 2h/\sqrt{3\varepsilon}$ in water of depth h. They used energy growth rate considerations and a non-separated parameterization by Donelan et al. [125] for periodic, shallow-water waves to approximate the wind speed as

$$\frac{U}{\sqrt{gh}} = 1 \pm \sqrt{\frac{1}{5}\left|\frac{P}{\rho_w g h\varepsilon}\right|\frac{\rho_w}{\rho_a}\frac{2}{4.91}} = 1 \pm \sqrt{\frac{1}{5}\left|\frac{P}{\rho_w g L\varepsilon}\right|\frac{\rho_w}{\rho_a}\frac{4}{4.91\sqrt{3\varepsilon}}}\,, \tag{4.33}$$

where U is measured at a height of half the solitary wave's width. Note that the radicand differs by a factor of 2 from Zdyrski and Feddersen [155] owing to the different definitions of ε. Even though (4.33) was originally applied to flat-bottomed KdV solitary waves (4.24), our assumption that $\gamma = L/L_b \ll 1$ implies that the bathymetry is approximately flat over the wave's width $2L$. Therefore, we use (4.33) to translate between the pressure $P/(\rho_w g L_0\varepsilon_0)$ and the wind speed U at any point on the sloping bathymetry by using the local ε and h and relating the initial pressure to the local pressure $P/(\rho_w g L\varepsilon) = (\varepsilon_0 L_0/\varepsilon L)P/(\rho_w g L_0\varepsilon_0)$.

Table 4.2 shows the onshore ($P > 0$) and offshore ($P < 0$) wind speeds corresponding to the pressures used in our simulations for two representative depths h. It shows that the pressure magnitudes in our simulations correspond to physically reasonable wind speeds, with onshore U up to 13 m s^{-1} for water 1 m deep or 20 m s^{-1} for water 2.5 m deep. Notice that unforced waves with $P = 0$ correspond to a wind speed of $U = \sqrt{gh}$, or a wind that is moving with the wave at its linear phase speed $c = \sqrt{gh}$. In particular, this means that onshore $P > 0$ and offshore $P < 0$ winds with the same pressure magnitude $|P|$ will have different wind speed magnitudes $|U|$. Additionally, note that keeping P fixed implies that the wind speed U changes as the wave shoals. This is mostly due to the decrease in the phase speed $U \propto \sqrt{gh}$, with higher-order effects coming from the ε and L dependence of the radicand in (4.33). Finally, note that as the wave shoals and ε increases, the height at which the wind speed is measured $z = L/2 = h/\sqrt{3\varepsilon}$ decreases.

We now re-examine our results regarding the pre-breaking zone width (figure 4.5) in terms of

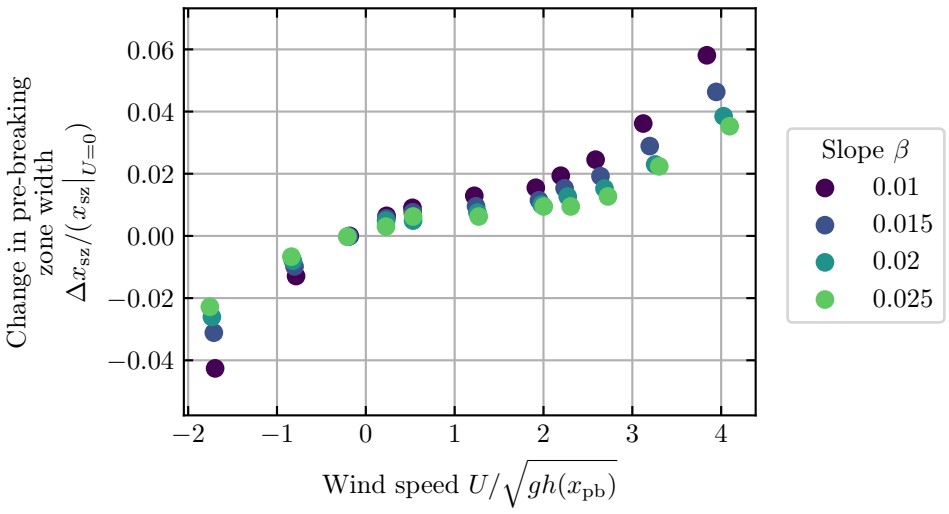

Figure 4.7. The fractional change in pre-breaking zone width Δx_{pz} compared to the unforced case $x_{pz}|_{U=0}$ (cf. § 4.3.8) versus the non-dimensional wind speed $U/\sqrt{gh(x_{pb})}$ normalized by the local, shallow-water phase speed $\sqrt{gh(x_{pb})}$ and evaluated at a height of half the solitary wave width L. The results are shown for beach slopes $\beta = 0.01$–0.025.

the wind speed $U/\sqrt{gh(x)}$ using (4.33). In addition to changing the abscissa of the plot (figure 4.7), we also modify the definition of the change in pre-breaking zone width $\Delta x_{pz} \coloneqq x_{pz} - x_{pz}|_{U=0}$ by comparing and normalizing each pre-breaking zone width to the $U = 0$ case rather than the $P = 0$ case. This transformation changes the initially straight lines of figure 4.5 into approximate pairs of upward- and downward-facing $\sqrt{\Delta x_{pz}}$ curves shifted to the right by one unit (figure 4.7). Furthermore, we see that Δx_{pz} is now much flatter for onshore winds ($U > 0$) than for equal magnitude offshore winds ($U < 0$). This is due to the inflection point of the unforced case ($P = 0$) being shifted to the right at $U/\sqrt{gh} = 1$.

4.5.2 Relationship to previous laboratory experiments and models

Previous laboratory experiments investigated wind's effect on the breaking characteristics of shoaling, periodic waves [e.g. 167, 168]. Douglass [167] considered waves with initial height $H_0/h_0 = 0.3$ and initial inverse wavelength $h_0/\lambda_0 = 0.1$ under wind speeds of up to $U/\sqrt{gh_0} = \pm 2.3$ on a beach with slope 0.04 while King and Baker [168] considered waves with initial height $H_0/h_0 = 0.2$ and initial inverse wavelength $h_0/\lambda_0 = 0.3$ with wind speeds of up to $U/\sqrt{gh_0} = \pm 1.1$ on a beach with slope 0.05. Douglass [167] measured how wind speed changes the width of the surf width for periodic waves. Directly comparing our figure 4.7 to figure 2 of Douglass [167], we see many qualitative similarities, including the flatter response

near $U = 0$ and a stronger response for offshore winds ($U < 0$) than the corresponding onshore winds ($U > 0$). The laboratory studies also found that the relative breaking height $H(x_{\text{break}})/h(x_{\text{break}})$, normalized by the breaking depth, decreased by as much as 40 % for offshore wind speeds of $U/\sqrt{gh(x_{\text{break}})} = 4$ and increased by up to 10 % for onshore wind speeds of $U/\sqrt{gh(x_{\text{break}})} = -2$ compared to the unforced case [e.g. 167, 168]. Likewise, over those same wind speed ranges of $U/\sqrt{gh(x_{\text{pb}})} = 1 \pm 3$, our simulations found that the relative pre-breaking height $H(x_{\text{pb}})/h(x_{\text{pb}})$ varied by approximately 1 % between onshore and offshore winds (figure 4.4*b*), qualitatively consistent with the laboratory experiments. Numerical studies have also investigated the effect of wind on the breaking of shoaling solitary [e.g. 97] and periodic [e.g. 98] waves using a RANS k–ε model to simulate both the air and water. Xie [97] considered solitary waves with initial height $H_0/h_0 = 0.28$ on a beach slope of 0.05 with onshore winds of up to $U/\sqrt{gh_0} = 3$, while Xie [98] investigated periodic waves with initial height $H_0/h_0 = 0.3175$ and initial inverse wavelength $h_0/\lambda_0 = 0.02$ on a beach slope of 0.029 forced by onshore winds up to $U/\sqrt{gh_0} = 2$. These studies determined that the (absolute) maximum wave heights $\max_t(\eta)/h_0$ increased with increasing onshore wind at each location $x < x_{\text{break}}$, consistent with our findings in figure 4.4(b). Furthermore, we can infer from their wave profiles at different wind speeds that the breaking depth $h(x_{\text{break}})$ increased for onshore winds compared to offshore winds, again consistent with our findings.

Our results qualitatively agree with prior experimental and numerical results [97, 167, 168], and the quantitative mismatch can be partly explained by the different non-dimensional parameters. Douglass [167], Xie [97], and Xie [98] all used larger initial waves ($\varepsilon_0 \approx 0.3$), so non-linear effects were likely more important. Likewise, all of the laboratory and numerical experiments discussed used steeper beach slopes, likely further enhancing shoaling and nonlinear interactions. Additionally, while the surfzone width change is nearly five times larger for Douglass [167] than for our simulations over the same wind speed range, Douglass [167] investigated waves that were actually breaking, while we stopped our simulations at pre-breaking $\max_x(\text{Fr}) = \text{Fr}_{\text{pb}} = 1/3$, significantly before actual breaking $\max_x(\text{Fr}) \approx 1$, so we expect smaller changes to the surfzone width. We further expect that, as the waves proceed closer to breaking, the difference between surf zone widths for onshore and onshore winds will increase, bringing our results closer to those of Douglass [167].

4.6 Conclusion

While shoaling-induced changes to wave shape are well-understood, the interaction of wind-induced and shoaling-induced shape changes has not been extensively studied. Utilizing a Jeffreys-type wind-induced

surface pressure, we defined four non-dimensional parameters that controlled our system: the initial wave height ε_0, the inverse wavelength squared μ_0, the pressure strength P_0, and the wave-to-beach width ratio γ_0. We leveraged these small parameters to reduce the forced, variable-bathymetry Boussinesq equations to a variable-coefficient Korteweg–de Vries–Burgers equation for the wave profile η. We also extended the convective breaking criterion of Brun and Kalisch [164] to include pressure and shoaling. A third-order Runge-Kutta solver determined the time evolution of a solitary wave initial condition up a planar beach under the influence of onshore and offshore winds. Stopping the simulations at a pre-breaking Froude number of 1/3 revealed that the pre-breaking relative height and maximum slope are largely independent of wind speed, but onshore winds cause a narrowing of the waves. The width of the pre-breaking zone is strongly modulated by wind speed, with offshore wind decreasing the pre-breaking zone width by approximately 5 % for the mildest beach slopes. Investigating the wave shape at pre-breaking revealed that the front of the wave is relatively unchanged and matches an unforced solitary wave, while the rear shelf is strongly affected by wind speed and bottom slope. By leveraging the relationship between surface pressure P and wind speed U, we directly compared our results to existing experimental and numerical results. We found qualitative agreement in surf width changes and wave height changes, and expect better quantitative agreement as the waves propagate closer to breaking. These results suggest that wind significantly impacts wave breaking, and our simplified model highlights the relevant physics. Future avenues of research could include deriving coupled equations for both the water and air motions to more accurately predict the surface pressure distribution.

4.7 Acknowledgements

We thank the National Science Foundation (OCE-1558695) and the Mark Walk Wolfinger Surfzone Processes Research Fund for their support of this work. The authors report no conflict of interest. Chapter 4, in full, is currently being prepared for submission for publication of the material to Journal of Fluid Mechanics by T. Zdyrski and F. Feddersen. The dissertation author was the primary investigator and author of this paper.

Bibliography

[4] A. Lucas and K. C. Fong, J. Phys. Cond. Matter **30**, 053001, 10.1088/1361-648X/aaa274 (2018).

[5] L. D. Landau and E. M. Lifshitz, *Fluid mechanics*, Course of Theoretical Physics (Pergamon, London, 1959).

[6] L. D. Landau, J. Exp. Theor. Phys. **3**, 920 (1956).

[7] K. S. Novoselov, A. K. Geim, S. V. Morozov, D. Jiang, M. I. Katsnelson, I. V. Grigorieva, S. V. Dubonos, and A. A. Firsov, Nature **438**, 197 (2005).

[8] J. Crossno, J. K. Shi, K. Wang, X. Liu, A. Harzheim, A. Lucas, S. Sachdev, P. Kim, T. Taniguchi, K. Watanabe, T. A. Ohki, and K. C. Fong, Science **351**, 1058 (2016).

[9] I. Torre, A. Tomadin, A. K. Geim, and M. Polini, Phys. Rev. B **92**, 165433, 10.1103/PhysRevB.92.165433 (2015).

[10] A. Tomadin, G. Vignale, and M. Polini, Phys. Rev. Lett. **113**, 235901, 10.1103/PhysRevLett.113.235901 (2014).

[11] L. Levitov and G. Falkovich, Nat. Phy. **12**, 672 (2016).

[12] M. Dyakonov and M. Shur, Phys. Rev. Lett. **71**, 2465 (1993).

[13] D. A. Bandurin, I. Torre, R. K. Kumar, M. B. Shalom, A. Tomadin, A. Principi, G. H. Auton, E. Khestanova, K. S. Novoselov, I. V. Grigorieva, L. A. Ponomarenko, A. K. Geim, and M. Polini, Science **351**, 1055 (2016).

[14] R. K. Kumar, D. A. Bandurin, F. M. D. Pellegrino, Y. Cao, A. Principi, H. Guo, G. H. Auton, M. B. Shalom, L. A. Ponomarenko, G. Falkovich, K. Watanabe, T. Taniguchi, I. V. Grigorieva, L. S. Levitov, M. Polini, and A. K. Geim, Nat. Phy. **13**, 1182 (2017).

[15] A. Lucas and S. Das Sarma, Phys. Rev. B **97**, 115449, 10.1103/PhysRevB.97.115449 (2018).

[16] Z. Sun, D. N. Basov, and M. M. Fogler, Phys. Rev. Lett. **117**, 076805, 10.1103/PhysRevLett.117.076805 (2016).

[17] M. Akbari-Moghanjoughi, J. Appl. Phys. **114**, 073302, 10.1063/1.4818707 (2013).

[18] D. Svintsov, V. Vyurkov, V. Ryzhii, and T. Otsuji, Phys. Rev. B **88**, 245444, 10.1103/PhysRevB.88.245444 (2013).

[19] R. N. Gurzhi, J. Exp. Theor. Phys. **17**, 521 (1963).

[20] D. A. Bandurin, A. V. Shytov, L. S. Levitov, R. K. Kumar, A. I. Berdyugin, M. B. Shalom, I. V. Grigorieva, A. K. Geim, and G. Falkovich, Nat. Commun. **9**, 10.1038/s41467-018-07004-4 (2018).

[21] T. Stauber, N. M. R. Peres, and F. Guinea, Phys. Rev. B **76**, 205423, 10.1103/PhysRevB.76.205423 (2007).

[22] M. Freitag, H.-Y. Chiu, M. Steiner, V. Perebeinos, and P. Avouris, Nat. Nanotechnol. **5**, 497 (2010).

[23] Z.-Y. Ong and E. Pop, Phys. Rev. B **84**, 075471, 10.1103/PhysRevB.84.075471 (2011).

[24] L. Chen, Z. Yan, and S. Kumar, Carbon **123**, 525 (2017).

[25] P. Virtanen, Phys. Rev. B **89**, 245409, 10.1103/PhysRevB.89.245409 (2014).

[26] A. O. Govorov, V. M. Kovalev, and A. V. Chaplik, JETP Lett. **70**, 488 (1999).

[27] L. Fritz, J. Schmalian, M. Müller, and S. Sachdev, Phys. Rev. B **78**, 085416, 10.1103/PhysRevB.78.085416 (2008).

[28] C. C. Mei, M. Stiassnie, and D. K.-P. Yue, *Theory and applications of ocean surface waves: nonlinear aspects*, Vol. 23 (World scientific, 2005).

[29] M. Akbari-Moghanjoughi, Indian J. Phys. **86**, 413 (2012).

[30] D. Svintsov, V. Vyurkov, S. Yurchenko, T. Otsuji, and V. Ryzhii, J. Appl. Phys. **111**, 083715, 10.1063/1.4705382 (2012).

[31] E. McCann and V. I. Fal'ko, Phys. Rev. Lett. **96**, 086805, 10.1103/PhysRevLett.96.086805 (2006).

[32] J. Zhu and P. Ji, Phys. Rev. E **81**, 036406, 10.1103/PhysRevE.81.036406 (2010).

[33] A. P. Dmitriev, V. Y. Kachorovskii, and M. S. Shur, Appl. Phys. Lett. **79**, 922 (2001).

[34] V. N. Popov, Phys. Rev. B **66**, 153408, 10.1103/PhysRevB.66.153408 (2002).

[35] H. Bong, S. B. Jo, B. Kang, S. K. Lee, H. H. Kim, S. G. Lee, and K. Cho, Nanoscale **7**, 1314 (2015).

[36] M. J. Ablowitz, D. J. Kaup, A. C. Newell, and H. Segur, Stud. Appl. Math. **53**, 249 (1974).

[37] C. S. Gardner, J. M. Greene, M. D. Kruskal, and R. M. Miura, Phys. Rev. Lett. **19**, 1095 (1967).

[38] E. I. Kiselev and J. Schmalian, Phys. Rev. B **99**, 035430, 10.1103/PhysRevB.99.035430 (2019).

[39] R. C. V. Coelho, M. Mendoza, M. M. Doria, and H. J. Herrmann, Phys. Rev. B **96**, 184307, 10.1103/PhysRevB.96.184307 (2017).

[40] M. a division of Waterloo Maple Inc., *Maple 2018*, Waterloo, Ontario, 2018.

[41] D. Wood, *The computation of polylogarithms*, tech. rep. 15-92* (University of Kent, Computing Laboratory, University of Kent, Canterbury, UK, June 1992), pp. 182–196.

[42] A. Lucas, J. Crossno, K. C. Fong, P. Kim, and S. Sachdev, Phys. Rev. B **93**, 075426, 10.1103/PhysRevB.93.075426 (2016).

[43] M. Müller, L. Fritz, and S. Sachdev, Phys. Rev. B **78**, 115406, 10.1103/PhysRevB.78.115406 (2008).

[44] K. Hasselmann, in Proc. symp. time series analysis, edited by M. Rosenblatt (John Wiley, 1962), pp. 125–139.

[45] S. Elgar, M. H. Freilich, and R. T. Guza, J. Geophys. Res. Oceans **95**, 16055 (1990).

[46] T. G. Drake and J. Calantoni, J. Geophys. Res. Oceans **106**, 19859 (2001).

[47] T.-J. Hsu and D. M. Hanes, J. Geophys. Res. Oceans **109** (2004).

[48] D. Gonzalez-Rodriguez and O. S. Madsen, Coast. Eng. **54**, 914 (2007).

[49] F. Hoefel and S. Elgar, Science **299**, 1885 (2003).

[50] F. Grasso, H. Michallet, and E. Barthélemy, J. Geophys. Res. Oceans **116** (2011).

[51] F. C. Jackson, J. Geophys. Res. Oceans **84**, 4939 (1979).

[52] G. Hayne, IEEE Trans. Antennas Propag. **28**, 687 (1980).

[53] N. E. Huang, S. R. Long, C.-C. Tung, Y. Yuan, and L. F. Bliven, J. Geophys. Res. Oceans **88**, 7597 (1983).

[54] D. B. Kunkee and A. J. Gasiewski, Radio Sci. **32**, 59 (1997).

[55] J. R. Piepmeier and A. J. Gasiewski, IEEE Trans. Geosci. Remote Sens. **39**, 606 (2001).

[56] J. T. Johnson and Y. Cai, IEEE Trans. Geosci. Remote Sens. **40**, 66 (2002).

[57] G. C. Soares, N. Fonseca, and R. Pascoal, J. Ship Res. **52**, 30 (2008).

[58] J. Oberhagemann, J. Ley, and B. O. el Moctar, in Asme 2012 31st international conference on ocean, offshore and arctic engineering (American Society of Mechanical Engineers Digital Collection, 2013), pp. 583–593.

[59] S. Elgar and R. T. Guza, J. Fluid Mech. **161**, 425 (1985).

[60] S. Elgar and R. T. Guza, J. Fluid Mech. **167**, 1 (1986).

[61] H. Chen and Q. Zou, J. Geophys. Res. Oceans **123**, 3761 (2018).

[62] H. Chen and Q. Zou, Appl. Ocean Res. **89**, 23 (2019).

[63] H. Jeffreys, Proc. R. Soc. Lond. A **107**, 189 (1925).

[64] M. L. Banner and W. K. Melville, J. Fluid Mech. **77**, 825 (1976).

[65] J. Touboul and C. Kharif, Phys. Fluids **18**, 108103 (2006).

[66] Z. Tian and W. Choi, Eur. J. Mech. B Fluids **41**, 11 (2013).

[67] S. E. Belcher and J. C. R. Hunt, J. Fluid Mech. **251**, 109 (1993).

[68] O. M. Phillips, J. Fluid Mech. **2**, 417 (1957).

[69] J. W. Miles, J. Fluid Mech. **3**, 185 (1957).

[70] M. J. Lighthill, J. Fluid Mech. **14**, 385 (1962).

[71] P. Janssen, *The interaction of ocean waves and wind* (Cambridge University Press, 2004).

[72] M. S. Longuet-Higgins, Proc. R. Soc. Lond. Ser. A Math. Phys. Sci. **265**, 286 (1962).

[73] R. L. Snyder, J. Mar. Res. **24**, 141 (1966).

[74] K. F. Hasselmann, T. P. Barnett, E. Bouws, H. Carlson, D. E. Cartwright, K. Enke, J. A. Ewing, H. Gienapp, D. E. Hasselmann, P. Kruseman, A. Meerburg, D. J. Müller andOlbers, K. Richter, W. Sell, and H. Walden, Dtsch. Hydrogr. Z **8** (1973).

[75] O. H. Shemdin and E. Y. Hsu, J. Fluid Mech. **30**, 403 (1967).

[76] W. J. Plant and J. W. Wright, J. Fluid Mech. **82**, 767 (1977).

[77] H. Mitsuyasu and T. Honda, J. Fluid Mech. **123**, 425 (1982).

[78] T. Lamont-Smith and T. Waseda, J. Phys. Oceanogr. **38**, 1597 (2008).

[79] Y. I. Troitskaya, D. A. Sergeev, A. A. Kandaurov, G. A. Baidakov, M. A. Vdovin, and V. I. Kazakov, J. Geophys. Res. Oceans **117** (2012).

[80] M. A. Donelan, A. V. Babanin, I. R. Young, M. L. Banner, and C. McCormick, J. Atmos. Ocean. Technol. **22**, 799 (2005).

[81] P. R. Gent and P. A. Taylor, J. Fluid Mech. **77**, 105 (1976).

[82] M. A. Al-Zanaidi and W. H. Hui, J. Fluid Mech. **148**, 225 (1984).

[83] F. Veron, G. Saxena, and S. K. Misra, Geophys. Rese. Lett. **34** (2007).

[84] M. P. Buckley and F. Veron, Exp. Fluids **58** (2017).

[85] M. P. Buckley and F. Veron, Eur. J. Mech. B Fluids **73**, 132 (2019).

[86] D. Yang and L. Shen, Phys. Fluids **21** (2009).

[87] D. Yang and L. Shen, J. Fluid Mech. **650**, 131 (2010).

[88] Z. Yang, B.-Q. Deng, and L. Shen, J. Fluid Mech. **850**, 120 (2018).

[89] D. Yang, C. Meneveau, and L. Shen, J. Fluid Mech. **726**, 62 (2013).

[90] T. Hara and P. P. Sullivan, J. Phys. Oceanogr. **45**, 868 (2015).

[91] X. Hao, T. Cao, Z. Yang, T. Li, and L. Shen, Procedia IUTAM **26**, 162 (2018).

[92] Y. Liu, D. Yang, X. Guo, and L. Shen, Phys. Fluids **22**, 041704 (2010).

[93] X. Hao and L. Shen, J. Fluid Mech. **874**, 391 (2019).

[94] L. Deike, N. Pizzo, and W. K. Melville, J. Fluid Mech. **829**, 364 (2017).

[95] Q. Zou and H. Chen, J. Phys. Oceanogr. **47**, 1817 (2017).

[96] S. Yan and Q. W. Ma, Eur. J. Mech. B Fluids **29**, 18 (2010).

[97] Z. Xie, Eur. J. Mech. B Fluids **43**, 135 (2014).

[98] Z. Xie, Ocean Dyn. **67**, 1251 (2017).

[99] C. Cox and W. Munk, Bull. Scripps Inst. Oceanogr. **6**, 401 (1956).

[100] I. A. Leykin, M. A. Donelan, R. H. Mellen, and D. J. McLaughlin, Nonlinear Process Geophys. **2**, 280 (1995).

[101] F. Feddersen and F. Veron, J. Phys. Oceanogr. **35**, 1223 (2005).

[102] M. J. Ablowitz, *Nonlinear dispersive waves: asymptotic analysis and solitons*, Vol. 47 (Cambridge University Press, 2011).

[103] G. G. Stokes, Trans. Cambridge Philos. Soc. **3**, 441 (1880).

[104] J. F. Toland, "On the symmetry theory for Stokes waves of finite and infinite depth", English, in *Trends in applications of mathematics to mechanics*, Monographs and Surveys in Applied Mathematics (Chapman and Hall/CRC, 1999).

[105] G. B. Whitham, *Linear and nonlinear waves*, Vol. 42 (John Wiley & Sons, 2011).

[106] M. Brunetti and J. Kasparian, Phys. Lett. A **378**, 3626 (2014).

[107] J. M. Kendall, J. Fluid Mech. **41**, 259 (1970).

[108] N. T. Husain, T. Hara, M. P. Buckley, K. Yousefi, F. Veron, and P. P. Sullivan, J. Phys. Oceanogr. **49**, 1997 (2019).

[109] M. S. Longuet-Higgins, Phys. Fluids **12**, 737 (1969).

[110] C. Fang, *An introduction to fluid mechanics* (Springer, 2019).

[111] M. L. Banner and J.-B. Song, J. Phys. Oceanogr. **32**, 2559 (2002).

[112] A. G. Kalmikov, "Modeling wind forcing in phase resolving simulation of nonlinear wind waves", PhD thesis (Massachusetts Institute of Technology, 2010).

[113] M. Brunetti, N. Marchiando, N. Berti, and J. Kasparian, Phys. Lett. A **378**, 1025 (2014).

[114] G. J. Komen, L. Cavaleri, M. Donelan, K. Hasselmann, S. Hasselmann, and P. A. E. M. Janssen, *Dynamics and modelling of ocean waves* (Cambridge University Press, 1994).

[115] A. S. Monin and A. M. F. Obukhov, Tr. Geofiz. Inst., Akad. Nauk SSSR **24**, 163 (1954).

[116] P. K. Taylor and M. J. Yelland, J. Phys. Oceanogr. **31**, 572 (2001).

[117] P. A. E. M. Janssen, J. Fluid Mech. **117**, 493 (1982).

[118] S. Leblanc, Phys. Fluids **19** (2007).

[119] C. Kharif, R. A. Kraenkel, M. A. Manna, and R. Thomas, J. Fluid Mech. **664**, 138 (2010).

[120] M. Onorato and D. Proment, Phys. Lett. A **376**, 3057 (2012).

[121] C. C. Mei, M. Stiassnie, and D. K. P. Yue, *Theory and applications of ocean surface waves: nonlinear aspects*, Advanced Series on Ocean Engineering 2 (World Scientific, 2005).

[122] E. V. Laitone, J. Geophys. Res. **67**, 1555 (1962).

[123] Z. Song, H. Zhao, L. Li, and G. Lü, Sci. China Earth Sci. **56**, 102 (2013).

[124] M. P. Buckley and F. Veron, J. Phys. Oceanogr. **46**, 1377 (2016).

[125] M. A. Donelan, A. V. Babanin, I. R. Young, and M. L. Banner, J. Phys. Oceanogr. **36**, 1672 (2006).

[126] P. P. Sullivan, J. C. McWilliams, and C.-H. Moeng, J. Fluid Mech. **404**, 47 (2000).

[127] W. R. Young and C. L. Wolfe, J. Fluid Mech. **739**, 276 (2014).

[128] G. Pedersen, *Multiple scale methods*, Lecture Notes, Mathematical Methods in Mechanics. University of Oslo, Mar. 2006.

[129] P. A. E. M. Janssen, J. Phys. Oceanogr. **21**, 1631 (1991).

[130] P. P. Sullivan and J. C. McWilliams, Annu. Rev. Fluid Mech. **42**, 19 (2010).

[131] T. Zdyrski and F. Feddersen, J. Fluid Mech. **903**, A31 (2020).

[132] F. Zonta, A. Soldati, and M. Onorato, J. Fluid Mech. **777**, 245 (2015).

[133] Y. S. Kivshar, IEEE J. Quantum Electron. **29**, 250 (1993).

[134] B. Sahu and M. Tribeche, Astrophys. Space Sci. **338**, 259 (2012).

[135] W. H. Munk, Ann. N. Y. Acad. Sci. **51**, 376 (1949).

[136] J. L. Hammack and H. Segur, J. Fluid Mech. **65**, 289 (1974).

[137] J. W. Miles, J. Fluid Mech. **91**, 181 (1979).

[138] P. Lin and P. L.-F. Liu, J. Fluid Mech. **359**, 239 (1998).

[139] J. J. Monaghan and A. Kos, J. Waterw. Port Coast. Ocean Eng. **125**, 145 (1999).

[140] P. Lin, Coast. Eng. **51**, 35 (2004).

[141] G. Xu, Q. Chen, and J. Chen, J. Bridge Eng **23**, 04018023 (2018).

[142] H. Sandstrom and N. Oakey, J. Phys. Oceanogr. **25**, 604 (1995).

[143] T. Zdyrski and J. McGreevy, Phys. Rev. B **99**, 235435 (2019).

[144] N. Antar and H. Demiray, Int. J. Eng. Sci. **37**, 1859 (1999).

[145] L. Cavaleri and P. M. Rizzoli, J. Geophys. Res. Oceans **86**, 10961 (1981).

[146] C. Kharif, J. P. Giovanangeli, J. Touboul, L. Grare, and E. Pelinovsky, J. Fluid Mech. **594**, 209 (2008).

[147] R. Johnson, J. Fluid Mech. **54**, 81 (1972).

[148] H. Ono, J. Phys. Soc. Japan **32**, 332 (1972).

[149] J. Hadamard, Princet. Univ. Bull., 49 (1902).

[150] K. J. Burns, G. M. Vasil, J. S. Oishi, D. Lecoanet, and B. P. Brown, Phys. Rev. Res. **2**, 023068 (2020).

[151] D. G. Dommermuth and D. K. Yue, J. Fluid Mech. **184**, 267 (1987).

[152] J. Wu, J. Fluid Mech. **34**, 91 (1968).

[153] O. M. Phillips and M. L. Banner, J. Fluid Mech. **66**, 625 (1974).

[154] C. J. Amick and J. F. Toland, Philos. Trans. R. Soc. A **303**, 633 (1981).

[155] T. Zdyrski and F. Feddersen, J. Fluid Mech. **913**, A27 (2021).

[156] M. H. Freilich and R. T. Guza, Philos. Trans. R. Soc. A **311**, 1 (1984).

[157] J. A. Zelt, Coast. Eng. **15**, 205 (1991).

[158] S. Beji and J. A. Battjes, Coast. Eng. **19**, 151 (1993).

[159] S. T. Grilli, R. Subramanya, I. A. Svendsen, and J. Veeramony, J. Waterway Port Coast. Ocean Eng. **120**, 609 (1994).

[160] J. Knowles and H. Yeh, J. Fluid Mech. **848**, 1073 (2018).

[161] S. T. Grilli, I. A. Svendsen, and R. Subramanya, J. Waterw. Port Coast. Ocean Eng. **123**, 102 (1997).

[162] M. Derakhti, J. T. Kirby, M. L. Banner, S. T. Grilli, and J. Thomson, J. Geophys. Res **125**, e2019JC015886 (2020).

[163] W. Mostert and L. Deike, J. Fluid Mech. **890** (2020).

[164] M. K. Brun and H. Kalisch, Anal. Math. Phys. **8**, 57 (2018).

[165] C. R. Iribarren, in Xviith international naval congress (lisbon, portugal), 1949 (1949), pp. 31–80.

[166] J. L. Lara, A. Ruju, and I. J. Losada, Proc. R. Soc. Lond. A **467**, 1215 (2011).

[167] S. L. Douglass, J. Waterw. Port Coast. Ocean Eng. **116**, 651 (1990).

[168] D. M. King and C. J. Baker, J. Hydraul. Res. **34**, 55 (1996).

[169] R. S. Johnson, Math. Proc. Camb. Philos. Soc. **73**, 183 (1973).

[170] I. A. Svendsen and J. B. Hansen, J. Fluid Mech. **87**, 433 (1978).

[171] P. Virtanen, R. Gommers, T. E. Oliphant, M. Haberland, T. Reddy, D. Cournapeau, E. Burovski, P. Peterson, W. Weckesser, J. Bright, S. J. van der Walt, M. Brett, J. Wilson, K. J. Millman, N. Mayorov, A. R. J. Nelson, E. Jones, R. Kern, E. Larson, C. J. Carey, İ. Polat, Y. Feng, E. W. Moore, J. VanderPlas, D. Laxalde, J. Perktold, R. Cimrman, I. Henriksen, E. A. Quintero, C. R. Harris, A. M. Archibald, A. H. Ribeiro, F. Pedregosa, P. van Mulbregt, and SciPy 1.0 Contributors, Nature Methods **17**, 261 (2020).

[172] J. W. Miles, J. Phys. Oceanogr. **13**, 551 (1983).